University of Catania

Doctoral Thesis

$K^*(892)^{\pm}$ resonance with the ALICE detector at LHC

Author:
Kunal Garg

Supervisor:
Prof. Francesco Riggi
Dr. Angela Badalà

A thesis submitted in fulfillment of the requirements
for the degree of Doctor of Philosophy Cycle XXXI

in the

Dipartimento di Fisica e Astronomia

November 30, 2018

“The greatest gift of education, Korya, is the years of shelter provided when learning. Do not think to reduce that learning to facts and the utterances of presumed sages. Much of what one learns in that time is in the sphere of concord, the ways of society, the proprieties of behaviour and thought. Haut would tell you that this is another hard-won achievement of civilization: the time and safe environment in which to learn how to live. When this is destroyed, undermined or discounted, then that civilization is in trouble (1)”

Steven Erikson

Contents

List of Figures

List of Tables

Introduction

The thesis reports a measurement of $K^{*}(892)^{\pm}$ in pp collisions at $\sqrt{s}$ = 13 TeV. In particular the transverse momentum spectrum has been measured in inelastic pp collisions and in different multiplicity classes. The $K^{*}(892)^{0}$ production has been studied at the same energy and compared with the charged resonance production.

Quantum ChromoDynamics (QCD), the theory of strong interactions, is well known in the perturbative regime, while it is not fully understood in the non-perturbative domain, where the generation of the hadronic matter and the quark confinement should be described. The gluon self-coupling is responsible for the asymptotic freedom of the interaction and confinement. QCD predicts that the strong coupling strength decreases with increasing energy or momentum transfer, and vanishes at asymptotically high energies. The observation of Higgs boson has been able to explain how elementary particles attain mass through Yukawa coupling and spontaneous symmetry breaking, but the quarks only account for about 5 % of the hadronic mass, that instead is generated dynamically by strong interaction inside the hadrons. The state of matter where quarks are deconfined and chiral symmetry is restored, named Quark-Gluon-Plasma (QGP), predicted on the basis of thermodynamical considerations and QCD calculations, has been observed in heavy ion collisions at the RHIC and LHC energies. This state of matter should be present after the electro-weak phase transition, about 1μs after the Big Bang. Then with a phase transition the initial deconfined partons plasma would have reached the hadronic phase. The study of the QGP phase and QCD phase transition is therefore necessary to solve the open puzzle of the onset of confinement and the hadron masses. This is done experimentally with ultra-relativistic heavy-ion collisions, where the energy density and temperature reached may be sufficient to form the QGP. Though recently, hints of collective effects or of features typical of ultrarelativistic heavy-ion collisions (such as enhancement of strangeness production) have begun to be observed in high multiplicity pp collisions as well.

The measurement of the production of strange resonances in ultrarelativistic proton-proton collisions permits characterisation of the global properties of the collisions and to probe strangeness production. Furthermore it helps in understanding hadron production processes and in improving the description of hadronisation of strange particles in event generators such as PYTHIA, EPOS-LHC. Additionally the measurement of resonances over a large transverse momentum range and at different collision energies permits to probe the perturbative (hard) and the non-perturbative (soft) QCD processes. Hadronic resonances are also important probes of the hadronic phase of the medium formed during the heavy-ion collisions. $K^*(892)^{\pm}$ and $K^*(892)^0$ are strange vector mesons with a lifetime of $\sim$ 4 fm/c, comparable to the fireball produced in heavy ion collisions. Thus it is expected that regeneration and rescattering processes occurring during the hadronic phase should modify the measured $K^{*\pm}$ and K^{*0} meson yields. Measurements in inelastic pp collisions constitute a reference for the study in larger colliding systems and a benchmark of the existing hadronisation models in elementary collisions, while measurements in pp collisions at high multiplicity should test the characteristics of the QCD matter formed in these collisions.

This thesis is divided in eight chapters.

Chapter 1 The general physics context, with an introduction to QCD and the connection with the idea of the QGP, obtained at high density and temperature, is given in this first chapter. In addition a general description of the fundamental characteristics of heavy-ion collision and the time evolution of the created system are presented. Some new interesting results observed in small systems as a function of the event multiplicity will be also presented.

Chapter 2 In this chapter the importance of the resonances for the characterisation of the hadronic phase will be discussed. Some of the main results recently observed will be presented. Strange hadron production in pp collisions is a key to understand strangeness production and hadronisation. Some of the main event generators and models as (PYTHIA, EPOS-LHC, PHSD) will be described

Chapter 3 In this chapter the detection capabilities of the ALICE apparatus are given with specific focus on Time Projection Chamber (TPC), Time of Flight Detector (TOF), and Inner Tracking System (ITS). Moreover, the details on the different steps necessary to convert the electronic signals from the detectors into data suitable for analysis are presented.

Chapter 4 The methods used to estimate the raw yields for K^{*0} and $K^{*\pm}$ is described. The measurement of the $K^{*\pm}$ characteristics such as mass and width is also described.

Chapters 5 Measurement of the transverse momentum spectrum of $K^{*\pm}$ and of its yield in inelastic pp collisions at $\sqrt{s}$ = 13 TeV is described in this chapter.

Chapter 6 Measurement of the K^{*0} transverse momentum spectrum in pp collisions at 13 TeV and its comparison with the charged K^* results are discussed here.

Chapter 7 Main physics results obtained with the measurement of the $K^{*\pm}$ p_T spectrum in inelastic pp collisions at 13 TeV. In particular, comparison with other collision energies, ratios with other particles (such as pion and Kaon) are discussed. Furthermore comparison with PYTHIA8, PYTHA6, EPOS-LHC event generators are presented. Transverse momentum spectra for

K^{*+} and K^{*-}, separately and prediction from event generators are also discussed.

Chapter 8 $K^{*\pm}$ results as a function of event charged particle multiplicity are presented here. In particular, p_T spectrum, $\langle p_T \rangle$, dN/dy, and ratio to kaons in different multiplicity classes are presented and compared to the same observables measured for K^{*0} at the same collision energy.

Chapter 1

Physics of the Hot QCD matter

1.1 Standard Model

Since the advent of Quantum Mechanics (2) in 1920s, the subsequent theories, and discoveries have resulted in a remarkable insight into the fundamental structure of matter. We have discovered that everything in the universe is built from some basic fundamental building blocks called elementary particles and four fundamental forces that govern their interactions. The Standard Model (SM) of particle physics is the theory describing three of the four known fundamental forces (the electromagnetic, weak, and strong interactions, and not including the gravitational force) in the universe, as well as classifying all known elementary particles. The Standard Model was developed in 1970s and since then has passed every experimental test thrown its way with astonishing accuracy. There are seventeen particles in the standard model, organised into the Figure 1.1. The last particles discovered were the W and Z bosons in 1983 (3), the top quark in 1995 (4), the tau neutrino in 2000 (5), and the Higgs boson in 2012 (6).

All elementary particles depending on their spin are separated into either bosons or fermions. These are differentiated via the spin-statistics theorem of quantum statistics. Particles of integer spin exhibit Bose-Einstein statistics and are bosons. Particles of half-integer spin exhibit Fermi-Dirac statistics and are fermions. They also follow the Pauli exclusion principle. This states that two fermions may not be described by the same quantum numbers. There are twelve fermions and five bosons in the standard models.

The mathematical formulation of the SM is quite complex. The information has been encoded into a single *Lagrangian* which can be compactified into a four line version as:

$$\begin{aligned}\mathcal{L} = &-\frac{1}{4}F_{\mu\nu}F^{\mu\nu} \\ &+ i\bar{\psi}D\psi + h.c. \\ &+ \bar{\psi}_i y_{ij}\psi_j\phi + h.c. \\ &+ |D_\mu\phi|^2 - V(\phi)\end{aligned}$$

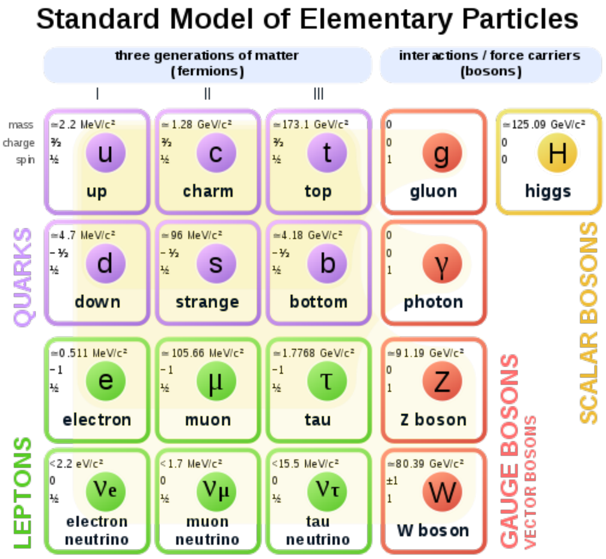

FIGURE 1.1: Standard Model chart

Here, $\mathcal{L}$ is defined such that the Lagrangian L is its integral over density space. The term $-1/4F_{\mu\nu}F^{\mu\nu}$ is the scalar product of the field strength tensor $F_{\mu\nu}$ containing the mathematical encoding of all interaction particles except the Higgs boson, where μ and ν are Lorentz indices representing the spacetime components. The term $i\bar{\psi}\not{D}\psi$ describes how interaction particles interact with matter particles. The fields ψ and $\bar{\psi}$ describe (anti)quarks and (anti)leptons. The bar over $\bar{\psi}$ means that the corresponding vector must be transposed and complex-conjugated; a technical trick to ensure that the Lagrangian density remains scalar and real. $\not{D}$ is the so-called covariant derivative, featuring all the interaction particles (except the Higgs), but this time without self-interactions. The term $\psi_i y_{ij} \psi_j \phi$ describes how matter particles couple to the Brout-Englert-Higgs field ϕ and thereby obtain mass. The entries of the Yukawa matrix y_{ij} represent the coupling parameters to the Brout-Englert-Higgs field, and hence are directly related to the mass of the particle in question. These parameters are not predicted by theory, but have been determined experimentally. The term $|D_\mu \phi|^2$ describes how the interaction particles couple to the BEH field. This applies only to the interaction particles of the weak interaction, which thereby obtain their mass. And lastly, the term $-V(\phi)$ describes the potential of the BEH field. Contrary to the other quantum fields, this potential does not have a single minimum at zero but has an infinite set of different minima.

1.2 Quantum Chromodynamics and QGP

Soon after the discovery of atomic nucleus, existence of a binding force holding together the nucleons in the nuclei was postulated to assure nucleus stability. This was termed as the strong nuclear force (1934). The discovery of neutron (7) and later of pion (8) started to provider a rather satisfactory picture of the nucleus with the pion recognised as the long searched Yukawa particle of the strong interaction. This early picture turned out to be too simplistic soon as new particles were being discovered in new experiments. The idea of protons with constituent particles, *quarks* began to emerge. Deep inelastic experiments shed further light on the nucleonic structure, and properties of the strong interaction. The quarks exist in six different flavours and carry strong "colour" charge in three different types. The "mediators" of the strong force, playing the same role of the photon for electromagnetism, are called *gluons*, which come in eight colour combinations. The major difference between gluons and photons comes from self-interaction which leads to two following properties of the "colour force":

Colour confinement: Quarks are always observed in a colourless combinations inside hadrons, and never as free quarks.
Asymptotic freedom: the value of the strong coupling constant, α_S, depends on the momentum transfer (Q^2) at which an observed process occurs (running coupling constant). α_S decreases with increasing energy and asymptotically, at infinite energy, goes to zero.

Another aspect which is important when discussing the strong force is the mass of the hadrons. Sum of constituent quarks of most hadrons made up of the three lightest quarks, is only a small fraction of the actual hadron mass. For instance, the proton (uud) mass is 1 GeV/c^2 while the sum of the bare masses of its constituent quarks is about 25 MeV/c^2. The explanation for this phenomenon is accomplished by a process named "Chiral symmetry breaking".

Chiral symmetry breaking

The interaction of quarks and gluons is described with a gauge field theory called "Quantum Chromodynamics" (QCD) in a manner very similar to what QED does for electrons and photons. In both cases, we have spinor matter fields interacting through massless vector gauge fields. In QCD however, the intrinsic colour charge is associated with the non-Abelian gauge group SU(3), in place of the Abelian group U(1) for the electric charge in QED. As a result, quarks carry three colour charges, and gluons carry eight combinations of these colour charges. Gluon as a result becomes self-interactive, in contrast to an ideal gas of photons. The three dimensional Laplace equation, which in non relativistic QED approximated to Coulomb potential ($V \propto 1/r$); for massive quarks becomes effectively one dimensional, with the confining potential ($V \propto r$) as a solution. The Lagrangian density of QCD is given by:

$$L = -\frac{1}{4} F^a_{\mu\nu} F_a^{\mu\nu} + \sum_f \overline{\psi}^f_a (i\gamma_\mu D^\mu) \psi^f_\beta \tag{1.1}$$

with the non-Abelian group tensor

$$F^a_{\mu\nu} = (\partial_\mu A^a_\nu - \partial_\nu A^a_\nu - g f^a_{bc} A^b_\mu A^c_{nu}) \tag{1.2}$$

and

$$D_\mu = \partial_\mu + ig\frac{\lambda_a}{2}A^a_\mu \tag{1.3}$$

The fundamental degrees of freedom of the theory are the 3 × 6 quark fermionic fields ψ, and the eight gluonic fields A_μ. λ_a and f^a_{bc} are the eight SU(3) group generators (the 3 × 3 Gell-Mann matrices) and structure constants. In the definition above, the ψ represents for each flavour, a vector (ψ_{red}; ψ_{green}; ψ_{blue}) of the fermionic fields. Since they are based on non-Abelian symmetry group, interaction terms between the vector bosons of the theory, the gluons, are present. The inclusion of quark mass adds a L_m term to the Equation 1.1.

$$L_m = \sum_f m_f \overline{\psi}^f_a \psi^{fa} \tag{1.4}$$

If the mass term is neglected, the QCD Lagrangian in the Equation 1.1 becomes chirally symmetric i.e. invariant under separate flavour rotations of the right and left-handed quarks. Neglecting the mass term is a good approximation for the very light up and down quarks and a reasonable approximation for strange quarks. The non-zero vacuum expectation value of the scalar quark density operator $\overline{\psi}\psi$ breaks this symmetry and leads to a dynamic mass of the order 300 MeV for the up and down quarks and about 450 MeV for the strange quarks. A pictorial view of the spontaneous chiral symmetry breaking mechanism can be seen in the Figure 1.2.

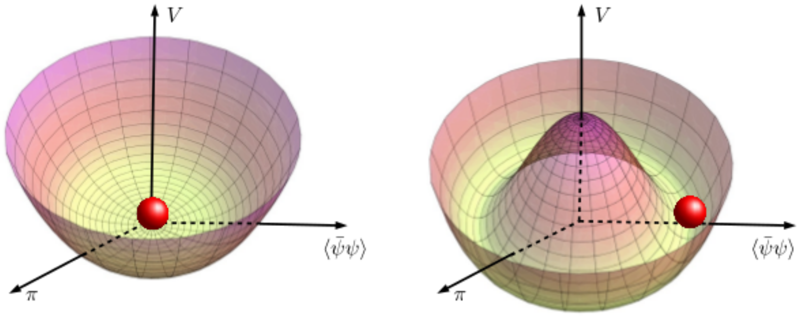

FIGURE 1.2: Pictorial view of the spontaneous breaking of the chiral symmetry. The quark, represented by the sphere, tends to occupy the minimum energy state: in the left configuration, it correspond to a symmetric state; in the right configuration, representing the confined quark in a nucleon, the parton is forced to break the symmetry and occupies an asymmetric state

1.2.1 QCD Phase trasition

Strongly interacting matter can exist in different phases characterised by a given temperature and densities, as summarised in the QCD phase diagram (see Figure 1.3) where temperature versus baryo-chemical potential μ_B is reported. The baryo-chemical potential is defined as the energy needed to increase by one unity, the total number of baryons and anti-baryons in a system (N_B),

$$\mu_B = \partial E / \partial N_B$$

and it is introduced to consider that at relativistic energies, the particle number in a system may not be conserved due to particle annihilation and creation processes at microscopic level. In this diagram, standard nuclear matter is represented at low temperatures and low μ_B. By increasing the temperature or the potential, the hadronic gas (HG) is attained. At a given temperature and potential, a new phase of matter, the Quark Gluon plasma should exist. In this phase, the quarks are no longer confined in hadrons and the chiral symmetry should be partially restored.

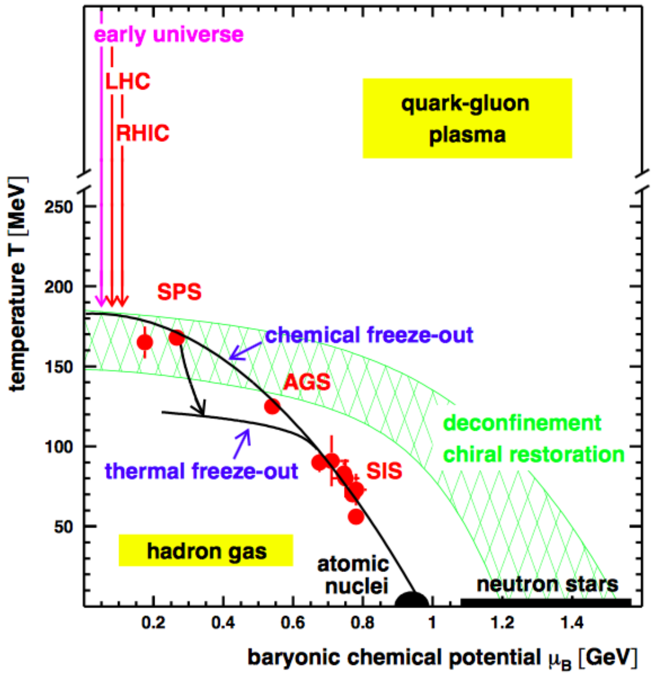

FIGURE 1.3: Phase diagram of the QCD (9)

Lattice studies of QCD thermodynamics have provided quantitative information on the QCD phase transition, the equation of state and many other aspects of QCD thermodynamics. Lattice QCD (LQCD) tells us (10) that for zero net baryon density, QCD matter undergoes a phase transition at T_{cr} = 173 ± 15 MeV from a colour-confined hadron resonance gas (HG) to a colour-deconfined quark-gluon plasma (QGP). The critical energy density $e_{cr} \simeq 0.7$ GeV/fm^3 corresponds roughly to that in the centre of a proton. At the phase transition, the normalised energy density e/T^4 rises rapidly by about an order of magnitude over a narrow temperature interval $\Delta T \lesssim 15$ - 20 MeV, whereas the pressure p/T^4 is continuous and rises more gradually (see Figure 1.4)

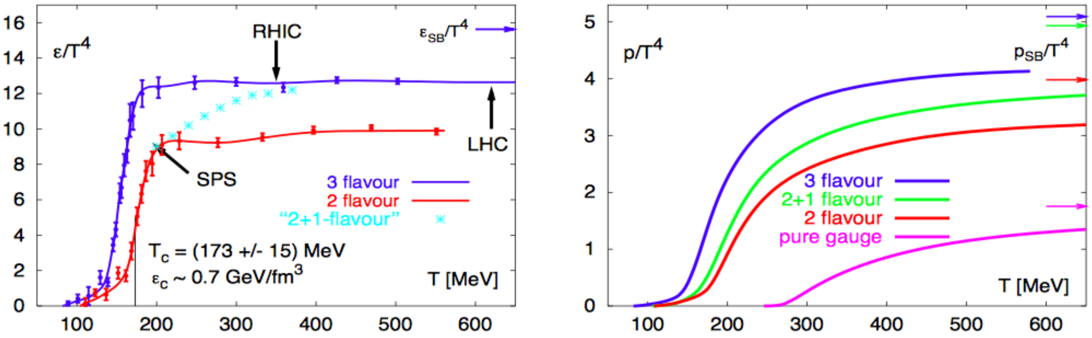

FIGURE 1.4: The normalized energy density ϵ/T^4 (left) and pressure p/T^4 (right) from lattice QCD for 0, 2 and 3 light quark flavors, as well as for 2 light + 1 heavier (strange) quark flavors. Horizontal arrows on the right indicate the corresponding Stefan-Boltzmann values for a non-interacting quark-gluon gas.(10)

Results shown in Figure 1.4 were obtained from Lattice Gauge Theory (LGT) for a different number of dynamical fermions. The energy density exhibits the typical behaviour of a system with a phase transition: an abrupt change in a very narrow temperature range. The corresponding pressure curve shows a smooth change with temperature. In the region below T_c, the basic constituents of QCD, quarks and gluons, are confined within hadrons and here the EoS is well parameterised by a hadron resonance gas. Above T_c the system appears in the QGP phase where quarks and gluons can travel distances that substantially exceed the typical size of hadrons.

1.2.2 Bag model and Temperature phase transition

Lack of a satisfactory theory to understand the confinement leads to many phenomenological models. Some of these attempts, though they lack a proper link with QCD equations, are quite successful in the predictions of hadronic properties. Prominent among them are the bag models (11). Motivated by field theoretical investigations, one can assume that the physical vacuum which is the "normal phase" outside hadrons, cannot support the propagation of quark and gluon fields. In such a vacuum, a small domain of different phase may be formed. It is like boiling the vacuum and creating small bubbles with a characteristic hadron size. Inside the bubble, quark and gluon fields can propagate freely. Hadrons are then pictured as small domain in the new phase with quark and gluon as constituents. This is the bag and the boundary surface of the bag between the two phases is impermeable against the colour fields, therefore they can't penetrate into the normal phase of the vacuum. The impermeability at the surface is expressed in the form of boundary conditions for the colour fields. The gluon electric fields E_i (i = 1,2. . . , 8) in an octet of eight colours are tangential whereas the gluon induction fields B_i are normal to the surface in the instantaneous rest frame of the surface element. As a consequence, there is no gluon field

energy or momentum flux through the surface. The dynamics of the quark and gluon fields inside the bag is governed locally by the field equations of quantum chromodynamics (QCD). Gluons are confined inside the hadron phase and quarks become also confined. Apart from the feature of the fully relativistic formulation, the most important new element in the bag model is that hadrons are described as deformable droplets whose shapes are determined dynamically.
In the naive bag model, hadrons are considered as spherical bag and the quarks are Dirac particles permanently confined within the volume of the bag which has a finite radius equal to that of the hadron size. The assumption that the quarks move freely inside the cavity tries to imitate the basic property of asymptotic freedom. A typical ingredient in the bag model is the small u and d quark masses ($\sim$ 10 MeV). This kind of bag Model has a Lorentz scalar term for confinement supplemented by a bag pressure (B) to prevent expansion. The bag potential acts on the mass of the quark or gluon which become very heavy at the surface of the bag and hence cannot escape. The pressure exerted by the gluon fields on the boundary of a hadron is balanced by volume energy B per unit volume and a surface energy per unit surface. The boundary of the bag is transparent against leptons and the mediators of electromagnetic and weak interactions.
In the bag model, the mass of a hadron increases roughly in proportion to the total number of quarks inside the bag. This is due to the fact that the quark kinetic energy dominates the total energy of the bag. This would imply that multiquark hadrons are heavier than three quark bags. However, if one takes into account the one gluon exchange interaction between the quarks, the mass of the hadron in the bag model is given by:

$$M(R) = \frac{N \times 2.04}{R} + \frac{4\pi R^3 B}{3} \mp \frac{N \times 0.117}{R}\alpha_s + \frac{Z_0}{R} \tag{1.5}$$

Here first term is just the Kinetic Energy of the N quarks in a spherical bag of radius R where N = 3 for baryons and N = 2 for mesons. Second term is the extra energy required to keep the bag stable, third term is the hyperfine interaction due to the one gluon exchange, the last term corresponds to all other effects which are difficult to account for, such as the centre of mass correction, the zero point energy, self energy etc. In the static spherical model, the pressure balance equation is equivalent to minimisation of M(R) as a function of R. Thus, for equilibrium at R = $\mathrm{R_h}$(R_h = radius of the hadron),

$$\frac{\partial M(R)}{\partial R}|_{R=R_h} = 0$$

provides

$$B = \frac{1}{4\pi}\frac{\alpha_h}{R_h^4} \tag{1.6}$$

where

$$\alpha_h = (2.04 \pm 0.117\alpha_s + Z_0/N)N \tag{1.7}$$

N is the number of quarks constituting the hadron. Substituting the equilibrium condition in Equation 1.5, we get

$$M_N = \frac{16}{3}BR^3N \tag{1.8}$$
$$= \frac{4}{3}\frac{\alpha_N}{R_N} \tag{1.9}$$

With the typical bag model parameters, $B^{1/4}$ = 145 MeV, Z_0 = -1.84, α_s = 2.2 and the strange quark mass = 279 MeV, the masses of the lowest baryon octet and decuplet as well as the lowest meson octets are reasonably well explained except the pion mass.
Moving further into the model, a transition is expected when the free gas pressure of the quarks/gluons exceeds the bag pressure: $P_{freegas} \geq B$. Now

$$P_{QGP} = d_{QGP}\pi^2T^4/90$$

where d_{QGP} is the degrees of freedom for QGP and is composed of two parts:

$$d_{QGP} = d_g + 7/8d_{q+\bar{q}} = 16 + 7/8.6N_f2$$

where d_g is the degrees of freedom for gluons and $d_{q+\bar{q}}$ is the degrees of freedom for quarks. Ideally, number of quark flavours ($N_f = 3$) for 3 massless quarks, but since the strange quark mass is not negligible compared to up an down quarks, an approximate value of $N_f = 2.5$ is taken. Thus we get $d_{QGP} = 37$. This leads to

$$37\pi^2T^4/90 \geq B \Rightarrow T_c \simeq (\frac{90}{37\pi^2})^{1/4}B^{1/4}$$

Giving us a critical temp $T_c = 145$ MeV if bag pressure is taken to be 200 MeV.

1.3 QGP in Big and Little Bang

A commonly quoted goal of the heavy-ion programs at Brookhaven Lab (BNL) and CERN, is to recreate conditions similar to those shortly after the Big Bang (about 10 μs) when the universe was filled with a quark-gluon plasma (QGP). There is now considerable evidence that the universe began as a fireball, the so called "Big-Bang", with extremely high temperature and high energy density (see left panel of Figure 1.5). At early enough times, the temperature was certainly high enough ($T > 100$ GeV) that all the known particles (including quarks, leptons, gluons, photons, Higgs bosons, W and Z) were extremely relativistic. Even the "strongly interacting" particles, like quarks and gluons, would interact fairly weakly due to asymptotic freedom and perturbation theory should be

sufficient to describe them. Thus this was a system of hot, weakly interacting colour charged particles, a quark-gluon plasma, in equilibrium with the other species.
QGP can be created by smashing heavy nuclei together at relativistic speeds in collisions called "little bangs" (see right panel of Figure 1.5). Heavy ion collisions at the LHC and at RHIC create macroscopic (compared to the relevant microscopic length scale given by the inverse temperature) amounts of QCD matter. Studying the properties of this "QCD condensed matter" through an active interaction between theory and experiments allows us to gain unique insights to the behaviour of the strong interaction.

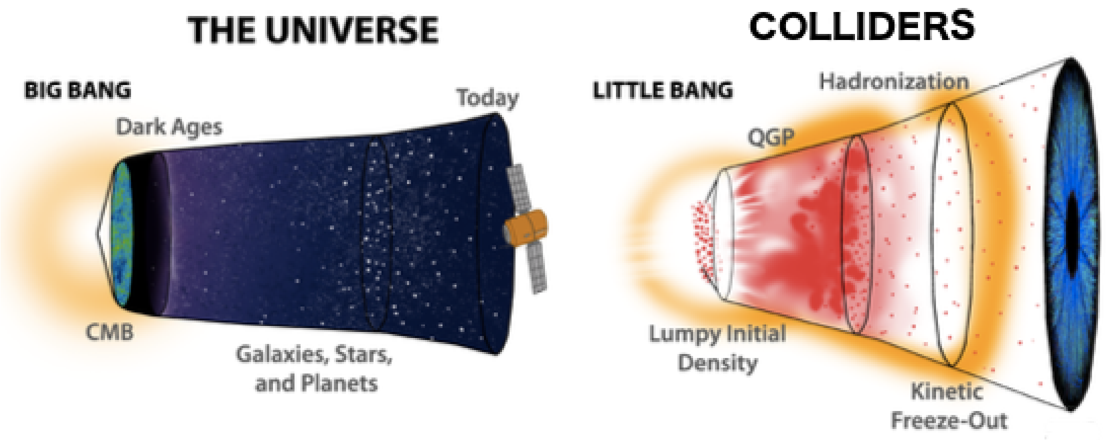

FIGURE 1.5: Schematic of the expansion of the universe after the Big Bang (left) and the expansion of a fireball after Little Bang (right)

Figure 1.6 (12) summarises the key stages of relativistic heavy-ion collisions: thermalisation, expansion, and decoupling. In the very early collision stages, a pre-equilibrium phase is present where, "hard" particles with either a large mass or large transverse momenta $p_T \gg 1$ GeV/c are created. Their creation involves large momentum transfers $Q^2 \sim p^2 > 1$ GeV/c. Then these 'hard probes' can be used to inspect the initial stages of the collisions and as hard scattering processes can be treated under perturbative QCD (pQCD). According to the uncertainty relation hard particle production happens on a time scale $\tau_{form} \simeq 1/\sqrt{Q^2}$; for a 2 GeV particle this means $\tau_{form} \simeq 0.1$ fm/c. In nucleus-nucleus collisions, the quanta created in the primary collisions between the incoming nucleons can't right away escape into the surrounding vacuum, but re-scatter of each other. In this way they create a form of dense, strongly interacting matter which thermalises quickly and at sufficiently large energy density, forms a quark-gluon plasma. Thus with heavy-ion collisions, there is a possibility to recreate the matter in the state that existed in the very early universe.
The plasma formed lives for a very short amount of time (about 10 fm/c) and during this time undergoes a rapid expansion in space into the vacuum surrounding the collision. As a consequence of collective expansion, the fireball

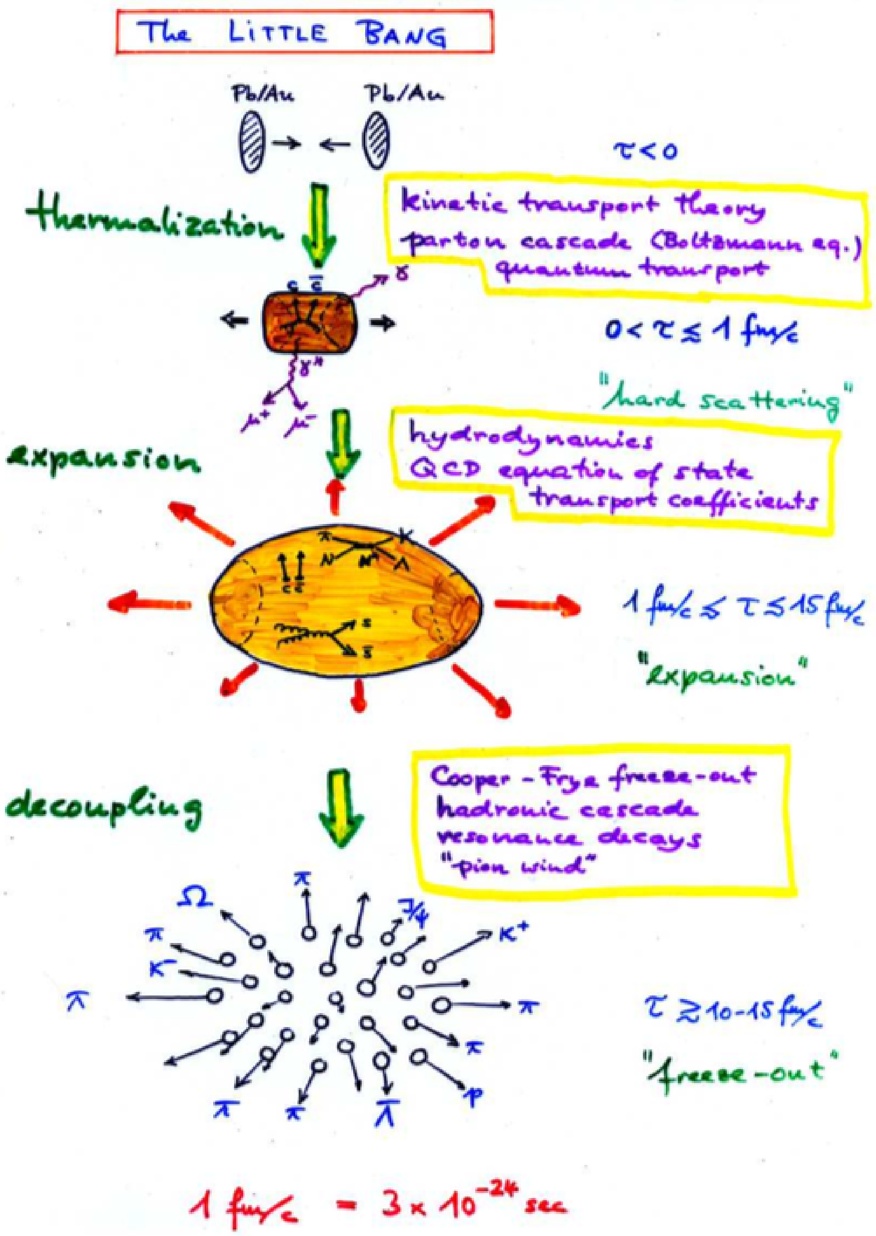

FIGURE 1.6: Stages of a relativistic heavy-ion collision and relevant theoretical concepts. (12)

cools and its energy density decreases. When the latter reaches the critical value of about 1 GeV/fm^3, the hadronisation takes place. The volume of the system expands as energy density decreases (to account for entropy) by a large factor in a small amount of time while the temperature remains approximately constant. This is the moment (called "chemical" freeze-out) where the particle abundances are fixed. Generally, the freeze-out moment (the end of a statistical system) is defined as a moment when hadrons cease to interact and start to stream freely to detectors. It is possible to distinguish two freeze-out: the chemical and the kinetic freeze-out. The first corresponds to the moment when the inelastic interactions between hadrons cease and the chemical composition of the system is fixed. The thermal (kinetic) freeze-out corresponds to the moment

when elastic interactions also cease and hadrons start to escape freely. Then the created hadronic medium after the chemical freeze-out keeps expanding and hadrons keep interacting quasi-elastically, cooling the system until the "kinematic" freeze-out is reached. At kinetic freeze-out all hadrons (including resonances) have an approximately exponential transverse momentum spectrum reflecting the temperature of the fireball at that point. The unstable resonances can decay producing daughter particles with a smaller transverse momenta on an average than their stable counterparts.
There are various probes which can help us in studying the interactions and properties of the formed QCD matter:

- **Kinematic probes and chemical composition**: The multiplicities, yields, momentum spectra and correlations of hadrons emerging from heavy-ion collisions at $p_T < 1.5$ GeV/c, reflect the properties of the bulk of the matter produced in the collision

- **Electromagnetic probes**: Spectral shape of thermal radiation emitted by the QGP via $q\bar{q}$ annihilation should provide a direct measurement of the plasma temperature

- **Strangeness enhancement**: Strange particles are of particular interest since the initial strangeness content of the colliding nuclei is very small and there is no net strangeness. Since the focus of this thesis is a strange resonance, this signature will be discussed in detail later in this chapter

- **Charmonium and Bottomonium suppression**: The initially formed $c\bar{c}$ or $b\bar{b}$ pair would be unable to form a resonance in a QGP medium because of the colour screening due to the free quarks

- **High-p_T and jet suppression**: When a high-energy parton traverses a length L (dimension of the coloured medium) of hot or cold matter, the induced radiative energy loss is proportional to L^2. The energy loss of a high-energy jet in a hot QCD plasma appears to be much larger than in cold nuclear matter. This is termed as "jet quenching"

- **Elliptic Flow**: It is the azimuthal momentum space anisotropy of particle emission from non-central heavy-ion collisions in the plane transverse to the beam direction. It directly reflects the initial spatial anisotropy of the nuclear overlap region in the transverse plane and since spatial anisotropy is largest at the beginning of the evolution, elliptic flow is especially sensitive to the early stages of system evolution

Depending on the phase of the collision, there are two probes:

- hard probes are signals produced in the first stages of the collision by the interaction of high momentum partons, such as, production of heavy quarks and of their bound states (charmonium and bottomonium), jet quenching, thermal photons and dileptons

- soft probes are signals produced in the later stage of the collision. Even if they are produced during the hadronisation stage, they keep indirect information on the properties of the phase transition and on the QGP. These are momentum spectra, strangeness enhancement, anisotropic flow, particle correlations and fluctuations

In both models, the description of the transition from hydrodynamic fluid to free particles which reach the detector is done using the Cooper-Frye freeze-out picture (13). In this picture it is assumed that the momentum distribution of the final state particles is essentially the momentum distribution within the fluid, towards the end of the hydrodynamical expansion, and parts of the fluid are instantaneously converted into free particles

1.4 QGP as a Perfect fluid

Such a phase of matter, named the Quark-Gluon Plasma (QGP), where the degrees of freedom are quarks and gluons, can be created by colliding heavy ions at the RHIC and LHC energies. Its detailed characterisation should provide insight into the unexplained features of QCD that are crucial for understanding hadron and nuclear properties.
The most important results obtained at RHIC before LHC are:

1. the saturation of the elliptic flow v_2 reaching the maximum value possible for an ideal liquid with vanishing shear viscosity (14)
2. the suppression of high p_T particles, caused by energy loss or "jet quenching" in the hot and dense matter (15)

These two results established that the in heavy ion collisions the state of hot, dense matter is created. This matter is quite different and even more remarkable than had been predicted. The new state of matter created in the ion collisions is more like a liquid than a gas. Now the standard model of the ion physics is the sQGP, i.e. strongly interacting (almost) perfect liquid. These effects then have been confirmed by the observations at LHC at even higher energies. In the following some results on soft particle production, including particle abundances and collective flow will be presented.

1.4.1 Global event properties

Heavy-ion nuclei when accelerated to ultra-relativistic energies, are Lorentz contracted into pancakes while travelling along the beam axis (z-axis). In a way, their collisions can be assumed to be a superposition of binary nucleons-nucleon collisions. Since not all collisions are head on, there are nucleons that participate (called "participants") and those which do not interact (called "spectators") as seen in the Figure 1.7. However, a participant nucleon from the projectile can interact with multiple nucleons from the target. The number of participant-participant interactions is called the number of binary collisions, N_{coll}.

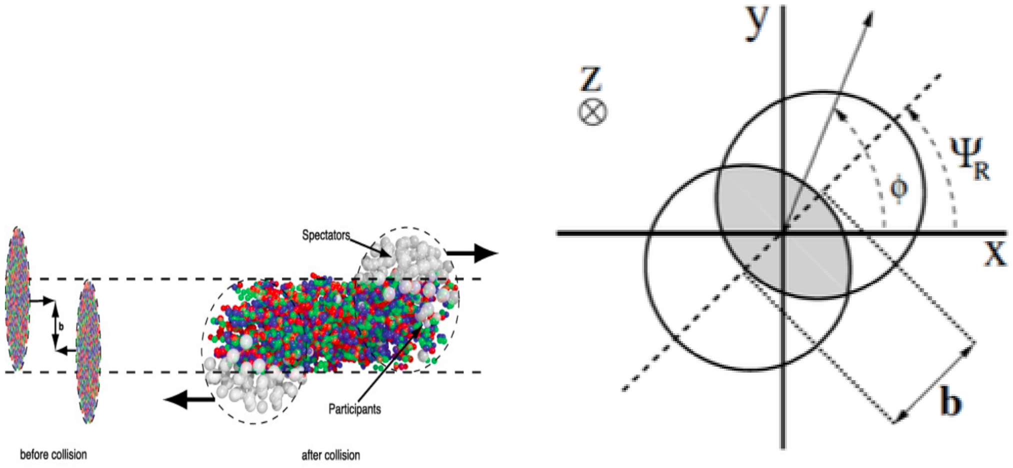

FIGURE 1.7: Ultra-relativistic heavy ions collision as seen from the yz plane (left) and transverse (xy) plane (right). b is the impact parameter. Ψ_R is the reaction plane angle and ϕ the general azimuthal angle

The impact parameter b is defined as the vector between the centres of the two nuclei in the transverse plane and quantifies the overlap region of the colliding nuclei. Smaller the value of b, more the number of participants and the collision is more head-on. Centrality is one of the main parameters that are used to characterise the collisions. In general, centrality is directly related to the impact parameter b. In practice, the centrality is estimated from the multiplicity assuming that $\mathrm{d}N_{ch}/\mathrm{d}\eta$ is monotonically increasing with N_{part} (i.e. as the collision becomes more central). The highest centrality events then also yield the highest multiplicities. Parameters like N_{part} and N_{coll} are extracted by a Glauber Monte Carlo simulation (16).

The impact parameter vector is important for the determination of the event plane of the collision, defined by the angle Ψ_R between the beam direction (z axis) and the impact parameter vector, as depicted in Figure 1.7. Particle production in the final state is normally defined in terms of new variables rapidity (y) and pseudo-rapidity(η). Rapidity (y) is defined as :

$$y = \frac{1}{2} ln \frac{E + p_L}{E - p_L}$$

where E is the particle energy and p_L is its longitudinal momentum i.e. the component of the momentum along the beam axis. The other two components of the momentum are combined as transverse momentum $\mathrm{p}_T = \sqrt{\mathrm{p}_x^2 + \mathrm{p}_y^2}$. In composite particle collisions such as protons or nucleons, only p_T conservation can be applied since distribution of momentum along the longitudinal axis amongst various participants cannot be quantified, as opposed to electron-positron collision. The rapidity can be approximated by pseudo-rapidity in the ultra-relativistic limit, $E \simeq \mathrm{p}$:

$$\eta = \frac{1}{2} ln \frac{p + p_L}{p - p_L} = -ln \left[tan \frac{\theta}{2} \right]$$

with θ being the angle of the particle momentum with respect to the z axis. The particles produced with high transverse momentum (p_T) in hard scattering processes also have $\eta \sim 0$.

The most basic quantity, and indeed the one measured within days of the first ion collisions, is the number of charged particles produced per unit of (pseudo)rapidity, $\mathrm{d}N/\mathrm{d}y$ ($\mathrm{d}N_{ch}/\mathrm{d}\eta$), in a central collision. The value finally measured at LHC in Pb-Pb collisions at $\sqrt{s_{\mathrm{NN}}}$ = 2.76 TeV was $\mathrm{d}N_{ch}/\mathrm{d}\eta \sim 1600$ (17). From the measured multiplicity one can derive a rough estimate of the energy density with the help of the formula proposed by Bjorken (18) which relates the initial energy density ϵ to the transverse energy E_T:

$$\epsilon \geq \frac{dE_T/d\eta}{\tau_0 \pi R^2} = 3/2 \langle E_T/N \rangle \frac{\mathrm{d}N_{ch}/\mathrm{d}\eta}{\tau_0 \pi R^2} \tag{1.10}$$

where τ_0 denotes the thermalisation time, R is the nuclear radius, and $E_T/N \sim$ 1 GeV is the transverse energy per emitted particle. The value measured at the LHC implies that the initial energy density (at $\tau_0 = 1$ fm/c) is about 15 GeV/fm^3, approximately a factor three higher than in Au+Au collisions at the top energy of RHIC. The corresponding initial temperature increases by at least 30%, with respect to RHIC, to T $\sim$ 300 MeV, even with the conservative assumption that the form at on time τ_0, when thermal equilibrium is first established, remains the same as at RHIC. .

1.4.2 Identified Particle $\mathrm{p_T}$ spectra and Yield

The level of equilibrium in produced particles can be tested by analysing the particle abundances or their momentum spectra. The earlier is established through the chemical composition of the system, while the latter extracts additional information about the dynamical evolution and collective flow. The particle production (π, K, p, Λ, ..) is a non-perturbative process and cannot be calculated directly from first principles (QCD). In the phenomenological QCD inspired event generators, the particle spectra and ratios are adjusted to the data of elementary collisions (pp, e^+e^-) using a large number of parameters. In heavy ion reactions, however, inclusive particle ratios and spectra at low transverse momentum (about 95% of all particles are below 1.5 GeV/c at LHC energies), are consistent with simple descriptions by statistical/thermal (19) and hydrodynamical models (20).

In particular particle ratios are determined during hadronisation at or close to the QGP phase boundary ("chemical freeze-out"), while particle momentum spectra reflect the conditions somewhat later in the collision, during the "thermal freeze-out".

The expansion of the hadrons emitted in Pb-Pb collisions is characterised by the appearance of collective flow in the soft region of the spectrum. Collective flow

implies a strong correlation between position and momentum variables and arises in a strongly interacting medium in the presence of local pressure gradients. Collective motion can be studied in the framework of hydrodynamic models, where the momentum spectra and the motion patterns are determined by the fluid properties (viscosity, equation of state, speed of sound) and the boundary conditions in the initial and in the final state (collision geometry, pressure gradients, freeze-out conditions). Radial flow is the component of the collective motion isotropic (or angle averaged) with respect to the reaction plane. It determines the expansion in the radial direction and can be estimated by measuring the primary hadron transverse momentum (p_T) spectra.
The average radial flow velocity ($\langle\beta_T\rangle$) and kinetic freeze-out temperature (T_{kin}, temperature when the hadrons cease to interact) can be estimated by fitting simultaneously the π, K and p spectra with a hydrodynamic-inspired function, called a Blast Wave (21). For the most central Pb-Pb collisions at $\sqrt{s_{\rm NN}}$ = 2.76 TeV, ALICE (17) measures $T_{kin} \sim$ 95 MeV and $\langle\beta_T\rangle$ = 0.66c, which corresponds to a value about 10% higher than the one measured by STAR (22). Similar value has been extracted also in most central Pb-Pb collisions at $\sqrt{s_{\rm NN}}$ = 5.02 TeV (23).
Hadron multiplicities and their correlations are observables which can provide information on the nature, composition, and size of the medium from which they originate. Of particular interest is the extent to which the measured particle yields approach equilibrium. The chemical freeze-out is the moment, in the evolution of the heavy-ion collisions at which all inelastic collisions between particles cease. The chemical composition is fixed at this point.
The application of statistical concepts to multi-particle production in high energy collisions was first done by Fermi in 1950s (24) and then further strengthened by Hagedorn in 60s (25). Hagedorn was also able to explain the almost universal slope of p_T spectra in his renowned statistical bootstrap model, assuming that resonances are made of hadrons and resonances in turn. In these models multiple hadron production proceeds from highly excited regions emitting hadrons according to a pure statistical law.
In modern view, the statistical or thermodynamical models are model of hadronisation , describing the process of hadron formation at the scale where QCD is no longer perturbative. The basic quantity required to compute the thermal composition of particle yields is the partition function Z(T,V). In the Grand Canonical (GC) ensemble:

$$Z^{GC}(T, V, \mu_Q) = Tr[e^{-\beta(H - \sum_i \mu_{Q_i} Q_i)}] \tag{1.11}$$

where H is the Hamiltonian of the system, Q_i are the conserved charges and μ_{Q_i} are the chemical potentials that guarantee that the charges Q_i are conserved on the average in the whole system. Finally $\beta = 1/\mathrm{T}$ is the inverse temperature.
It is observed that the bulk hadron yields in heavy-ion collisions are well described in the framework of thermal (statistical) hadronisation models (26),(27). In these models particles are created in thermal (phase space) equilibrium, with two relevant parameters the chemical freeze-out temperature T_{chem} and the baryochemical potential μ_B (which accounts for baryon number conservation). The production of a particle with mass m is suppressed by a Boltzmann factor $e^{-m/T_{ch}}$.

An additional strangeness saturation parameter, γ_s is introduced to describe the observation that in some collision systems particles containing strange quarks are suppressed compared to the grand canonical thermal expectation. This parameter has the value of about 1 at RHIC and LHC energies. Statistical models are able to successfully describe almost all bulk hadron yields, from centre of mass energies of a few GeV to a few TeV (28), (29). The T_{chem} extracted from thermal and statistical model fits to the data is close to the phase transition temperature obtained from recent lattice calculations and is found to saturate from RHIC to LHC energies, where heavy-ions collide at an order of magnitude higher centre of mass energy.
In particular for recent central (0-10%) Pb-Pb collisions at 5.02 TeV (30), T $\approx$ 152 $\pm$ 3 MeV has been observed at μ_B =0, while a value of T $\approx$156 MeV at μ_B = 0 has been obtained for Pb-Pb collisions (0-10% centrality) at 2.76 TeV (19). In Figure 1.8 are reported the particle production rates measured by ALICE in central (0-10%) Pb-Pb collisions at $\sqrt{s_{\mathrm{NN}}}$ = 2.76 TeV with a grand canonical thermal fit. It is interesting to note as at 2.76 TeV, yields of light flavour hadrons are qualitatively well described by equilibrium thermal models over seven orders of magnitude.
In a large system with a large number of produced particles, the conservation law of a quantum number (e.g. strangeness) can be implemented on the average by using the corresponding chemical potential, within the Grand Canonical formulation. In a small system, such as a pp collision, with small particle multiplicity, conservation laws must be implemented locally on an event-by-event basis, requiring a Canonical formulation (C). The C conservation of quantum numbers is known to severely reduce the phase space available for particle production. This is the canonical suppression (CS) mechanism (31).

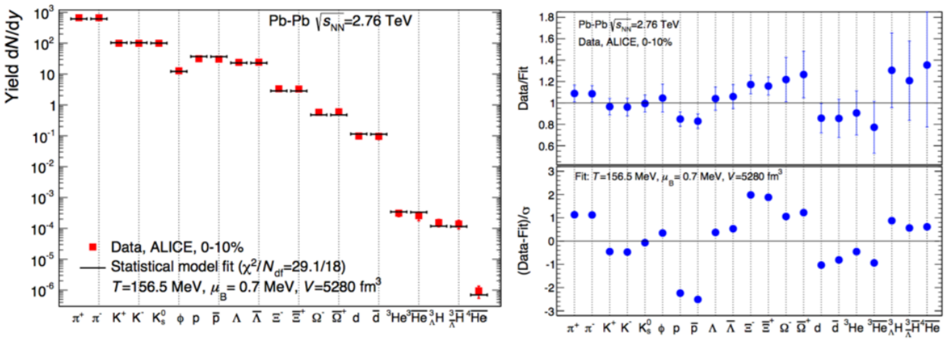

FIGURE 1.8: Grand canonical thermal fit to ALICE central (0-10%) Pb-Pb particle production rates in collisions at $\sqrt{s_{\mathrm{NN}}}$ = 2.76 TeV (19)

1.4.3 Strangeness production

The enhancement of strange quark production, relative to light u and d quarks, in heavy ion collisions, respect to the corresponding signals from elementary reactions, proposed by Johann Rafelski and Berndt Müller (32), has been among the first signals for probing the Quark Gluon Plasma formation. Indeed, in QGP the production of a strange - antistrange quark pair can proceed as described in Figure 1.9 by the fusion of two gluons or massless light quarks. The reaction threshold in the second case is twice the mass of the produced $s\bar{s}$ pair, which due also to the partial chiral restoration is equal to the naked strange quarks, i.e. 2× 100 = 200 MeV. Moreover in QGP the equilibration of strangeness is more efficient due to the large gluon density. Then the production of multi-strange baryons could be enhanced during the deconfined phase due to recombination mechanisms. An enhanced production of hyperons is therefore expected to be a signal of a deconfined phase.

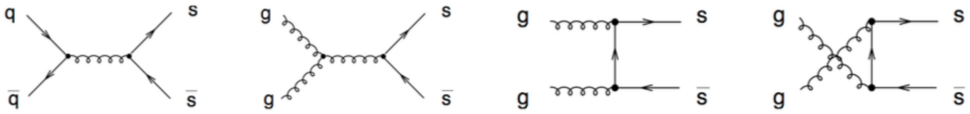

FIGURE 1.9: Feynman diagrams for the $s\bar{s}$ production in QGP: the leftmost diagram represents a quark-antiquark annihilation, while the other three correspond to gluon fusion processes

QCD matter can exists in two different phases::

1. **Hadron Gas: (HG)** where the degrees of freedom are the hadronic ones, as quarks and gluons are confined;
2. **Quark Gluon Plasma: (QGP)** where the degrees of freedom are the partonic ones, with quarks and gluons free with respect to each other.

The difference of the production rates of the strange quark in the two systems has been discussed on the basis of the "Reaction threshold" and " Equilibration time " (33).

Reaction threshold:

The energy needed to produce strange mesons or baryons in a thermally equilibrated HG is significantly higher than in the case of a QGP. In HG, there is an abundance of pions hence the production $\pi + \pi \rightarrow \pi + \pi +$ strange hadron + antiparticle, should be dominant. However it is penalised due to the baryon and strange number conservation thus it is necessary to produce strange particle and antiparticle jointly. Then the reaction threshold corresponds to two times the rest mass of the hadrons: 2230 MeV for the $\Lambda + \overline{\Lambda}$, 2642 MeV for the $\Xi^- + \Xi^+$, 3344 MeV for the $\Omega^- + \Omega^+$. A lower threshold is obtained in the case of indirect production. In this case multi-strange hadrons will be created in a reaction chain. First the production of lighter hadrons ($\pi + N \rightarrow K + \Lambda$) followed by a reaction ($\pi + \Lambda \rightarrow K + \Xi$ and $\pi + \Xi \rightarrow K + \Omega$). In this case the combined threshold for Ω production is (535 + 565 + 710) MeV = 1810 MeV.

In the QGP the gluon density is high and provides the possibility to have strange quark production from gluon fusion processes as depicted in the three right

Feynman diagrams of Figure 1.9. These become the dominant processes, producing 80% of the $s\bar{s}$ pairs. In these reactions the energy threshold, due also to the partial chiral symmetry restoration, is equal to the naked mass of the two strange quarks $\simeq 2 \times 100$ MeV

Equilibration time:

The second important point is that the equilibration times in QGP, especially due to gluon fusion processes are much shorter those of the hadronic reactions. Difference is more pronounced in case of multi-strange baryons due to their low hadronic cross sections. In a partonic scenario, with a typical temperature of T = 200 MeV, equilibration times of $\tau_{QGP}^{eq} \sim 10$ fm/c are theoretically achievable in an ideal gas of quarks and gluons (32) which is of the order of the expected total duration of a heavy-ion reaction, from the first parton collisions to the final freeze-out of the hadrons. Figure 1.10 shows the time evolution of the relative strangeness to baryon density

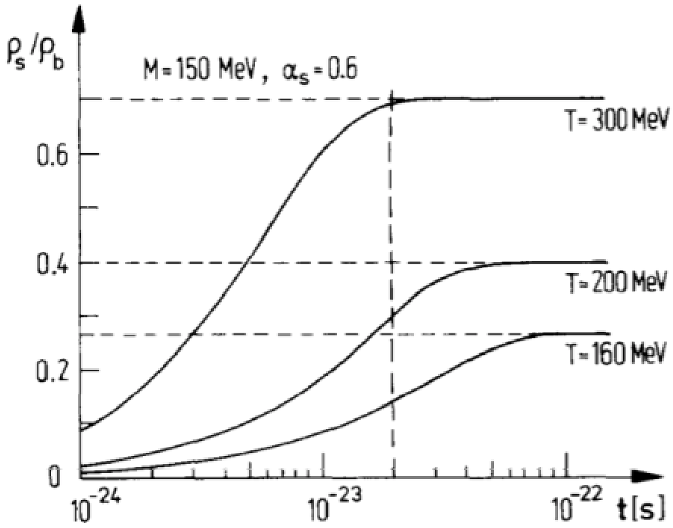

FIGURE 1.10: Time evolution of the relative strangeness to baryon density (ρ_s/ρ_b) produced in the plasma for various temperatures T, with m_s = 150 MeV and α_S = 0.6. The vertical line corresponds to a time of ~ 6 fm/c. (34)

Following these arguments, production of multi-strange particles in HG is much more difficult as compared to QGP. In a QGP, the production probability depends on the density of the strange quarks to the power of number of strange quarks inside a hadron. The following relations are obtained in light of these arguments:

$$\Omega/\Xi(QGP) \approx \Xi/\Lambda(QGP) \tag{1.12}$$
$$\Omega/\Xi(HG) < \Xi/\Lambda(HG) \tag{1.13}$$
$$\Omega/\Xi(QGP) > \Omega/\Xi(HG) \tag{1.14}$$
$$\Xi/\Lambda(QGP) > \Xi/\Lambda(HG) \tag{1.15}$$

Therefore, the signature of the QGP proposed by Rafelski and Müller, known as strangeness enhancement, lie on the overabundance of strangeness production in a QGP scenario (A-A collisions) with respect to a HG scenario (pp collisions). The enhancement is defined as the ratio between the yields in A-A collisions and the yields in pp collisions, where the former must be appropriately scaled by the number of participant nucleons to account for the increased interaction volume. This enhancement has been studied at different energies and using various colliding systems, both at SPS (WA97, NA57 ($\sqrt{s_{\mathrm{NN}}}$ = 17.2 GeV)(35), (36)), RHIC (STAR ($\sqrt{s_{\mathrm{NN}}}$ = 200 GeV)(37)), and LHC (ALICE (38)). In these experiments, the expected enhancement and hierarchy ($E_{\Lambda} < E_{\Xi} < E_{\Omega}$) have been observed. In Figure 1.11, the measured enhancement factors of baryons with increasing strangeness content ($|S| = 2, 3$) measured in Pb-Pb collisions at $\sqrt{s_{\mathrm{NN}}}$ = 2.76 TeV (38) are reported as a function of the number of participant nucleons, $\langle N_{part} \rangle$, in comparison with similar measurements at SPS and RHIC energies.

The comparison of the results at the different energies shows that the relative enhancements decreases with increasing collision energy. This trend can be explained, within a thermodynamical description of the system, with a progressive removal of the "canonical suppression" from the proton-proton system. In fact, in a smaller system, with small particles multiplicities, quantum numbers conservation laws (such as strangeness) are applicable locally, event-by-event, whereas in a large system, with many degrees of freedom, they can be applied in average, by means of the corresponding chemical potential. The conservation of quantum numbers is known to reduce the phase space available for particle production. This canonical suppression factor increases with lower energy in the centre of mass of the collisions and could explain the larger enhancement for lower energy systems (39).

To avoid any dependence on the particle multiplicity at the different collision energies, a different manner to investigate the enhancement of the strangeness production is to study the behaviour of the hyperon-to-pion ratios (see Figure 1.12 (38)). Firstly, the relative production of strangeness in pp collisions at the LHC energies is larger than at lower energies. This is consistent with a reduction of the canonical suppression at higher energies. A clear increase in the strangeness production (relative to π production) is visible moving from pp to A-A. This increase in the hyperon-to-pion ratios is of the order of $\sim$ 1.6 and 3.3 for Ξ and Ω respectively, and is of about half that of the standard enhancement ratio as defined by the participant-scaled yields. This enhancement rises with centrality up to about $\langle N_{part} \rangle \sim 150$, and apparently saturates thereafter.

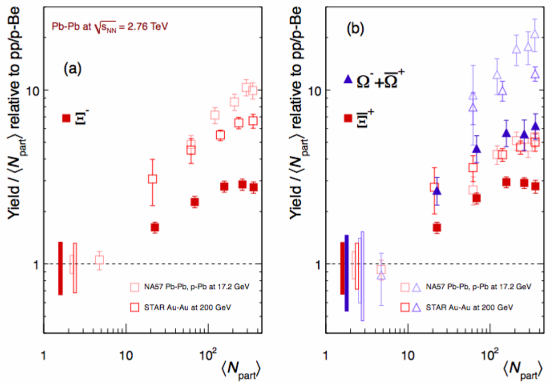

FIGURE 1.11: Enhancements in the rapidity range $|y| < 0.5$ as a function of the mean number of participants $\langle N_{part} \rangle$, showing LHC (ALICE, full symbols), RHIC and SPS (open symbols) data (38)

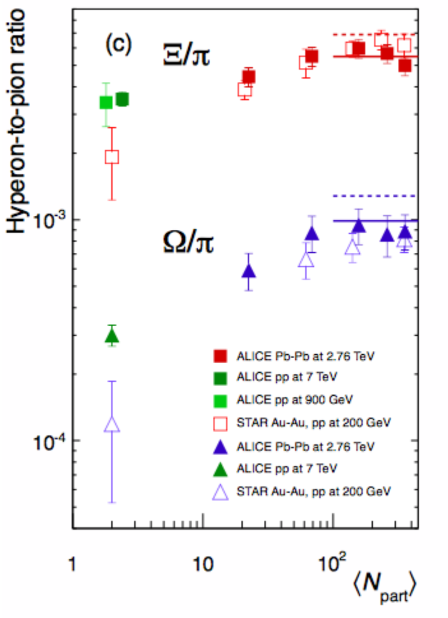

FIGURE 1.12: Hyperon-to-pion ratios as a function of $\langle N_{part} \rangle$, for A-A and pp collisions at LHC and RHIC energies (38). The lines mark the thermal model predictions (40) (full line) and (41)

1.4.4 Anisotropic Flow

In this strongly interacting matter collective expansion originates from the initial pressure gradients, which transform the initial spatial deformations and inhomogeneities of the created matter into momentum anisotropies of the final state particle production. This is what is called anisotropic flow. When two nuclei collide with non-zero impact parameter, the spatial asymmetries due to the initial shape of the nuclear overlapping region are reflected into azimuthal anisotropies of particle emission. Since these anisotropies are generated before matter reaches the critical temperature and hadronises, the anisotropic flow is sensitive to the equation of state of the QGP phase. Large anisotropies indicate a strong collective behaviour and early local thermal equilibrium of the fireball. The magnitude of the anisotropic flow depends strongly on the friction of the strongly interacting matter, characterised by the viscosity over entropy density ratio(η/s).The anisotropy is quantified in terms of the azimuthal Fourier coefficients of the transverse momentum spectrum:

$$E\frac{d^3}{d^3p} = \frac{d^3N}{\mathrm{p_T}d\mathrm{p_T}dyd\phi} = \frac{d^2N}{\mathrm{p_T}d\mathrm{p_T}dy}\frac{1}{2\pi}\left[1+\sum_{1}^{\infty}2v_n\cos n(\phi-\Psi^R)\right] \tag{1.16}$$

where n is the order of the harmonic, ϕ indicates the particle azimuthal angle and Ψ^R is the reaction plane angle and the sine terms vanish due to reflection symmetry with respect to the reaction plane. The flow coefficients are $\mathrm{p_T}$ and η dependent and are given by $v_n(\mathrm{p_T},\eta) = \langle\cos n(\phi-\Psi^R)]\rangle$, where the brackets denote an average over particles in a given $\mathrm{p_T}$ bin and over events in a given centrality class.
The elliptic ïňĆow magnitude was measured RHIC, where v_2 reaches a value compatible with the one predicted by hydrodynamics for a "perfect fluid", that is a fluid without internal friction and vanishing shear viscosity (42). At LHC, the elliptic flow has been studies by ALICE (43) as function of centrality and found to reach its maximum between 30% and 50% centrality, where the asymmetry of the collision is more enhanced. In comparison to RHIC, the integrated v_2 of charged particles increases by about 30%, indicating that the hot and dense matter created at LHC still behaves like a fluid with almost zero viscosity.

Based on asymptotic freedom in QCD and colour Debye screening, the properties of the QGP were expected to be similar to a weakly interacting gas of quarks and gluons. In that case, the mean free path in the QGP is large, which implies a large viscosity. A direct consequence of a large viscosity is that the system will not develop strong collective expansion. Therefore the discovery of a very large 2nd order flow harmonic (44; 45), called elliptic flow, at the RHIC and afterward at the LHC (43) changed dramatically our understanding of the QGP (see Figure 1.13).

1.5 Collective behavior in small systems

The observation of a novel long-range di-hadron correlation ("ridge") in very high multiplicity proton-proton (pp) collisions by CMS at the LHC (46) opened up the door to a variety of frontiers in the crucial non-perturbative phenomena of Quantum Chromodynamics (QCD) at a very high density regime. A large variety of theoretical models have been proposed to explain the origin of these so-called ridge-like correlations (see (47)). The proposed mechanisms range from colour connections in hard scattering processes and collective effects in the initial interaction of the protons to hydrodynamic effects in the high-density system possibly formed in these collisions.

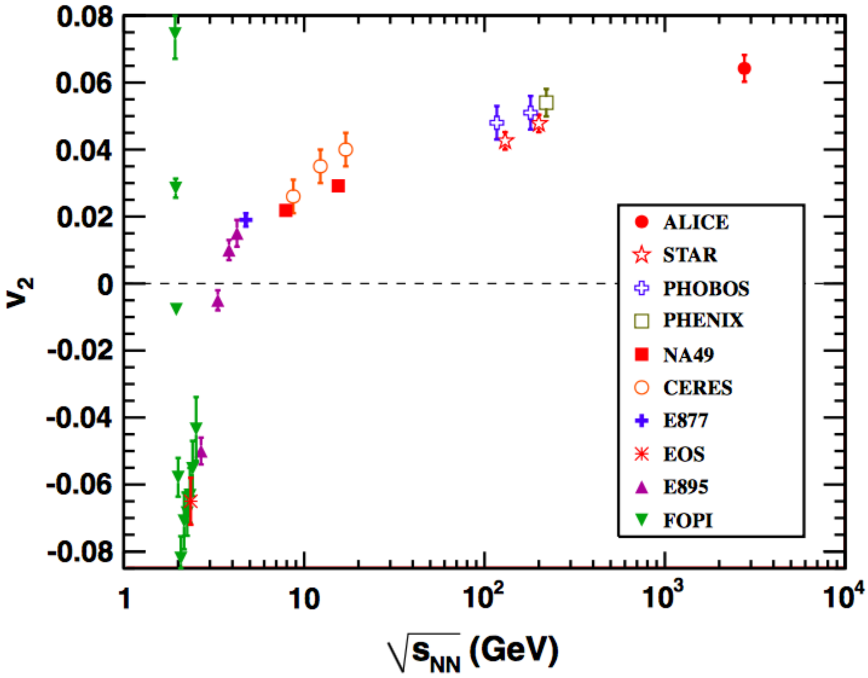

FIGURE 1.13: Integrated elliptic flow at 2.76 TeV in Pb-Pb 20%-30% centrality class compared with results from lower energies taken at similar centralities (43)

Two-particle correlations are a powerful tool to explore the mechanism of particle production in collisions of hadrons and nuclei at high energy. Such studies involve measuring the distributions of relative angles $\Delta\phi$ and $\Delta\eta$ between pairs of particles: a "trigger" particle in a certain transverse momentum p_T, trigger interval and an "associated" particle in a p_T, associated interval, where $\Delta\phi$ and $\Delta\eta$ are the differences in azimuthal angle ϕ and pseudorapidity η between the two particles.

Long-range angular correlations (ridge structure) were a well known phenomena in heavy ion collisions at RHIC energies (48), and they were attributed to the hydrodynamical evolution of the produced strongly interacting medium (49). The measurements in pp collisions at $\sqrt{s}$ = 7 TeV (Figure 1.14) have revealed a long-range ($2< |\Delta\eta| < 4$) near-side($\Delta\phi \approx 0$) correlations in high multiplicity events with $1 < p_T < 3$ GeV/c. Similar structures were also observed in p-Pb collisions at $\sqrt{s_{NN}}$ = 5.02 TeV (50; 51; 52).

As described in previous paragraph in heavy-ion collisions, the flattening of transverse momentum distribution and its mass ordering find their natural explanation in the collective radial expansion of the system. Global fit with a Blast Wave are used to extract quantities such as the kinetic freeze-out temperature (T_{kin}) and the mean transverse velocity of the medium (β_T). Similar analysis has been performed on p-Pb data at $\sqrt{s_{NN}}$ = 5.02 TeV (53). As can be seen in Figure 1.15 (Left) , the T_{kin} and β_T parameters show a similar trend as the ones obtained in Pb-Pb. Within the limitations of the blast-wave model, this observation is consistent with the presence of radial flow in p-Pb collisions.

Other processes not related to hydrodynamic collectivity could also be responsible for the observed results. Then in the same figure are reported the results

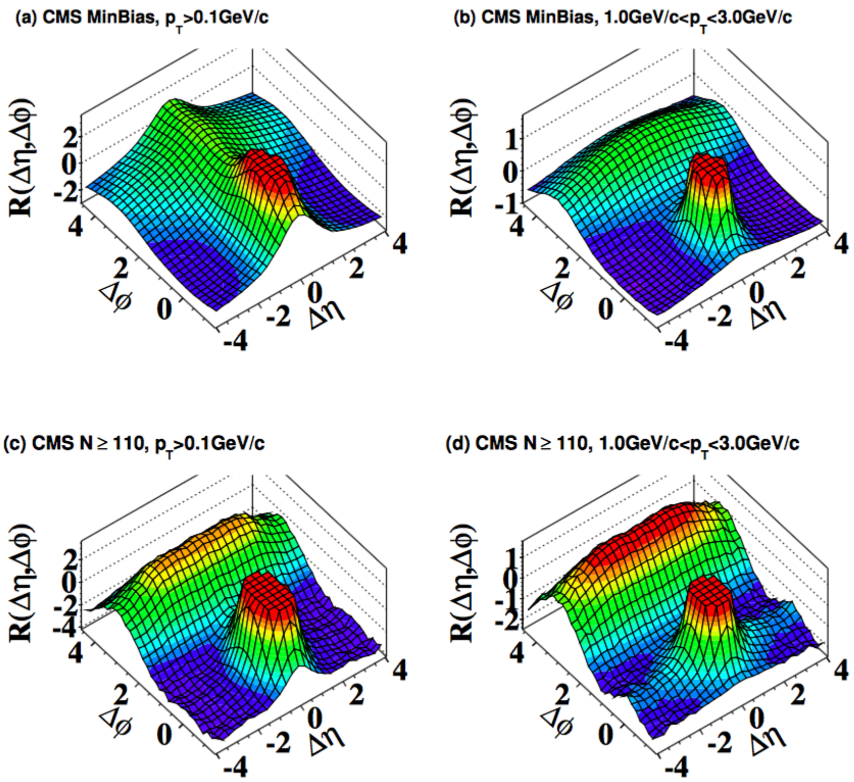

FIGURE 1.14: 3D two-particle correlation functions ($\Delta\eta$ and $\Delta\phi$) for 7 TeV pp (a) minimum bias events with $p_T > 0.1$GeV/c, (b) minimum bias events with $1 < p_T < 3$ GeV/c, (c) high multiplicity events with $p_T > 0.1$GeV/c and (d) high multiplicity events with $1 < p_T < 3$ GeV/c. The sharp near-side peak from jet correlations is cut off in order to better illustrate the structure outside that region. (46)

obtained by applying the same fitting procedure to transverse momentum distributions generated from PYTHIA8 for pp collisions at $\sqrt{s}$ = 7 TeV, a model not including any collective system expansion. It is interesting to see as colour reconnection can mimic the effect of the radial flow. In fact with colour reconnection the evolution of PYTHIA8 transverse momentum distributions follows a similar trend as the one observed for p-Pb and Pb-Pb collisions (see next chapter for colour reconnection description).
Recently, the distributions obtained for p-Pb and Pb-Pb have been compared (see Figure 1.15 (Right)) to the values obtained fitting the particle p_T spectra (π, K and p) in pp collisions at $\sqrt{s}$ = 7 TeV (54). The spectra in pp and p-Pb lead to very similar $\langle\beta_T\rangle$ and T_{kin} values when considering similar multiplicities, while in Pb-Pb at similar multiplicities, lower $\langle\beta_T\rangle$ are observed with respect to the other two systems. This behaviour could be connected to the presence of a stronger radial flow gradients in the smaller collision systems (55). The recent comparison of particle production in pp collisions at $\sqrt{s}$ = 7 TeV with predictions from different event generators (54) have shown as these to be able to describe the evolution of p_T-differential particle spectra with charged particle multiplicity needed for collectivity mechanisms such as colour reconnection, colour ropes

or radial flow, as is the case for PYTHIA8 (56), DIPSY (57) and EPOS-LHC (58), respectively.

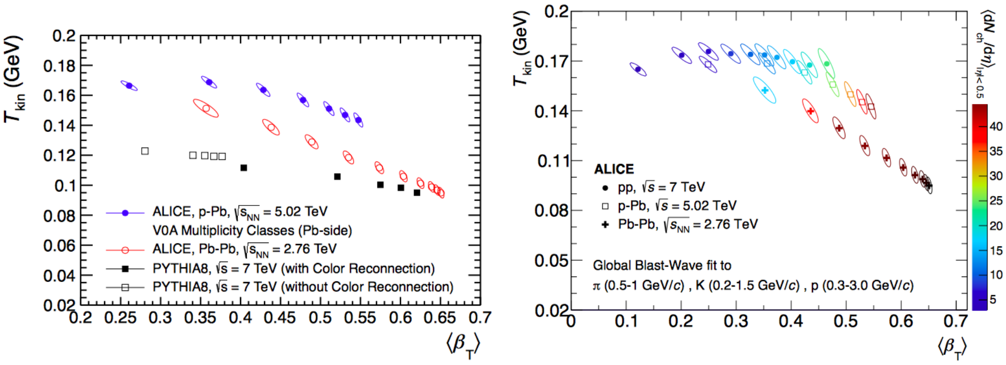

FIGURE 1.15: (Left) Results of blast-wave fits (53), compared to Pb-Pb data and MC simulations from PYTHIA8 (56) with and without colour reconnection (59). Charged-particle multiplicity increases from left to right. (Right) Kinematic freeze-out temperature parameter T_{kin} versus average expansion velocity $\langle\beta_T\rangle$ from a simultaneous Blast Wave fit to π, K and p spectra measured in pp, p-Pb and Pb-Pb collisions. (54)

Recently, elliptic flow patterns, often ascribed to collective behaviour, have been observed in smaller systems such as pp and p-Pb collisions. Figure1 [ref. Kalwait QM2018) shows an impressive collection of measurements of the elliptic flow coefficient v_2 in various collision systems for several multiplicities and centralities. The data is extracted for higher order multi-particle cumulants in which the contributions from non-flow effects, as for instance due to mini-jets, are deliberately suppressed.

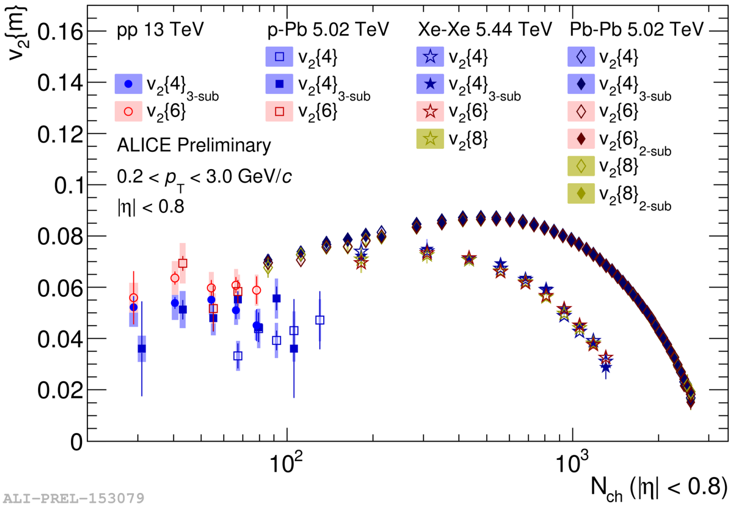

FIGURE 1.16: Multiplicity dependence of $v_2\{4\}$, $v_2\{6\}$, and $v_2\{8\}$ with standard, 2-subevent or 3-subevent method in 13 TeV pp, 5.02 TeV p-Pb, 5.44 TeV Xe-Xe and 5.02 TeV Pb-Pb collisions (30)

As discussed in the previous paragraph, strangeness enhancement was one of the first signature proposed for existence of QGP. As sen in Figure 1.12, the

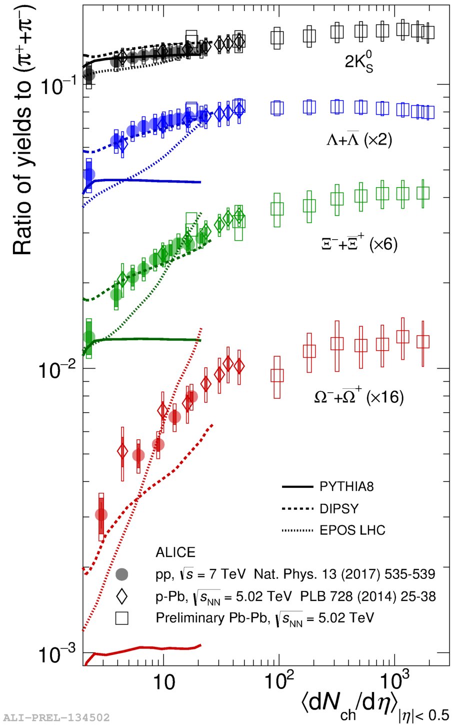

FIGURE 1.17: p_T-integrated yield ratios to pions ($\pi^+ + \pi$) as a function of charged particle multiplicity density measured in $|y| < 0.5$ in pp, p-Pb, and Pb-Pb collisions. Predictions of Monte Carlo event generators PYTHIA8, DIPSY and EPOS-LHC are also shown (60).

abundances of strange particles relative to pions in heavy ion collisions from top RHIC to LHC energies do not show a significant dependence on either the initial volume (collision centrality) or the initial energy density (collision energy). With the exception of the most peripheral collisions, particle ratios are found to be compatible with those of a hadron gas in thermal and chemical equilibrium and can be described using a grand-canonical statistical model. Suppression of strangeness production in small systems could be be explained by statistical models implementing strangeness canonical suppression (61) or by core-corona superposition models (62).
Recent measurements by the ALICE experiment (60) show that strangeness enhancement is also present in high-multiplicity pp and p-Pb events. In Figure 1.17, the ratios of the p_T-integrated yields of K^0_S, Λ, Ξ, and Ω to the pion yield as a function of charged particle multiplicity in pp collisions at $\sqrt{s}$ = 7 TeV are compared to p-Pb and Pb-Pb results at $\sqrt{s_{NN}}$ = 5.02 TeV. It is observed that

1. a significant enhancement of strange to non-strange hadron production with increasing charged-particle multiplicity in pp collisions
2. pp collisions behaviour is similar to that in p-Pb collisions at a slightly lower centre-of-mass energy

This suggests that strangeness production is driven by the event multiplicity (or activity) rather than by the initial-state collision system or energy. The ratios $\Lambda/K^0_S$and p/π do not change significantly with multiplicity demonstrating that the observed enhanced production rates of strange hadrons with respect to pions is not due to the difference in the hadron masses (60). A multiplicity-dependent enhancement is observed respect to INEL $>$ 0 sample, which follows a hierarchy determined by the hadron strangeness. Th is is illustrate in Figure 1.18 which presents the yield ratios to pions divided by the values measured in the inclusive INEL $>$ 0 pp sample, both for pp and p-Pb collisions.

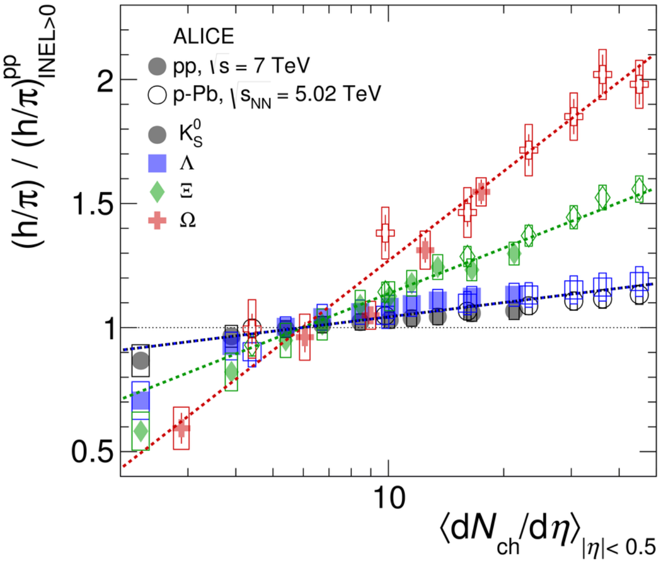

FIGURE 1.18: Particle yield ratios to pions normalized to the values measured in the inclusive INEL $>$ 0 pp sample. The results are shown for pp and p-Pb collisions, both normalized to the inclusive INEL $>$ 0 pp sample. The lines represent a simultaneous fit of the results with the empirical scaling formula in Equation 1.17 (60)

$$\frac{(h/\pi}{(h/\pi)^{\mathrm{pp}}_{\mathrm{INEL}>0}} = 1 + aS^b log\left[\frac{\langle \mathrm{d}N_{ch}/\mathrm{d}\eta\rangle}{\langle \mathrm{d}N_{ch}/\mathrm{d}\eta\rangle^{\mathrm{pp}}_{\mathrm{INEL}>0}}\right] \tag{1.17}$$

Chapter 2

Hadronic resonance production at LHC

Resonances are hadrons which have the same quark contents with its ground state particle but different excited quantum states, and therefore larger masses. The study of resonance production plays an important role both in elementary and in heavy-ion collisions. In pp and $e^{+}e^{-}$ collisions, it contributes to the understanding of the hadron production as the decay products of the resonances represent a large fraction of the final state particles. In particular when strange resonances are studied it can give insight on the strangeness production mechanisms. In addition, it provides a reference for tuning event generators inspired by QCD such as PYTHIA, EPOS etc. Description of the characteristic of some event generators and models as PYTHIA, EPOS and PHSD can be found in Section 2.1.

In heavy-ion collisions, hadronic resonances are a sensitive probe of the dynamical evolution of the fireball formed in the collisions. They have a short lifetime of the order (few fm/c) which is comparable to the lifetime of the fireball created in the heavy-ion collisions, and the competition between resonance generating processes and rescattering can be exploited to characterise the hadronic medium. They can also provide information about strangeness production, in-medium energy loss (via nuclear modification factor R_{AA}), elliptic flow, effects that shape the $\mathrm{p_T}$ spectrum e.g. hydrodynamics, and modification of the line shape e.g. chiral symmetry restoration. In Sections 2.2 and 2.3, some of the more recent results on resonance production in elementary and heavy-ion collisions will be discussed.

2.1 Event Generators and Theoretical Models

The high-energy collisions between elementary particles normally give rise to complex final states, with large multiplicities of hadrons, leptons, photons and neutrinos. Two main factors contribute to the difficulty of finding the relation between final states and underlying physics description. First one being that we

only have an approximate understanding of the underlying physics, and secondly any analytical approach is rendered intractable by the large multiplicities involved. Event generators are software libraries that generate simulated events similar to those produced in real interactions. Monte Carlo (MC) event generators are very widely used, especially by experimentalists in analyses but also by many theorists, who use them to make predictions for collider experiments and to develop techniques to propose to the experiments.
To accomplish this task, Monte Carlo simulation methods are used. The general idea is to simulate a large number of experiments using random number generation instead of performing long complex calculations. The Monte Carlo methods were formally developed by John von Nuemann and had been previously used to study radiation shielding and distance that neutrons would likely travel through material. Monte Carlo methods assume that the system can be described by **P**robability **D**ensity **F**unctions which can be modelled using data-driven, theory driven, or data + theory driven methods. Event generators using such methods allows theoretical and experimental studies of complex multiparticle physics. Event generators are widely used, especially in analysis but also to make predictions for collider experiments and to develop techniques to be adopted in experiments. They can be used to:

- Study the feasibility of an experiment predicting event rates and topologies
- Simulate possible sources of background to improve analysis strategies
- Study detector requirements to optimise detector/trigger design
- Study detector imperfections to estimate the acceptance and efficiency corrections

The simulation chain and analysis using a Monte Carlo based event generator can be summed up in the Figure 2.1

A large variety of event generators have been developed both for pp and heavy ion collisions. Predictions of the particle yields and distributions are also done from models which can be subdivided into microscopic, statistical and hybrid models. In the following sections the event generators used in this thesis, i.e. PYTHIA and EPOS, are described. A brief description of the PHSD model and some of its interesting results on K^* are also presented.

2.1.1 PYTHIA

PYTHIA (63) is a general purpose Monte Carlo event generator which combines perturbative picture of hard processes with non perturbative picture of hadronisation, which provide a link between theory (quarks, gluons) to experiment (baryons, mesons). The structure of a proton-proton collision as built up by a standard event generator as PYTHIA can be described by a few main steps: 1)

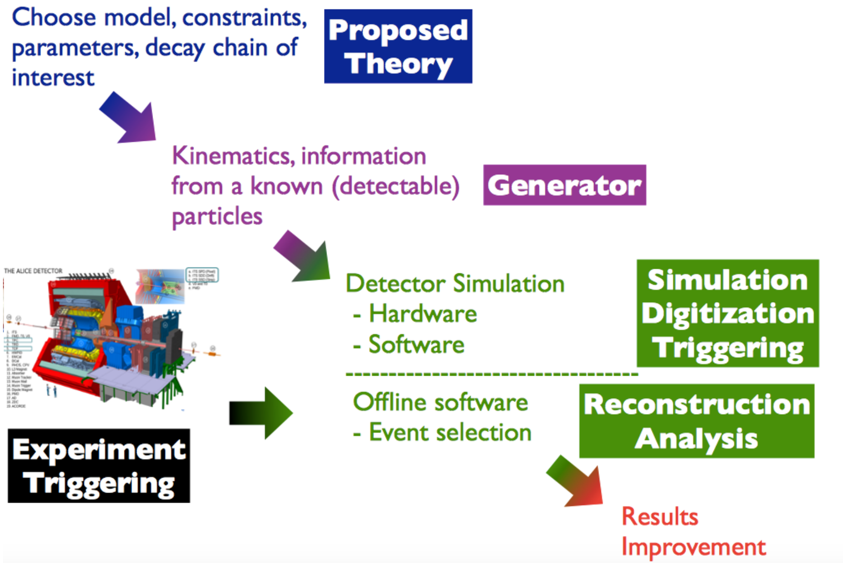

FIGURE 2.1: Monte Carlo Simulations in High Energy Physics

Hard process, 2) Parton shower, 3) Hadronisation, 4) Underlying event, 5) Unstable particle decays.

In Figure 2.2 (64), a typical sketch of a proton-proton interaction is shown. The generation begins with a hard signal process, (in the figure in red). Simulating the hard process is relatively straightforward because Parton Distribution Functions (PDFs) describe partons coming into the process and lowest order (LO) perturbation theory gives a probabilistic distribution of the outgoing partons.
A more interesting stage of event generation is the parton shower phase. In fact scattered colour charges radiate gluons and this happens for partons on their way in (Initial State Radiation) and out (Final State Radiation) of a collision. Due to the non-Abelian structure of SU(3), gluons themselves are coloured and so an emitted gluon can itself trigger new radiation. This leads to an extended shower and the phase space fills up with (mostly) soft gluons. The parton shower evolution starts from the hard process and works downwards to lower and lower momentum scales to a point where perturbation theory breaks down (about 1 GeV).
At this scale the partonic degrees of freedom are converted into hadrons (light green circles) via hadronisation model. Pythia's hadronisation model is based on the Lund string model (65). The last step of event generation is based on the fact that many of these hadrons are not stable particles and therefore decay. In addition to this sequence of steps, all initiated by the hard subprocess, there may be additional semi-hard processes, called Multiple Partonic Interactions (MPIs). These are mostly fairly soft QCD interactions that also undergo all of the steps described above for the hard process and produce additional particles in all the available phase space
In hadron-hadron interactions it is possible to have multiple parton-parton interactions in the same event, because beam particles contains a multitude of

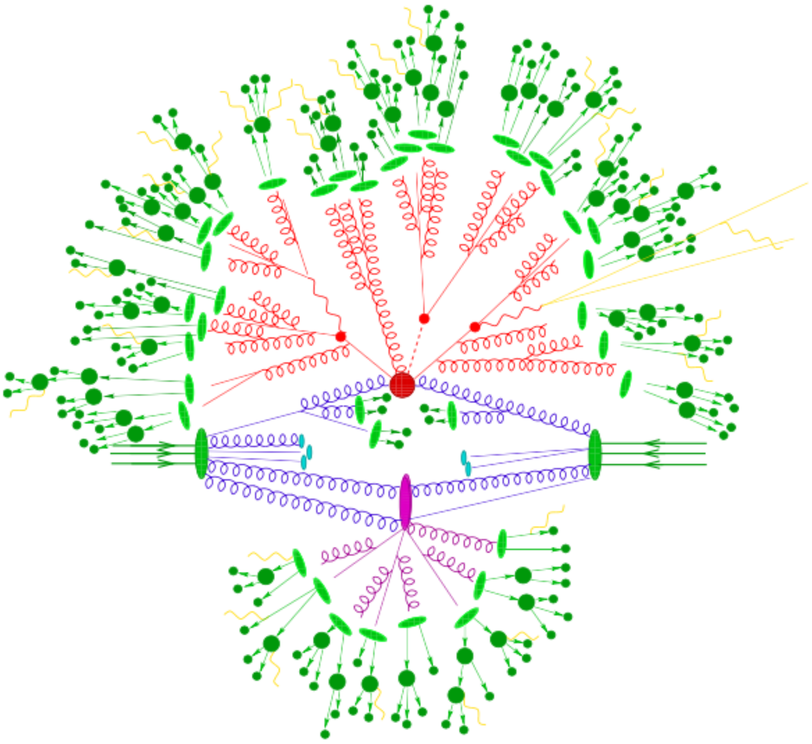

FIGURE 2.2: Sketch of a hadron-hadron collision as simulated by a Monte-Carlo event generator. The red blob in the center represents the hard collision, surrounded by a tree-like structure representing Bremsstrahlung as simulated by parton showers. The purple blob indicates a secondary hard scattering event. Parton-to-hadron transitions are represented by light green blobs, dark green blobs indicate hadron decays, while yellow lines signal soft photon radiation. (64)

partons which can interact. A simple manner to understand underlying events is to consider the fact that in the lab frame the two protons are moving towards each other at very high speed and the Lorentz contraction flattens them into extremely thin pancakes. The collision happens at a point where these flat discs are completely overlapping each other in space time and so there is a very high probability that there will be other interactions apart from the hard interaction. This gives rise to the underlying event, which is made up of secondary interactions between proton remnants. It produces soft hadrons everywhere in the event, which overlie and contaminate the hard process that was already simulated.

In this thesis the obtained results has been compared with prediction from two different PYTHIA versions (PYTHIA6 (63) and PYTHIA8 (56)). For each version different tunes are available. The tunes used in this thesis have been: Perugia 2011 for PYTHIA6 and Monash 2013 for PYTHIA8. The latest PYTHIA6 tune, Perugia 2011 (66) takes into account first results from the LHC, in particular minimum-bias and underlying event data at 0.9 and 7 TeV. Strange baryon production was increased in this tune leading to a larger Λ/K ratio with respect to the Perugia 0 tune. Monash 2013 (67) is an updated set of parameters for the PYTHIA8 event generator, with particular attention to heavy-quark fragmentation and strangeness production. In these PYTHIA tunes, multiple parton-parton interactions in the same event and colour reconnection mechanism are taken into account. These effects are important in hadron-hadron interactions at high energies as the LHC ones. In particular, the colour string formation between final parton may mimic effects similar to that induced by collective flow in heavy-ion collisions (59).

Colour reconnection (CR) is an ad hoc mechanism aiming to describe the interactions that can occur between chromo-electric fields during the hadronisation transition. Since its introduction as a mechanism to explain the increase of the average transverse momentum as a function of the charged particle multiplicity, observed by UA1 (68), several CR models have been developed and incorporated in PYTHIA 6 and PYTHIA8.

All these models are based on the calculation of the probability to connect partons by colour lines. In PYTHIA, final partons are colour connected in such a way that the total string length becomes as short as possible. Therefore, the fragmentation of two independent hard scatterings are dependent and induces the rise of $\langle p_T \rangle$ with multiplicity. PYTHIA 8 Monash tune uses MPI-based model of colour reconnection as the default parametrisation. Such model allows partons of each MPI system to form their own structure in colour space and then, they are merged into the colour structure of a higher p_T MPI system, with a probability $\mathcal{P}$ given by:

$$\mathcal{P}(p_T) = \frac{(R \times p_{T0})^2}{(R \times p_{T0})^2 + p_T^2} \tag{2.1}$$

where R is the reconnection range ($0 \leq R \leq 10$) and p_{T0} is the energy dependent parameter used to dampen the low-p_T divergence of the $2 \rightarrow 2$ QCD cross section.

2.1.2 EPOS

EPOS (58) is a Monte-Carlo event generator for minimum bias hadronic interactions, that offers a unique approach for pp, pA, and AA systems with same formalism and procedures. EPOS aims to be a comprehensive model and event generator, describing all p_T domains (from 100 GeV (lab) to 1000 TeV (c.m.)) with same dynamical picture while incorporating hydrodynamics. In Figure 2.3, a) the classical description of a p-p scattering in HEP models is represented. For LHC p-p scattering, "Projectile" and "Target" refer only to two opposite directions along the beam axis, but the system is naturally completely symmetric. EPOS use the standard chain (Figure 2.3b) commonly used for HI collisions. One of the major features of EPOS is that final state depends on the energy used for each event (multiplicity) and not only on the energy available, thus it can model collective hadronisation when density of particles is high. EPOS-LHC (58) is a tune of the EPOS Monte Carlo generator (EPOS 1.99) containing flow put in by hand, parametrising the collective flow at freeze-out.

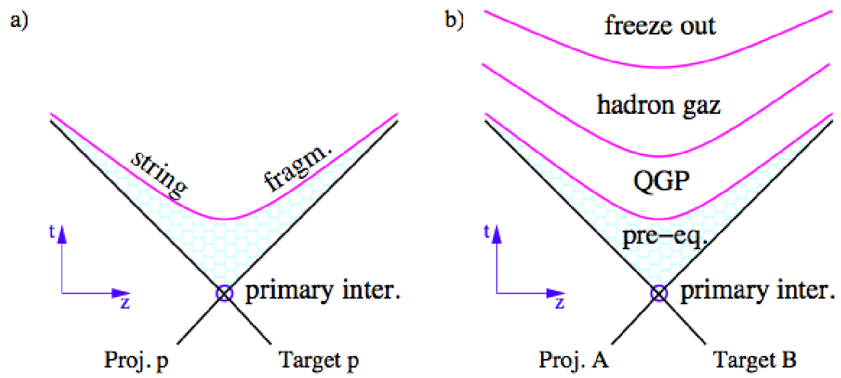

FIGURE 2.3: Space time evolution of the particle production in a hadronic interaction. A hyperbola (line) represents particles with the same proper time. Figure a) is the standard approach for p-p scattering while figure b) is a more complete treatment used usually for HI collision

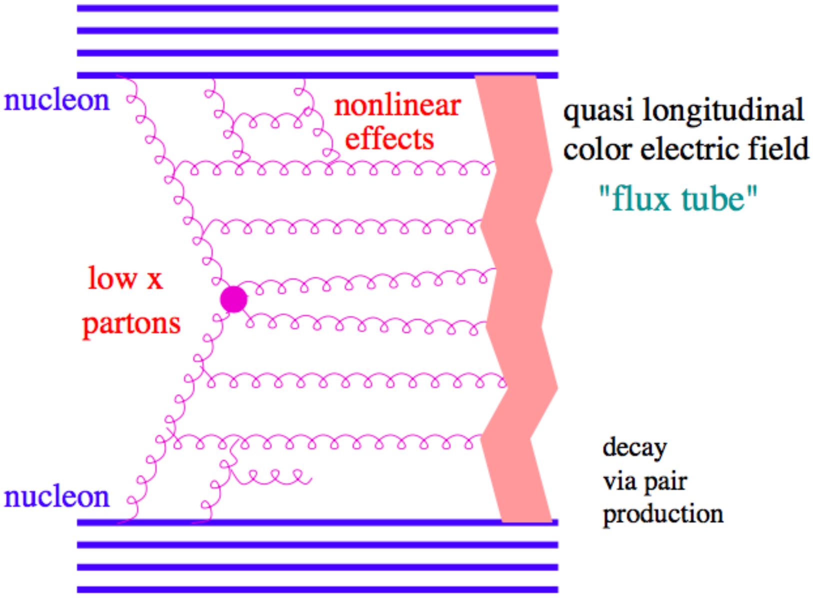

FIGURE 2.4: Elementary interaction in the EPOS model

Parton model of hadrons was proposed by *Richard Feynmann* in 1969 (69) as a way to analyse high energy hadron collisions and was used by Bjorken and Paschos (70) to electron/proton deep-inelastic scattering. Any hadron (for example, a proton) can be considered a composition of a number of point-like constituents, termed "partons". Partons when used in the Monte Carlo event generators also refers to algorithms that approximate the interactions. Nucleus-nucleus

scattering and even proton-proton amounts to many elementary collisions happening in parallel. Such an elementary scattering is the so-called "parton ladder", also known as a "pomeron". Figure 2.4 shows an elementary interaction as modelled in the EPOS. EPOS model is based on parton based Gribov-Regge theory (71) and incorporates many binary parton-parton interactions, each one creating a parton ladder. A parton ladder represents parton evolutions from the projectile and the target side towards the center (small x). These partons can be considered as quasi-longitudinal colour field and thus can be treated as a relativistic string. The intermediate gluons are treated as kink singularities in the language of relativistic strings, providing a transversely moving portion of the object. This flux tube decays via the production of quark-antiquark pairs, creating in this way fragments - which are identified with hadrons.
Initial conditions in EPOS are modelled on strings and partons. At an early time τ_0, before hadronisation, it is possible to distinguish between strings in a region above a critical density (ρ_0) and below this critical density referred to as core and corona respectively (see Figure 2.5) (72). The corona is important for certain aspects like the centrality dependence of all observables in HI collisions. Here it will correspond to unmodified string fragmentation like in usual HEP models and will dominate at large rapidity and in low multiplicity events. While the core is subjected to hydrodynamic evolution i.e. it is hadronised including additional contributions from longitudinal and radial flow effects. The core appears only if the local density of string segments is high enough. This limit is of course easily reached in case of central HI collisions at LHC or RHIC (or even SPS) because of the large number of pairs of nucleons suffering an inelastic interaction. But it's intriguing that core can form even in case of pp collisions at LHC energies, via multiple scattering of partons for a given pair of nucleons.

In EPOS after hadronisation has been introduced the possibility to have hadron-hadron re-scatterings, realised via UrQMD (Ultra-Relativistic-Quantum-Molecular-Dynamics) (73). This model describes the phenomenology of hadronic interactions at low and intermediate energies ($\sqrt{s} < 5$ GeV) in terms of interactions between known hadrons and their resonances. At higher energies ($\sqrt{s} > 5$ GeV) the excitation of colour strings and their subsequent fragmentation into hadrons dominates the multiple production of particles. this introduction is particularly important to study the short-lived resonances. Figure 2.6 shows the lifetime difference between EPOS with the UrQMD hadronic phase (EPOS+UrQMD ON) and EPOS without the UrQMD hadronic phase (EPOS+UrQMD OFF), which defines the lifetime of the interactions in the hadronic phase. The estimated lifetime of the hadronic phase is the difference of the production time of stable hadrons (π, K, N and $\overline{N}$) between the EPOS+UrQMD ON $\langle\tau_{on}\rangle$ and EPOS+UrQMD OFF $\langle\tau_{off}\rangle$ scenarios:

$$\tau_{hadr} = \langle\tau_{on}\rangle - \langle\tau_{off}\rangle$$

Figure 2.7 (74) show that EPOS3 with URQMD is well able to reproduce the data for the ϕ/π and K^{*0}/π ratio across various collision systems. The suppression of K^{*0} observed in the data is also consistently predicted by the model.

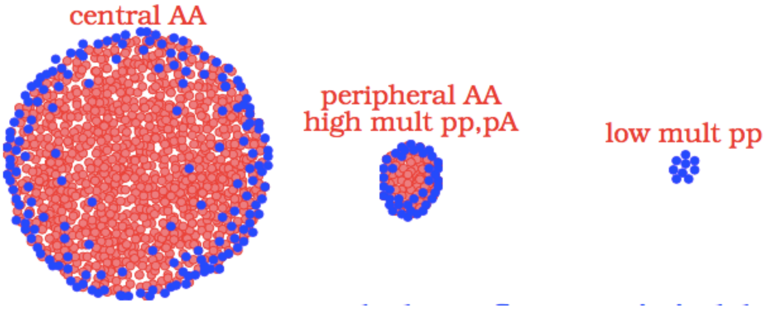

FIGURE 2.5: Core corona picture as modelled in the EPOS

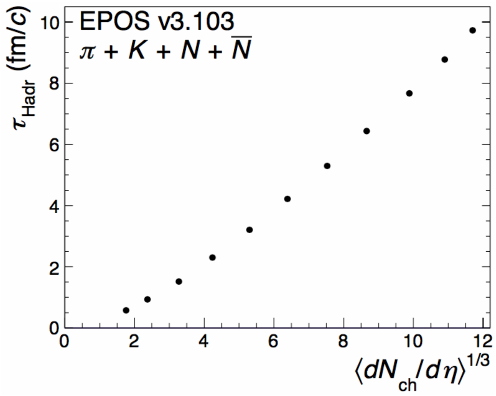

FIGURE 2.6: Centrality dependence of the lifetime of the hadronic phase calculated from the estimated difference in the hadronic-phase lifetime between the EPOS+UrQMD ON and EPOS+UrQMD OFF scenarios, calculated using hadrons (π,K,N and $\overline{N}$). (73)

2.1.3 Parton-Hadron-String Dynamics Model

Parton-Hadron-String Dynamics Model (PHSD) (75) is a non-equilibrium microscopic covariant dynamical approach for the strongly interacting systems in and out-of equilibriums. The PHSD is able to describe well on a microscopic level the time evolution of a relativistic heavy-ion collisions, including both the

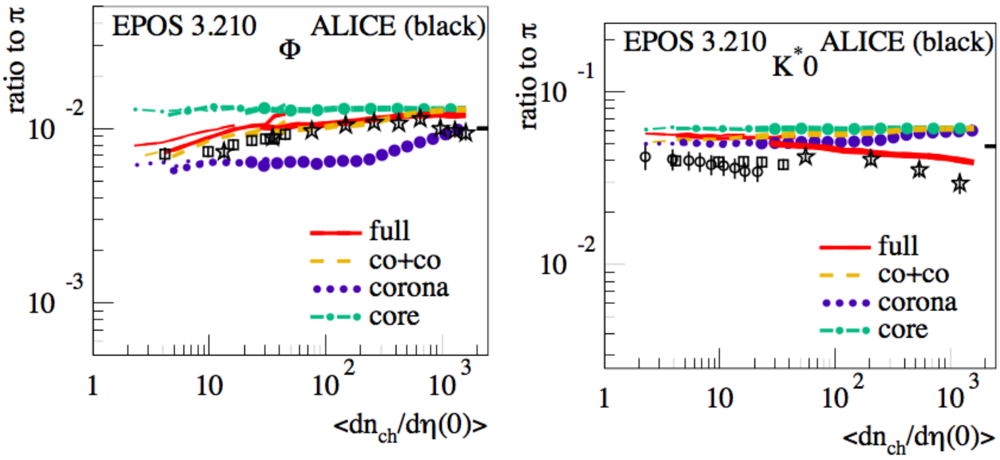

FIGURE 2.7: ϕ/π and K^{*0}/π ratio as a function charged particle multiplicity from pp collisions at 7 TeV (circles and thin lines), pPb at 5 TeV (squares and intermediate lines), and Pb-Pb at 2.76 TeV (stars and thick lines) (74)

hadronic and partonic phase as well as a transition between the effective degrees of freedom. The dynamical description of the strongly interacting system is realised by solving the generalised off-shell Cassing's transport equations (76) which are obtained from the Kadanoff-Baym equations in first-order gradient expansion and go beyond the mean-field and on-shell Boltzmann approximation for the collision terms. The theoretical approximation includes reproduction of the lattice-QCD results in thermodynamical equilibrium and provide the properties of the partons i.e. masses and widths in their spectral function. In equilibrium, PHSD is able to reproduce the partonic transport coefficients such as shear and bulk viscosities or the electric conductivity from the lattice-QCD calculations as well. This model has been tested for various colliding systems (pp, pA, AA) at a wide range of energies of collisions, from AGS to LHC, and has been able to describe a large number of experimental observables, such as charged particle spectra, collective flow coefficients(μ_n) etc.

In PHSD, primary hard scatterings between nucleons are described by string formation and decay, where a string is an excited colour-singlet state (77) which is composed of two string ends corresponding to the leading constituent quarks of the colliding hadrons and a colour flux tube in between. Chiral symmety restoration is incorporated in the PHSD via the Schwinger mechanism for the quark-antiquark production in the string decay and related to the dressing of the quark masses in the medium due to a linear coupling to the quark condensate $(q\bar{q})$. As seen in the Figure 2.8 (78), PHSD is well able to reproduce the ratio K^{*0}/K^- ratio as a function of energy of collisions in both pp and AA collisions and as a function of the centrality of the collision.

PHSD predicts that K*'s coming from the K $+\pi$ channel are created throughout all stages of the collisions, and thus can occur at high and low baryon densities. Contrary to experiment, within a microscopic transport models it is possible to follow all K and $\overline{K}^*$ through their history of production and decay. As can

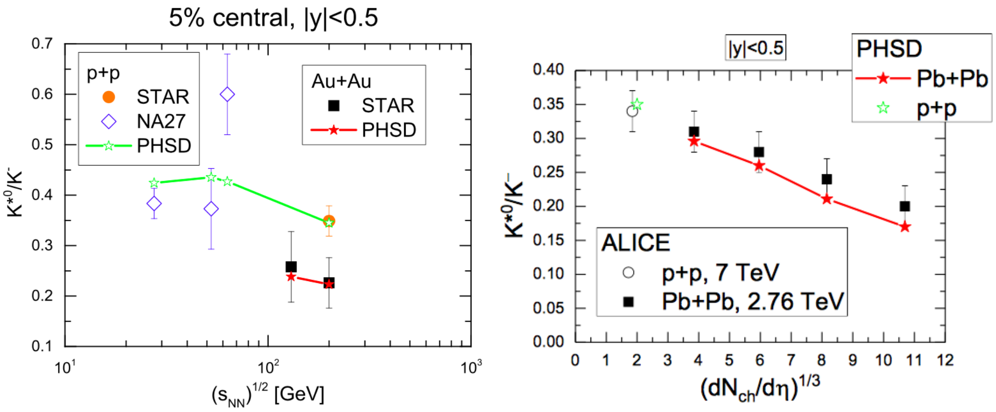

FIGURE 2.8: (Left)The K^{*0}/K^{-} ratio as a function of the centre of mass energy(CM) $\sqrt{s_{NN}}$. Black squares and orange circles represent STAR results for Au+Au and pp collisions, respectively. The orange circle shows STAR data from pp collisions. Additionally data from the NA27 experiment are shown for lower c.m. energies as open blue diamonds. The red and green symbols show results from a PHSD calculation (78). (Right panel) K^{*0}/K ratio as a function of the cubic root of the charged particle multiplicity density obtained from the ALICE experiment compared with results from PHSD model (red stars) (79)

be see from Figure 2.9, at LHC the dominant production channel of the vector kaons and anti-kaons is due to the annihilation of the $K + \pi$ pairs. In this figure is shown the differential mass distribution dN/dM for the vector kaons $K^{*+} + K^{*0}$ (a, upper part) and for vector anti-kaons $K^{*-} + K^{*0}$ (b, lower part) for central Pb-Pb collisions at $\sqrt{s_{NN}} = 2.76$ TeV at midrapidity ($|y| < 0.5$) from the PHSD calculations (75). Here are compared the 'true' K^* spectra, i.e. obtained directly at their decay point (solid black lines) and the reconstructed spectra from the final pions and kaons as in experiment (solid orange lines with circles). A clear shift towards lower invariant masses is present. This modification arises from the rescattering and absorption of the final pions and kaons. Moreover in the same figures, the mass spectrum of K and $\overline{K}^*$ produced in the hadronisation of the QGP is also reported. It is clear that at the LHC energy the main sources of measured K^* is the π + K annihilation in the hadronic phase while only a small fraction of the measured K^* is generated in the hadronisation of the QGP. Then possible modifications of the resonance lineshape due to the chiral symmetry restoration might not be visible in the invariant mass distribution of K^* and anti-K^* vector meson.

2.2 Resonances and characterisation of hadronic phase

Resonances usually have a short lifetime in the order of a few fm/c (see Table 2.1) which is comparable to the lifetime of the fireball created in heavy-ion collisions (about 10 fm/c at LHC energies (80)). This makes resonances one of

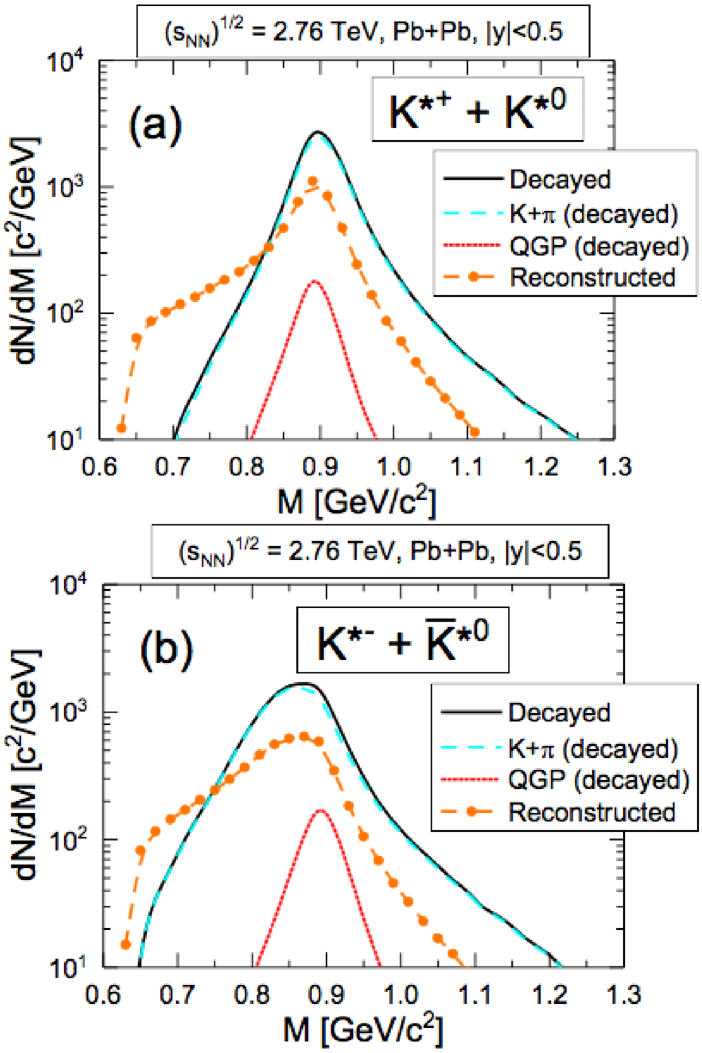

FIGURE 2.9: The differential mass distribution $\frac{dN}{dM}$ for the vector kaons $K^{*+} + K^{*0}$ (a, upper part) and for vector anti-kaons $K^{*-} + \overline{K}^{*0}$ (b, lower part) for central Pb-Pb collisions at a centre-of-mass energy of $\sqrt{s_{NN}}$ = 2.76 TeV at midrapidity ($|y| < 0.5$) from PHSD calculations. The solid orange lines with circles show K^*'s and $\overline{K}^*$'s reconstructed from final kaon and pion pairs while all of the other lines represent the different production channels at the decay point of the K^* and $\overline{K}^*$, i.e. the black lines show the total number of the K^*'s and $\overline{K}^*$'s at their decay points, while the light blue dashed lines show the decayed K^*'s and $\overline{K}^*$'s that stem from the $\pi+$ K annihilation and the short-dotted red lines indicate the decayed K^*'s and $\overline{K}^*$'s which have been produced during the hadronisation of the QGP (79).

the better tools to investigate hadronic medium between chemical and kinetic freeze-out when reconstructed by their hadronic decay products.

A hot and dense state of matter, the quark-gluon plasma is created in ultrarelativistic heavy ion collisions. At a critical temperature (T_c) of about 160

TABLE 2.1: Properties of hadronic resonances: lifetime (τ), quark composition, hadronic decay used to identify them with its branching ratio (%)) (81)

Resonance	ρ^0 (770)	$\Delta(1232)$	K^{*0}	$K^{*\pm}$	$\Sigma(1385)^\pm$	$\Lambda(1520)$	$\Xi(1530)^0$	$\phi(1020)$
τ (fm/c)	1.3	1.7	4.2	3.6	5.5	12.6	27.7	46.4
Quark Composition	$u\bar{u}+d\bar{d}/\sqrt{2}$	udd	$d\bar{s}$	$u\bar{s}$	dds	uds	uss	$s\bar{s}$
Decay (BR %)	$\pi\pi$ (100)	$N\pi$ (99.4)	$K\pi$ (66.6)	$K^0_S\pi$(66.6)	$\Lambda\pi$ (87)	pK (22.5)	$\Xi\pi$ (66.7)	KK (48.9)

MeV (82), a (cross-over) transition between the partonic (i.e. a system with deconfined quarks) and hadronic phases is expected to take place. In Chapter 1 we have seen as statistical models (19) have been successfully applied to particle yields in order to estimate the values of the chemical freeze-out temperature and the baryo-chemical potential. Then relative particle abundances are determined at the chemical freeze-out. Interactions between the chemical and the kinetic freeze-out may affect the hadron momenta distribution but the final yield of the most of particles is fixed.

However, resonance yields may deviate from the values expected from thermal models due to hadronic processes (re-scattering and regeneration) that might change the reconstructible resonance yield. In Figure 2.10 some of the possible hadronic interactions for K* between chemical and kinetic freeze-out are drawn. Resonances due to their short lifetime can decay during hadronic phase and processes as (pseudo-)elastic collisions can occur. Resonance yields may be regenerated through pseudo-elastic scattering, in which particles scatter through a resonance state (e.g., πK $\rightarrow$ K^{*0} $\rightarrow$ π K). On the other hand, resonance may not be reconstructed if at least one of its decay products elastically scatters in the hadronic medium or undergoes pseudo-elastic scattering via a different resonance state (e.g., a pion from a K^{*0} decay scatters with another pion, ($\pi^-\pi^+ \rightarrow \rho(770)^0 \rightarrow \pi^-\pi^+$). As a result, the observed yield after kinetic freeze-out can be more larger or smaller than the yield originally produced. Increase or decrease is connected to the competition between the regeneration (increase) respect to the regeneration effects (decrease). The final resonance yield depends on the lifetimes of resonances and the duration of the hadronic phase which can be connected to the temperature of the chemical/kinetic freeze-out. Thus, the relative suppression of resonances in the final state compared to the behaviour expected from thermal estimates could provide a chronometer for the time interval between the different reaction stages. In particular the rescattering probability of the resonance decay products depends on the cross section of the decay products with the surrounding matter, on the lifetime of the surrounding hot and dense matter, on the lifetime of the resonance and on the specific properties of the daughter hadrons in the resonance decay channels. The rich variety of resonances (different mass and width and different decay daughters) that can be reconstructed allows us to characterise the hadronic phase.

The hadronic phase following the chemical freeze-out can be simulated in a hadronic cascade model, such as UrQMD(Ultra-Relativistic-Quantum-Molecular-Dynamics) (83). This models describes the phenomenology of hadronic interactions at low and intermediate energies ($\sqrt{s}$ < 5 GeV) in terms of interactions between known hadrons and their resonances. At higher energies ($\sqrt{s}$ > 5 GeV)

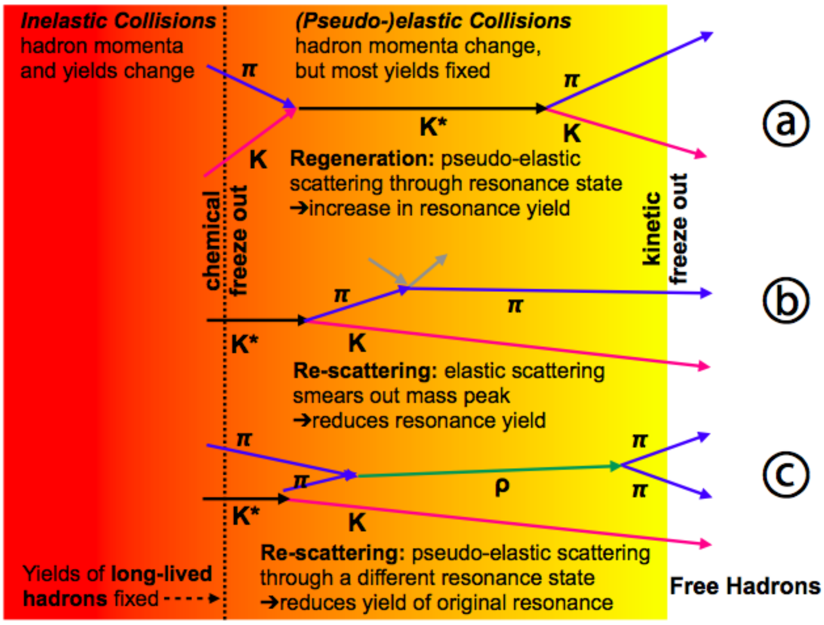

FIGURE 2.10: Possible hadronic interactions between chemical and kinetic freeeze-out

the excitation of colour strings and their subsequent fragmentation into hadrons dominates the multiple production of particles.. The time evolution of the chemical composition of an expanding fireball, in Au-Au collisions at $\sqrt{s_{\mathrm{NN}}}$ = 200 GeV at RHIC is shown in Figure 2.11. This has been estimated in a transport approach that combines hydrodynamics for the early, dense, deconfined stage of the reaction with a microscopic non-equilibrium model for the later hadronic stage at which the hydrodynamic equilibrium assumptions are not valid (84). It is interesting to observe as hadronic resonances are formed and are populated for a long time ($\sim$ 20 fm/c).

It has been shown (85) that light resonances containing strange quarks, such as the K^{*0}, ϕ, Λ^* have very short formation time and large probability to be produced within the QGP phase. The hadronic formation time as function of the particle mass for several quark transverse momenta is qualitatively reported in Figure 2.12. At the LHC, hadron formation happens within the medium lifetime, measured to be $\sim$ 10 fm/c from HBT interferometry (80). Hadronic states that are formed and decay within the lifetime of the partonic medium, experience in-medium interactions with the surrounding QGP system and decay off-shell if chiral symmetry restoration reduces its mass. The presence of a partial chiral symmetry restoration can be investigated by studying intermediate momentum resonances, which are formed early and decay into particles that escape the partonic medium ad suffer of only little re-scattering and regeneration during the subsequent hadronic medium expansion phase.

In heavy ion collisions, the yields for stable and long-lived hadrons reflect the thermodynamic conditions (temperature, chemical potentials) at freeze-out, whereas the yield for short-lived resonances can be modified by final state interactions inside the hot and dense reaction zone. Then the ratio of resonance over

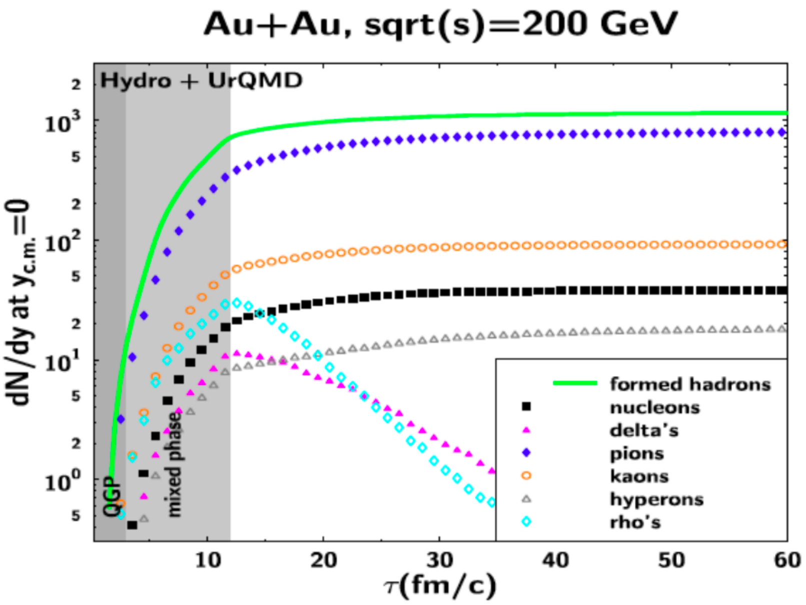

FIGURE 2.11: Evolution of the chemical composition of an expanding hadronic fireball produced in Au-Au collisions at $\sqrt{s_{NN}}$ = 200 GeV as function of the medium proper time, from a hydro + UrQMD model. The dark grey shaded area shows the duration of the QGP phase, whereas the light grey shaded area depicts the coexistence phase (84).

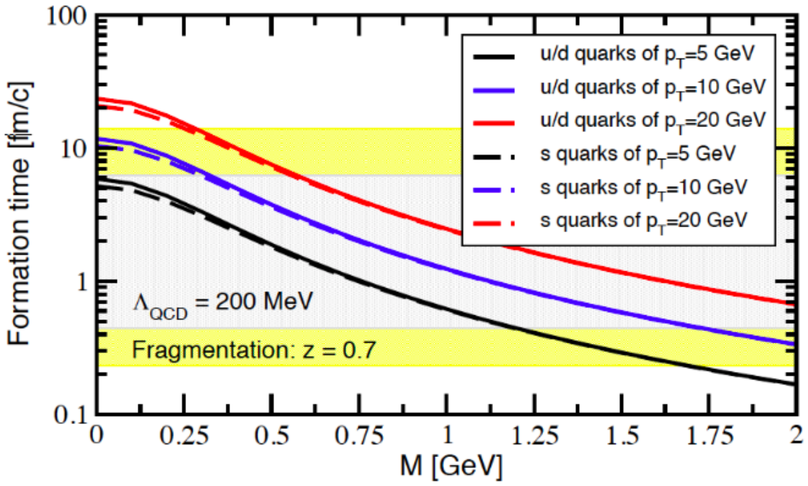

FIGURE 2.12: Hadronic formation time as function of the particles mass M, for different quark p_T and fixed fractional momentum (z). The yellow shaded areas indicate the upper and lower limits for the medium lifetime of the partonic phase at RHIC and LHC, respectively (85).

long-lived particle can provide valuable information about the interactions during the hadronic phase and the lifetime of this phase. Experiments at RHIC and the LHC have measured many of the resonances listed in Table 2.1 in various

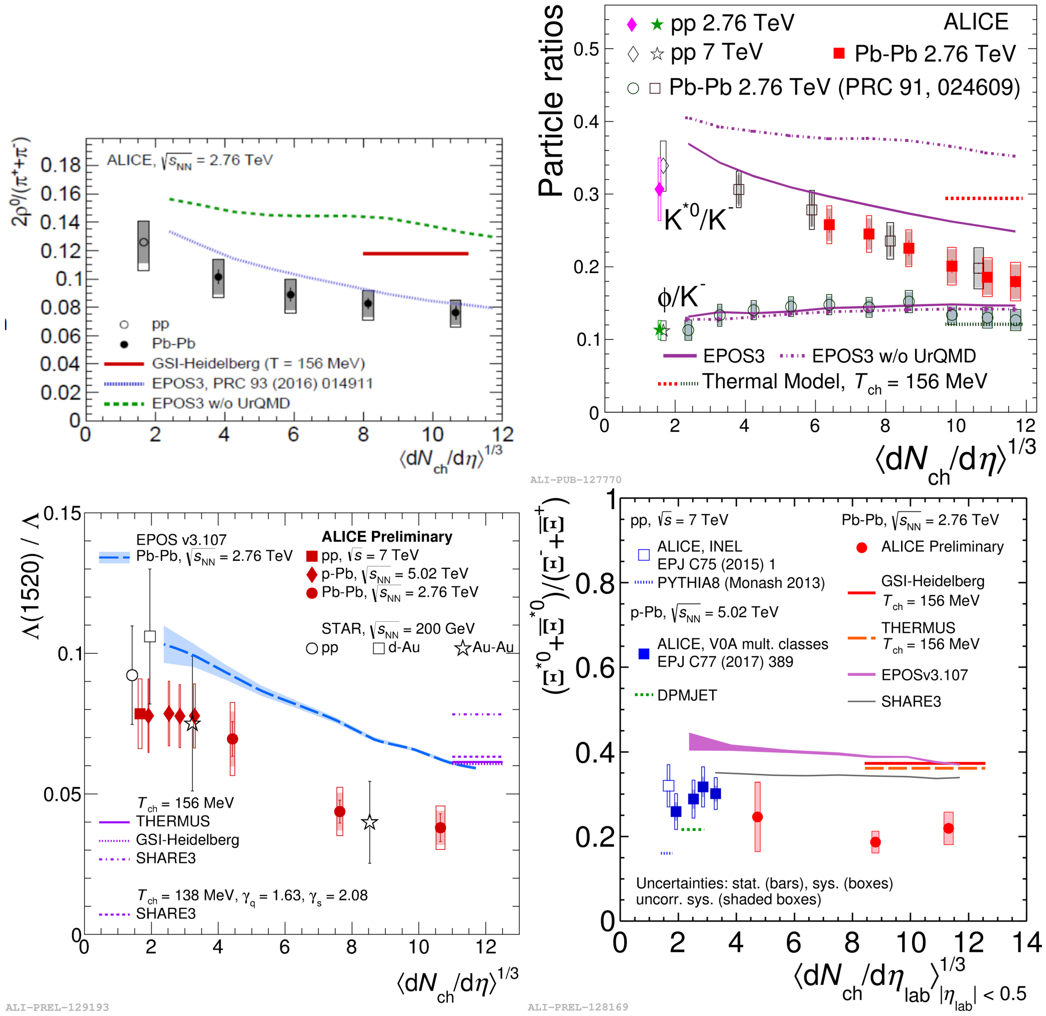

FIGURE 2.13: ρ/π (86)(Top Left), K^{*0}/K and ϕ/K(Top Right) (87), $\Lambda(1520)/\Lambda$(Bottom Left) (88), and Ξ^{*0}/Ξ(Bottom Right) (88) ratios as a function of the cube root of the charged particle multiplicity density $dN_{ch}/d\eta$ for pp, p-Pb, d-Au, Au-Au, and Pb-Pb collisions

collision systems. The ratios ρ/π, K^*/K, ϕ/K, Λ^*/Λ and Ξ^*/Ξ as a function of cubic root of the charged particle multiplicity density ($dN_{ch}/d\eta^{1/3}$) measured by the ALICE experiment and the ratios Σ^*/Λ and Δ^{++}/p as a function of the charged particle multiplicity density $dN_{ch}/d\eta$ measured by STAR experiment are shown in Figures 2.13 and 2.14, respectively. In these figures, the results of different collision systems and different energies are compared. If it is assumed that the strength of rescattering effects is related to the distance which the decay products travel through the hadronic medium the ratio resonance/stable particle should decrease as a decaying exponential of this distance. The fireball radii estimated by HBT (Hanbury Brown-Twiss) technique have been observed to increase approximately linearly with ($dN_{ch}/d\eta^{1/3}$) (80) and then this quantity has been used as a proxy of the radius in the description of the ALICE results.

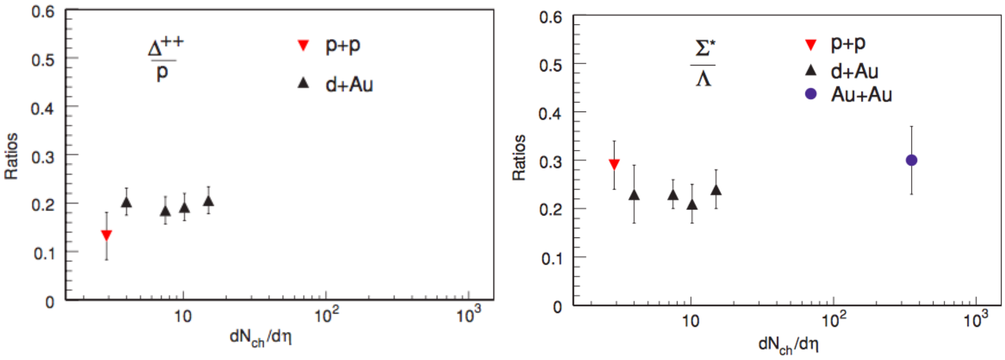

FIGURE 2.14: Δ^{++}/p (Left) and Σ^{*}/Λ ratios as a function of the charged particle multiplicity density $dN_{ch}/d\eta$ for pp, d-Au, and Au-Au collisions at RHIC energies (89)

A centrality-dependent suppression of the ρ/π, K*/K, Λ^{*}/Λ ratios has been observed in Pb-Pb collisions. These ratios in central Pb-Pb collisions are also suppressed with respect to grand-canonical thermal-model calculations (19) with a chemical freeze-out temperature of 156 MeV. The observed dependence of the K^{*0}/K^{-} and Λ^{*}/Λ ratio on the multiplicity is consistent with the behaviour that would be expected if re-scattering were the cause of the suppression. This suppression points to rescattering dominating over regeneration effects. Suppression effects have also been observed by STAR Collaboration in Au-Au collisions at $\sqrt{s_{\rm NN}}$= 200 GeV (89). In contrast, no suppression is observed for the ϕ/K ratio. The ϕ lives 10 times longer than the K^{*} and 35 times longer than the ρ; it decays predominantly after the end of the hadronic phase and is not significantly affected by re-scattering or regeneration. It is also interesting to observe as the measured ratio is substantially independent from the collision system (same results were obtained in Xe-Xe as in Pb-Pb collisions for K^{*} and ϕ (88).
Possible weak suppression of Ξ^{*0} has been observed respect to pp collisions, but no multiplicity-dependence suppression is present in Pb-Pb collisions. This is compatible with its large lifetime compared to other resonances. These behaviours are, at least qualitatively, reproduced by calculations using the EPOS model with an afterburner made by the UrQMD model (73) (see Figure 2.13). As shown in Figure 2.8 the PHSD model (79) can also describe qualitatively the K^{*0}/K suppression measured by ALICE in Pb-Pb collisions at $\sqrt{s_{\rm NN}}$ = 2.76 TeV. The behaviour observed by STAR in Au-Au collisions at $\sqrt{s_{\rm NN}}$ = 200 GeV for the Σ^{*}/Λ ratio (89) is intriguing where no suppression has been pointed out (see Figure 2.14). Furthermore for the same resonances, no multiplicity dependence is reported for the ratio measured in p-Pb collisions at 5.02 TeV (90). Considering its rather low lifetime, the fact that this resonance is not sensitive to the hadronic medium, it is presumably connected to its large regeneration cross section, as observed also in EPOS calculations (73). Similar effect could be present also for the Δ^{++}. In fact, no suppression has been observed for Δ^{++}/p measured by STAR in d-Au at $\sqrt{s_{\rm NN}}$ = 200 GeV (89).
Furthermore, an apparent multiplicity dependent suppression of the K^{*}/K ratio has been observed in pp and p-Pb collisions, which might be an indication of a

hadron-gas phase with non-zero lifetime in high-multiplicity pp and p-Pb collisions (91) (see Figure 2.15).
Starting from these ratios using models it is possible to have an estimate of the lifetime and temperature of the hadronic phase. For example as described in paragraph 2.1.2, using EPOS3 it is possible to estimate for central Pb-Pb collisions at $\sqrt{s_{NN}}$ = 2.76 TeV, a lifetime of the hadronic phase of about 10 fm/c (see Figure 2.6).

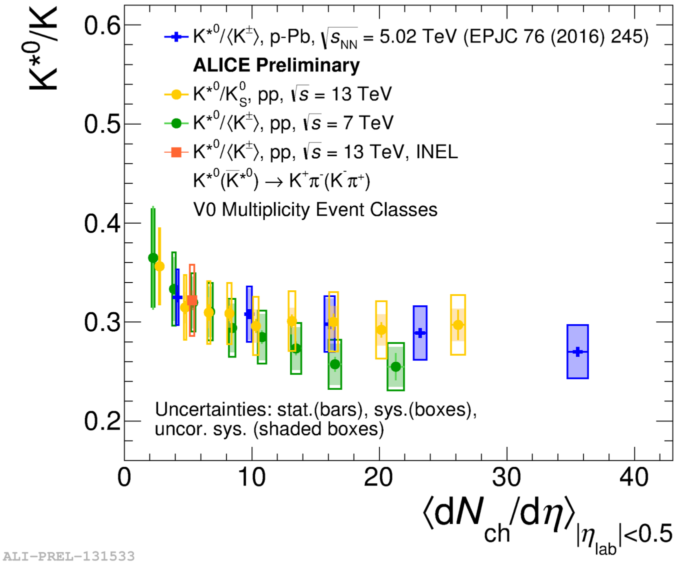

FIGURE 2.15: Ratios of the integrated yields, K^{*0}/K measured in pp collisions at $\sqrt{s}$ = 7 and 13 TeV and in p-Pb collisions at $\sqrt{s_{NN}}$ = 5.02 and 8.16 TeV as a function of charged particle multiplicity (91)

2.3 Some Resonance results at LHC energies

In general hadron yield should give a 'snapshot' of the system at the chemical freeze-out, and the integrated particle yield is directly proportional to the density energy of the system. In pp collisions, a significant fraction of the produced particles do not originate from hard interactions, even at LHC energies. Current models of hadron-hadron collisions at high energies, such as the event generators, combine perturbative QCD for the description of hard parton interactions with phenomenological approaches to model the soft component of the produced particle spectrum.
Thus it is instructive to look at the yields of hadronic resonances as a function of p_T as well as charged particle multiplicity.

Figures 2.16 and 2.17 show the transverse momentum spectra of resonance $K^*(892)^0$, $\phi(1020)$, $\Sigma^*(1385)^{\pm}$, and $\Xi^*(1530)^0$ measured in pp collisions at $\sqrt{s}$ = 7 TeV (92; 93) compared to some of the usual QCD inspired Monte Carlo Generators. The best agreement is found for the PYTHIA Perugia 2011 tune, which reproduces both the K^{*0} spectrum and the high p_T part (p_T > 3 GeV/c) of the ϕ spectrum rather well. PHOJET (94) and ATLAS-CSC significantly overestimate

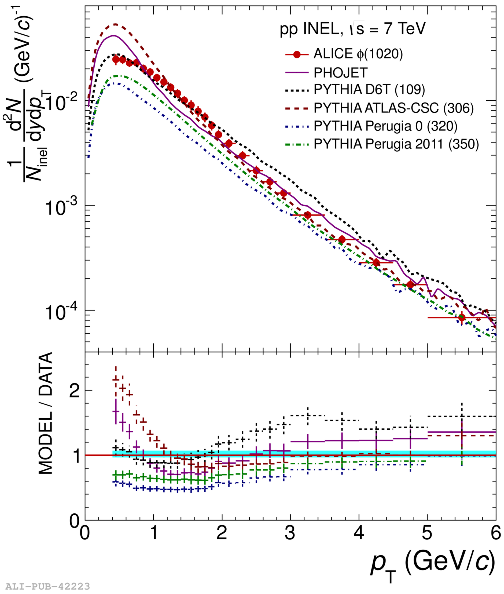

FIGURE 2.16: $d^2N/(dydp_T)$ distribution for $\phi(1020)$ (Left) and $K^*(892)^0$ (Right) as a function of p_T in pp collisions at $\sqrt{s}$ =7 TeV. The results are compared to theoretical models such as PHOJET and PYTHIA (92).

the low momentum part ($p_T < 1$ GeV/c) of the transverse momentum distribution but reproduce the high momentum distribution of both mesons well. The PYTHIA D6T tune gives the best description at low p_T, but deviates from the data at p_T >2 GeV/c. Finally, the PYTHIA Perugia 0 tune underestimates the meson yield for p_T larger than 0.5 GeV/c.

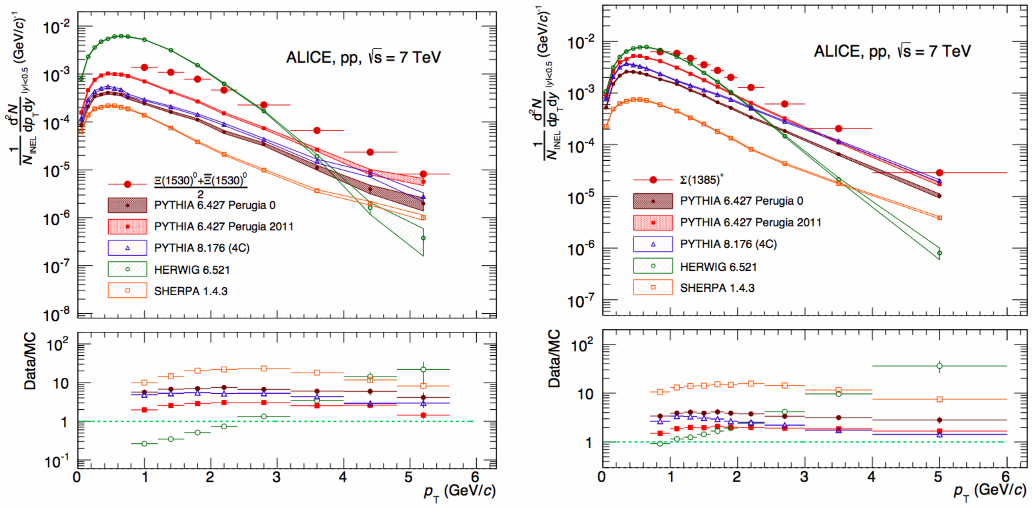

FIGURE 2.17: $d^2N/(dydp_T)$ distribution for $\Xi(1530)$(Left) and $\Sigma(1385)$(Right) as a function of p_T in pp collisions at $\sqrt{s}$ =7 TeV. The results are compared to theoretical models such as PYTHIA, HERWIG, and SHERPA (93).

As can be seen from Figure 2.17, no event generator is able to reproduce the spectra of strange and multi-strange baryon resonances. PYTHIA 6 Perugia 2011 (tune 350) performs better than any other tested generator, but still underpredicts the data by a factor $\sim$ 2-3 in the intermediate-p_T region ($2 < p_T < 3$ GeV/c).

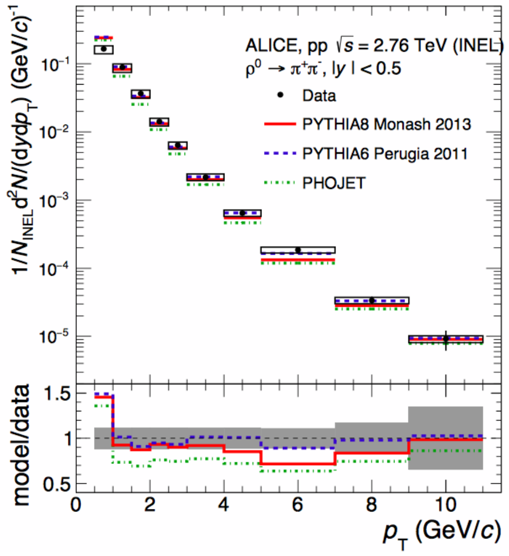

FIGURE 2.18: Differential yields of ρ^0 as a function of transverse momentum in inelastic pp collisions at $\sqrt{s}$ = 2.76 TeV (86). The results are compared with model calculations from PYTHIA 6 (Perugia 2011 tune) (66), PYTHIA 8.14 (Monash 2013 tune) (67) and PHOJET (94).

In Figure 2.18, the p_T spectrum of $\rho(770)$ (86) measured in pp collisions at $\sqrt{s}$ = 2.76 TeV is shown. The best agreement with $\rho(770)$ data at $\sqrt{s}$ = 2.76 TeV is given by PYTHIA6 - Perugia 2011 (66). In general, the models tend to overestimate the ρ meson production at low transverse momentum ($p_T < 1$ GeV/c).

As seen for long-lived particles (95), studies of the resonance yield as a function of the charged particle multiplicity generated in the collision, show that at a given multiplicity, particle production is independent of the system size and collision energy. This is clearly seen in Figure 2.19 where, the p_T-integrated yields of K^{*0} and ϕ normalised to the charged particle multiplicity density ($\langle dN_{ch}/d\eta \rangle$) measured in pp collisions (at $\sqrt{s}$ = 7 and 13 TeV) and p-Pb collisions (at $\sqrt{s_{NN}}$ = 5.02 and 8.16 TeV) are shown as a function of the charged-particle multiplicity. Results for pp and p-Pb collisions at different energies follow approximately the same trends, indicating that K^{*0} and ϕ production also does not depend on the collision system or energy, but on the local charged-particle density of the selected collision. Furthermore for both resonances, dN/dy exhibits an approximately linear increase with $\langle dN_{ch}/d\eta \rangle$.

Resonances can also be useful for studies of the mechanisms that determine the shapes of hadron p_T spectra. The mean transverse momentum $\langle p_T \rangle$ can be used to study how the shape of hadron p_T spectra depend on particle properties, including quark content and mass. The $\langle p_T \rangle$ values of the resonances and long

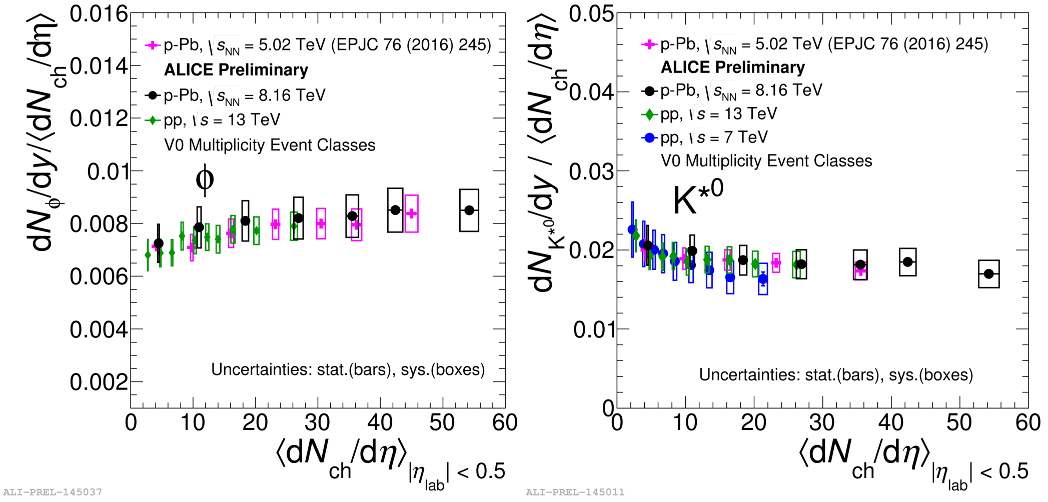

FIGURE 2.19: Integrated yields of ϕ (left) and K$^*(892)^0$ (right) normalized to $\langle dN_{ch}/d\eta \rangle$ in pp collisions (at $\sqrt{s}$ = 7 and 13 TeV) and p-Pb collisions (at $\sqrt{s_{\rm NN}}$ = 5.02 and 8.16 TeV) for different multiplicity classes([91])

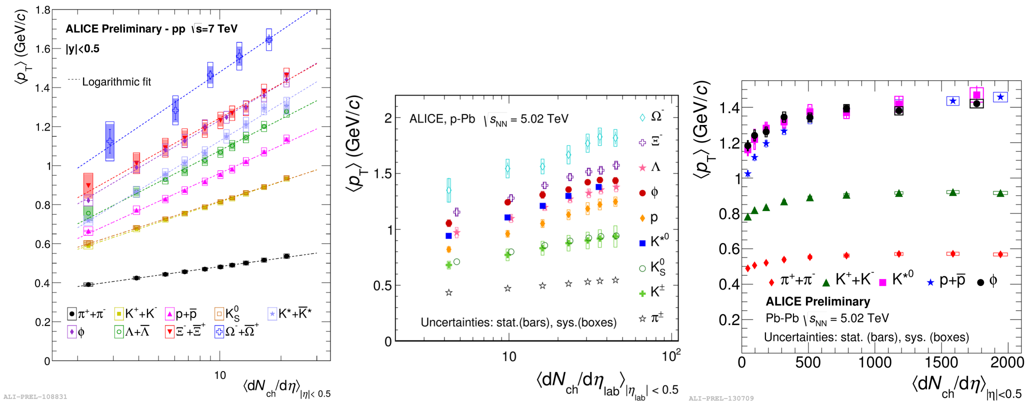

FIGURE 2.20: Mean p_T distribution for various resonances, stable hadrons and hyperons as a function of charged particle multiplicity density in pp (Left) ([88]), p-Pb (middle) ([96]) and Pb-Pb collisions (Right) ([88])

lived particles are shown in Figure 2.20 as a function of charged particle multiplicity for different collision systems (pp at 7 TeV ([88]), p-Pb at 5.02 TeV ([96]) and Pb-Pb at 5.02 TeV ([88])). In particular it is interesting to compare K^{*0}, p, and $\phi(1020)$, which all have similar masses. For central Pb-Pb collisions, the $\langle p_T \rangle$ values for these three particles are consistent, suggesting that the shapes of the p_T spectra are determined primarily by the particle masses, as could be expected for a simple hydrodynamic behaviour ([97]). However, recombination models which take in to account the radial flow mass effect like in a hydrodynamic picture can also describe a near-constant behaviour of the p/ϕ ratio ([98]). In central A+A collisions, $\langle p_T \rangle$ values are ordered with particle mass. However, this behaviour is not observed for smaller collision systems, where the proton is observed to have lower $\langle p_T \rangle$ values than the two mesonic resonances. This is further indication that radial flow is the dominant mechanism determining spectra shapes only in very high multiplicity Pb-Pb collisions. Furthermore in pp and low-multiplicity p-Pb collisions the ϕ-meson $\langle p_T \rangle$ values even approach the values for Ξ (which has a 30% greater mass). It is not clear whether this violation of mass ordering is due to differences between baryons and mesons or due to the fact that the ϕ and K^{*0} are resonances. For all light-flavor hadron species (including resonances), the $\langle p_T \rangle$ values in p-Pb collisions follow different trends and rise faster with multiplicity than in Pb-Pb collisions. In pp and p-Pb collisions the $\langle p_T \rangle$ values can reach (or even exceed) the values measured in central Pb-Pb collisions.

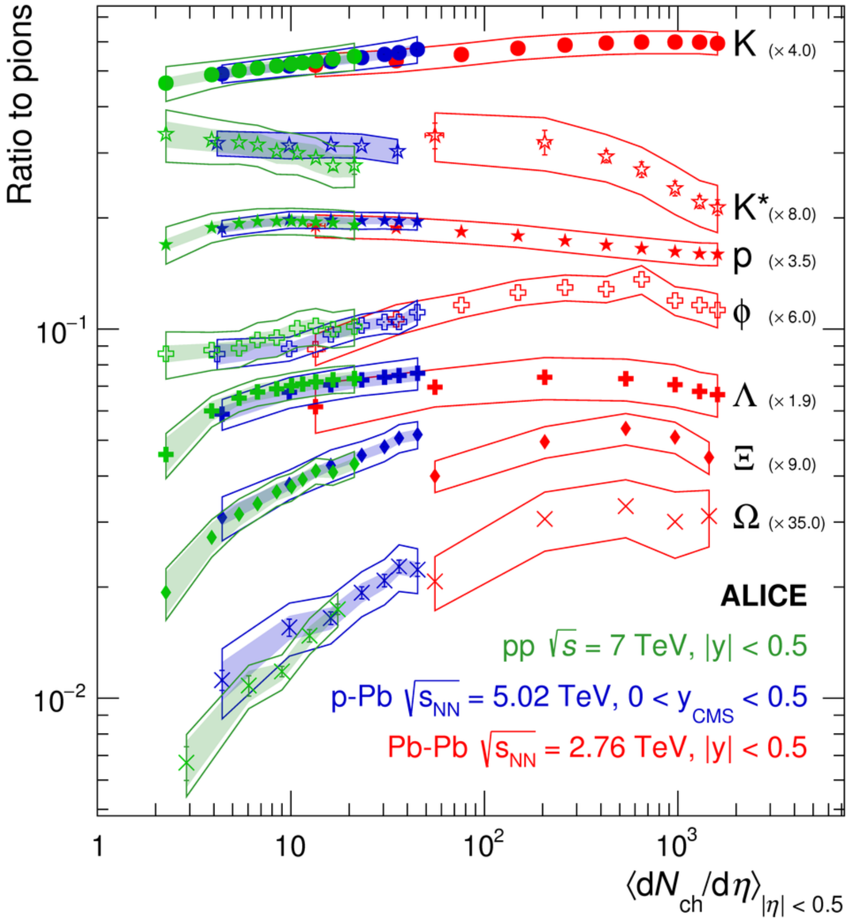

FIGURE 2.21: Ratios of K, K^*, p, ϕ, Λ, Ξ, and Ω to π in pp, p-Pb, and Pb-Pb collisions as a function of charged particle multiplicity density (54)

Strangeness enhancement as pointed out in Chapter 1 was one of the first proposed signal for formation of Quark Gluon Plasma in heavy-ion collisions. The production of strangeness, including its possible enhancement in central A+A collisions and/or canonical suppression in (low-multiplicity) pp collisions, is usually studied using common long lived hadrons. Resonances may also contribute to such studies due to the fact that have different masses than their long-lived counter parts and that some, like the ϕ, have a unique quark content. In

Figure 2.21, ratio of various strange particles and resonances to the π as a function of cube root of charge particle multiplicity density in pp, p-Pb, and Pb-Pb collisions is reported. All identified particle to pion ratios seem to depend solely on charged-particle multiplicity density, regardless of system type and collision energy. About strangeness production we can observe that as the ratios of strange hadrons to pions show a significant enhancement that increases with increasing strangeness content of the numerator particle, i.e $\Lambda/\pi < \Xi/\pi < \Omega/\pi$ (strangeness content $1, 2$ and 3 respectively). While in the same figure also the ratio of a non strange particle such as the proton is reported. While the yield of protons normalised to pions remains approximately constant as a function of multiplicity. This indicates that the increase of hyperon production with respect to pions is a phenomenon that does not originate from mass differences but is connected to strangeness content.

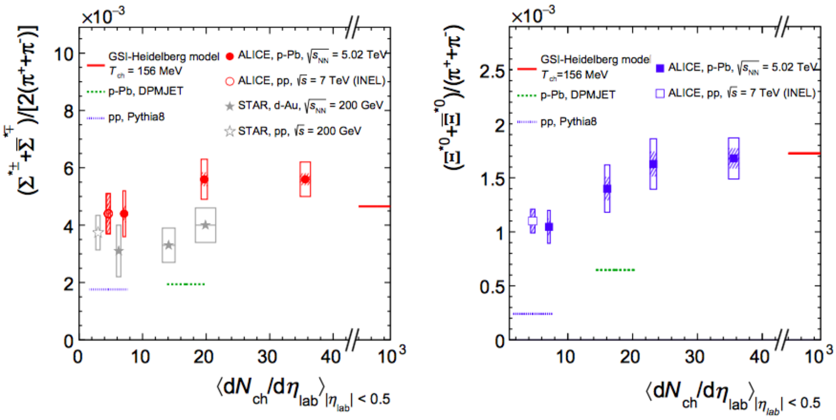

FIGURE 2.22: (Left) Ratio of $\Sigma(1385)^{*\pm}$ to $\pi^{\pm}$ and (Right) Ratio of $\Xi(1530)^{*0}$ to $\pi^{\pm}$, measured in pp, d-Au and p-Pb collisions, as a function of the average charged particle density ($\langle dN_{ch}/d\eta \rangle$) measured at midrapidity. A few model predictions are also shown as lines at their appropriate abscissa (90).

The integrated yield ratios of excited hyperons ($\Sigma(1385)^{\pm}$ and $\Xi(1520)^{0}$) to pions as a function of the charged multiplicity density are shown in Figure 2.22. This allows us to check the evolution of relative strangeness production yields with increasing collision system size. For $\Sigma^{*\pm}/\Lambda$ and Ξ^{*0}/Ξ^{-} ratios in p-Pb collisions rather constant values with multiplicity have been measured (see Figure 2.13 (90) and Figure 2.14 (89)). This indicates that the $\Sigma^{*\pm}$ and Ξ^{*0} resonances (which are more massive than the Ξ) are enhanced by the same amount as their ground-state counterparts, suggesting that it is indeed the strangeness, and not the mass, that controls the enhancement.
Furthermore, the relative production of the ϕ, particle with strange net content equal to zero, increases with $dN_{ch}/d\eta$ by approximately by 20%, similarly to the Λ, a single-strange baryon. This suggests that ϕ production cannot be described solely by considering net strangeness or number of strange quark constituents. In pp collisions the K^{*0}/π ratio, on the other hand, exhibits a hint of a decrease with multiplicity (see Figure 2.21). In nuclear collisions, this decrease is more

pronounced and as described in the previous paragraph is considered a consequence of the rescattering of K^{*0} decay daughters during the hadronic phase of the system evolution.
In Figure 2.23, the comparison of the p_T distributions for two extreme multiplicity classes, of K^{*0}/K^0_S (left panel) and ϕ/K^0_S (right panel) measured in pp collisions at $\sqrt{s} = 13$ TeV are shown. The ratios of high to low multiplicity classes are reported in the bottom panel of the same figures. Both ratios of K^* and ϕ increase at low p_T and saturate for $p_T > 3$ GeV/c. However from the bottom panels it is clear that the K^{*0}/K^0_S ratio is more suppressed compared to ϕ/K^0_S for $p_T < 2$ GeV/c. As re-scattering is important at low p_T, this behaviour is consistent with the presence of re-scattering effect in an hadronic phase in high multiplicity pp collisions.

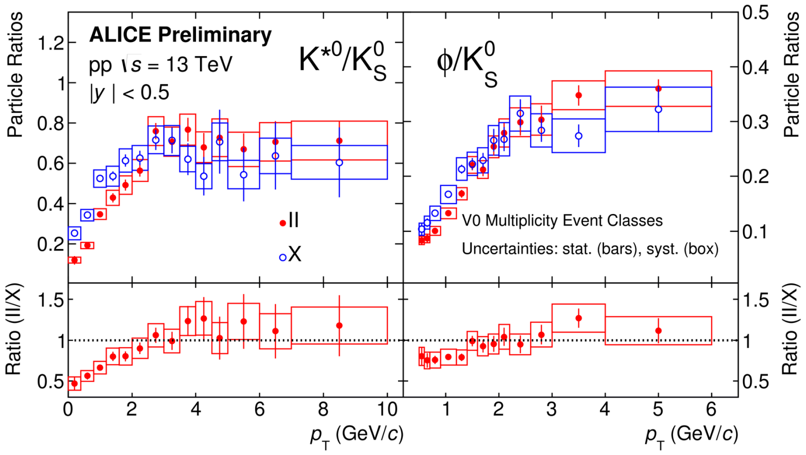

ALI-PREL-156819

FIGURE 2.23: p_T differential ratio of K^{*0}/K^0_S (left panel) and ϕ/K^0_S (right panel) in pp collisions at $\sqrt{s} = 13$ TeV for two different extreme multiplicity classes, where $\langle dN_{ch}/d\eta \rangle$ in high (II) and low (X) multiplicity classes are ~ 20 and 2.4, respectively. The bottom panel shows the ratio between the yield ratio in high to low multiplicity class (91).

Chapter 3

A Large Ion Collider Experiment at LHC

3.1 The Large Hadron Collider

The Large Hadron Collider (LHC)(99) is the world's largest and most powerful particle accelerator. It was inaugrated on 10 September 2008, and consists of a 27-kilometre ring of superconducting magnets with a number of accelerating structures to boost the energy of the particles along the way. By design, the maximum energies reached in the accelerator are 7 TeV for a beam of protons and 2.76 TeV per nucleon for a beam of lead ions, thus providing collisions at $\sqrt{s}$ = 14 TeV and $\sqrt{s_{NN}}$ = 5.5 TeV, respectively. During Run 2, LHC was able to reach 13 TeV for pp and 5.02 TeV for Pb-Pb collisions. and These are the largest energies ever achieved in particle collision experiments.

Inside the accelerator, two high-energy particle beams travel at close to the speed of light before they are made to collide. The beams travel in opposite directions in separate beam pipes - two tubes kept at ultrahigh vacuum. They are guided around the accelerator ring by a strong magnetic field maintained by superconducting electromagnets. The accelerator bends the beams around the ring, keeping the bunches focused and accelerate them to their collision energy. Finally, bunches are squeezed in order to ensure a high number of collisions per time interval at the collision points, i.e. a high luminosity[1]. A combination of magnetic and electric fields components perform the mentioned tasks. Despite the high luminosity reached, only a very small fraction of the particles from the two bunches collide in a single bunch crossing. The others leave the interaction region essentially uninfluenced, and continue to circulate in the accelerator.

Injection of bunches into the LHC (Figure 3.1) is preceded by acceleration in the LINAC2, PS booster, PS, and SPS accelerators. The acceleration sequence is slightly different for heavy-ions, in which case bunches pass the LINAC3,

---

[1] For a particle accelerator experiment, the luminosity is defined by: $\mathcal{L} = fnN^2/A$ with n number of bunches in both beams, N number of particles per bunch, cross-sectional area A of the beams that overlap completely, and revolution frequency f. The frequency of interactions (or in general of a given process) can be calculated from the corresponding cross-section σ and the luminosity: $dN/dt = \mathcal{L}\sigma$.

LEIR, PS, and SPS accelerators. Several injections to the LHC are needed until all bunches of both beams are filled. The LHC produces collisions in four so called Interaction Points (IPs) in correspondence of which are located six detectors of different dimensions and with different goals, all able to study the products of the interactions. These are:

- **ALICE (A Large Ion Collider Experiment - IP2):** (100) is a dedicated heavy-ion experiment designed to study strongly-interacting matter at very high energy density. A detailed description of ALICE detector will be covered in the next section.
- **ATLAS (A Toroidal LHC ApparatuS - IP1)(101) and CMS (Compact Muon Solenoid - IP5):**(102) are general-purpose detectors for pp collisions that are built to search for the Higgs boson and physics beyond the Standard Model, e.g. new heavy particles postulated by supersymmetric extensions (SUSY) of the Standard Model and evidence of extra dimensions. They have discovered the Higgs boson in 2012 (6).
- **LHCb (The Large Hadron Collider beauty experiment - IP8):**(103) is a dedicated experiment to study heavy flavour physics at the LHC. The experiment complements the studies conducted at B-factories and the search for new particles at ATLAS and CMS.
- **LHCf (Large Hadron Collider forward experiment - IP1):**(104) is placed closed to the ATLAS experiment and studies the forward particles created during LHC collisions.
- **TOTEM (TOTal Elastic and diffractive cross-section Measurement - IP5):** (105) is located close to the CMS detector and measures the total cross-section, elastic scattering, and diffractive processes.

3.2 The ALICE Detector

ALICE (A Large Ion Collider Experiment)(100) is a general-purpose, heavy-ion detector at the LHC, which focuses on Quantum Chromodynamics, the strong-interaction sector of the Standard Model. It has been collecting data since the beginning of LHC operations in 2008, and will continue to do so until the end of 2018 for the planned long shutdown. During the first three years of operations LHC provided pp collisions at 0.9, 2.76, 7, and 8 TeV, Pb-Pb collisions at 2.76 TeV and finally p-Pb collisions at 5.02 TeV and in the second phase, LHC reached close to it's designed maximum energies at 13 TeV for pp, 5.02 TeV for Pb-Pb and 8.16 TeV at p-Pb collisions. The experiment has been designed to study the physics of strongly interacting matter and the quark-gluon plasma at extreme values of energy density and temperature in nucleus-nucleus collisions. ALICE allows for a comprehensive study of hadrons, electrons, muons, and photons produced in the collision of heavy nuclei (Pb-Pb), up to the highest multiplicities at the LHC. The physics programme also includes analysis of proton-proton and proton-nucleus collisions to address various QCD topics. The detector, located

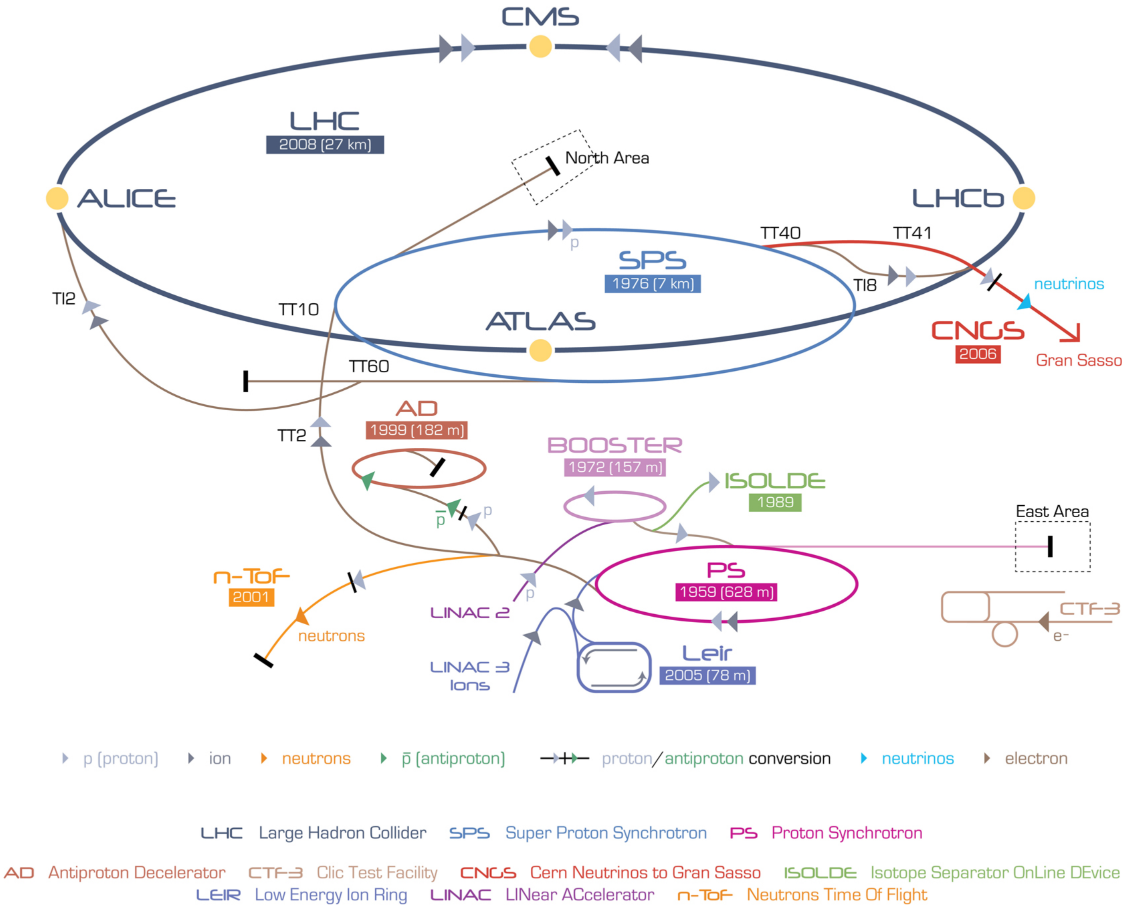

FIGURE 3.1: The CERN accelerator complex

at the interaction point 2 along the LHC ring, has been designed to cope with a high particle multiplicity environment and to provide unique particle identification (PID) performance that allow a comprehensive study of hadrons, electrons, muons, and photons produced in the collision, down to very low transverse momentum (0.1 GeV/c).

Figure 3.2 shows the ALICE detector schema and Figure 3.3 shows the cross section of the central barrel. The central barrel covers a mid rapidity region $|\eta| < 0.9$ and azimuthal range of 2π. The central barrel of the detector is enclosed in the L3 solenoid magnet which provides a 0.5 T magnetic field, and is followed by a forward muon spectrometer which has its own dipole magnet providing a field of 0.67 T. Going from beam pipe outwards, the central barrel consists of, a six layer Inner Tracking System (ITS) that provides precise tracking and vertex reconstruction, a large volume Time Projection Chamber (TPC) which is responsible for global tracking and particle identification (PID) through the measurement of specific energy loss in a gas, a Transition Radiation Detector (TRD) allowing for identification of electrons and a Time of Flight detector (TOF) which allows for identification of charged hadrons.

Transition radiation detector (TRD) covers full azimuth of the mid-rapidity region ($-0.84 < \eta < 0.84$) from 2.90 m to 3.68 m from the interaction vertex. It has the main task to provide electron identification in the ALICE central barrel for

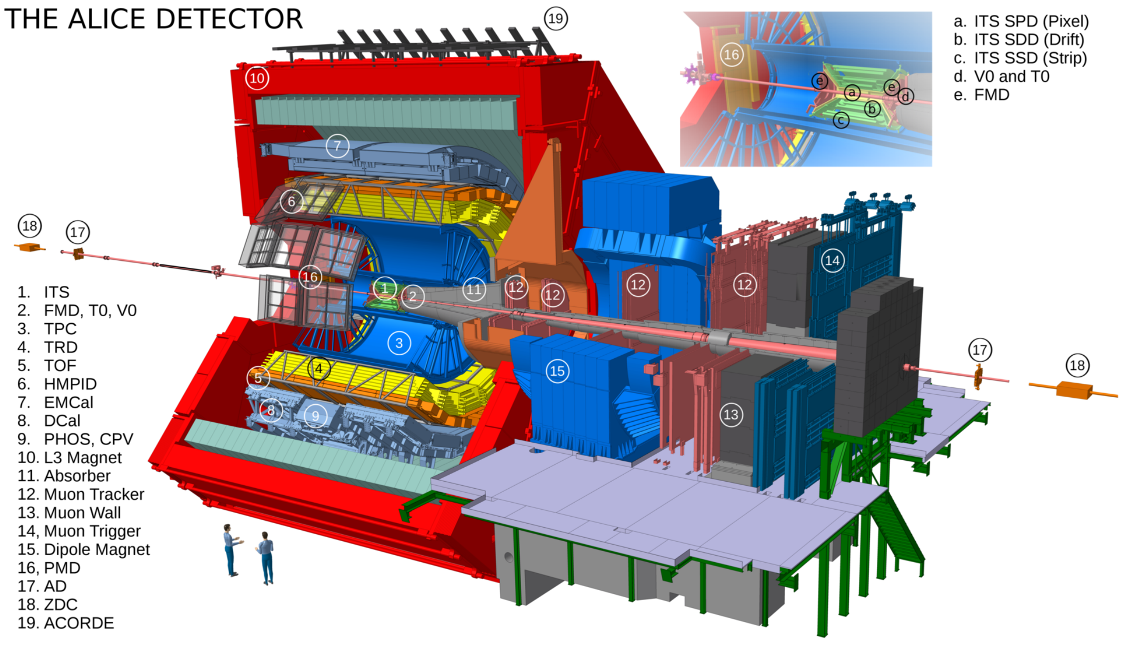

FIGURE 3.2: The ALICE detector

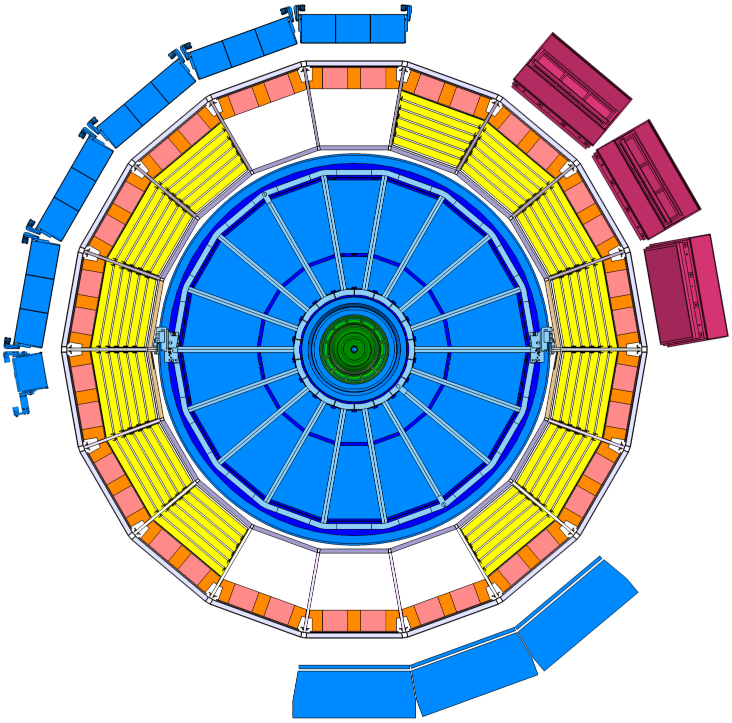

FIGURE 3.3: Cross Section of Central Barrel of ALICE

particle momenta greater than 1 GeV/c. Electrons with momentum above this value emit transition radiation [2] which can be exploited to extend the pion rejection capability of the TPC to higher momenta. Furthermore, the TRD provides tracking information with a larger tracking lever arm, thus improving momentum resolution at high p_T. The detector can also derive a fast trigger for high-momentum charged particles and it contributes to the Level-1 trigger of ALICE.

The detectors which are important for this thesis will be explained in the following sections: TPC, ITS, TOF and VZERO

Besides the aforementioned detectors, the following detectors located inside the L3 magnet provide limited acceptance, outside the TOF:

- **HMPID**: High Momentum Particle Identification Detector is a dedicated detector for inclusive measurements of identified hadrons at p_T >1 GeV/c. It is based on proximity-focusing Ring Imaging Cerenkov (RICH) counters [3] arranged in an array with an acceptance of 5% of the central barrel phase space with the aim of enhancing the PID capability of ALICE by enabling identification of charged hadrons beyond the momentum interval attainable through energy-loss (in ITS and TPC) and time-of-flight measurements (in TOF). Identification of light nuclei and anti-nuclei (d, t, ^{3}He, α) at high transverse momenta in the central rapidity region can also be performed with the HMPID.
- **Calorimeters**
  1. **EMCal/DCal:** The aim of ElectroMagnetic Calorimeter and Di-Jet Calorimeter is to enable ALICE to measure jet properties and to provide trigger on jets and high momentum photons and electrons. The EMCal and DCal are large Pb-scintillator sampling calorimeters with cylindrical geometry, located adjacent to the ALICE magnet coil at a radius of $\sim$ 4.5 metres from the beam line. EMCal subtends 110° and the DCal subtends 60° in ϕ, with both detectors covering $|\eta| <$

---

[2] Transition radiation is produced by relativistic charged particles ($\gamma \geq 1000$) when they cross the interface of two media of different dielectric constant. Photons are emitted in the keV range with typical energy

$$\hbar\omega \approx \frac{1}{4}\hbar\omega_p\gamma,$$

where ω_p is the plasma frequency

$$\omega_p = \sqrt{\frac{n_e e^2}{\epsilon_0 m_e}}$$

where n_e is the electron density

[3] Cherenkov radiation is emitted when a charged particle passes a dielectric medium with velocity

$$\beta \geq \beta_{thr} = 1/n$$

, where n is the refractive index of the medium. The photons are emitted at an angle

$$cos\theta_c = \frac{1}{n\beta}$$

0.7, thereby providing good acceptance for di-jets with $R \leq 0.4$ up to transverse momenta $\mathrm{p_T} \sim 150\mathrm{GeV}/c$

2. **PHOS**: **Pho**ton **S**pectrometer is a high-resolution electromagnetic calorimeter which detects electromagnetic particles in a limited acceptance region at central rapidity to provide photon identification as well as neutral-meson reconstruction, through the 2-photon decay channel. Its main physics objectives are the test of thermal and dynamical properties of the initial phase of the collision extracted from low $\mathrm{p_T}$ direct photon measurements, and the study of jet quenching through the measurement of high-$\mathrm{p_T}$ π^0 and γ-jet correlations. It is positioned at a distance of 460 cm from the interaction point, azimuthally opposed to the EMCAL, and covers a limited acceptance ($|\eta| < 0.12$ and $\Delta\phi = 100^\circ$).

In addition to the central barrel detectors described above, ALICE has a dedicated Muon Spectrometer, a set of forward detectors and ACORDE.

Muon Spectrometer

This detector, placed in the forward pseudo-rapidity region ($-4.0 < \eta < -2.5$), consists of a dipole magnet, and tracking and trigger chambers. It is optimised to reconstruct heavy quark resonances (such as J/Υ through their $\mu^+\mu^-$ decay channel) and single muons.

Forward Detectors

These detectors are placed in the high pseudo-rapidity region (small angles with respect to the beam pipe) they are small and specialised detector systems used for triggering or to measure global event characteristics.

- **(T0):** Time Zero detector consists of two arrays of Cherenkov counters, 12 counters per array. They are used to measure the event time with precision of the order of tens of picoseconds, as needed by TOF.

- **VZERO:** to reject the beam-gas background, to trigger minimum bias events, and for multiplicity estimation.

- **FMD:** Forward Multiplicity Detector provides multiplicity information over a large fraction of the solid angle ($-3.4 < \eta < -1.7$ and $1.7 < \eta < 5$).

- **PMD:** Photon Multiplicity Detector consists of large arrays of gas proportional counters in a honeycomb cellular structure. The detector has been optimised to measure the multiplicity and the spatial distribution of photons on an event-by-event basis in the $2.3 < \eta < 3.7$ region.

- **ZDC:** Zero Degree Calorimeter are quartz fibres sampling calorimeters complimented by electromagnetic calorimeter, optimised to measure and trigger on the impact parameter.

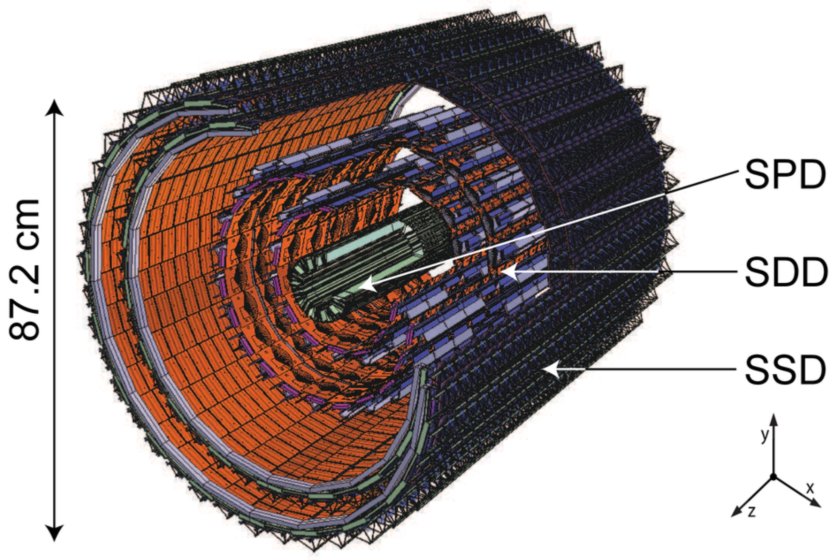

FIGURE 3.4: The Inner Tracking System of ALICE

ACORDE

ALICE **Co**smic **R**ay **De**tector (ACORDE) is an array of scintillators installed on top of the L3 magnet to trigger on cosmic rays. It plays a two-fold role in ALICE:

- the first task is to provide a fast (Level-0) trigger signal, for the commissioning, calibration and alignment procedures of some of the ALICE tracking detectors
- it will also detect, in combination with the TPC, TRD and TOF, single atmospheric muons and multi-muon events (so-called muon bundles) allowing the study high-energy cosmic rays in the energy region of the knee in the cosmic ray spectrum

3.2.1 Inner Tracking System

ITS (100) is the main detector responsible for measuring the primary vertex of the collisions being the innermost tracking detector closest to the beam pipe. It has 6 layers of concentric cylindrical detectors based on three different technologies of silicon detectors : pixels, drifts, and strips (Figure 3.4). It is positioned at radius between 4 and 43 cm, surrounding the LHC beryllium beam pipe that is $800 \mu m$ thick and has a radius of 2.9 cm.

The two innnermost ITS layers constitute the SPD, the Silicon Pixel Detector. The SPD is based on hybrid silicon pixels, consisting of a two-dimensional matrix (sensor ladder) of reverse-biased silicon detector diodes bump-bonded to readout chips. Each diode is connected through a conductive solder bump to a contact on the readout chip corresponding to the input of an electronics readout cell. The basic detector module is the half-stave. Each half-stave consists of two ladders, one Multi-Chip Module (MCM) and one high density aluminium/polyimide multi-layer interconnect. The ladder consists of a silicon sensor matrix bump bonded to 5 front-end chips. The sensor matrix includes 256 x 160 cells measuring 50 μm ($r\phi$) by 425 μm (z). Longer sensor cells are used in the boundary region to ensure coverage between readout chips. The sensor matrix has an active area of 12.8mm ($r\phi$) x 70.7mm (z). The front-end chip reads out a sub-matrix of 256 ($r\phi$) x 32 (z) detector cells. In total, the SPD (60 staves) includes 240 ladders with 1200 chips for a total of 9.8 x 10^6 cells. The inner (outer) SPD layer is located at an average distance of 3.9 cm (7.6 cm) from the beam axis. The detector design implements several specific solutions to minimise the material budget. The SPD has the best spatial resolution of the ITS detectors, thus providing a resolution on the impact parameter measurement adequate for charm flavour detection.

The Silicon Drift Detector (SDD) is based on modules with a sensitive area of 70.17 ($r\phi$) x 75.26 (z) mm^2, which is divided into two drift regions where electrons move in opposite directions under a drift field of approximately 500 V/cm. The SDD modules are mounted on a linear structure called a ladder. The SDD inner layer is made of 14 ladders with 6 modules each, the outer layer has 22 ladders, each of them with 8 modules. The position of the particle along z is reconstructed from the centroid of the collected charge along the anodes, while the position along the drift r coordinate is obtained from the measured drift time with respect to the trigger time. This reconstruction requires a precise knowledge of the drift speed, that is measured during frequent calibration runs, given its strong dependence from the humidity and temperature gradients in the SDD volume.

The Silicon Strip Detector (SSD) building block is a module composed of one double-sided strip detector connected to two hybrids hosting the front-end electronics. The sensors are 300 μm thick and with an active area of 73 (r) x 40 (z) mm^2. There are 768 strips, with a pitch of 95 μm on each side, almost parallel to the z beam axis direction. The innermost SSD layer consists of 34 ladders, each of them housing 22 modules along the beam direction, while the other SSD layer has 38 layers, each of them with 25 modules. The outer four layers are used for particle identification via energy loss (dE/dx) measurement in the non-relativistic region for low momentum particles (down to p_T =100 MeV) via analogue readout. Figure 3.5 shows an example of the particle identification capabilities of the ITS for pp collisions at $B = 0.2T$. The resolution in the $r\phi$ plane is nearly 50 μm for 1 GeV/c particles and decreases at higher momentum. Resolution in Pb-Pb collisions is slightly better with respect to pp, as the high multiplicity of central Pb-Pb collisions implies a better primary vertex resolution.

3.2.2 The Time Projection Chamber

The Time Projection Chamber (TPC) (106) is the main tracking detector of ALICE covering the pseudorapidity range $|\eta| < 0.9$ and the full azimuth angle. The optimisation of the detector design has been done to provide excellent tracking performance in a high multiplicity environment, to keep the material budget as

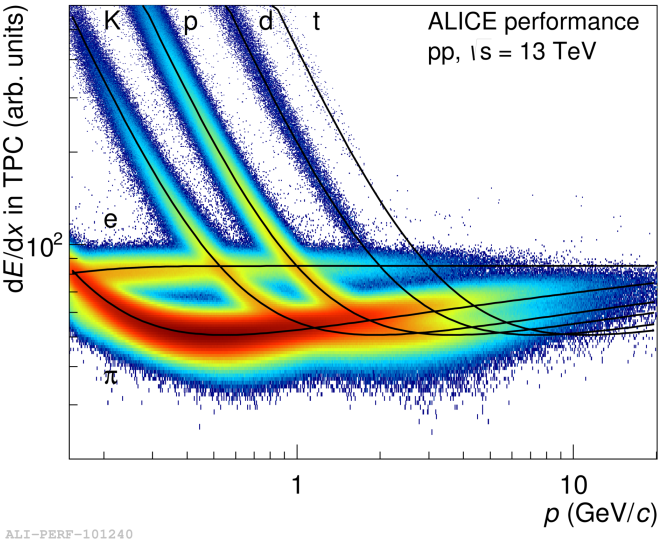

FIGURE 3.5: dE/dx distribution of charged particles as function of their momentum, both measured by the ITS alone, in pp collisions at 13 TeV. The lines are a parametrization of the detector response based on the Bethe-Bloch formula.

low as possible in order to have low multiple scattering and secondary particle production, to limit the detector occupancy at the inner radius but still guarantee a good momentum resolution for high -p_T particles. TPC is cylindrical in shape 500 cm long along the beam pipe, with 80 cm and 250 cm inner and outer radii respectively, determined by maximum acceptable track density and minimum track length for which the resolution on dE/dx is lower than 10%. The TPC volume was filled with 90 m^3 of a mixture of $Ne/CO_2/N_2$ during Run 1, optimised for drift velocity, low electron diffusion and low radiation length. Neon was replaced by Argon for the Run 2. The electron drift velocity of 2.7 cm/s over 250 cm (each of the two TPC drift region separated by the central cathode) gives a maximum drift time of 88 μs, therefore limiting the maximum event rate TPC can sustain. At high interaction rate, pile-up effects and the long TPC dead time are the two main factors that force ALICE to run at a lower instantaneous luminosity with respect to the other LHC experiments.

The TPC is able to track particles in a wide momentum range, from about $p_T \sim 0.1$ GeV/c up to $p_T \sim$ 100 GeV/c with good momentum resolution and efficiency $> 90\%$ for $p_T > 100$ MeV/c, where the limiting factor are the interactions in the ITS material. The ITS and the TPC are able to determine the momentum of the charged particles with a resolution better than 1% at low p_T and better than 20% for $p_T \sim$ 100 GeV/c (see Figure 3.6) by measuring the deflection in the magnetic field.

The charge collected in the TPC readout pads is used to measure particle energy loss. The momentum measurement and the dE/dx information allow to separate the various charged particle species in the low momentum region: thanks to its good dE/dx resolution, the TPC can identify particles with $p_T < 1$

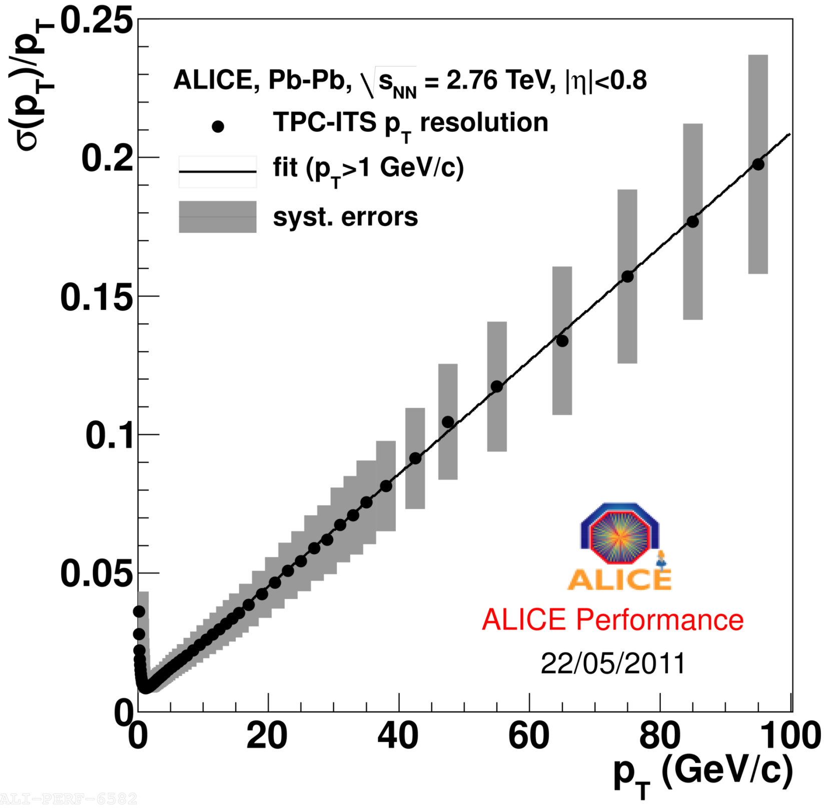

FIGURE 3.6: Momentum Resolution for TPC-ITS

GeV/c. An example of the TPC PID performance is shown in Figure 3.7, where the energy loss distribution for the different species is fitted by a Bethe-Bloch function, similarly to the ITS case.

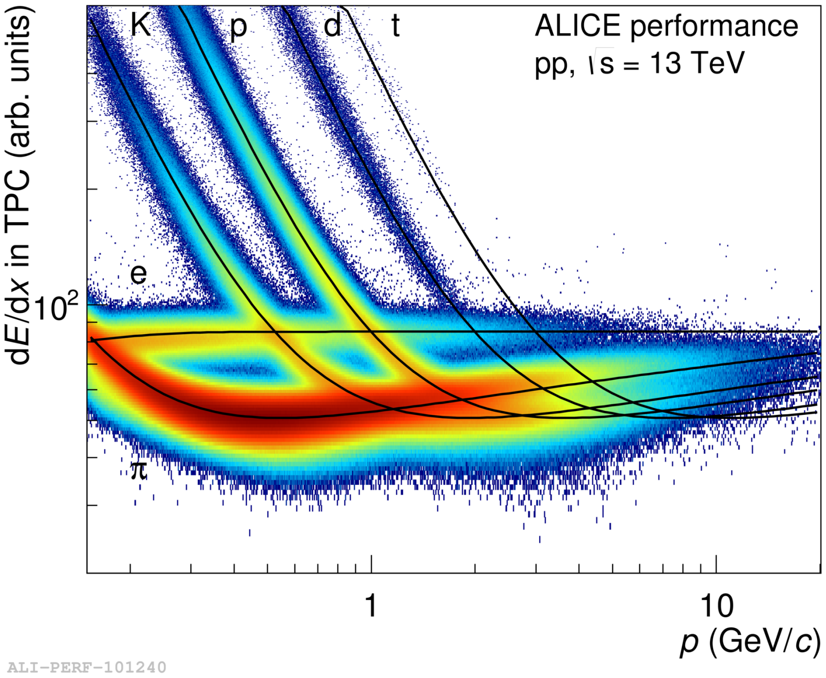

FIGURE 3.7: Energy loss in TPC in pp collisions at $\sqrt{s}$ = 13 TeV

3.2.3 The Time of Flight Detector

The Time of Flight (TOF) detector plays a key role in particle identification in the pseudorapidity region $|\eta| < 0.9$, by combining the measurement of the particle time-of-flight with the momentum information provided by the TPC. TOF is a large MRPC (Multi Resistive Plate Chamber) array located in the ALICE central barrel at a distance of 3.7 m from the beam line, externally to the TRD. The intrinsic time resolution of the MRPC is lower than 50 ps (from test beam studies) and it is dominated by the jitter in the electronics and the time resolution of the TDCs. The MRPC efficiency was measured to be close to 100%. The design of TOF is optimised to minimise the dead zones and to be perpendicular to the trajectories of the particles coming from the interaction point, so to limit the occupancy and reduce the time resolution. The TOF detector consists of 152928 readout channels (2.5 x 3.5 cm^2 each) covering a total area of 141 m^2. This highly segmented structure allow to have a low occupancy and good performance also in a high multiplicity environment, such that of Pb-Pb collisions. An example of TOF performance is shown in Figure 3.8.

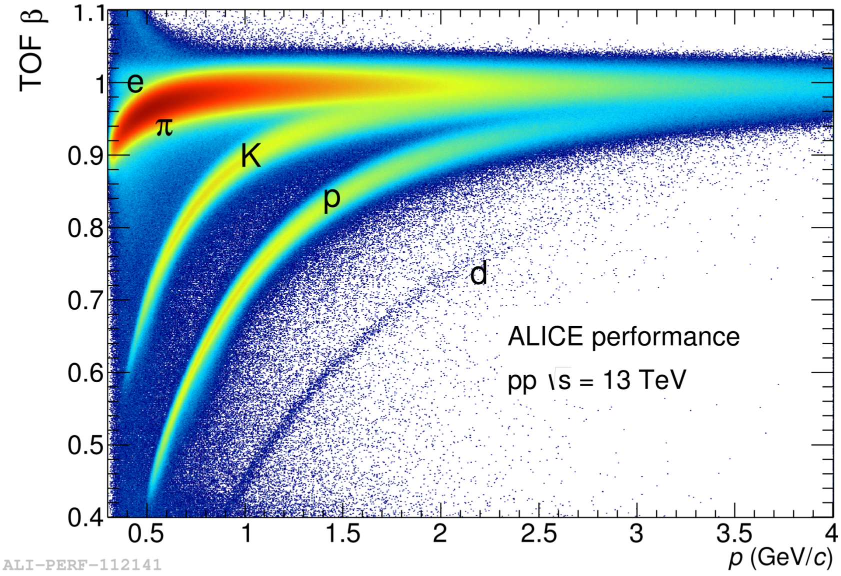

FIGURE 3.8: TOF β vs p$_{\mathrm{T}}$performance plot in pp collisions at $\sqrt{s}$ = 13 TeV

3.2.4 VZERO

The VZERO (107) is a trigger detector that provides a minimum-bias trigger for all colliding systems and three centrality triggers in Pb-Pb collisions (multiplicity, central and semi-central). It has an important role in rejecting background from beam-gas collisions exploiting the relative time-of- flight measurement between the two arrays: when the beam-gas collision takes place outside the region between the two arrays, particles arrive 6 ns before or after the time of a beam-beam collision. It consists of two segmented arrays of plastic scintillator counters, called VZERO-A and VZERO-C, placed around the beam-pipe on either side of the IP: one at $z = 340$ cm, covering the pseudo-rapidity range, 2.8

$< \eta <$5.1, and the other at z = -90 cm (in front of the absorber), covering the pseudo-rapidity range, -3.7$< \eta <$ -1.7

3.2.5 Data Acquisition (DAQ) and Trigger systems

Trigger System

The ALICE Central Trigger Processor (CTP) (108) has been designed to select events having a variety of different features at rates which can be scaled down to suit physics requirements and restrictions imposed by the bandwidth of the Data Acquisition (DAQ) system and the High-Level Trigger (HLT). Since the counting rates for different running modes (pp, pA, AA) can vary for almost two orders of magnitude, the biggest challenge for the ALICE trigger is to make optimum use of the detectors and to perform trigger selections in an optimised way for these different modes.

The first response of the trigger system has to be fast to suit detector requirements. The "fast" part of the trigger is split into two levels: a Level-0 (L0) signal from CTP reaching the detectors after 1.2 μs and a Level-1 (L1) signal arriving after 6.5 μs. The L0 signal is too fast to enable the trigger inputs from all the detectors while the L1 signal can pick up all the remaining fast inputs. CTP decisions are made in 100 ns.

Data Acquisition (DAQ)

The trigger and Data Acquisition (DAQ) (108) systems of ALICE have been designed to give different observables, a fair share of the trigger and DAQ resources with respect to DAQ bandwidth. They have also to balance the capacity to record Pb-Pb central collisions (which generate large events) with the ability to acquire large fractions of rare events. To provide adequate physics statistics it has been estimated that a bandwidth of 1.25 GB/s to mass storage is suitable. This bandwidth is consistent with constraints imposed by technology, cost and storage capacity.

The architecture of the data acquisition is shown in Figure 3.9. Detectors receive the trigger signals from CTP (Central Trigger Processor) through LTU (Local Trigger Unit). The data produced by the detectors are injected on the DDL (Detector Data Link) using the same protocol. At the receiving end of the DDL, D-RORC (DAQ Readout Receiver Card) PCI-X based cards receive and assemble the event fragments into sub-events in the LDCs (Local Data Concentrators). The role of the LDC is to ship the sub-events to a farm of machines (Global Data Concentrator, GDC) where the whole events are built. The GDCs feed the recording system which eventually records the events in the Permanent Data Storage (PDS).

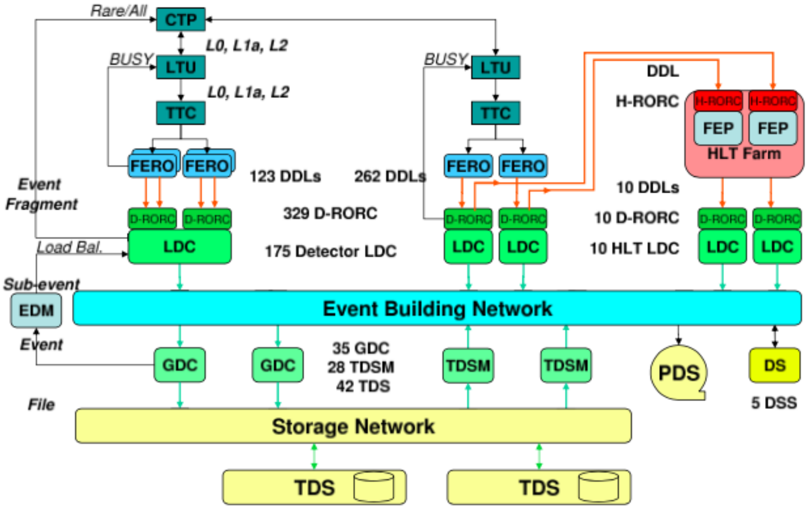

FIGURE 3.9: The overall architecture of the ALICE DAQ system and the interface to the HLT system

High Level Trigger (HLT)

According to the simulation studies, the amount of data produced in the TPC alone, in a single central nucleus-nucleus collision, corresponds to about 75 MB assuming $dN_{ch}/d\eta = 8000$ at mid- rapidity. The data rate for all detectors, resulting after a trigger selection, can easily reach 25 GB/s, while archiving rate is about 1 GB/s. Therefore online processing is advisable to select relevant events and to compress data without loosing their physics content. The overall physics requirements of the HLT are the following:

- **Trigger** Accept or reject events based on detailed online analysis
- **Select** Select a physics region of interest within the event by performing only a partial readout
- **Compress** Reduce the event size without loss of physics information by applying compression algorithms on the accepted and selected data

3.2.6 Data flow: from the Online to the Offline

Several stages of processing of raw data taken by detectors before it is available in form of reconstructed events is depicted in Figure 3.10.

Data originating from the detectors (denoted by 1 in Figure 3.9) is processed by LDCs and global events are built by GDCs (2), as already mentioned. The so-called publish agent registers the assembled events into the AliEn system (3) and ships them to the CERN computing centre where they are stored first on disks (4) and then permanently on tapes (5) by the CASTOR system(109).

During data-taking the detectors also produce conditions data that are relevant

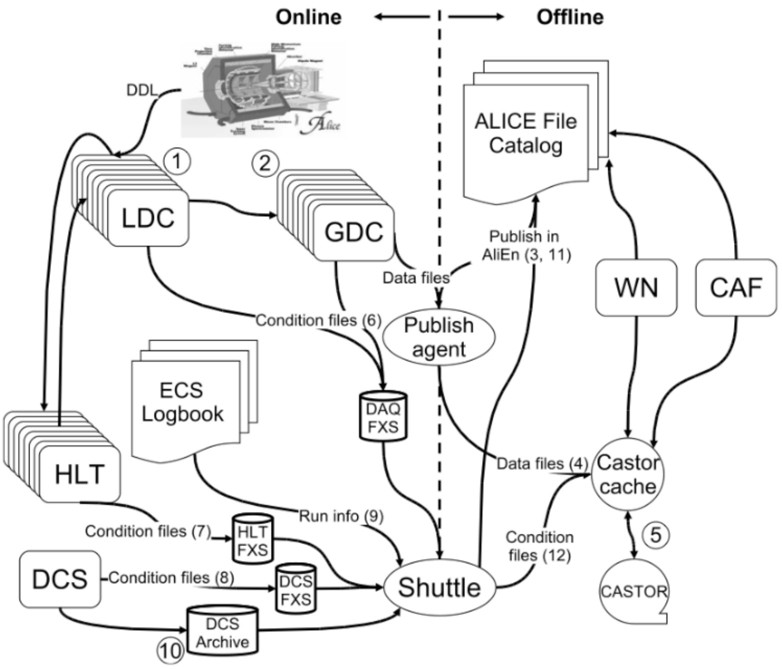

FIGURE 3.10: Global view of ALICE's data flow

for the calibration of individual detector signals. Conditions data provide information about the detector status and environmental variables during data-taking. Examples are inactive and noisy channel maps, distributions that describe the response of a channel, temperatures and pressure in a detector, and detector configuration. Many of the conditions data could in principle be calculated from the raw data and extracted offline after data-taking. However, such an approach would require an additional pass over the raw data before the reconstruction which is not feasible due to the limited computing resources. Therefore, conditions data are already extracted during data-taking and stored in the Offline Condition Data Base (OCDB). A dedicated program called Shuttle collects these outputs and makes them available to the reconstruction. Furthermore, it retrieves information about the run from the ECS [4] logbook (9) and collects continuously monitored values that are written by DCS into the DCS Archive (10). After processing the data, the Shuttle registers the produced condition files in AliEn (11) and stores the data in CASTOR (12).

With the registration of the raw and conditions data the transition from the online to the offline world has taken place. "Online" denotes all actions and programs that have to run in real time. "Offline" processing is the subsequent step, like for instance the event reconstruction, which is executed on worker nodes (WN) of Grid sites located around the Globe.

---

[4] The Experiment Control System (ECS) is the top level control of the ALICE experiment. Running an experiment implies performing a set of activities on the online systems that control the operation of the detectors. These online systems are: the Trigger (TRG), the Detector Control Systems (DCS), the Data-Acquisition System (DAQ) and the High-Level Trigger (HLT). The ECS provides a framework in which the operator can have a unified view of all the online systems and perform operations on the experiment seen as a set of detectors.

3.2.7 ALICE Offline software framework

The required computing resources for the reconstruction and analysis of the raw data, as well as the production of simulated events needed for the understanding of the data, exceed the computing power of single institutes and even centres like CERN. Therefore, institutes that are part of the Collaboration provide storage and computing resources. Distribution of the data for reconstruction and analysis cannot be performed manually leading to the need for an automated system. The concept of a decentralised computing model called Grid was identified as a solution.

The AliEn Framework

The Grid (110) unifies the resources of distributed computing centres, in particular computing power and storage, to provide them to users all over the World. It allows computing centres to offer their resources to a wider community, and the local resources to be shared by an entire collaboration.

Software that implements the Grid concept is called Grid middleware. Since 2001, ALICE has developed a Grid middleware called AliEn. An ALICE user employs AliEn to connect to the ALICE Grid which is composed of a combination of general services that are provided by many Grid middleware solutions and ALICE-specific services provided by AliEn. Parts of the ALICE Grid are:

1. a global file catalog that is a directory of files in storage elements distributed over the globe
2. the automatic matching of jobs for execution to a suitable location in one of the connected sites
3. a shell-like user interface
4. API9 services for the ROOT framework

Currently the ALICE Grid consists of about 179 sites located in more than 21 countries. Figure 3.11 shows a map of the ALICE Grid sites.

The AliRoot Framework

AliRoot is the offline framework for simulation, alignment, calibration, reconstruction, visualisation, quality assurance, and analysis of experimental and simulated data. It is based on the ROOT (111) framework. Most of the code is written in C++ with some parts in Fortran that are wrapped inside C++ code. Re-usability and modularity are the basic features of the AliRoot framework. Modularity allows parts of the code to be replaced, with minimum or no impact on the rest (for example changing the event generator, the transport Monte Carlo or the reconstruction algorithms) which is achieved by implementing abstract interfaces. In addition codes for each detector subsystem are independent modules with their specific code for simulation and reconstruction, which can be developed concurrently with minimum interference. Re-usability is meant to

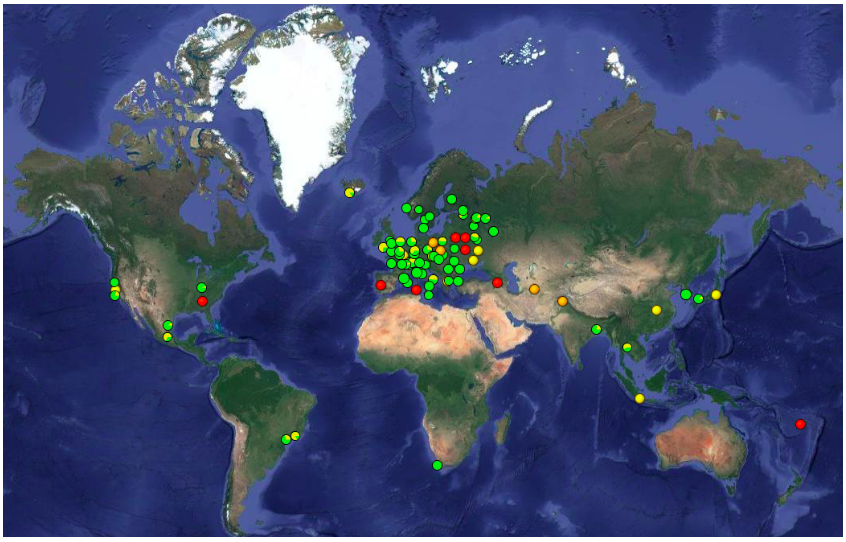

FIGURE 3.11: ALICE Grid sites

maintain a maximum amount of backward compatibility as the system evolves.

The central module of the AliRoot framework is STEER (Figure 3.12) which provides several common functions such as steering of program execution for simulation, reconstruction and analysis; general run management; creation and destruction of data structures; initialisation and termination of program phases; base classes for simulation, event generation, reconstruction, detectors elements. For event simulation the framework provides the following functionality:

- **Event Generation:** Many MC event generators (e.g. Pythia, Phojet, EPOS for pp events and HIJING for Pb-Pb events) are interfaced with AliRoot. For each generated particle a list of information (such as type, momentum, charge, production process, originating particle and decay products) is stored in a file (kinematics tree).
- **Transport:** The detector structure, the motion of the particles through it and the possible interactions with the material are simulated using programs such as Geant3 (112), Geant4 and Fluka(113). For all the interactions of particles with sensitive parts of the detector (hits), information such as position, time, energy deposition and the tag of track they belong to, are recorded during this process
- **Digitisation:** Finally all the hits are translated in the corresponding digital output of the detector, taking into account the detector's response function. All this information are then stored in the specific hardware format of the detector (raw data).

3.2.8 Event reconstruction

At this stage the raw data correspond to the signals that would have been produced by an interaction of the same kind within the detector. The subsequent

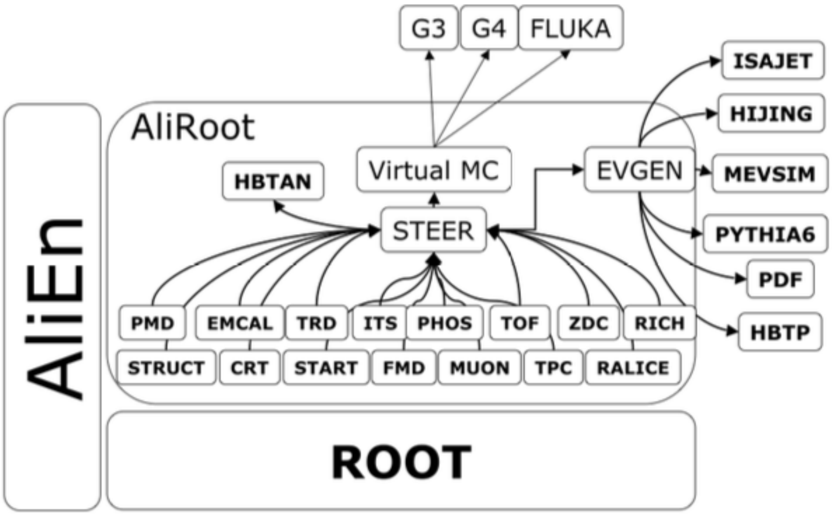

FIGURE 3.12: Schema of the AliRoot framework

reconstruction is identical, both for simulated as well as real events. It consists of the following steps:

- **Primary Vertex Reconstruction:**The first step of the reconstruction is a local cluster finding procedure, executed by each detector within its own sensitive volume. The signals of particles crossing the sensitive area are usually detected by neighbouring detector elements, that are combined into a single cluster to better estimate the position of traversing particle and reduce the effect of the random noise. The cluster information is saved in temporary trees with the format of "rec points" and is at the basis of the subsequent tracking procedure.

  ALICE exploits the Kalman Filter algorithm for simultaneous track finding and track fitting. Each track candidate is represented by a state vector and the algorithm is a recursive procedure to determine the status of the track based on a finite number of measurements at given positions (the active volume of the detector). The evolution of the status between two points along the track is given by a deterministic component, namely a locally linear equation of motion, and by a stochastic component, to account for multiple scattering. For each vector that enters the evolution equations a covariance matrix is defined and evolves accordingly. The ALICE track reconstruction is based on the following steps (see Figure 3.13):

  - the position of the primary vertex is needed to build the "track seeds" that are used as starting points for the Kalman filter. The clusters in the two ITS inner layers are used for the primary vertex reconstruction.
  - The track finding in the TPC proceeds from the outer to the inner part. The outermost pad rows and the primary vertex position from previous step are used as seed. A limited number of TPC cluster is associated to the track with the "center of gravity" method.

    - For each seed the track following is performed: the state vector and the co- variance matrix are propagated as mentioned before along the pad rows. At this stage no constraint on the primary vertex is applied, in order to maximize the efficiency for primary tracks
    - Starting from the higher-momentum candidates, the TPC tracks are matched to the SSD layers and with ITS points down to the innermost SPD layer
    - The track is then back-propagation and refitted outward in ITS and TPC, up to the outer radius of the TPC
    - The next step is the extrapolation and track matching in the TRD, followed by the propagation to the outer layer to the PID detectors, TOF, HMPID, PHOS and EMCal
    - Reconstructed tracks are refitted inward through TRD, TPC and ITS and re- propagated to the primary vertex. The track parameters are constrained, that is evaluated in proximity of the vertex
    - The primary vertex position is finally recalculated using tracks to obtain the optimal resolution

  The output of the whole reconstruction operation is the Event Summary Data (ESD) which contains all the information about the event both at track or event level.

- **Secondary Vertex Reconstruction:** The other tracks, sufficiently far away from the primary vertex, are combined to find secondary vertices, corresponding to the decays of unstable particles like the heavy flavour mesons. Such a reconstruction is based on geometrical selection, suggested by the topology of the decay of the considered particles.

The output of the reconstruction is called Event-Summary Data (ESD). This file contains only high-level information such as the position of the event vertex, parameters of reconstructed charged particles together with their PID information, positions of secondary-vertex candidates, parameters of particles reconstructed in the calorimeters and integrated signals of some detectors. This data is further reduced to Analysis-Object Data (AOD) format. These smaller-sized objects contain only information needed for the analysis. Therefore, the transformation procedure may already contain a part of the analysis algorithm, like track selection. Several AODs, focusing on different physics studies, can be created for a given event which stored and distributed worldwide on the Grid, where the users can access them through AliEn, the ALICE Environment framework

3.2.9 Particle identification with the TPC

One of the main characteristics of the ALICE detector, are PID capabilities at a very low transverse momentum threshold of detection(114). The identification can be performed in two different ways: by direct identification and by the reconstruction of the topology of the disintegration process of a particle.

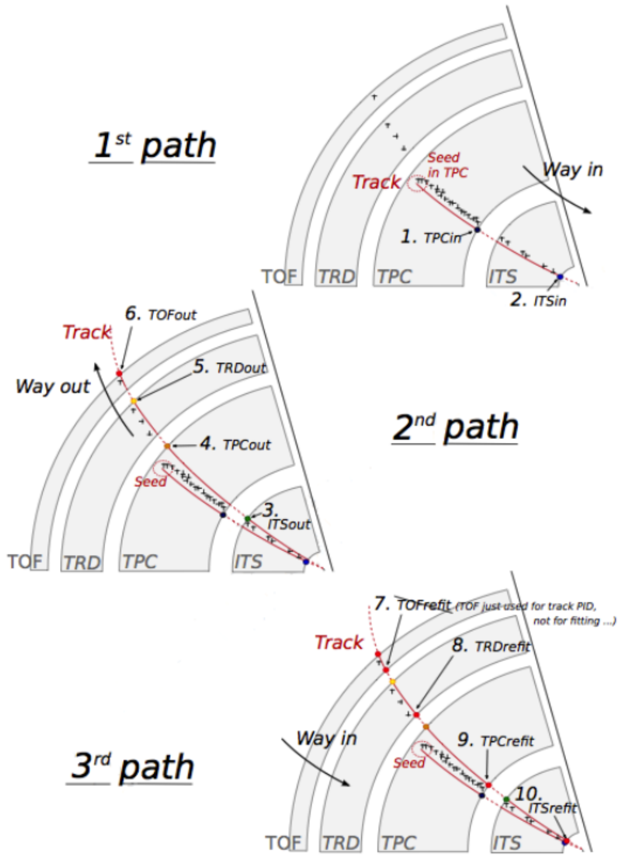

FIGURE 3.13: Principle of track reconstruction in an ALICE event: all the three steps of the iterative procedure are shown. The numbers on the plots marks the bits that are activated in each step during the Kalman filter procedure, in case of success

Particles that live long enough to be identified at track level: $e^{\pm}$, $\mu^{\pm}$, $\pi^{\pm}$, $K^{\pm}$, $p^{\pm}$, are identified directly. Eight of the detectors that compose ALICE (SDD, SSD, TPC, TRD, TOF, HMPID and the EMCal, DCal) can provide PID, based on different techniques: specific energy loss (dE/dx), time of flight and photon radiation characteristics. This information can be used individually or combined.

A second way to identify particles is via invariant mass computation for its daughter particles, as for instance in the case of a strong decay of a resonance, or a weakly decayed particle. In this latter case, reconstruction can be performed via topological reconstruction, since the tracks originate from a decay point that is not the primary interaction vertex. In this second case the direct identification of the daughter particles has an important role in the background reduction.

The TPC provides Particle IDentification (PID) for charged tracks. The gas in the detector is ionised by charged particle traveling through the chamber. In order to identify a particle, the physics observable which is required is energy loss per unit length within the matter crossed by the charged particle. This specific energy loss denoted by dE/dx, is described by Beth-Bloch parameterisation (see Equation 3.1) that highlights the key of the identification technique. The dE/dx depends on the charge and the velocity (β) of the particle, which, in turn, depends only on the momentum and the mass of the ionising particle. Since momentum is already known from the track curvature and the charge is unitary for most measured tracks, measuring the dE/dx allows us to determine mass indirectly and thus determine the particle species. The following Bethe-Bloch parameterisation gives the mean specific energy loss:

$$-\left\langle \frac{dE}{dx} \right\rangle = k_1.z^2\frac{Z}{A}.\frac{1}{\beta^2}\left[\frac{1}{2}\ln(k_2.m_e c^2.\beta^2\gamma^2) - \beta^2 + k_3\right] \tag{3.1}$$

where $\beta\gamma = p/Mc$ and

Z: atomic number of the ionised gas (in this case $Ar/CO_2/N_2$)
A: mass number of the ionised gas (g/mol)
m_e: electron mass
z: electric charge of the ionising particle in unit of electron charge e
M: ionising particle mass
p: ionising particle momentum
β: ionising particle velocity normalised to the light velocity c
$\gamma = 1/\sqrt{1-\beta^2}$, Lorentz factor
k_1, k_2, k_3: constants depending on the ionised medium

The specific energy loss in the TPC as a function of momentum is shown in Figure 3.7. The different bands show expected values for $e^\pm$, $\pi^\pm$, $K^\pm$, $p^\pm$ and deuteron. These correspond to the statistical distribution of the measured energy loss.

The expected value which corresponds to the prediction by the Bethe-Bloch parameterisation is shown as black lines on Figure 3.7. For a track within the TPC, the relevant quantity to be considered for PID is the difference between the specific energy loss measured by the detector and the corresponding value predicted by the Bethe-Bloch parametrisation. The difference could be expressed in a number of σ as shown in Equation 3.2. In this way, it is possible to estimate the goodness of a mass hypothesis more quantitatively. It also provides the possibility to choose strictness to be adopted for the identification by applying a different value of n_σ.

$$n_\sigma = \frac{(dE/dx)_{measured} - (dE/dx)_{Bethe-Bloch}}{\sigma_{TPC}} \tag{3.2}$$

3.2.10 Multiplicity Determination in pp collisions

The VZERO system (107) also provides a charged particle multiplicity measurement based on the energy deposited in the scintillators. Most of the particles entering the VZERO scintillators are highly relativistic ($\beta \rightarrow 1$) and then deposit similar amounts of energy in the material. As a result, the response of each of the VZERO segment, to a good approximation, is proportional to the number of particles that passed the sensitive part of the segment (despite their mass or momenta). The sum of the amplitudes measured in all VZERO segments is therefore correlated to the total number of particles reaching the detector and can serve as a probe for the total charged-particle multiplicity. In order to study the multiplicity dependence of light flavour hadron production, the sample is divided into event classes based on the total charge deposited in both of the V0 detectors (V0M amplitude). The V0M amplitude is found to be linearly proportional to the total number of charged particles produced in the pseudorapidity window corresponding to the acceptance of the V0 scintillators.

The analysis technique employed for the measurement of the charged-particle pseudorapidity distribution is based on the reconstruction of tracklets, which are built using the position of the reconstructed primary vertex and two hits, one on each SPD layer. This technique effectively allows to reconstruct charged particles with $\mathrm{p_T}$ above the 50 MeV/c cut-off determined by particle absorption in the material. The charged particle pseudorapidity density is obtained from the measured distribution of tracklets $dN_{tracklets}/d\eta$ as

$$\mathrm{d}N_{ch}/\mathrm{d}\eta \ = \alpha(1-\beta) dN_{tracklets}/d\eta$$

The correction α accounts for the acceptance and efficiency for a primary particle to produce a tracklet, while β is the contamination of reconstructed tracklets from combinations of hits not produced by the same primary particle.

The percentile of the hadronic cross section is determined for any value of the VZERO amplitude by integrating the measured VZERO amplitude distribution normalised at the anchor point $\mathrm{V0}_{AP}$, i.e. 90% of the hadronic cross section. For example, if we define V as the VZERO amplitude, the top 10% central class is defined by the boundary $\mathrm{V0}_{10}$ which satisfies

$$\frac{\int_{V0_{10}}^{\infty}(dN_{evt}/dV)dV}{\int_{V0_{AP}}^{\infty}(dN_{evt}/dV)dV} = \frac{1}{9} \tag{3.3}$$

The anchor point (AP) is the amplitude of the VZERO detector equivalent to 90% of the hadronic cross section, which determines the absolute scale of the centrality. The determination of the AP requires the knowledge of the trigger efficiency and the remaining background contamination (115; 116).

Chapter 4

K^{*0} and $K^{*\pm}$ resonance reconstruction in pp collisions

K*(892)$^\pm$ and K*(892)^0 are resonance particles with a small lifetime ($\sim$ 4 fm$/c$) (Table 4.1), comparable to that of the fireball formed in the heavy ion collisions (80).

TABLE 4.1: K^{*0} and K$^{*\pm}$ properties (81)

Particle	K^{*0}	K$^{*\pm}$
Mass	895.81 ± 0.19 MeV$/c^2$	891.66 ± 0.26 MeV$/c^2$
Width	47.4 ± 0.6 MeV$/c^2$	50.8 ± 0.9 MeV$/c^2$
Branching Ratio	0.66 ($K^\pm + \pi^\mp$)	0.33 ($\pi^\pm + K^0_S$)
Lifetime	4.2 fm/c	3.6 fm/c

In this analysis, K$^{*\pm}$ and K^{*0} have been identified via their hadronic decay channel K$^{*\pm}$ $\rightarrow \pi^\pm$ + K^0_S and K^{*0} $\rightarrow \pi^\pm + K^\mp$ (See Figure 4.1 for a schema of the decays). They are reconstructed by the invariant mass distribution of their daughters, $\pi^\pm$ and $K^\pm$ for neutral K^* and $\pi^\pm$ and K^0_S for charged K^*. The K^0_S has been identified by its weak decay topology $K^0_S - > \pi^+ + \pi^-$ (B.R : 69.2 ± 0.05%). Different strategies for the identification of daughter particles ($\pi^\pm$, $K^\pm$, K^0_S) are described in the Chapter 5 and 6. Normally the invariant mass distribution is characterised by a peak signal over a broad background. Depending on the underlying physics and event multiplicity, the background originates from uncorrelated particles and from the correlated particles i.e. with a common origin. The background distribution from the uncorrelated particles can be estimated by different techniques such as event mixing, like-sign, or rotational. To estimate the raw yield, the invariant mass distribution after the subtraction of uncorrelated background is fitted by a function which is formed by the sum of two terms. One describes the resonance signal while the second is used to describe the shape of the residual (mainly correlated) background.

The vacuum properties of the resonances such as mass and width could be modified by the medium effects(117). When chiral symmetry is partially restored, modifications of the resonance characteristics such as mass shift and width broadening are predicted. However regeneration of resonances in the late hadronic phase increases the fraction of resonances with vacuum masses and widths and this may inhibit the observation of the chiral symmetry restoration. As described in Section 2.1.3 by PHSD model, only a small percentage of the detected K^* are created inside the QGP formed (75). Evidently, QGP effects are not expected in inelastic pp collisions.

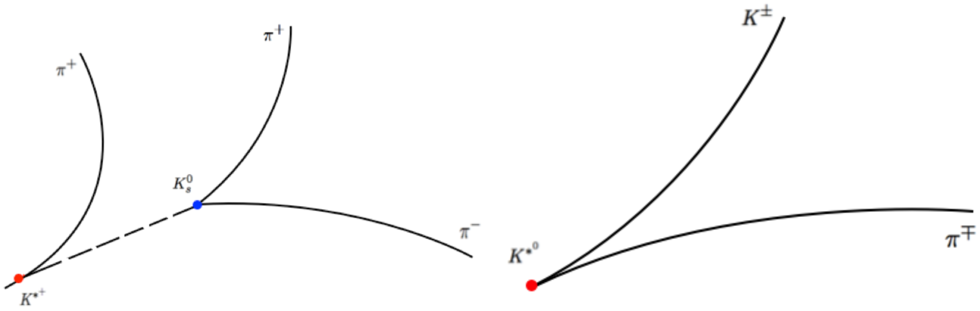

FIGURE 4.1: (Left) Decay Topology of the $K^{*\pm}$ into a neutral K^0_S and a charged pion. (Right) Decay Channel for K^{*0}

4.1 Signal Extraction

The invariant mass W of a set of N particles is

$$W^2c^4 = E^2 - \bar{p}c^2$$

.

where E and p are the total energy and momentum. By definition, W^2c^4 has the same value in all reference frames. In the CM mass frame, $\bar{p} = \sum \bar{p}_i = 0$ and $W^2c^4 = E_{CM}$ is the total energy in the CM frame. The invariant mass of a particle is the pseudo-Euclidean length of the four-vector (E, p), calculated using the relativistic version of the Pythagorean theorem which has a different sign for the space and time dimensions. This length is preserved under any Lorentz boost or rotation in four dimensions. The invariant mass (M_A) of a resonance which decays into multiple particles can be calculated as:

$$M_A^2c^4 = \left(\sum_i E_i\right)^2 - \left(\sum_i p_i c\right)^2 \tag{4.1}$$

where
$\sum_i E_i$ is the sum of the energies of the daughter particles

$\sum_i p_i$ is the vector sum of the momentum of the particles (includes both magnitude and direction of the momenta)
For different p_T bins, invariant mass distributions of daughters for particle and

their anti-particle are obtained separately and then summed to obtain the total signal for $K^{*\pm}$ and K^{*0}. In this work, K^{*0} will refer to $K^{*0} + \overline{K^{*0}}$. In Figure 4.2 and Figure 4.3, the $K^0_S\pi^\pm$ and $K^\pm\pi^\mp$ distributions for the p_T bins 1.2-1.4 GeV/c are shown. Red points in the figures represent the uncorrelated background estimated by the event-mixing technique.

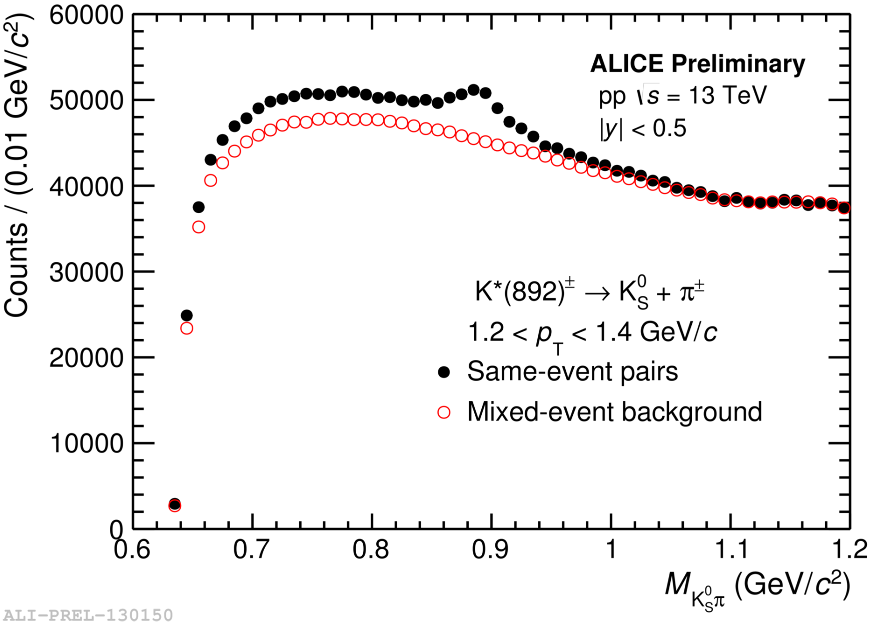

FIGURE 4.2: The $K^0_S\pi^\pm$ invariant mass distribution in $|y| < 0.5$ for the bin $1.2 < p_T < 1.4$ GeV/c in pp collisions at $\sqrt{s}$ = 13 TeV. The background shape estimated using pairs from different events (event-mixing technique) is shown as red points.

The strength of the signal can be expressed in terms of the statistical significance (118).

$$Significance = \frac{S}{\sqrt{S+B}} \tag{4.2}$$

where S and B are the integral of the signal and background respectively. The significance quantifies how much the signal stands out from the statistical fluctuations of the background and it is intimately related to the signal over background ratio, that depends on the power of the selection cuts. For the $K^{*\pm}$ analysis described in thesis signals at the different p_T bins present a good significance (see left panel Figure 4.4). Significance is larger than 10 for all the p_T bins except the highest p_T bins. In the right panel of Figure 4.4 the Signal/Background distribution as a p_T function is shown. We observe that it increases consistently with p_T.

4.1.1 Uncorrelated background estimate

In the invariant mass distributions, a background which originates from uncorrelated and correlated particles is present. The uncorrelated background can

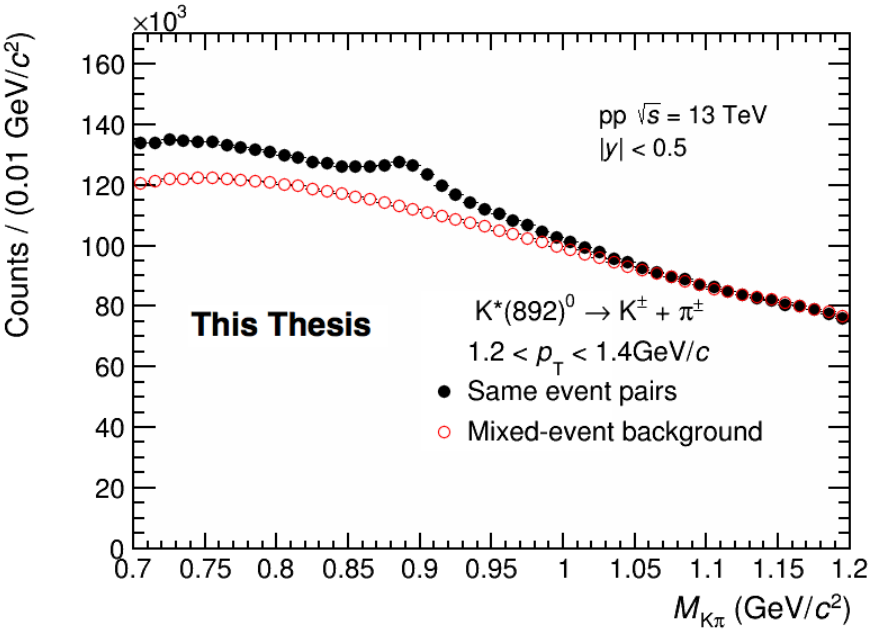

FIGURE 4.3: The $K^{\pm}\pi^{\pm}$ invariant mass distribution in $|y| < 0.5$ for the bin $1.2 < p_T < 1.4$ GeV/c in pp collisions at $\sqrt{s}$ = 13 TeV. The background shape estimated using pairs from different events (event-mixing technique) is shown as red circles.

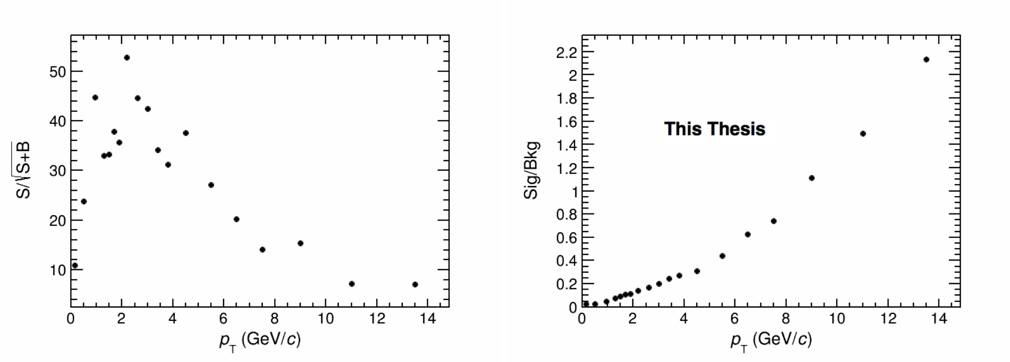

FIGURE 4.4: (Left) Significance for $K^{*\pm}$ (Right) Signal/Background ratio for $K^{*\pm}$

be handled by combinatorics. In order to extract the $K^{*\pm}$ or K^{*0} signal, it is necessary to first remove the uncorrelated background. Different techniques have been developed to estimate the shape of this background(119): Like-sign technique, event mixing technique, and rotated background. In the analysis described in this thesis, uncorrelated background has been estimated by the event mixing technique. The other two methods have been used in the estimation of the systematic uncertainties. With the like-sign pair technique, the uncorrelated background in the unlike-sign pair distribution is estimated by the invariant mass distribution of the same sign (++ and - -) distributions in the same event. Then this method can be used only when the daughter particles are of the opposite charge. The main assumption of this method is that the so called unlike sign pair distribution must contain the resonance signal, while the like-sign distribution does not contain any resonances. One major problem of the like-sign method is that the distribution of the like-sign uncorrelated pairs and unlike-sign uncorrelated pairs are not exactly the same. This difference between the positive and negative charged particles may result from the limited detector acceptance ability. In this analysis, this method can only be used for the neutral K^*. The like-sign invariant mass distribution can be estimated as (since the number of positively charged and negatively charged particles may not be the same):

$$N_{Like-Sign}(m) = 2 \times R \times \sqrt{N_{K^+\pi^+}(m) \times N_{K^-\pi^-}(m)}$$

where N is the number of entries in a bin with its centre at the $K\pi$ pair invariant mass, m. R is a factor which accounts for a possible asymmetry in the production of the positive and negative charged particles or asymmetry due to the detector acceptance bias. In the analysis discussed here, this factor has been set to 1. Figure 4.5 shows the unlike-sign distribution for the $\pi^{\pm}K^{\mp}$ pairs in the p_T range 2.6 - 3.0 GeV/c. In the same figure, the red points show the like-sign background.

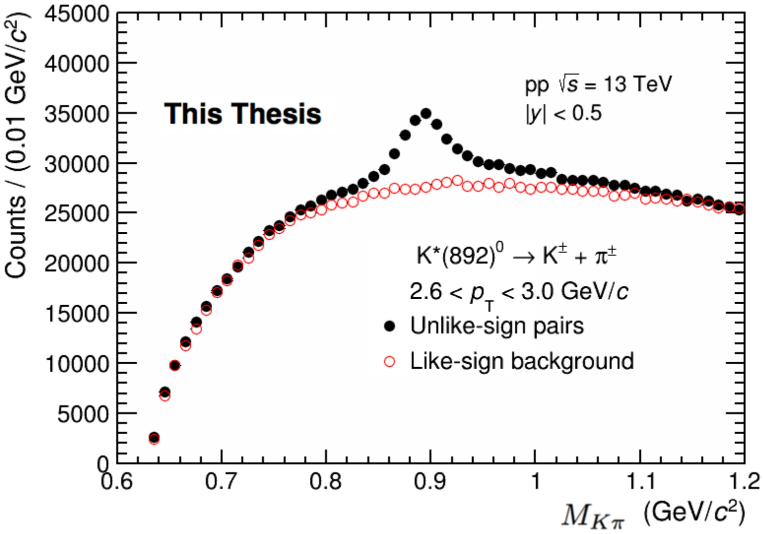

FIGURE 4.5: The $K^{\mp}\pi^{\pm}$ invariant mass distribution in $|y| < 0.5$ in pp collisions at 13 TeV for $2.6 \leq p_T \leq 3$ GeV/c from same event (black circles) and the background estimated using like-sign technique (red circles)

In the event mixing technique, the background invariant mass distribution is built by combining uncorrelated particles from different events. To keep the event characteristics as similar as possible among different events, in this analysis, we have mixed only particles from events that:

- Have a similar primary vertex i.e. the difference in the primary vertex of the events is lower than 1 cm
- Have similar charged particle multiplicity. The difference in the event multiplicity is less than 5 units.

In the event mixing technique, it's possible to reduce the statistical uncertainty by increasing the number of mixed events. In this analysis, the pairs were selected from 10 different events. Before subtraction, the total event mixing invariant mass distribution has to be normalised to the same event distribution, because the statistics of the event-mixing distribution is higher as consequence of the number of mixed events. In the analysis described in this thesis, the normalisation range was $1.1 < M_{\mathrm{inv}} < 1.2$ GeV/c for $\mathrm{K}^{*\pm}$ and $1.1 < M_{\mathrm{inv}} <1.15$ GeV/c for K^{*0}. These ranges are sufficiently far from the signal peak. Figure 4.2 and Figure 4.3 shows in red points the background estimated in this manner.

In addition to mixed event background estimation, combinatorial background can also be estimated by rotating one daughter particle in the detector's plane transverse to the beam direction and combining it with non rotated daughter ones. This breaks the correlation between pairs of the same event and produces a distribution devoid of any signal. By rotating particles direction over several angles, the statistics can be increased allowing a better control over the fluctuations. The number of rotations and the actual values of the rotation angles should be chosen carefully. It is observed that results from multiple-rotations method are very similar to those from the mixed-event technique. Figure 4.6 shows an example of rotational background for $\mathrm{K}^{*\pm}$.

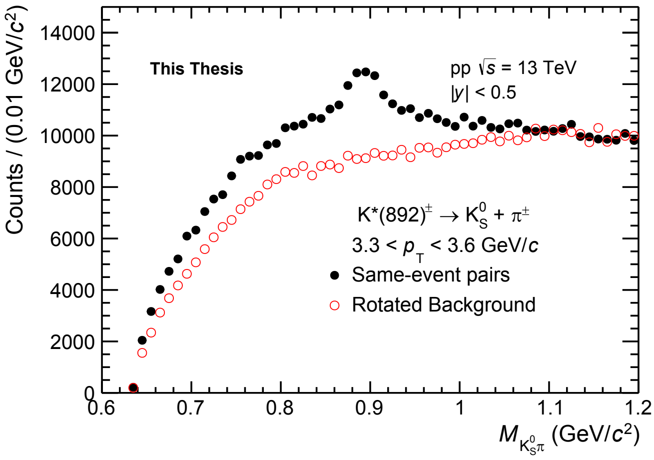

FIGURE 4.6: $K^0_S\pi^\pm$ invariant mass distributions for the bin 3.3 GeV/$c < \mathrm{p_T} < 3.6$ GeV/c in pp collisions at $\sqrt{s} = 13$ TeV. The background shape estimated using the rotational method is shown as red points.

Each method has its advantages and drawbacks. Event-mixing technique can lead to incorrect results in case of large signal to background ratio because in such scenarios, mixed event technique can produce fake background. On the other hand it is obvious that the like-sign method, which relies on the fact that a like-sign pair is always uncorrelated, will fail if the events contain like-sign correlated particle pairs (119). Also important is the fact that in the like-sign technique, unlike-sign and like-sign pairs are taken from the same event, so there is no event structure difference between the two distributions which might be caused by physical effects like elliptic flow etc. Mixed-event technique has the advantage that it has smaller statistical uncertainties compared to like-sign technique. Rotated background technique offers the same statistical advantage as the mixed-event technique but unfortunately in its actual implementation in the resonance code in AliRoot (120), only a single rotation (of π) is possible, thus the statistical improvement is not possible.

4.1.2 Raw Yield Extraction

In Figure 4.8 and 4.9, the invariant mass distributions for $K_S^0\pi^\pm$ and $K^\pm\pi^\mp$ after the subtraction of the uncorrelated background are reported. A clean K^* signal is observed on top of a residual background. This residual background may come in principle from two dominant sources:

- correlated real $K\pi$ pairs
- correlated but unrecognised pairs

The fit of signal distribution is performed with the Root(111) package which uses MINUIT, after event mixing background normalisation and subtraction. As in the other ALICE resonance analysis (92), the total fit function is the sum of a non relativistic Breit-Wigner(121) and a function to describe the residual background $F_{BG}(M_{K\pi})$:

$$NRBW(M_{K\pi}) + F_{BG}(M_{K\pi}) = \frac{A}{2\pi}\frac{\Gamma_0}{(M_{K\pi} - M_0)^2 + \frac{\Gamma_0^2}{4}} + F_{BG}(M_{K\pi}) \tag{4.3}$$

where M_0 and Γ_0 are the mass and the width of the K^*. The parameter A is the integral of the peak function from 0 to ∞. For F_{BG}, a second order polynomial has been chosen for the K^{*0} analysis (92), while for the $\mathrm{K}^{*\pm}$ analysis, the $F_{BG}(M_{K\pi})$ has the form of Equation 4.4.

$$F_{BG}(M_{K\pi}) = [M_{K\pi} - (m_\pi + m_K)]^n exp(A + BM_{K\pi} + CM_{K\pi}^2) \tag{4.4}$$

where m_π = 139.57018 GeV/c^2 (81) and m_K = 497.611 GeV/c^2 (81) are the pion, and $\mathrm{K_S^0}$ mass and n, A, B and C are fit parameters. Similar function was used for the background description in the $\rho(770)$ analysis by ALICE (86) and for $\mathrm{K}^{*\pm}$ measurement at LEP energies (122). This equation was chosen by comparing different shapes (polynomial first, second, third order, or as Equation 4.4) with the residual background extracted in different $\mathrm{p_T}$ bins in Monte Carlo reconstructed. To this purpose, mixed event background was subtracted from reconstructed $\mathrm{K_S^0}$ π pairs. The result is events containing signal and residual background. The residual background distribution is then obtained subtracting from the previous histogram the invariant mass distribution of the reconstructed $\mathrm{K}^{*\pm}$. This background is then fitted with the second and third order polynomial and exPol (Equation 4.4). Figure 4.7 shows for the $\mathrm{p_T}$ bin 2.4-2.6 GeV/c, with the red lines, the fit results for the three evaluated functions. The function exPol was then chosen giving lowest χ^2 value and correct shape of the residual background in all the different $\mathrm{p_T}$ bins.

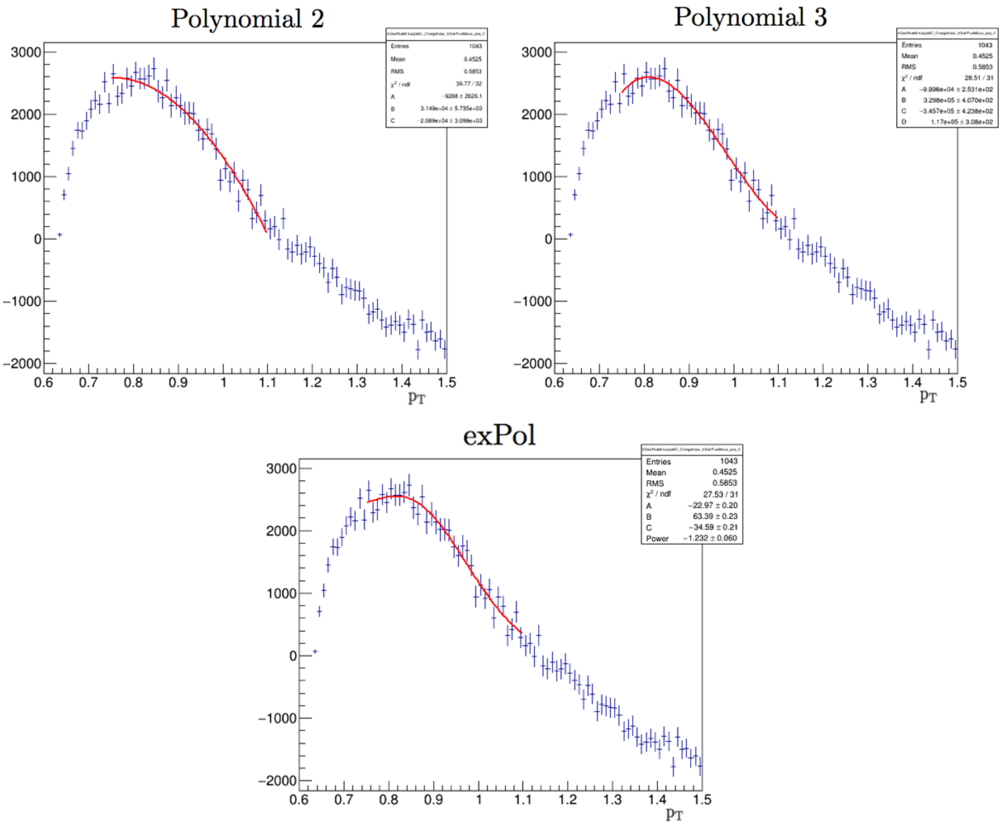

FIGURE 4.7: Residual background distribution for the p_T bin 2.4-2.6 GeV/c obtained (see text) using Monte Carlo reconstructed events. Red lines represent the fit results for the three different functions: second and third order polynomial, exPol (Equation 4.4).

The width, after compatibility, was fixed to its PDG value to optimise the fit. The fitting range was chosen accurately for each p_T bins, to improve the global χ^2 of the fit. For the large part of the p_T bins the fit range was 0.66 - 1.1 GeV/c^2 for $K^{*\pm}$ and 0.75-1.08 GeV/c^2 for K^{*0} .

Figure 4.8 and Figure 4.9 show for different p_T bins, the invariant mass distribution obtained after the subtraction of the uncorrelated background respectively for $K^{*\pm}$ and K^{*0} . These distributions are fitted by Equation 4.3 . The solid red curve is the results of the fit, the dashed line describes the residual background.

The raw yield can then be estimated using two different methods: integration of the fit function (Y_{FI}), or bin counting (Y_{BC}). In this thesis, bin counting is used as the default method while the function integration is used for the estimation of systematic uncertainty.

Function Integral(Y_{FI}):

The easiest method to estimate the raw yields is to simply perform an integral of the signal function (non relativistic Breit-Wigner in this case). The parameter A of the non relativistic Breit-Wigner function is the integral of the peak function from 0 to ∞. However we need to subtract the integral of the kinematically forbidden region ($0 < M_{K\pi} < m_\pi + m_K$) from the value of A. Therefore

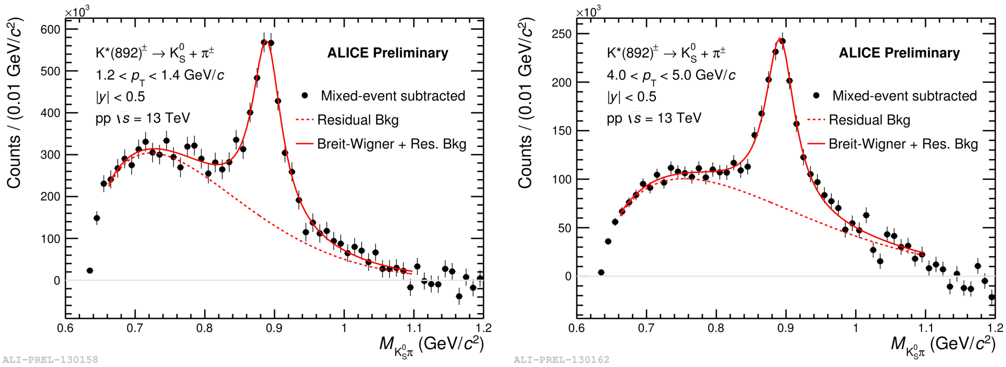

FIGURE 4.8: The $K^0_S\pi^{\pm}$ invariant mass distribution in $|y| < 0.5$ in pp collisions at 13 TeV for two different p_T bins after uncorrelated background subtraction. The solid red curve is the results of the fit by Equation. 4.3, the dashed red line describes the residual background distribution estimated by Equation 4.4.

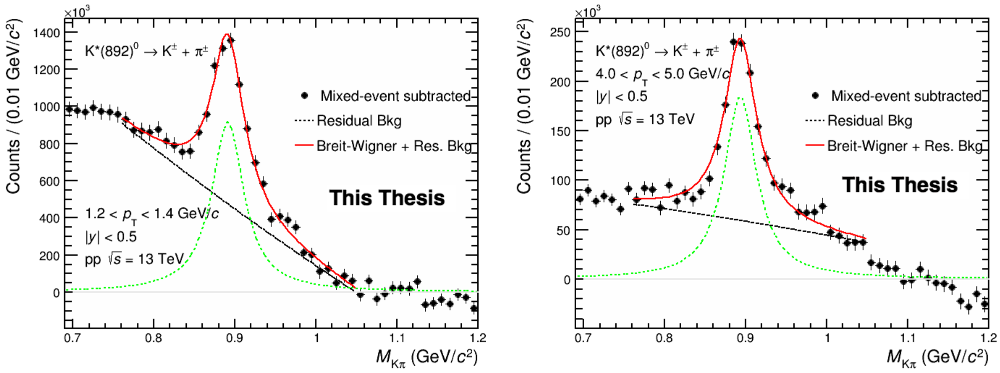

FIGURE 4.9: The $K^{\mp}\pi^{\pm}$ invariant mass distribution in $|y| < 0.5$ in pp collisions at 13 TeV for two different p_T bins after uncorrelated background subtraction. The solid red curve is the results of the fit by Equation. 4.3, the dashed black line describes the residual background distribution estimated by a second order polynomial.

$$Y_{FI} = A - \int_0^{m_\pi + m_K} NRBW(M_{K\pi})dM_{K\pi} \tag{4.5}$$

where
$m_\pi = 139.57018$ MeV$/c^2$,
$m_K = m_{K^0_S} = 497.611$ MeV$/c^2$for $K^{*\pm}$ and $m_K = m_{K^\pm} = 493.677$ MeV$/c^2$for K^{*0} .
The integral in the kinematically forbidden region is about 2.5% of the total yield, with the exact ratio depending on the peak parameters. The reliability of this method depends on the accurate theoretical modelling of the invariant mass distribution.

Bin counting (Y_{BC}):

The bin counting method is model independent and thus is considered more reliable. In this method, the raw yield (N_{BC}) in the region $I_{min} < M_{K\pi} < I_{max}$ (where $I_{min} = M_0 - 2\Gamma_0$ and $I_{max} = M_0 + 2\Gamma_0$, respectively) is extracted by integrating the invariant mass histogram (N_{counts}) over the region $I_{min} < M_{K\pi} < I_{max}$, and subtracting the integral of the residual background portion estimated over that same interval (N_{RB}).

$$N_{BC} = N_{counts} - N_{RB} \tag{4.6}$$

The error on N_{RB} is calculated using the the root function IntegralError().

It is assumed that the statistical uncertainties of the yields in the tail regions are fully correlated with each other and with the statistical uncertainty of the yield calculated from the histogram. N_{low} and N_{high} are estimated by integrating the non-relativistic Breit-Wigner function in the regions $m_\pi + m_K < M_{K\pi} < I_{min}$ and $I_{max} < M_{K\pi} < \infty$, with the parameters estimated from the fit.

$$N_{low} = \int_{m_\pi + m_K}^{M_0 - 2\Gamma_0} NRBW(M_{K\pi}) dM_{K\pi} \tag{4.7}$$

$$N_{high} = \int_{M_0 + 2\Gamma_0}^{\infty} NRBW(M_{K\pi}) dM_{K\pi} \tag{4.8}$$

The total raw yield is obtained adding low and high invariant mass tail contributions to the bin counting yield.

$$N_{raw} = N_{BC} + N_{low} + N_{high}$$

This accounts for about 13% of the total yield.

In Fig. 4.10 the raw yield p_T distributions for $K^{*\pm}$ obtained with the two methods are compared.

The event mixing technique is able to well describe the background. However some discrepancies are observed for $p_T > 4$ GeV/c. Then the yield has been estimated by fitting the invariant mass distributions without any background subtraction with Equation 4.3. The result obtained for the p_T bin 6 -7 GeV/c is shown in the left panel of Fig. 4.11. In the right panel of Fig. 4.11, the comparison of the p_T spectrum for $K^{*\pm}$ obtained by the standard fit procedure (i.e fitting the distribution after the background subtraction) and by fitting the invariant mass distribution without background subtraction is reported. In the lower panel, the ratio of the two spectra is reported. The mean differences are less than 0.5% and hence were not taken into account in the estimation of systematic uncertainties.

4.2 $K^{*\pm}$ Mass Determination

Mass and width versus p_T for K^{*0} obtained from STAR in pp and Au-Au collisions at $\sqrt{s_{NN}}$ = 200 GeV (121) and from ALICE at $\sqrt{s_{NN}}$ = 2.76 TeV in Pb-Pb

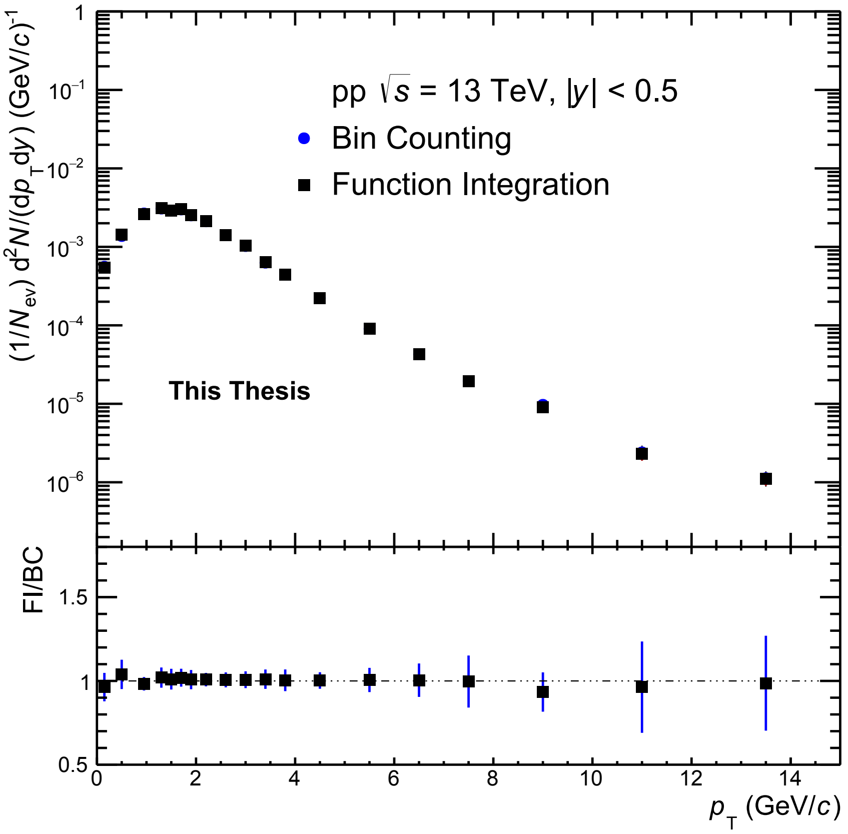

FIGURE 4.10: Transverse momentum raw yield distributions estimated by bin-counting method (blue circles) and by function integration (black squares). Ratio of the two distributions (function integration/bin-counting) is shown in the lower panel.

collisions (123) are shown in Figure 4.12 and Figure 4.13, respectively. Comparison with the mass and width extracted from reconstructed Monte Carlo events is also shown. In both cases, the mass and width are found to be consistent within systematic and statistical uncertainties to the PDG (81) values. The slight drop observed at low p_T at RHIC energies was explained by the experiment as due to cuts effect

To estimate the mass and width of the K$^{*\pm}$, the background subtracted invariant mass distribution was fitted by a function given by a sum of a function to describe the shape of the resonance and a term to take into account the residual background:

$$BW \times PS + RBG \tag{4.9}$$

Here BW is a relativistic Breit-Wigner function with a width dependent mass. PS(117) is a Boltzmann factor used to take into account the K^* produced through kaon and pion scattering i.e.

$$K_S^0 + \pi^\pm \to K^{*\pm} \to K_S^0 + \pi^\pm$$

(122)

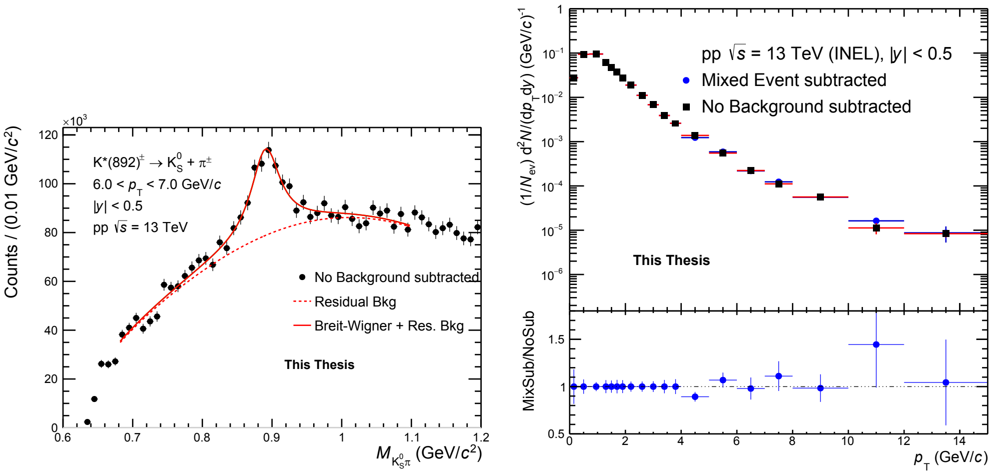

FIGURE 4.11: (Left panel) The $K^0_S\pi^\pm$ invariant mass distribution in $|y| < 0.5$ in pp collisions at 13 TeV for $6 \leq p_T \leq 7$ GeV$/c$. The solid red curve is the results of the fit by eq. 4.4, the dashed blue line describes the residual background distribution. (Right panel) Ratio of the yields obtained by the standard fit procedure (i.e fitting the distribution after the uncorrelated background subtraction) and by fitting the invariant mass distribution without background subtraction.

RBG represents the residual background function which in case of $K^{*\pm}$ was chosen to be parametrised by Equation 4.4. Relativistic Breit-Wigner function is accepted as the standard spectral function for all hadronic resonances which arises from the propagator of an unstable particle with a denominator of the form $p^2 - M^2 + iM\Gamma$ (117). This function inherently contains dependence on the nuclear matter density and thus is applicable across all system sizes. The functional form of the relativistic Breit-Wigner function is :

$$BW = \frac{AM_{K\pi}M_0\Gamma_{M_{K\pi}}}{(M_0^2 - M_{K\pi}^2)^2 + M_0^2\Gamma_{M_{K\pi}}^2} \tag{4.10}$$

where M_0 is the mass of $K^{*\pm}$ and A is a normalisation constant. To take into account, the dependence of the resonance width on its transverse momentum, the following function is used for the $\Gamma_{M_{K\pi}}$:

$$\Gamma_{M_{K\pi}} = \left(\frac{M_{K\pi}^2 - (m_\pi + m_K)^2}{M_0^2 - (m_\pi + m_K)^2}\right)^{(2J+1)/2} \times \Gamma_0 \times M_0/M_{K\pi} \tag{4.11}$$

where Γ_0 is the width of the $K^{*\pm}$, m_π and m_K are respectively the mass of the charged pion and of the K^0_S. The spin $J = 1$ for $K^{*\pm}$. The function for the phase space factor is given as (121):

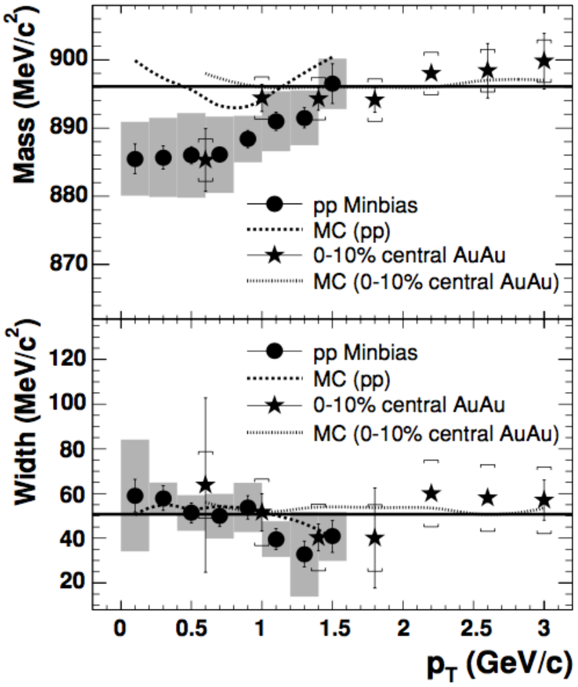

FIGURE 4.12: The K^{*0} mass (upper panel) and width (lower panel) as a function of p_T for minimum bias pp interactions and for central Au+Au collisions at $\sqrt{s_{NN}}$ = 200 GeV at RHIC detector. The solid straight lines are the standard K^{*0} mass (896.1 MeV/c^2) and width (50.7 MeV/c^2) (81), respectively. The dashed and dotted curves are the MC results in minimum bias pp and for central Au+Au collisions, respectively, after considering detector effects and kinematic cuts (121).

$$PS(M_{K\pi}) = \frac{M_{K\pi}}{\sqrt{M_{K\pi}^2 + p_T^2}} \times exp(-\sqrt{M_{K\pi}^2 + p_T^2}/T) \qquad (4.12)$$

Here T is the temperature at which the resonance is emitted in pp collisions, particle production is well reproduced by the statistical model (124) with T = 160 MeV and therefore this was the temperature used for the estimation of the PS factor.
Before fitting with Equation 4.9, the invariant mass distributions at the different p_T were corrected for the estimated reconstruction efficiency as a function of the invariant mass. In Figures 4.14 and 4.15, the K$^{*\pm}$ reconstruction efficiencies (rescaled to the value at $M = M_0$) versus mass at various p_T intervals are shown. For each m_{inv} bin, the efficiency is given by the number of reconstructed K$^{*\pm}$ divided by the number of generated K$^{*\pm}$.

A dependence of the efficiency from the invariant mass is clearly seen. In particular, for p_T < 0.7 GeV/c, the efficiency increases with the mass, while it is constant for $0.7 < p_T < 1.2$ GeV/c and then decreases with the mass at higher

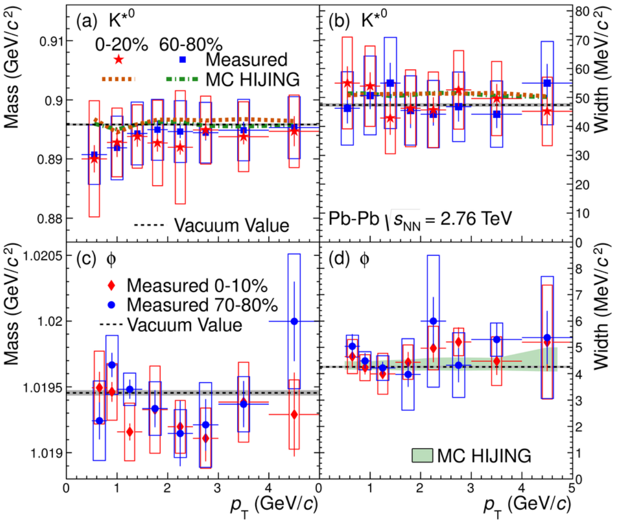

FIGURE 4.13: Measured K^{*0} meson mass (a) and width (b) in Pb-Pb collisions at $\sqrt{s_{NN}}$ = 2.76 TeV in the 0-20% and 60-80 % centrality intervals, along with the values extracted from Monte Carlo HIJING simulations. Measured ϕ meson mass (c) and width (d) in Pb-Pb collisions at $\sqrt{s_{NN}}$ = 2.76 TeV in the 0-10% and 70-80% centrality intervals. The ϕ width extracted from HIJING simulations is also shown. The vacuum values of the K^{*0} and ϕ mass and width are indicated by the horizontal dashed lines (123).

$\mathrm{p_T}$. The efficiency is constant for $\mathrm{p_T} > 3.5$ GeV/c. The correction factors were estimated by fitting the efficiency distribution by a second order polynomial function in the range 0.76 - 1.1 GeV/c^2. In the right panel of Figure 4.16 the widths obtained in the different $\mathrm{p_T}$ intervals fitting the invariant mass distributions by Equation 4.9 are shown. The obtained values are equal, inside the estimated uncertainties, to the PDG value (81). The value of Γ_0 in Equation 4.11 was than fixed to 50.8 MeV/c^2. In the left panel of Figure 4.16 the mass values obtained in the different $\mathrm{p_T}$ bins fitting invariant mass distributions by Equation 4.9 are shown. Estimated values are equal, inside the estimated statistical uncertainties, to the PDG value.

The shape of invariant mass distributions generated by PYTHIA8 -Monash 2013 (67) and PYTHIA6 -Perugia 2011 (66) have been studied. It has been observed that a Relativistic Breit-Wigner function describes the mass distribution as a function of $\mathrm{p_T}$ estimated with PYTHIA8 generator while a non Relativisitic Breit-Wigner function is the better fit for the mass spectrum estimated with PYTHIA6 generator. In Figures 4.17 and 4.18, mass and width distributions obtained from PYTHIA8 and PYTHIA6 respectively are shown. For both event generators, a lower mass value of about 1 MeV/c^2 is observed for $\mathrm{p_T} < 1$ GeV/c. A constant width value of about 49 GeV/c has been obtained for PYTHIA6 events. The extracted width for PYTHIA8 has a $\mathrm{p_T}$ dependent shape.

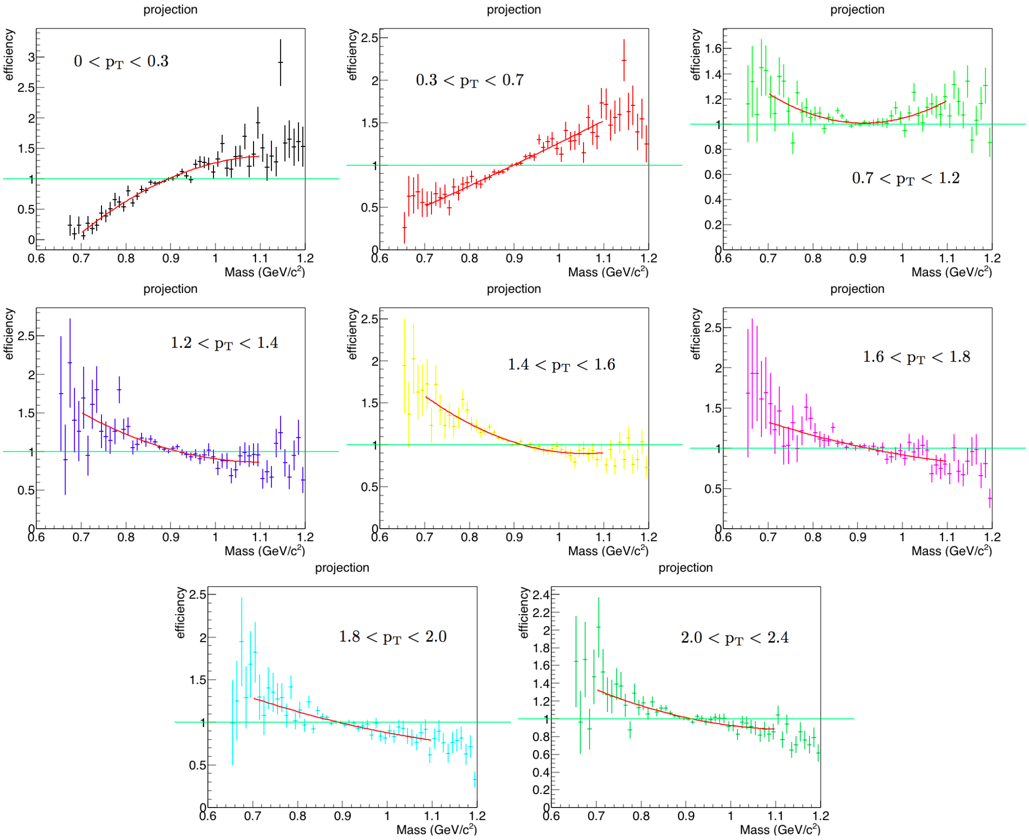

FIGURE 4.14: Efficiency vs. invariant mass for different p_T bins. Efficiency is rescaled to the value at $M = 0.892$ GeV$/c^2$. The colored lines represent the linear fit done in the range $0.76 < M < 1.1$ GeV$/c^2$.

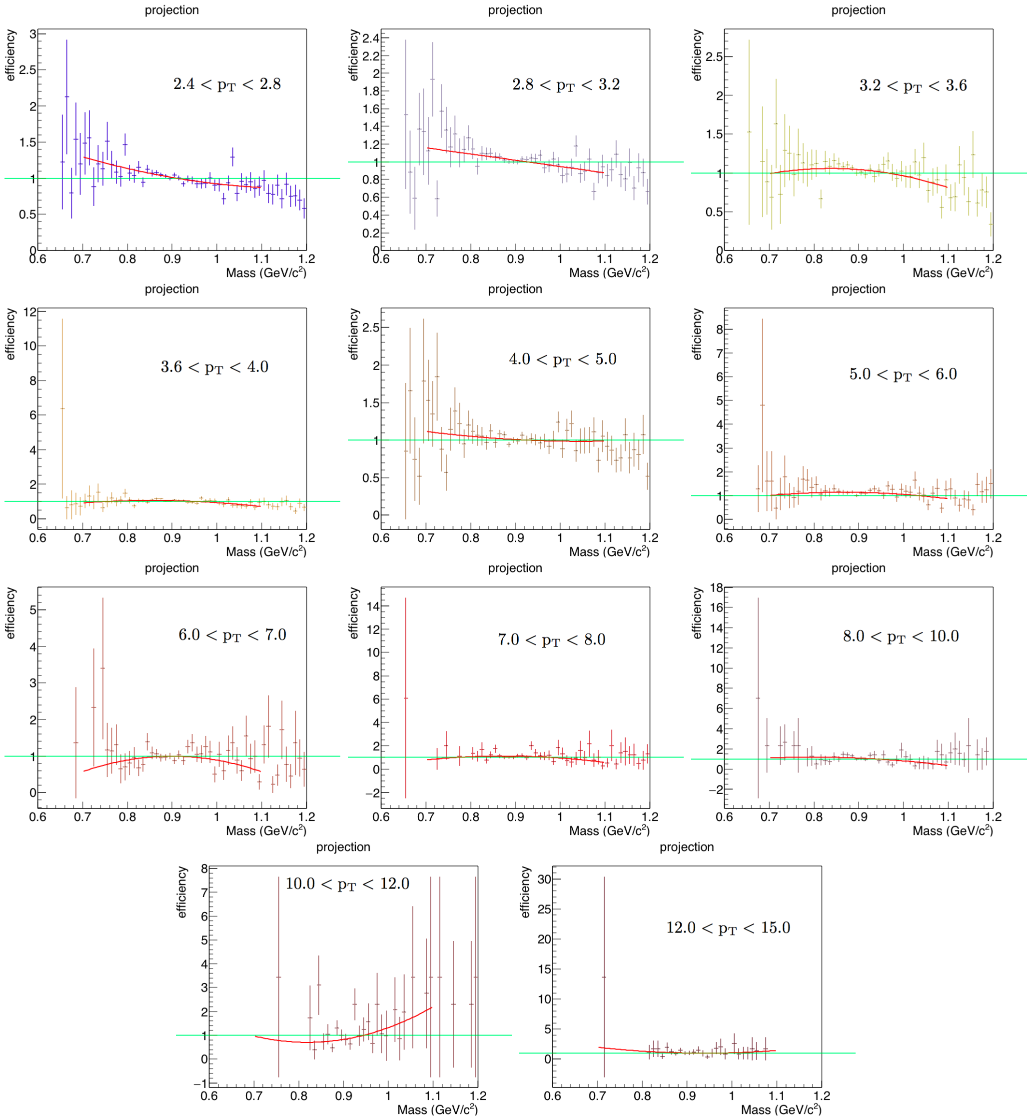

FIGURE 4.15: Efficiency vs. invariant mass for different p_T bins. Efficiency is rescaled to the value at $M = 0.892$ GeV/c^2. The colored lines represent the linear fit done in the range $0.76 < M < 1.1$ GeV/c^2.

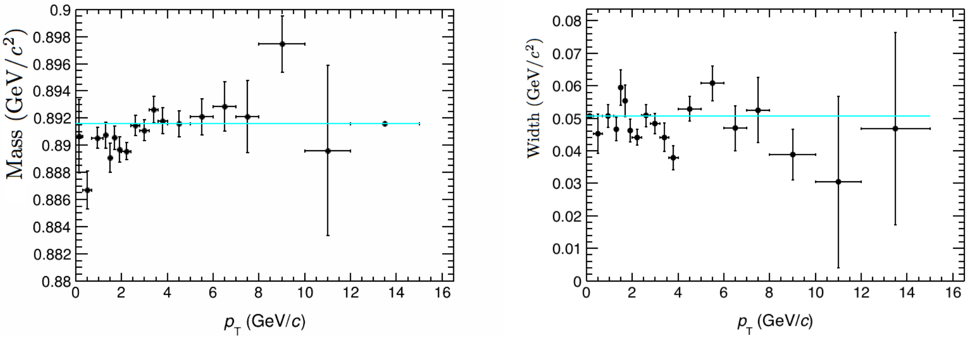

FIGURE 4.16: Mass vs. p_T (Left panel) and Width vs. p_T (right panel) obtained by a fit of the invariant mass distributions by Equation 4.9

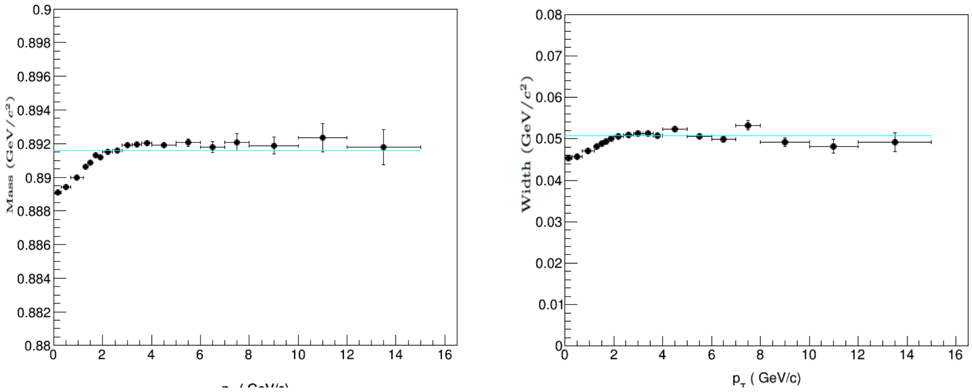

FIGURE 4.17: Mass vs. p_T (left panel) and Width vs. p_T (right panel) extracted from PYTHIA8 - Monash 2013 generated data fitted by a relativistic Breit-Wigner. The sky-blue lines represent the PDG values (81).

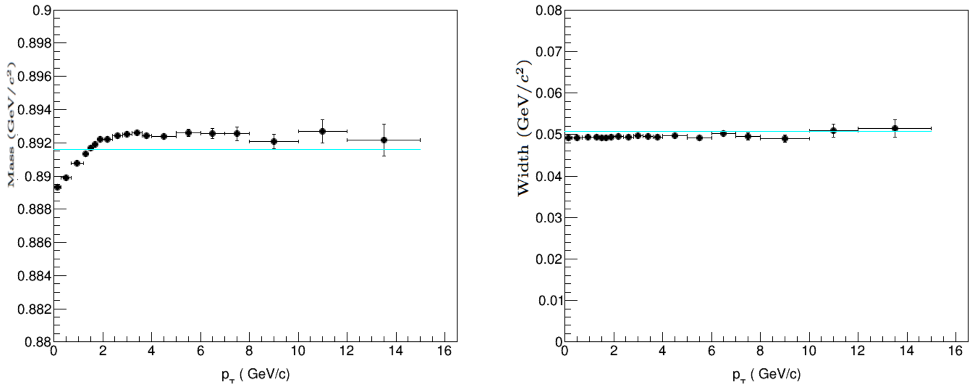

FIGURE 4.18: Mass vs. p_T (left panel) and width vs. p_T (right panel) extracted from PYTHIA6 - Perugia 2011 generated data fitted by a non-relativistic Breit-Wigner. The sky-blue lines represent the PDG values (81).

Chapter 5

Measurement of $K^{*}(892)^{\pm}$ production in pp collisions at 13 TeV

The $K^{*\pm}$ resonance production at central rapidity ($|y| < 0.5$) has been measured in inelastic pp collisions at $\sqrt{s} = 13$ TeV with the ALICE experiment, via the reconstruction of its hadronic decay into $K^0_S\pi^{\pm}$ where K^0_S further decays into two charged pions. The main detectors used for this analysis are ITS, TPC and V0. Detector V0 (V0A. AND.V0C) is used as a trigger detector

5.1 $K^{*\pm}$ reconstruction in pp collisions

5.1.1 Data sample and event selection

The data used for this analysis were collected during the December 2015 pp run (LHC15f period, pass 2). Of the total runs, 52 runs were marked by the Collaboration as "good runs" for the central barrel i.e they are characterised by good performance of the detectors and good running conditions (e.g. low level of beam induced background). In particular, all these "good runs" have both the TPC and all the ITS sub-detectors turned on. This corresponds to approx 50 million events after event and primary selection criteria are applied.

The purpose of the event selection is to select hadronic interactions with the highest possible efficiency, while rejecting the machine-induced and physical backgrounds. The ALICE on-line minimum bias (MB) trigger for this pp run was configured to have an AND logic operation for the following two conditions:

1. a signal above threshold in the V0-A
2. a signal above threshold in the V0-C

This condition is labelled as kINT7 trigger. Furthermore, events were selected with z-vertex within ±10 cm from the nominal interaction point. In addition, following event selection criteria are considered as standard within the ALICE experiment for the resonances analysis.

- Standard Physics Selection.
- AliESDEvent::IsInCompleteDAQ check is used to reject events for which the event building does not work.
- Pile-up events have been rejected using AliAnalysisUtils::IsPileUpEvent()
- SPD clusters vs. tracklets are checked using AliAnalysisUtils::IsSPDClusterVsTrackletBG() with default parameters.
- By default the track vertex is chosen. If it is missing, the vertex from the SPD is selected or at least event needs to have a track. Only events with vertex-z position $|v_z| < 10$ cm have been taken into account.
- SPD vertex-z resolution < 0.25 cm and SPD vertex dispersion < 0.04 cm
- z-position difference between track and SPD vertex < 0.5 cm

A ± 10 cm cut on the $z-$ vertex is applied and the distribution of the $z-$ vertex position is reported in Figure 5.1

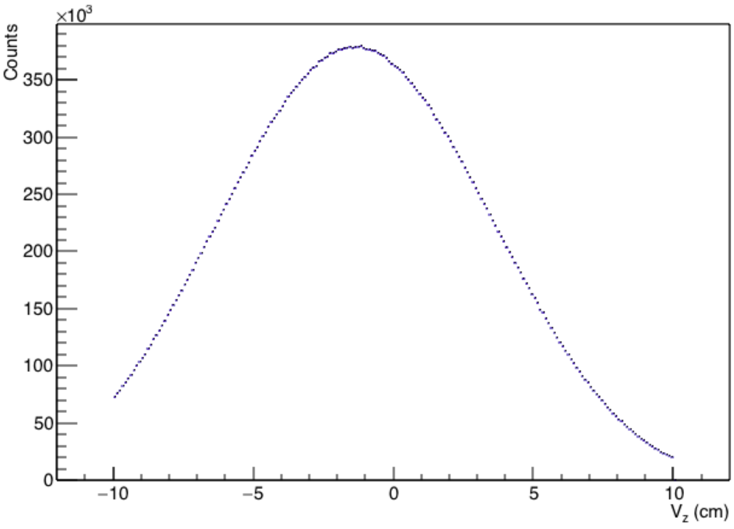

FIGURE 5.1: Primary vertex distribution for LHCf15 data sample of 13 TeV pp collisions

5.1.2 Primary tracks selection

The Distance of Closest Approach (DCA) to the primary vertex is used to discriminate between primary and secondary particles. Primary charged particles are those produced directly in the interaction and all decay products from particles with a proper decay length $c\tau < 1$ cm; secondary particles include those from the weak decay of strange hadrons and from interactions in the detector material. Several cuts were applied to achieve a high track quality in the analysed sample. Tracks were required to have at least 70 reconstructed clusters in the TPC out of the maximum 159 available. This ensured a high efficiency and good $\mathrm{d}E/\mathrm{d}x$ resolution, keeping the contamination from secondary and fake tracks small.

Tracks were accepted only in the range $|\eta| < 0.8$ (i.e. well within the TPC acceptance) and with $p_T > 0.15$ GeV/c to improve the global resolution. In order to reduce secondary particles, tracks were required to have at least one hit in one of the two innermost tracking detectors (SPD) and to have a DCA to the primary vertex less than 2 cm along the beam direction. The DCA in the transverse plane was required to be smaller than 7 $\sigma_{DCA}(p_T)$, where $\sigma_{DCA}(p_T) = (0.0026 + 0.0050\ {p_T}^{-1})$ cm where p_T is in GeV/c. Additional criteria for quality control which are labelled as ITSTPCTrackCuts2011 are as follows:

- Ratio of number of crossed rows to number of findable clusters in TPC > 0.8
- Require TPC refit
- Require ITS refit
- TPC χ^2 per clusters < 4.0
- ITS χ^2 per clusters < 36.0

5.1.3 Pion Identification

Pion identification is performed using the TPC and it is based on the energy it deposits in the drift gas, compared with the expected value computed using a parameterised Bethe-Bloch function (Figure 3.7) (For a description of the procedure see Section 3.2.9).

During the runs analysed in this thesis, some of the chambers of the TPC were not functional and thus a special p_T dependent PID cut was used for the pions identification as:

- $|N\sigma_{\mathrm{TPC}}| < 6$ for $p < 0.3$ GeV/c
- $|N\sigma_{\mathrm{TPC}}| < 4$ for $0.3 \leq p \leq 0.4$ GeV/c
- $|N\sigma_{\mathrm{TPC}}| < 3$ for $p > 0.4$ GeV/c

In Figure 5.2 $N\sigma_{\mathrm{TPC}}$ versus momentum p estimated in the pion hypothesis without any PID cut (left panel) and after that p-dependent PID cut is applied (right panel) are shown.

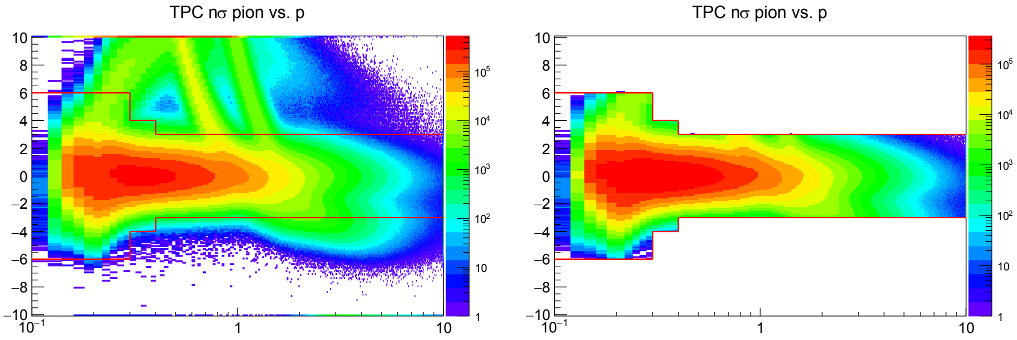

FIGURE 5.2: $N\sigma_{\mathrm{TPC}}$ versus momentum p estimated in the pion hypothesis without any PID cut (left panel) and after p-dependent PID cut is applied (right panel). The dotted lines indicate the TPC PID cuts as a function of momentum.

5.1.4 V^0 selection

The $\mathrm{K^0_S}$ decays weakly into two daughter oppositely charged pions. We reconstruct $\mathrm{K^0_S}$ by applying topological cuts on the daughter tracks. Candidate V^0 decays in the selected sample of events are found by considering all pairs of oppositely charged pions. Following selection criteria was then applied to the tracks

Secondary track selection criteria

- Tracks were selected only in the range $-0.8 < \eta < 0.8$ to improve the resolution.
- Require TPC refit
- Reject Kink Daughters.
- Minimum number of rows crossed in TPC > 70
- Ratio of number of crossed rows to number of findable clusters in TPC > 0.8
- A strict cut on the impact parameter of tracks to PV > 0.06 cm was applied to make sure the track originated not from the primary vertex.

Only V^0 reconstructed in an offline procedure were selected for the analysis.The V^0 reconstructed by the identified secondary tracks have to fulfil the following topological cuts:

- V^0 candidates should decay at a radial distance from the interaction point larger than 0.5 cm.
- V^0 cosine of pointing angle was required to be greater than 0.97 to make sure the particle arrives from the primary vertex. Pointing angle is the angle between $\vec{p}$ and a vector connecting the primary vertex and the V^0 position.

- Distance of closest approach between the two daughter tracks of V^0 was fixed to be less than 1.0 σ

In addition, following conditions were required for the selection of K^0_S candidates.

- Rapidity $|y| < 0.8$
- To define the mass range for K^0_S selection, events where no mass criteria is applied were studied. For different p_T intervals, mass and width of K^0_S were estimated from these events fitting the invariant mass by a function given by the sum of a Gaussian (signal) and a first order polynomial (background). A mass tolerance cut of 4σ around the estimated mass of the K^0_S was used to select V^0 candidates.
- Rejection of pairs for which the mass estimated within the hypothesis to be a πp pair which originated from a Λ decay is compatible within 4 σ ($\sigma = 0.0011$ GeV/c^2) to the PDG mass of the Λ
- Proper Lifetime (mL/p) $<$ 20 cm. This is a very loose cut since lifetime of K^0_S is 2.3 cm

5.1.5 Signal Extraction

Signal extraction and raw estimation procedure have already been discussed in Chapter 4.

5.2 Monte Carlo corrections

The raw yields have to be corrected for the efficiency and acceptance of the detector. A simulated data set was analysed in order to extract the $K^{*\pm}$ reconstruction Acceptance × Efficiency . The following data sets (ESDs) are available: LHC15g3a3 production (Monash 2013 tune of PYTHIA 8) with 51.5 million events, LHC15g3c3 production (Perugia 2011 tune of PYTHIA 6) with 49.0 million events and LHC16d3 production (EPOS-LHC) with 51.2 million events. Particle production and decays are simulated using the event generator while particle interactions with the ALICE detector are simulated using GEANT3. The same event selection, track quality cuts and topological cuts are used for the real and simulated data. The particles produced by the event generator (without any detector effects) are referred to as the "generated" particles. These particles are the input for the GEANT3 detector simulation and the track, V^0 and signal reconstruction algorithms. The tracks and the V^0 which are identified by the reconstruction algorithms and which pass track and topological selection and PID cuts are referred to as "reconstructed" tracks and V^0. A reconstructed $K^{*\pm}$ meson is a $K^{*\pm}$ for which both daughters (track and V^0) have been reconstructed.

Acceptance × Efficiency: The reconstruction acceptance×efficiency, denoted ϵ_{rec}, was calculated using LHC15g3a3, LHC15g3c3 and LHC16d3 simulation sets. ϵ_{rec} is as:

$$\epsilon_{rec} = \frac{\mathrm{N}_{\mathrm{Generated}}\mathrm{K}^{*\pm} \rightarrow \mathrm{K}^0_{\mathrm{S}} + \pi^{\pm}}{\mathrm{N}_{\mathrm{Reconstructed}}\mathrm{K}^{*\pm} \rightarrow \mathrm{K}^0_{\mathrm{S}} + \pi^{\pm}} \tag{5.1}$$

The average of the the three ϵ_{rec} distributions obtained from three Monte Carlo samples is used. In the left panel of Fig. 5.3 the comparison of the acceptance × efficiency distributions obtained with the three Monte Carlo sets is shown. In the right panel of the same figure the $\mathrm{K}^{*\pm}$ acceptance × efficiency is also compared with the acceptance× efficiency of K^{*0} . The efficiency of $\mathrm{K}^{*\pm}$ is observed to be lower than K^{*0} and this is connected to the $\mathrm{K}^0_{\mathrm{S}}$ branching ratio and reconstruction efficiency.

Since the events of numerator and denominator are correlated the uncertainty in ϵ_{rec} was calculated using the Bayesian approach described in (125). The standard deviation in an efficiency $\epsilon = k/n$, where the numerator k is a subset of the denominator n, is:

$$\sigma_{\epsilon} = \sqrt{\frac{k+1}{n+2}\left(\frac{k+2}{n+3} - \frac{k+1}{n+2}\right)} \tag{5.2}$$

The fractional statistical uncertainty in ϵ_{rec} was added in quadrature with the statistical uncertainty in the uncorrected $\mathrm{K}^{*\pm}$ yield to give the total statistical uncertainty of the corrected $\mathrm{K}^{*\pm}$ yield.

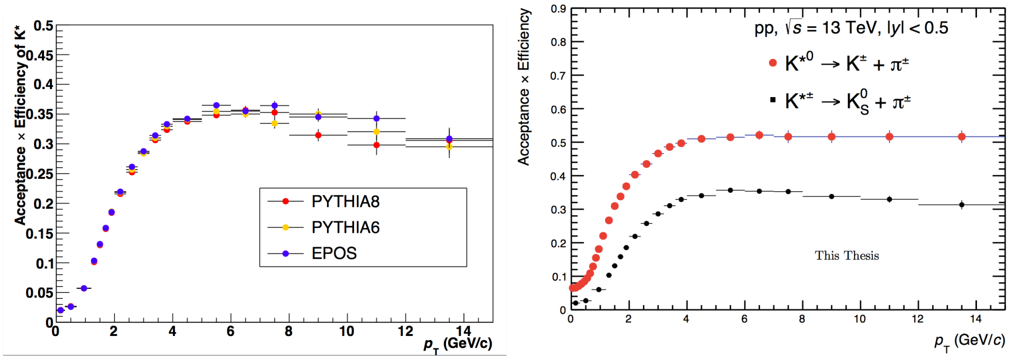

FIGURE 5.3: (Left panel) Comparison of the acceptance × efficiency distributions obtained with LHC15g3a3 (PYTHIA8), LHC15g3c3 (PYTHIA6) and LHC16d3 (EPOS-LHC) productions. (Right panel) Acceptance × Efficiency of $\mathrm{K}^{*\pm}$ and K^{*0} mesons as a function of $\mathrm{p_T}$.

5.2.1 Reweighted Acceptance×Efficiency

To have a correct efficiency estimation it is important that the generated Monte Carlo spectrum should be similar to the real spectrum, thus it is necessary to weight the generated and reconstructed spectra. Figure 5.4 shows the generated $\mathrm{K}^{*\pm}$ spectra (average of the $\mathrm{p_T}$ spectra from three Monte Carlo productions) plotted with the (corrected) measured K*(892)$^{\pm}$ spectrum and the Levy-Tsallis

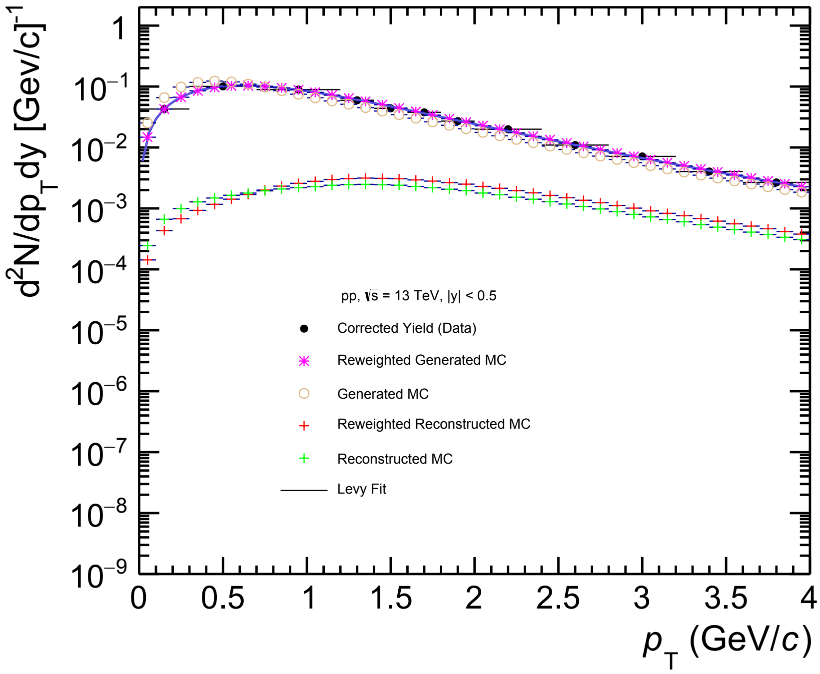

FIGURE 5.4: Corrected $K^*(892)^{\pm}$ spectrum (black dots) with Levy-Tsallis fit (black curve). The unweighted generated (brown circles) distribution is compared to the reweighted one (purple crosses). The reweighted reconstructed (red crosses) and the reconstructed (green crosses) spectra are also shown.

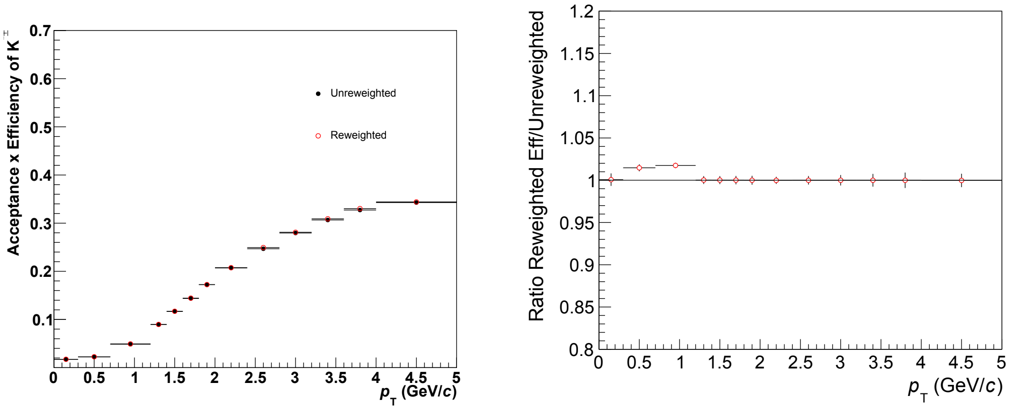

FIGURE 5.5: (Left) Comparison of weighted and unweighted efficiency. (Right) Ratio of weighted and unweighted efficiency.

fit (see Section 5.4) (126)(96) of that measured spectrum. To correct the reconstruction efficiency (ϵ_{rec}), the following iterative procedure was used:

- 1) The unweighted ϵ_{rec} is calculated using the generated and reconstructed $K^{*\pm}$ spectra.
- 2) This ϵ_{rec} is used to correct the measured $K^{*\pm}$ spectrum.

- 3) The corrected $K^{*\pm}$ spectrum is fitted using a Levy-Tsallis function.
- 4) This fit is used to weight the simulated $K^{*\pm}$ spectra. A p_T-dependent weight is applied to the generated spectrum so that it follows the fit. The same weight is applied to the reconstructed spectrum.
- 5) The (weighted) ϵ_{rec} is calculated (see Fig. 5.5).
- 6) Steps 2-5 are repeated (with the weighted ϵ_{rec} from step 5 used as the input for step 2) until the ϵ_{rec} values are observed to change by less than 0.1% between iterations. It was observed that two iterations are usually sufficient for this procedure to converge.

In the left panel of Figure 5.5 the weighted and unweighted efficiency are compared. Their ratio is plotted in the right panel.

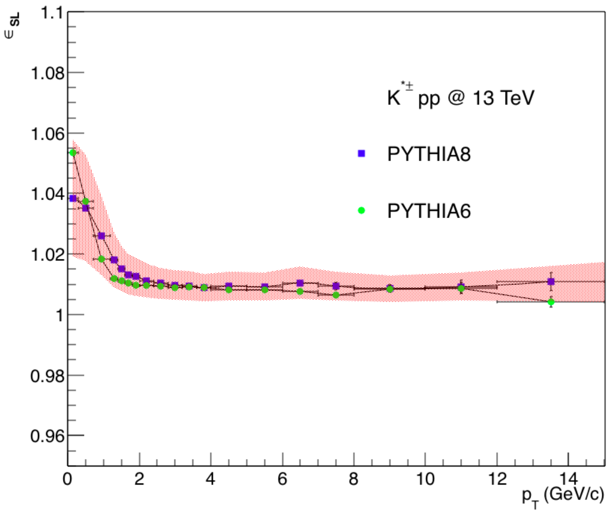

FIGURE 5.6: Comparison of signal-loss correction (ϵ_{SL}) p_T distribution estimated with LHC15g3a3 (PYTHIA8) and LHC15g3c3 (PYTHIA6) production

5.2.2 Signal-Loss correction

The signal-loss correction ϵ_{SL} accounts for the loss of $K^{*\pm}$ mesons incurred by selecting events that satisfy the kINT7 trigger, rather than all inelastic events. This is a p_T-dependent correction factor which is peaked at low p_T, indicating that events that fail the kINT7 selection have softer $K^{*\pm}$ p_T spectra than the average inelastic event. This correction is the ratio of the p_T spectrum in inelastic events to the p_T spectrum in kINT7 events. The p_T spectrum in inelastic events were generated without any trigger selection and with a check that the generated vertex is inside ± 10 cm. The ϵ_{SL} was estimated using two different productions: PYTHIA8 and PYTHIA6. The obtained p_T distributions of the signal-loss correction with the different Monte Carlo production are shown in Figure5.6. They are slightly different especially at low p_T. To be uniform with other resonance analyses at the same collision energy the ϵ_{SL} distribution obtained with PYTHIA8 was used to estimate the $K^{*\pm}$ inelastic p_T spectrum. The uncertainty of this correction in each p_T bin was estimated as the maximum between:

- (ϵ_{SL}(PYTHIA8) -1)/2
- the difference between PYTHIA8 and PYTHIA6 distribution.

5.3 Systematic Uncertainties

For the p_T spectrum the following sources of systematic uncertainty were considered: Signal extraction, primary track selection, PID cut for primary pions, secondary track selection + PID and topological cuts for K^0_S, primary vertex selection, material budget, hadronic interaction, global tracking uncertainty.

5.3.1 Global tracking uncertainty

The tracking uncertainty, due to the uncertainty in ITS-TPC matching of the primary pions, was derived for the $K^{*\pm}$ as follows. The one-particle uncertainty $u(p_{T\pi^\pm})$ was inherited from the analysis of unidentified charged hadron production in the same collision system. A PYTHIA simulation (the LHC15g3a3 production) was used to find the p_T distributions of the primary pion of the $K^{*\pm}$ decay of the different p_T bins of the $K^{*\pm}$ transverse momentum. These p_T distributions (p_T ($\pi^\pm$)) were then used to obtain the weighted average of the tracking uncertainty for each $K^{*\pm}$ transverse-momentum bin. The global tracking uncertainty is, for each $K^{*\pm}$ transverse momentum bin, the ratio of two histograms (a weighted average):
Numerator: the sum, for all generated $K^{*\pm}$ mesons, of
$N(p_{T K^{*\pm}}, p_{T\pi^\pm}) \times w(p_{T K^{*\pm}}) \times u(p_{T\pi^\pm})$
Denominator: the sum, for all generated $K^{*\pm}$ mesons, of
$N(p_{T K^{*\pm}}, p_{T\pi^\pm}) \times w(p_{T K^{*\pm}})$.
The distribution of the uncertainty due to the global tracking as a function of p_T is shown in Figure 5.7.

5.3.2 Systematic due to material budget

The systematic uncertainty, due to the not perfect description in GEANT of the ALICE detector material budget, was derived for the $K^{*\pm}$ using the π and K^0_S material budget uncertainty p_T distributions inherited from other analyses.
The π particle uncertainty has been inherited from the analysis of identified charged hadrons for p-Pb 2013 data, used also for other resonances analyses. The K^0_S uncertainty has been inherited from the strange particle analysis in pp collisions at the same energy. The $K^{*\pm}$ uncertainty is derived from the daughter uncertainties weighting them by their p_T distributions. A PYTHIA simulation is used to find the p_T distributions of the $K^{*\pm}$ decay daughters as a function of the resonance transverse momentum. These decay-daughter distributions are

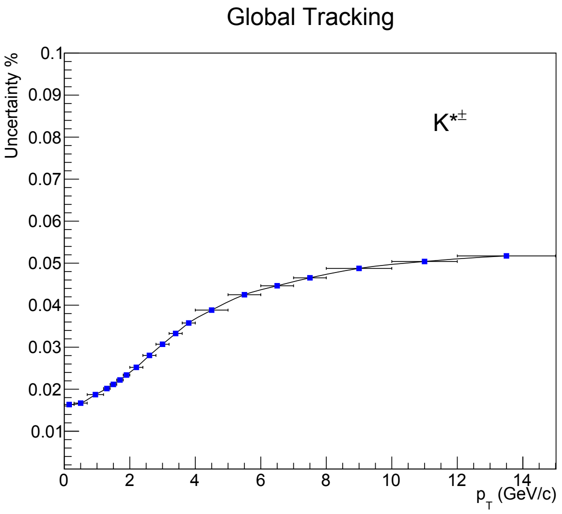

FIGURE 5.7: Tracking (ITS-TPC Matching) efficiency uncertainty for $K^{*\pm}$.

then used to obtain the weighted average of the material budget uncertainty for each $K^{*\pm}$ transverse-momentum bin. The calculation is also weighted so that the simulated p_T spectrum has a realistic shape.
Let $w(p_{T_{K^{*\pm}}})$ be the ratio between the measured and generated $K^*(892)^{\pm}$ p_T spectra. Let $up(p_T)$ and $uk(p_T)$ be the pion and K^0_S material budget uncertainty, respectively. Let $p_{T\pi}$ and $p_{T_{K^0_S}}$ be the transverse momenta of the π and K^0_S decay daughters of each simulated $K^{*\pm}$ meson. Let $N(p_{T_{K^{*\pm}}}, p_{T\pi}, p_{T_{K^0_S}})$ be the number of $K^{*\pm}$ with $p_{T_{K^{*\pm}}}$ that decay to pion and K^0_S with $p_{T\pi}$ and $p_{T_{K^0_S}}$. For each $p_{T_{K^{*\pm}}}$ bin, the two-particle uncertainty is the ratio of two histograms (a weighted average):

Numerator: the sum of $N(p_{T_{K^{*\pm}}}, p_{T\pi}, p_{T_{K^0_S}}) w(p_{T_{K^{*\pm}}})$ $[up(p_{T\pi}) + uk(p_{T_{K^0_S}})]$ for all generated $K^{*\pm}$ mesons.
Denominator: the sum, for all generated $K^{*\pm}$ mesons, of $N(p_{T_{K^{*\pm}}}, p_{T\pi}, p_{T_{K^0_S}}) w(p_{T_{K^{*\pm}}})$

The calculation assumes that the uncertainties of the two decay daughters are fully correlated. The obtained distribution is reported in Figure 5.8.

5.3.3 Systematic due to hadronic interactions

The systematic uncertainty due to hadronic interaction was estimated following the same procedure as for the material budget uncertainty described in Section 5.3.2. The hadronic interaction uncertainties for pions was the one estimated for p-Pb 2013 data. The hadronic interaction uncertainty for K^0_S is negligible. We have considered two extreme hypotheses: 1) K^0_S uncertainty equal to zero; 2) K^0_S uncertainty distribution equal to the K^+ one. The obtained distributions are

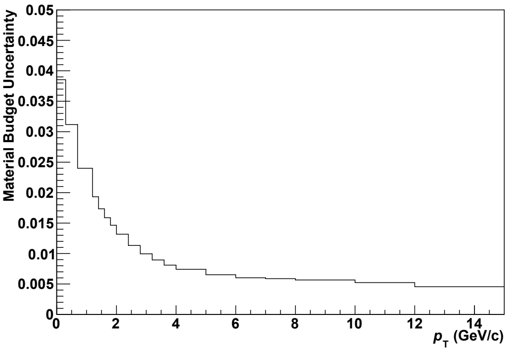

FIGURE 5.8: Material budget uncertainty p_T distribution for $K^{*\pm}$.

in left and right panel of Figure 5.9, respectively. The uncertainty estimated with hypothesis 1) was used.

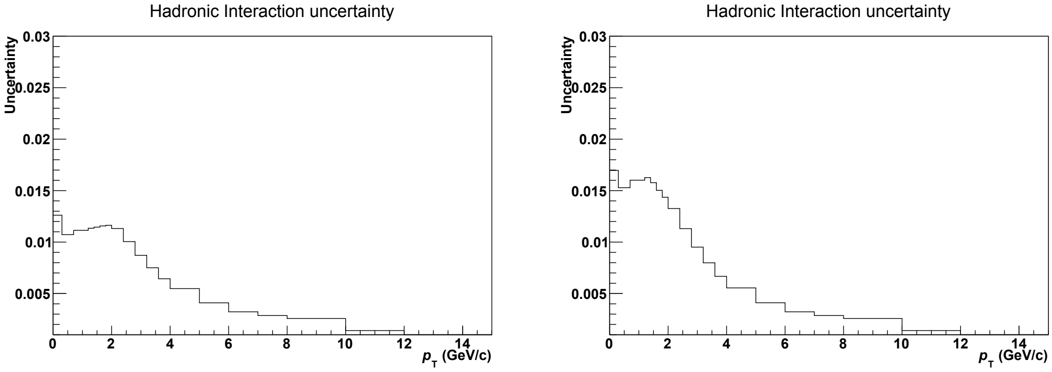

FIGURE 5.9: (Left panel) Hadronic uncertainty p_T distribution for $K^{*\pm}$ in pp collisions at $\sqrt{s}$ = 13 TeV, estimated in the hypothesis that K^0_S uncertainty is equal to zero. (Right panel) Hadronic uncertainty p_T distribution for $K^{*\pm}$ in pp collisions at $\sqrt{s}$ = 13 TeV, estimated in the hypothesis that K^0_S uncertainty is equal to K^+ one.

5.3.4 Systematic estimation procedure using grouping method

To estimate the systematic uncertainty due to primary pions selection, secondary pion selection and K^0_S identification cuts, primary vertex selection the procedure used is described in this section.

For each cut in the group, one or two variations from the standard value of the cut were considered. In Tables 5.1, 5.2, 5.3 the different used cuts are listed. For each cut (standard or variation) the signal extraction parameters can be varied. For each signal extraction parameter (fit function, fit range, bin counting range, width) the standard and the used variation values are listed in Table 5.4. Then for each cut raw yield has been estimated employing the 12 different configurations (1 standard + 11 variations) of the signal extraction. So for each cut 12 different raw yield spectra have been estimated, i.e. for each p_T bin 12 fits have been done, each with a given probability. The used procedure is described in the following:

1. For each cut (index j) in the group a weighted mean of the 12 different spectra is calculated using the probability of the fit as weight:

   $$V_{mean_j} = \frac{\sum_i V_i p_i}{\sum_i p_i}$$

   where V_i and p_i are respectively the efficiency corrected yield and fit probability from the 12 different configurations of signal extraction. The mean weighted probability is given for each cut as

   $$p_{mean_j} = < p_i >$$

2. The systematic uncertainty for each cut (U_{SX_j}) is given by the RMS value of $V_{mean_j} - V_i$, i = 1-12
3. A Barlow check (or consistency check, see next subsection) is done for all the variations of a particular cut. The cuts which pass the Barlow check are not considered in the final systematic uncertainties.
4. For each group a weighted mean of spectra estimated with the standard cuts and with the cuts which fail the Barlow check is calculated

   $$V_{MEAN} = \frac{\sum_j V_{mean_j} p_{mean_j}}{\sum_j p_{mean_j}}$$

   .
5. The systematic uncertainty for each group (labelled as U$_{RSX}$) is given by the RMS value of $V_{MEAN} - V_{mean_j}$
6. The systematic uncertainty connected to the signal extraction procedure (U_{MSX}) is estimated by a weighted mean of the systematic uncertainties of all the cuts which fail the Barlow check:

   $$U_{MSX} = \frac{\sum_j U_{SX_j} p_{mean_j}}{\sum_j p_{mean_j}}$$

   .

5.3.5 Consistency Check

To estimate the systematic uncertainties the same yield is estimated many times with different analysis parameters (cuts, signal extraction, background estimation, etc...). However, it is necessary to ensure that the observed variations are not simply accounting for statistical fluctuations. As described in (127), since the default and alternate measurements use (mostly) overlapping data sets, agreement within the statistical uncertainties is not sufficient. Instead, agreement within the difference in quadrature of the statistical uncertainties is required.
If two measurements are found to be consistent within the quadrature difference

TABLE 5.1: Standard and modified cuts for primary pion identification.

Selection criteria	Standard	Variation 1	Variation 2
TPC crossed rows	70	100	80
Crossed rows/Findable clusters	0.8	0.9	-
TPC χ^2	4.0	2.3	-
ITS χ^2	36	25	4
Global χ^2	36	25	-
No. SPD clusters	1	0	-
$\mathrm{DCA_z}$ (cm)	2	1	0.2
$\mathrm{DCA_r}$	7σ	4σ	-
TPC PID Primary π (σ)	3	3.5	2.5

TABLE 5.2: Standard and modified cuts for secondary tracks and $\mathrm{K^0_S}$ identification.

Selection criteria	Standard	Variation 1	Variation 2
TPC crossed rows	70	100	80
Crossed rows/Findable clusters	0.8	0.9	-
DCA tracks to PV (cm)	0.06	0.07	0.05
PID secondary π (σ)	5	4.5	4
$\mathrm{V^0}$ decay radius (cm)	0.5	0.7	0.3
Cosine PA	0.97	0.95	0.99
DCA $\mathrm{V^0}$daughters (σ)	1	1.25	0.75
Lifetime (cm)	20	12	-
Competing $\mathrm{V^0}$ rejection $\left\lvert M_{\pi p} - M_{\Lambda}\right\rvert$ (MeV/c^2)	4.3	5.4	3.2
$\mathrm{K^0_S}$ mass tolerance (σ)	4	5	6 and 3
$\mathrm{K^0_S}$ rapidity	0.8	0.9	0.7

TABLE 5.3: Standard and modified cuts for primary vertex identification.

Selection criteria	Standard	Variation 1	Variation 2
Primary vertex (cm)	10	12	8

TABLE 5.4: Standard and modified parameters for signal extraction.

Signal extraction parameters	Standard	Variation 1	Variation 2
Fit Function	Expol	Polynomial 2	Polynomial 3
Normalization range (GeV/c^2)	1.1 - 1.2	1.1 - 1.3	1.1 - 1.4
Fit Range (GeV/c^2)	0.66 - 1.1	0.65 - 1.15	0.7 - 1.05
Bin Counting Range (GeV/c^2)	0.79 - 0.99	0.8 - 0.98	0.78 - 1.0
Width (GeV/c^2)	0.0508	0.0517 or 0.0499	Free Width

of their statistical uncertainties, then it is not necessary to account for the differences between them in the systematic uncertainties. As an example, consider two p_T spectra, one obtained with the default setting and a second obtained with an alternative setting (for example, with a different fiducial volume). Let us denote the yield and the statistical uncertainty as y_{def} and σ_{def} for the default case and as y_{al} and σ_{al} for the alternative setting. For each p_T bin we can estimate Δ/σ_{cc}, where Δ is the difference between the default and the alternative measurement (Δ=y_{def}-y_{al}) and σ_{cc} is the difference in quadrature of the statistical uncertainties of these measurements ($\sigma_{cc} = \sqrt{\sigma_{def}^2 - \sigma_{al}^2}$). In general, if two measurements are consistent, it is expected that the distribution of Δ/σ_{cc} would have a mean near 0, a standard deviation near 1, and that 68% (95%) of the entries would lie within $|\Delta/\sigma_{cc}| < 1$ ($|\Delta/\sigma_{cc}| < 2$). For this analysis we don't consider a cut as a systematic source if 3 of the following 4 criteria are satisfied:

1. $|\Delta/\sigma_{cc}| < 0.12$
2. standard deviation < 1.3
3. fraction of entries within ± 1 ($I_1 > 0.55$)
4. fraction of entries within ± 2 ($I_2 > 0.75$)

As an example, in Figure 5.10, there are reported the Δ/σ_{cc} distributions of one included (left) and one excluded (right) case for the final systematic uncertainties. In Figures 5.11, 5.12 and 5.13 the V_{mean_j} p_T distributions for the used cuts for primary pions, K^0_S and primary vertex uncertainty are shown. In these figures the V_{MEAN} p_T distribution is also reported. The p_T distribution of the V_{mean_j}/V_{MEAN} ratio is shown in the lower panel of these figures.

5.3.6 Smoothing procedure for systematic uncertainties

The systematic uncertainties exhibit a few large fluctuations from bin to bin, while one might expect the "true" systematic uncertainties to be more uniform or smoothly varying. The total systematic uncertainty was not directly smoothed;

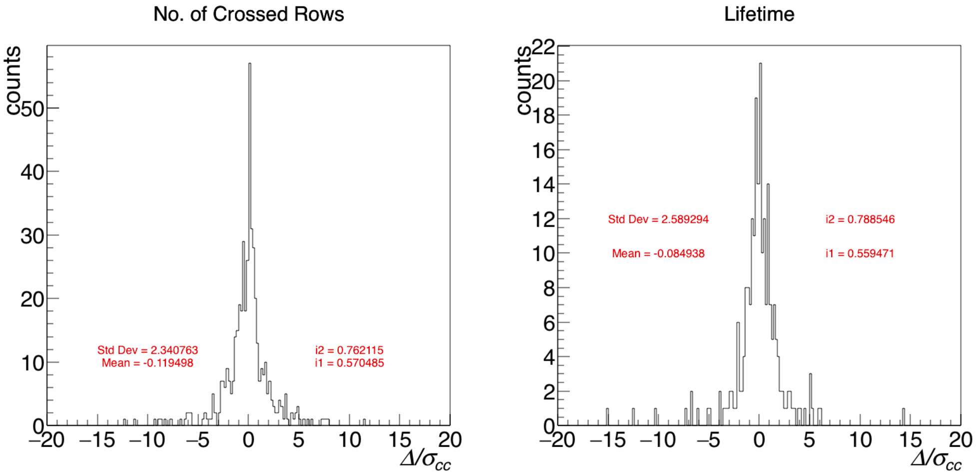

FIGURE 5.10: (Left) Consistency check for the number of crossed rows on primary tracks. (Right) Consistency check for the cut on lifetime of K^0_S.

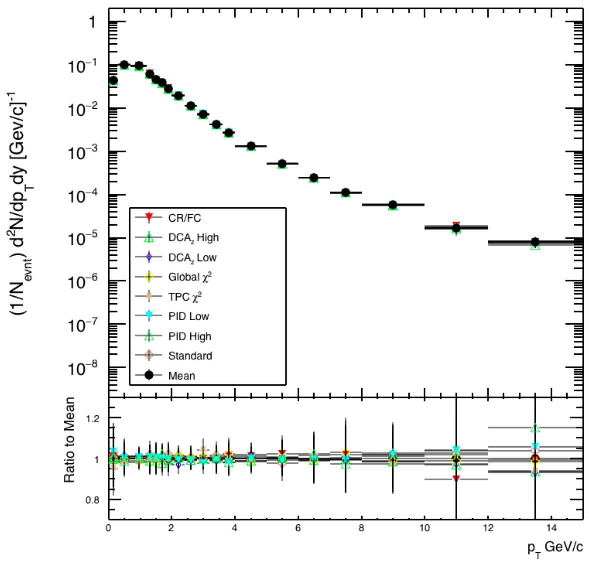

FIGURE 5.11: V_{mean_j} p_T distributions for the used cuts for primary pions systematic uncertainty estimation. The V_{MEAN} p_T distribution is also reported. (Lower panel) The V_{mean_j}/V_{MEAN} ratio as a p_T function.

rather, each source of systematic uncertainty was smoothed individually. If necessary, the following smoothing procedure was applied. For p_T bin j the uncertainty σ_j^{i+1} was obtained averaging the initial uncertainty σ_j^i with $\sigma_{j\pm1}^i$, i.e.

$$\sigma_j^{i+1} = (\sigma_{j-1}^i + \sigma_j^i + \sigma_{j+1}^i)/3 \tag{5.3}$$

If necessary the smoothing procedure was iterated.

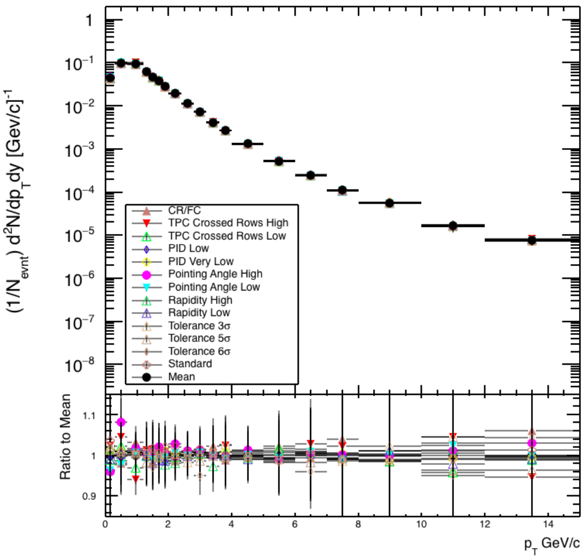

FIGURE 5.12: V_{mean_j} p_T distributions for the used cuts for K^0_S systematic uncertainty estimation. The V_{MEAN} p_T distribution is also reported. (Lower panel) The V_{mean_j}/V_{MEAN} ratio as a p_T function.

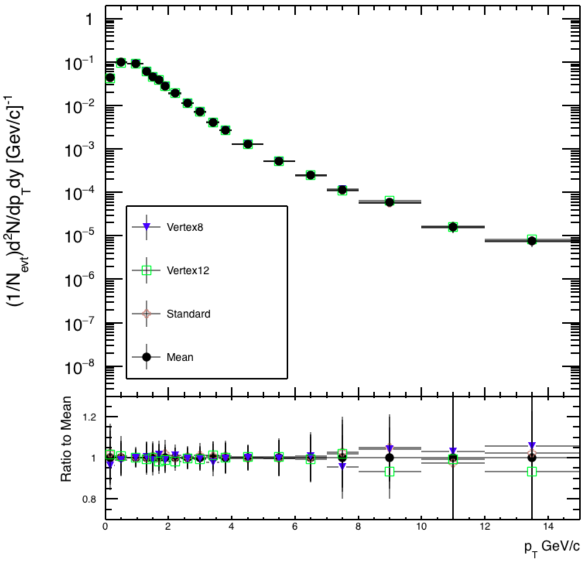

FIGURE 5.13: V_{mean_j} p_T distributions for the used cuts for Primary Vertex systematic uncertainty estimation. The V_{MEAN} p_T distribution is also reported. (Lower panel) The V_{mean_j}/V_{MEAN} ratio as a p_T function.

5.3.7 Total systematic uncertainty

The systematic uncertainties from different sources were added in quadrature to obtain the total systematic uncertainty. The p_T distributions of the systematic uncertainty of the different sources previously described are shown in Figure 5.14. In the same figure the p_T distribution of the total systematic uncertainty estimated for the $K^{*\pm}$ production in pp collisions at $\sqrt{s}$ = 13 TeV is also

TABLE 5.5: Main sources and weighted values of the relative systematic uncertainties (expressed in %) of the differential yield of $K^*(892)^{\pm}$ resonance for low, intermediate and high p_T ranges.

p_T (GeV/c)	0-1.2	1.2-4	4-15
Signal extraction (%)	4.4	3.7	4.5
Primary pion identification (%)	2.1	1.4	1.3
K^0_S identification (%)	2.2	1.3	1.2
Primary vertex (%)	1.2	1.2	1.2
Global tracking efficiency (%)	1.7	2.3	4.1
Material budget (%)	3.0	1.6	0.7
Hadronic interaction (%)	1.1	1.1	0.5
Signal Loss (%)	1.6	0.7	0.5

shown. The main sources and the weighted values of the relative systematic uncertainties (expressed in %) of the differential yield of $K^{*\pm}$ resonance for low, intermediate and high p_T ranges are reported in Table 5.5. To these we have to add an uncertainty of 2.5 % due to the INEL normalisation.

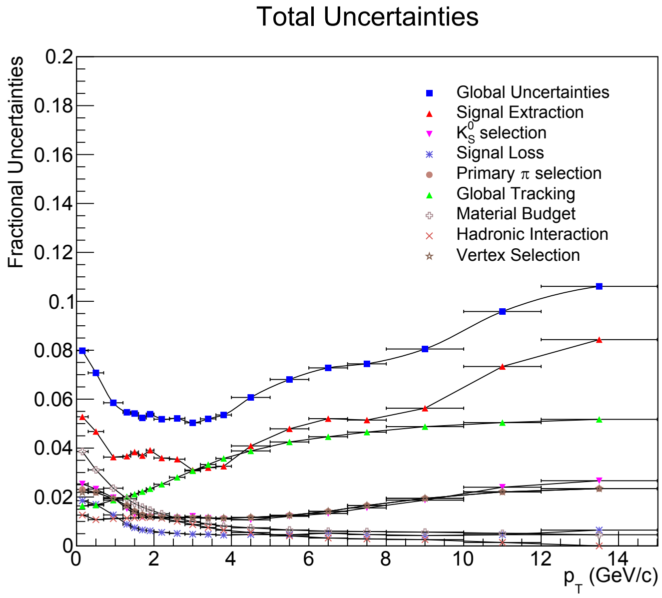

FIGURE 5.14: The p_T distributions of the systematic uncertainty of the different sources (see text) are shown by lines of different colors. The p_T distribution of the total systematic uncertainty estimated for the $K^*(892)^{\pm}$ production in pp collisions at $\sqrt{s}$ = 13 TeV is also shown.

5.4 K$^{*\pm}$ Transverse momentum spectrum

In Figure 5.15 the transverse momentum spectrum for K$^{*\pm}$ at mid-rapidity in inelastic pp collisions at $\sqrt{s}$ = 13 TeV is shown. The inelastic yield was estimated by the following formula:

$$\frac{d^2N}{dp_T dy} = \frac{\text{RawCounts}}{N_{MB} \times BR \times \Delta p_T \times \Delta y} \frac{\epsilon_{SL}}{\epsilon_{rec}} \times f_{norm} \times f_{vertex} \tag{5.4}$$

where Δy = 1, N_{MB} is the number of the minimum bias trigger selected by the event cuts, BR = 0.33 is the branching ratio in K^0_S + $\pi^{\pm}$, ϵ_{rec} is the weighted acceptance× efficiency. The signal-loss correction ϵ_{SL} accounts for the loss of K$^{*\pm}$ mesons incurred by selecting events that satisfy the kINT7 trigger, rather than all inelastic events. It is a small $\mathrm{p_T}$ dependent factor. The inelastic normalization factor is f_{norm} = 0.7448 ± 0.019 (128), it takes into account the efficiency for trigger selection for inelastic pp collisions. It is the ratio between the trigger cross and the inelastic cross section. Values for the inelastic cross section were taken from (129), which performs a fit using measured values from several experiments. The factor f_{vertex} = 0.9313 accounts for the signal loss introduced by the requirement that a primary vertex must be reconstructed. It is given by a ratio with

- **Denominator**: the number of triggered events (after application of the IsIncompleteDAQ cut and the pileup cuts)
- **Numerator**: the subset of the events in the denominator for which a good vertex was found (i.e., it passes the vertex quality cuts, but without the cut on the z-position of the vertex).

The corrected spectrum for K$^{*\pm}$ as reported in this chapter is then fitted with a Levy-Tsallis function (126), which describes both the exponential and power law shape of the spectrum at low and high transverse momentum:

$$\frac{1}{N_{evt}} \frac{d^2N}{dy d\mathrm{p_T}} = \mathrm{p_T} \frac{dN}{dy} \frac{(n-1)(n-2)}{nT[nT + m(n-2)]} \left(1 + \frac{\sqrt{m^2 + \mathrm{p_T^2}} - m}{nT}\right)^{-n} \tag{5.5}$$

This function describes both the exponential shape of the spectrum at low $\mathrm{p_T}$ and the power law at high $\mathrm{p_T}$. The $\mathrm{p_T}$ -integrated yield (dN/dy) is obtained by integrating the spectrum in the measured range. The measured values are listed in Table 5.6:

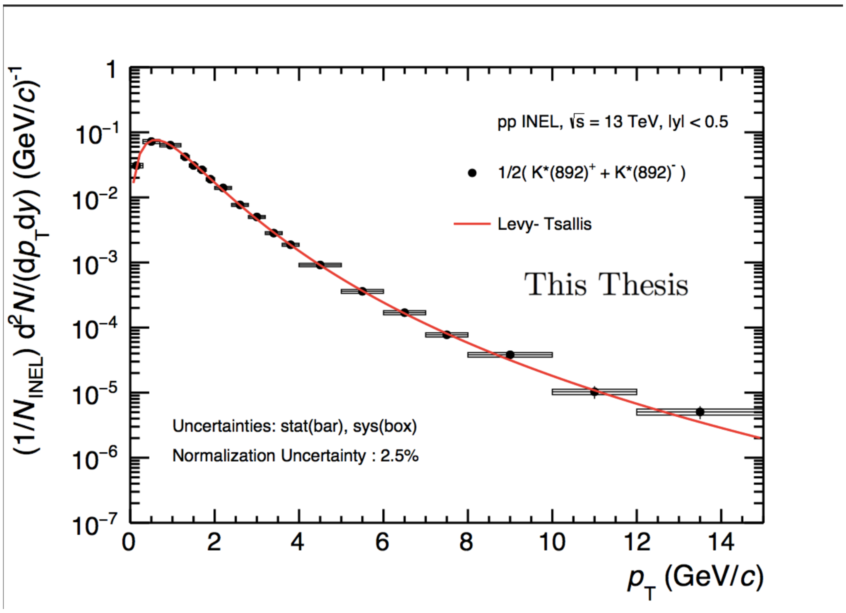

FIGURE 5.15: Inelastic K$^*(892)^{\pm}$ spectrum at mid-rapidity in pp collisions at $\sqrt{s}$ = 13 TeV. Statistical (bars) and systematics (boxes) uncertainties are also reported.

dN/dy	$\langle p_{\mathrm{T}} \rangle$(GeV/$c$)
0.1077 ± 0.0024 ± 0.0067	1.150 ± 0.0148 ± 0.0186

TABLE 5.6: The p_{T} integrated $(\mathrm{K}^{*+} + \mathrm{K}^{*-})/2)$ yield dN/d$y_{|y|<0.5}$, the mean transverse momentum, $\langle p_{\mathrm{T}} \rangle$ pp collisions at $\sqrt{s}$ = 13 TeV. The first error represents the statistical uncertainty and the second one is the systematic uncertainty.

Chapter 6

K^{*0} results in pp collisions at 13 TeV

The $K^{*}(892)^{0}$ resonance production at central rapidity ($|y| < 0.5$) has been measured in inelastic pp collisions at $\sqrt{s} = 13$ TeV with the ALICE experiment, by the reconstruction of its hadronic decay into $K\pi$. A sample of about 50 M events (same as used for $K^{*\pm}$ analysis) collected in July 2015, have been analysed. For this measurement, charged pions and kaons have been identified using TPC and TOF information. The TOF PID improves particle identification in the transverse momentum range, and then increases the significance of the K^{*0} signal

6.1 K^{*}(892)^{0} reconstruction in pp collisions

K^{*0} have been reconstructed by their hadronic decay into $K^{\pm}\pi^{\mp}$ (B.R = 0.66)(81) via invariant mass distribution as described in the Chapter 4. The decay products are identified as oppositely charged pions and kaons among the tracks reconstructed in the central barrel. The data sample and the event selection are the same as the ones used for $K^{*\pm}$ analysis and described in Chapter 5. Also for the selection of the primary tracks, the same criteria used for $K^{*\pm}$ analysis and described in Section 5.1.1 have been used. Following here, K^{*0} will indicate $\frac{K^{*}(892)^{0}+\overline{K^{*}(892)^{0}}}{2}$.

6.1.1 Pion and Kaon Identification

Charged kaons and pions have been identified by using Time Projection Chamber (TPC) and Time Of Flight (TOF) detectors. Particle identification in TPC is performed by measuring the specific energy loss ($\mathrm{d}E/\mathrm{d}x$) in the detector gas as described in Chapter 3.2.9.

Particles are identified in the TPC via the difference between the measured energy loss and the value expected for different mass hypotheses. The cut on this difference, normalised to the resolution σ_{TPC}, is optimised for each analysis and depends in general on the signal-to-background ratio and on the transverse momentum. Particles are identified in the TOF by comparing the measured time of flight to the expected time for a given particle species. The start time for the TOF measurement is provided by the T0 detector, which consists of two arrays of Cherenkov counters T0C and T0A, positioned at opposite sides of the interaction point (IP) at $-3.28 < \eta < -2.97$ and $4.61 < \eta < 4.92$, respectively. The expected flight time for each particle species is calculated during the reconstruction, and then PID is performed via a comparison between the measured and expected times. Both pions and kaons are selected by a cut of p_T dependent PID cut for TPC as was done for $K^{*\pm}$ and with a TOF veto of $|N\sigma_{TOF}| < 3.0$. TOF veto means that the TOF cut is applied only for cases where the track matches a hit in the TOF. (see Figures. 6.1 and 6.2)

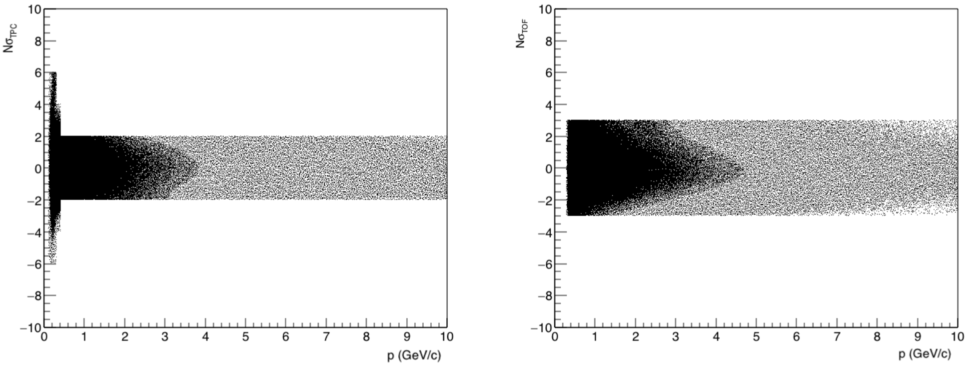

FIGURE 6.1: $N\sigma_{TPC}$ (left panel) and $N\sigma_{TOF}$ (right panel) versus momentum p for pion mass hypothesis after 2 sigma (left) or 3 sigma (right) PID cut is applied.

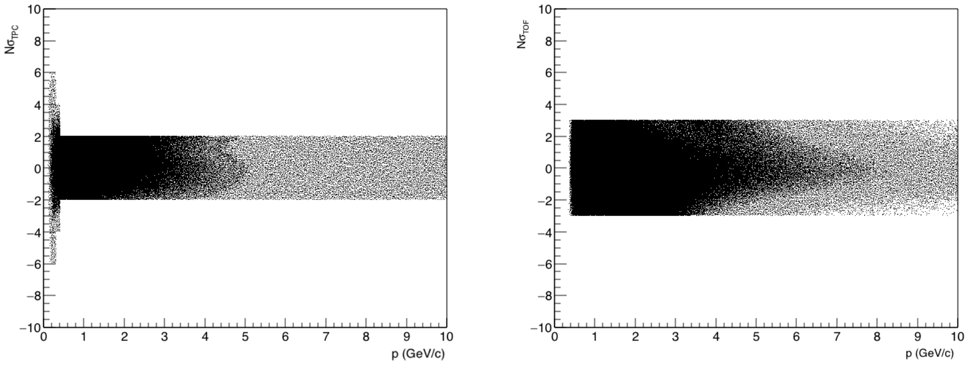

FIGURE 6.2: $N\sigma_{TPC}$ (left panel) and $N\sigma_{TOF}$ (right panel) versus momentum p for kaon mass hypothesis after 2 sigma (left) or 3 sigma (right) PID cut is applied.

6.1.2 K^{*0} raw yield and acceptance × efficiency

Signal extraction and raw yield estimation procedure have already been discussed in Chapter 4. Figure 6.3 reports a comparison of Acceptance x Efficiency estimated for K^{*0} and $K^{*\pm}$. A factor of ~ 2 is observed in the efficiencies of the two particles. The main source of this difference is due to the branching ratio and the acceptance of K^0_S (daughters of $K^{*\pm}$) with respect to the charged kaons (daughters of K^{*0}).

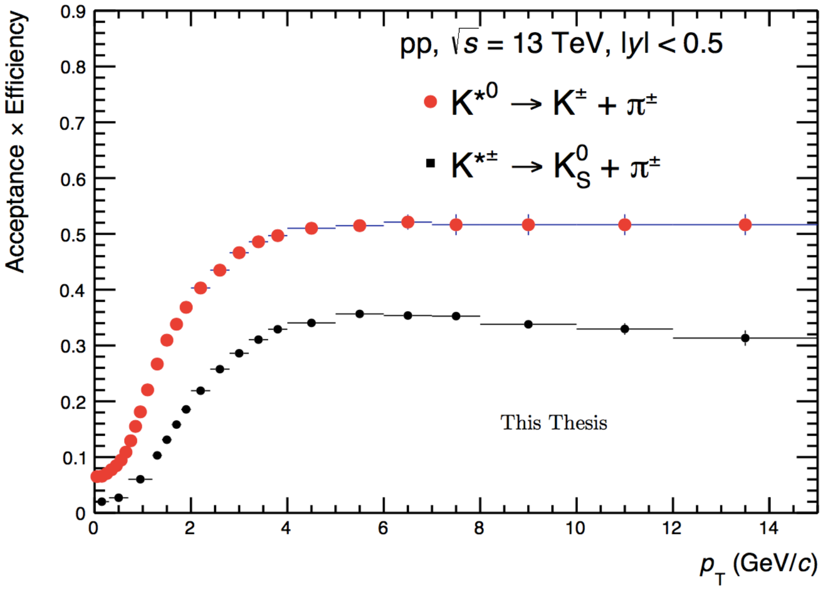

FIGURE 6.3: Acceptance × Efficiency of K$^{*\pm}$ and K^{*0} mesons as a function of p$_T$ in pp collisions at 13 TeV

6.2 K^{*0} p$_T$ spectrum and comparison with K$^{*\pm}$

The inelastic yield was estimated by the following formula:

$$\frac{d^2N}{dp_T dy} = \frac{\text{RawCounts}}{N_{MB} \times BR \times \Delta p_T \times \Delta y}\frac{1}{\epsilon} \times f_{norm} \times f_{vertex} \tag{6.1}$$

where Δy = 1, N_{MB} is the number of the minimum bias trigger selected by the event cuts, BR = 0.66 is the branching ratio in K$^{\pm}$ + $\pi^{\pm}$, ϵ is the weighted acceptance× efficiency. The inelastic normalization factor is $f_{norm} = 0.7448 \pm 0.019$, it takes into account the efficiency for trigger selection for inelastic pp collisions. The factor f_{vertex} = 0.931264 accounts for the signal loss introduced by the requirement that a primary vertex must be reconstructed. See Chapter 5 for more information.

In Figure 6.4, inelastic spectrum from pp collisions at 13 TeV for K^{*0} obtained in the official ALICE analysis is compared to the one obtained with the analysis described in this thesis. A good agreement is observed between the two distributions. Small differences could be due to the fact the Signal Loss correction and reweighed efficiency are not taken into account for the spectrum estimated in this thesis.

In Figure 6.5, inelastic p$_T$ spectrum for K$^{*\pm}$ for pp collisions at 13 TeV is compared to the spectrum for K^{*0} at the same collision energy. As expected considering the similarity of quark content, isospin, and mass, the spectra of charged and neutral resonance are equal, inside the estimated uncertainties.

.

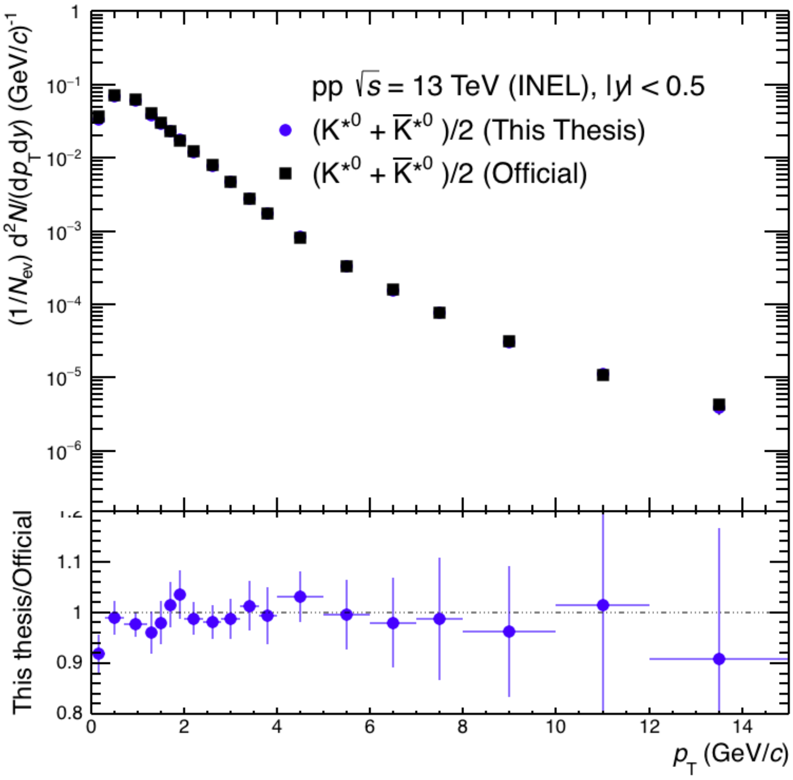

FIGURE 6.4: Comparison of K^{*0} spectra obtained in this thesis and in the official ALICE analysis

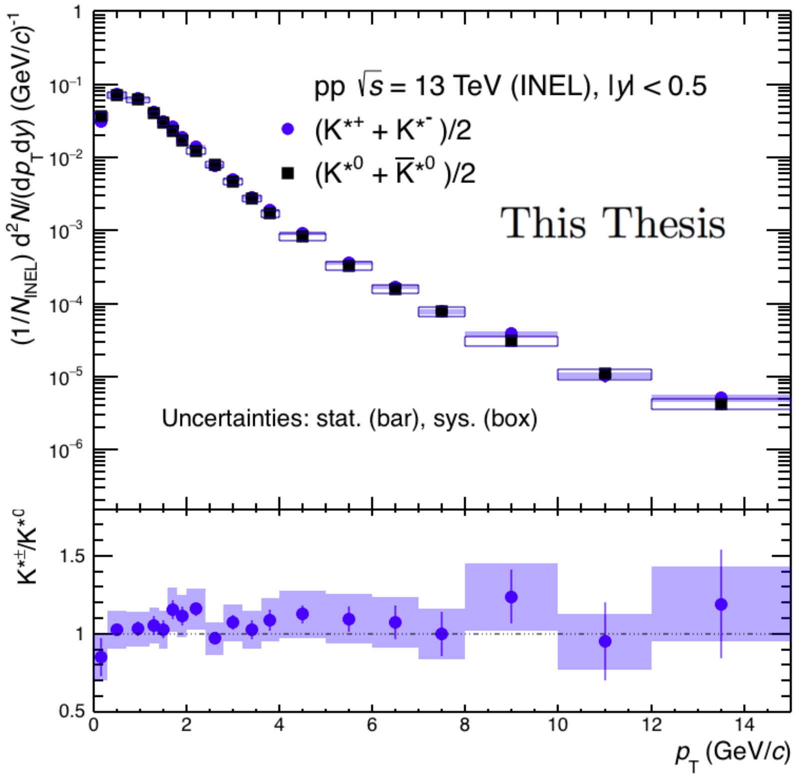

FIGURE 6.5: INEL p$_T$ spectra of K$^{*\pm}$ (blue points) and K^{*0} (black squares) mesons (preliminary ALICE result) as a function of p$_T$. In the bottom panel, ratio of K$^{*\pm}$/K^{*0} spectra is shown.

Chapter 7

Results for $\mathrm{K}^{*\pm}$ in pp collisions at 13 TeV

In the following sections, various results and inferences will be discussed which can be derived from the analysis described in Chapter 5. The measured $\mathrm{p_T}$ spectrum obtained for $\mathrm{K}^{*\pm}$ will be compared with different theoretical models and spectra obtained. The dependence of K^{*}/π and $\mathrm{K}^{*}/\mathrm{K}$ ratios on collision energy and collision system will be shown. Furthermore $\mathrm{p_T}$ spectra of positive and negative K^{*} have been extracted and compared.

7.1 Energy Dependence

Soft scattering processes and parton hadronisation dominates the bulk of particle production ($\mathrm{p_T} < 2$ GeV/c) in pp collisions at LHC energies. On the contrary hard QCD processes characterise the high $\mathrm{p_T}$ production. The measurement of particle yield and particle ratios in pp collisions are important as a baseline for comparison with heavy ion reactions.

In Figures 7.1 and 7.2 the measured $\mathrm{d}N/\mathrm{d}y$ and $\langle \mathrm{p_T} \rangle$ for $\mathrm{K}^{*\pm}$ in pp collisions at 13 TeV are compared with the same quantities measured at lower collision energies (5.02 and 8 TeV) and with K^{*0} results at different energies. The charged K^{*} values are, inside the estimated uncertainties, equal to the neutral ones. The resonance yield production increases with the collisions energy. However a saturation seems to be present for $\sqrt{s}$ larger than 7 TeV. A clear increase of the mean $\mathrm{p_T}$ is observed increasing the collision energy.

In Figure 7.3 the ratios of the $\mathrm{K}^{*\pm}$ $\mathrm{p_T}$ spectra at $\sqrt{s} = 8$ and 13 TeV to the one at 5.02 TeV are shown (130).

For $\mathrm{p_T} > 1$ GeV/c a clear hardening of the $\mathrm{K}^{*\pm}$ $\mathrm{p_T}$ spectrum is observed when increasing the energy, while at low $\mathrm{p_T}$ the same yield is measured, within the estimated uncertainties, at the three energies. This suggests that particle production mechanism in the soft energy region is independent of the collision energy, while the increase of the slope for $\mathrm{p_T} > 1$ GeV/c suggests an increase of the relevance of the hard scattering processes with the collision energy. It is

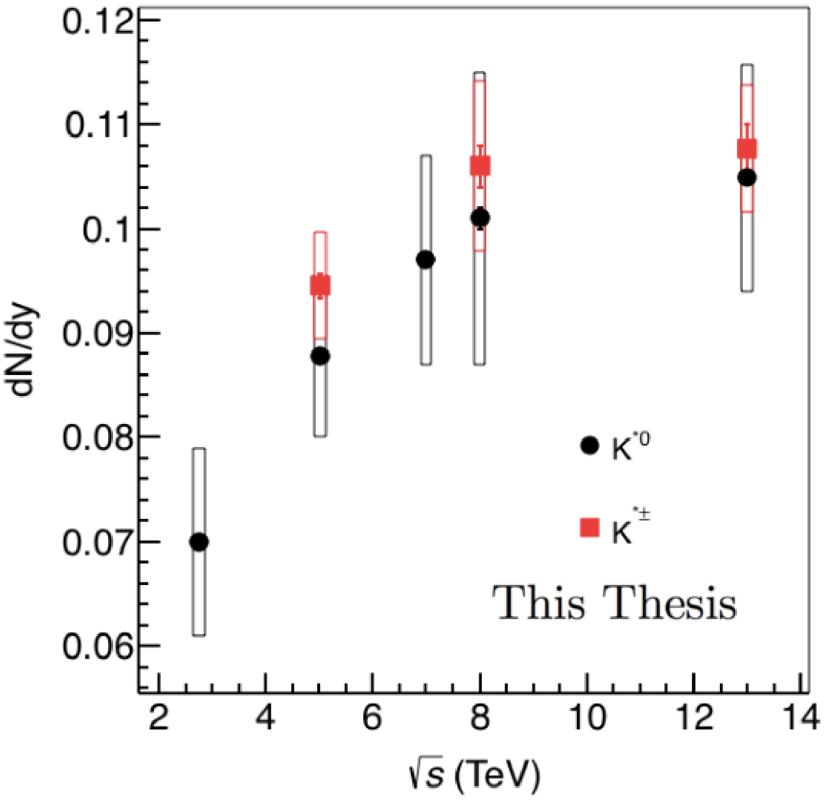

FIGURE 7.1: Yield for K^{*0} and K$^{*\pm}$ in inelastic pp collisions at various collision energies

worth noting that a similar behaviour is also observed for K^{*0}, π, and ϕ as reported in the Figures 7.4.

7.2 Model Comparison

Modern event generators as PYTHIA combine perturbative picture of hard processes with non perturbative picture of hadronisation which is simulated using the Lund string fragmentation model (131). In the presented PYTHIA tunes (PYTHIA6 - Perugia 2011 (66) and PYTHIA8 - Monash 2013 (67)), multiple parton-parton interactions in the same event and colour reconnection mechanism are taken into account (59). These effects are important in hadron-hadron interactions at high energies as the LHC ones. In particular, the colour string formation between final parton may mimic effects similar to that induced by collective flow in heavy-ion collisions. Differences between EPOS-LHC and PYTHIA have been discussed in the Chapter 2. EPOS-LHC differs substantially from the PYTHIA models in its modelling of hadronisation and the underlying events. It is a microscopic model, which relies on parton-based Gribov-Regge theory and incorporates an hydrodynamical evolution if the energy density is high enough (i.e. "core" part of the created system).

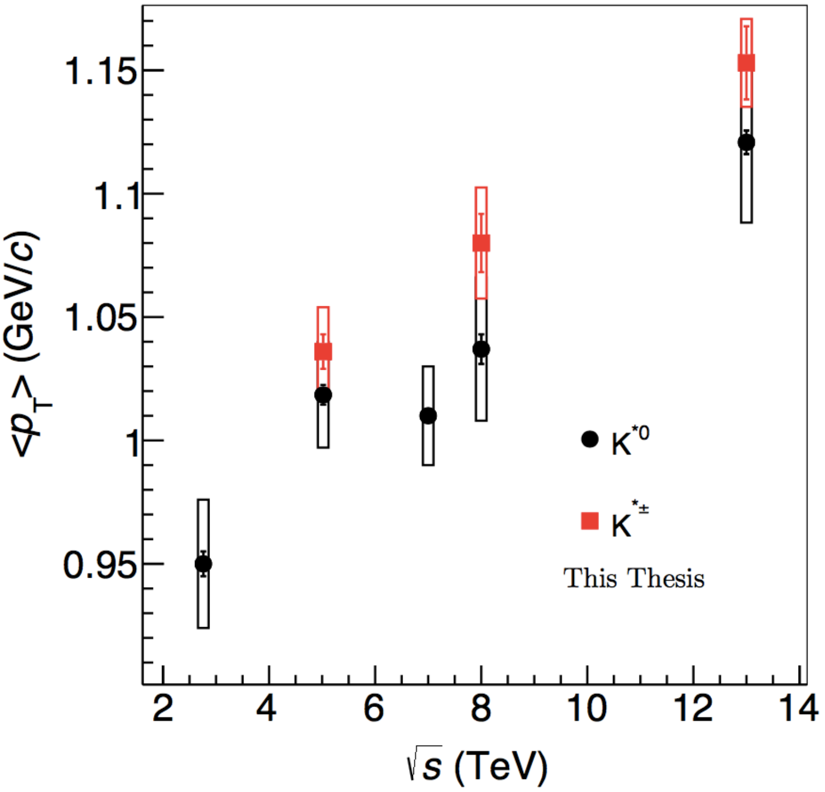

FIGURE 7.2: K^{*0} (black circles) and $K^{*\pm}$ (red squares) mean transverse momentum as a function of pp collision energy. Statistical and systematic uncertainties are shown by error bars and empty boxes, respectively.

In Figure 7.5 the inelastic $K^{*\pm}$ spectrum measured in pp collisions at 13 TeV is compared with the PYTHIA 8 - Monash 2013, PYTHIA 6 - Perugia 2011, EPOS-LHC predictions. It is observed that all the event generators overestimate the $K^{*\pm}$ production at $p_T < 1$ GeV/c. PYTHIA8 and PYTHIA6 underestimate of about 20% the measured p_T spectrum in the intermediate p_T region, while good agreement is observed in the high p_T region. EPOS-LHC slightly underestimates the yield in the intermediate p_T region, while it overestimates the production at high transverse momentum. In Figure 7.6, ratios of the p_T spectra generated by PYTHIA8-Monash 2013, PYTHIA6-Perugia 2011, and EPOS-LHC are also reported. It is interesting to note as EPOS-LHC is able to better estimate the measured energy dependence as compared to PYTHIA8 and PYTHIA6 event generators which substantially overestimate the hardening with the increasing energy.

7.3 Particle Ratios

K^*/π ratio is the ratio of a strange particle to non-strange particle, thus providing information about strangeness production. While K^*/K ratio is the ratio of a resonance to its stable state, thus providing information about the possible influence of the hadronic phase. In Figure 7.7 the $K^{*\pm}/K$ ratio for pp collisions at

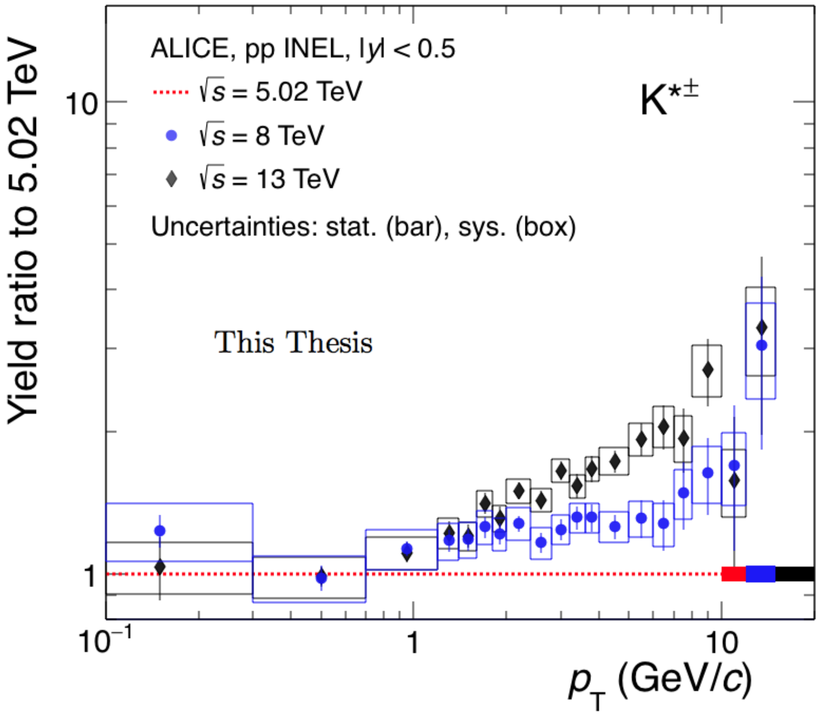

FIGURE 7.3: Ratios of transverse momentum spectra of $\mathrm{K}^*(892)^{\pm}$ in inelastic pp events at $\sqrt{s}$ = 8 and 13 TeV to 5.02 TeV. Statistical and systematic uncertainties are shown by error bars and empty boxes, respectively. The normalisation uncertainties are shown as coloured boxes around 1 and they are not included in the point-to-point uncertainty. (130)

$\sqrt{s}$ = 13 TeV is compared with the same quantities measured at 5.02 and 8 TeV and with the $\mathrm{K}^{*0}/\mathrm{K}$ one for different systems and collision energies. The measured values for the $\mathrm{K}^{*\pm}$ are in agreement within the estimated errors with the K^{*0} one. No energy dependence is observed in pp collisions, however neutral K^*/K ratios are suppressed in central heavy-ion collisions with respect to pp collisions. This points to rescattering dominating over the regeneration effects during the hadronic phase both at RHIC and LHC energies. The observed suppression increases with the collision energy.
In Figure 7.8 the $\mathrm{K}^{*\pm}/\pi$ ratio measured at $\sqrt{s}$ = 13 TeV is compared with the same quantity measured at lower collision energy and with K^{*0}/π ratio measured at RHIC and LHC energies by STAR and ALICE experiments. It is observed that the K^*/π ratio is independent of the collision energy within the systematic uncertainty which suggests no strangeness enhancement in minimum bias pp collisions.

7.4 K^{*+} vs K^{*-}

In pp collisions at ultrarelativistic energies production of positive and negative light flavour particles as pion and kaon has been observed to be equal (132). Same analysis described for $\mathrm{K}^{*\pm}$ was also done for K^{*+} and K^{*-} separately. For

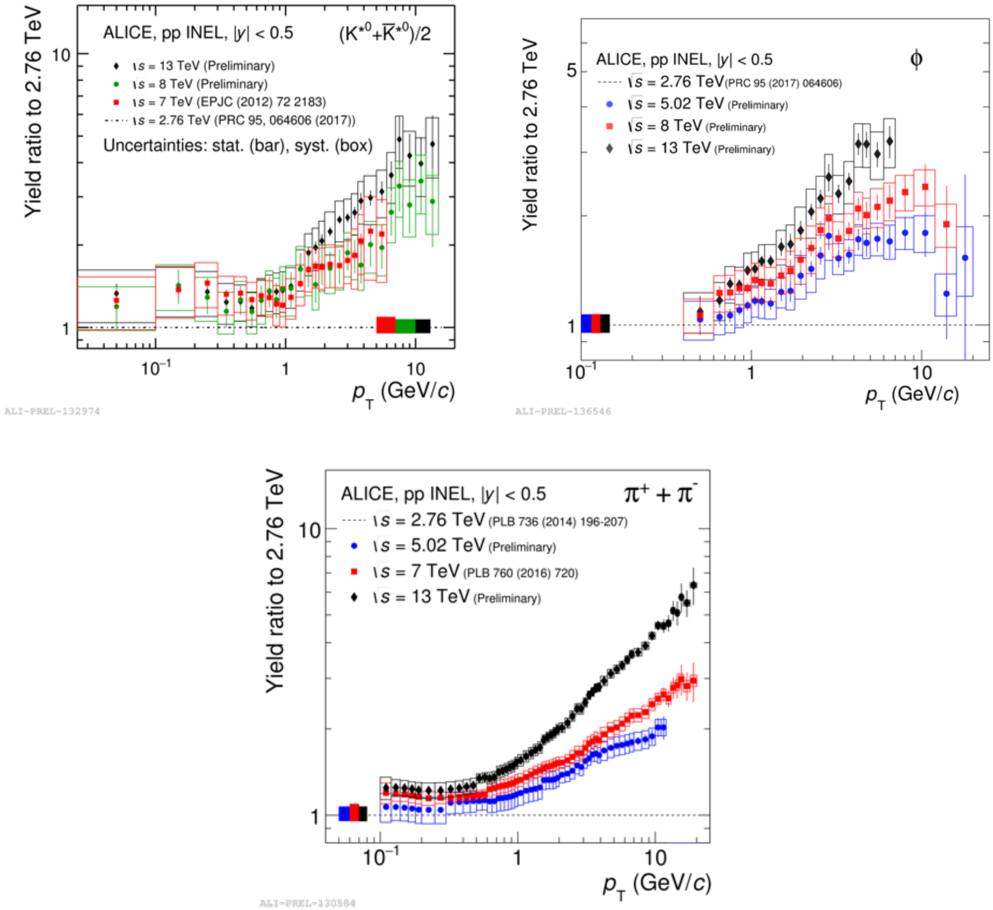

FIGURE 7.4: Ratios of transverse momentum spectra of K^{*0}, ϕ, and π in inelastic pp collisions at $\sqrt{s}$ = 5.02, 7, 8, and 13 TeV to 2.76 TeV (130)

the systematics, same values as for $K^{*\pm}$ are used for both mesons separately. Acceptance × efficiency for K^{*+} and K^{*-} have been estimated using PYTHIA8 -Monash 2013 event generator. Similar distributions have been estimated (see Figure 7.9). In the Figure 7.10, the p_T spectra of K^{*+} and K^{*-} measured in pp collisions at 13 TeV are shown. They are equal within estimated uncertainties for positive and negative resonances. However, a p_T dependent ratio was observed for the charged K* generated from PYTHIA6 - Perugia 2011(see Figure 7.11). However no such ratio was observed for PYTHIA8 - Monash 2013 (see Figure 7.11). Origin of this discrepancy is not well understood. It could be for example connected to a different implementation of Colour Reconnection in the two models.

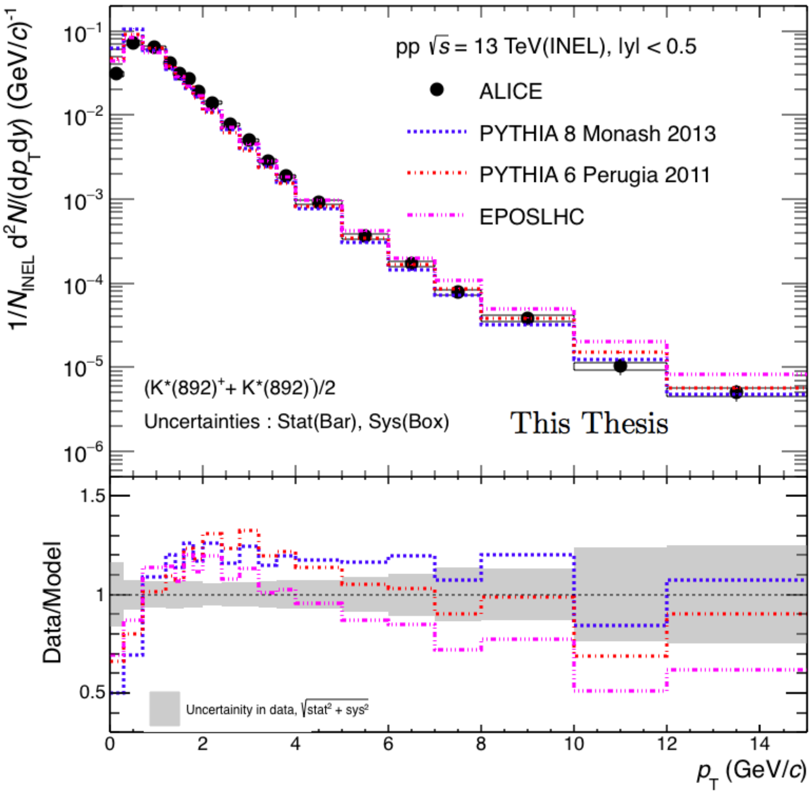

FIGURE 7.5: K*(892)$^{\pm}$ inelastic $p_{\rm T}$ spectrum for pp collisions at $\sqrt{s}$ = 13 TeV compared with the $p_{\rm T}$ spectrum predicted by PYTHIA8 - Monash 2013 (blue lines), PYTHIA 6 - Perugia 2011 (red lines), and EPOS-LHC (magenta lines). In the bottom panel the Data/Model ratios are reported. The gray band shows the fractional uncertainty of the measured data points.

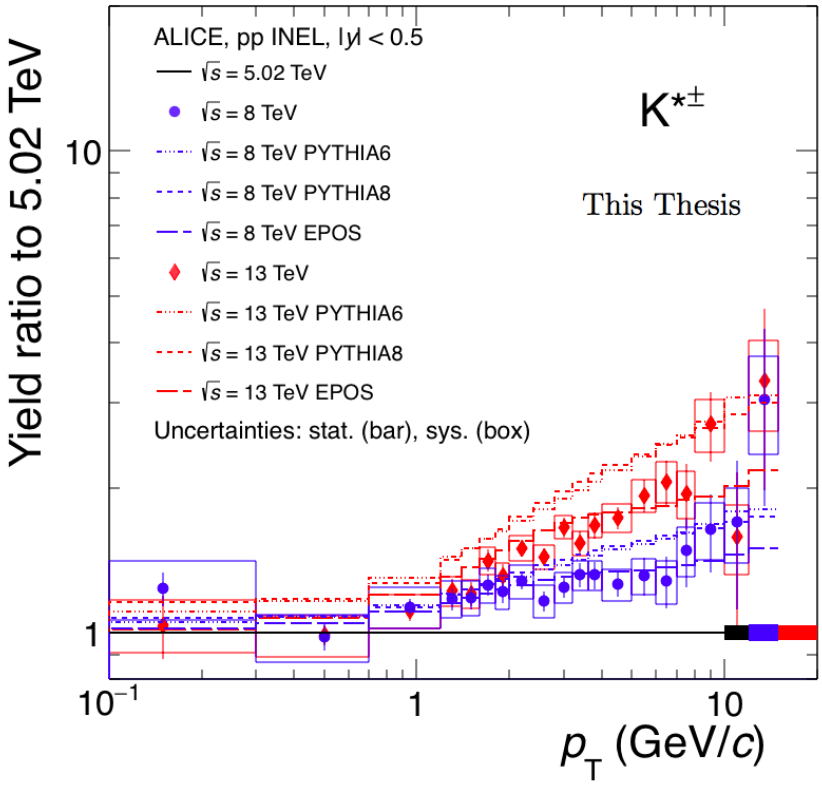

FIGURE 7.6: Ratios of transverse momentum spectra of $K^{*\pm}$ in inelastic pp collisions at $\sqrt{s}$ = 8 and 13 TeV to 5.02 TeV. Predictions from diffferent event generators are reported.

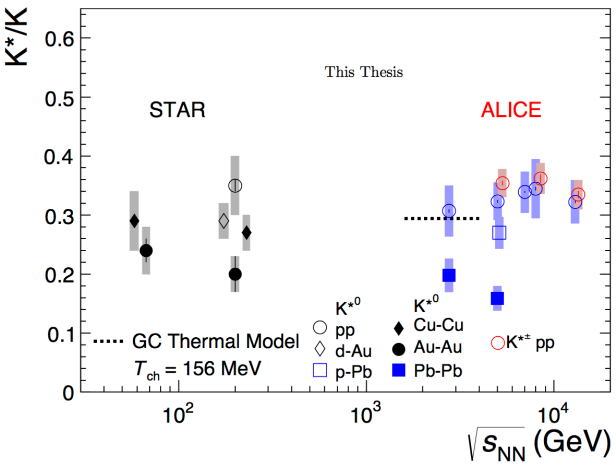

FIGURE 7.7: $K^*(892)^{\pm}/K$ ratio (red circles) for pp collisions at $\sqrt{s}$ = 5.02, 8, and 13 TeV compared with the K^{*0}/K (blue and black symbols) one for different systems and collision energies. The symbols for $K^{*\pm}$ are slightly displaced for readability of the figure

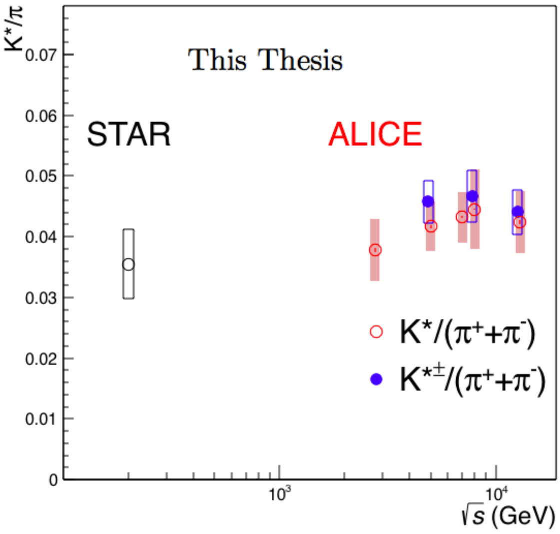

FIGURE 7.8: K*(892)$^{\pm}$/π ratio for pp collisions at $\sqrt{s}$ = 5.02, 8, and 13 TeV compared with the K^{*0}/K one for different systems and collision energies. The symbols for K*(892)$^{\pm}$ are slightly displaced for readability of the figure.

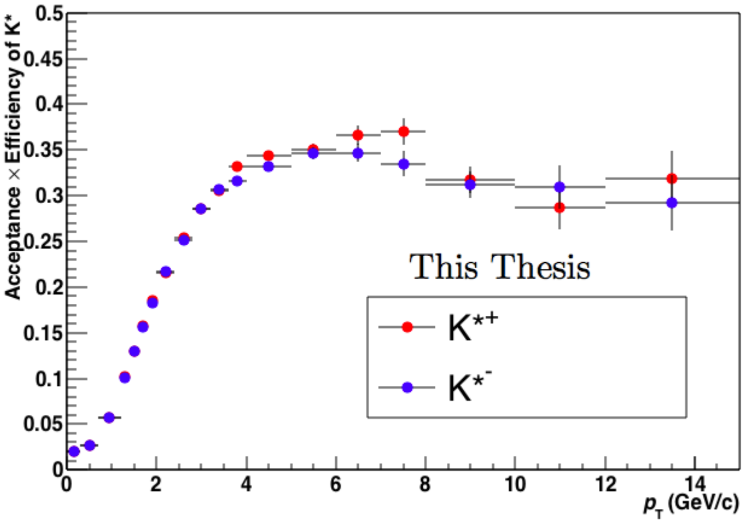

FIGURE 7.9: Acceptance × Efficiency for K^{*+} vs K^{*-}

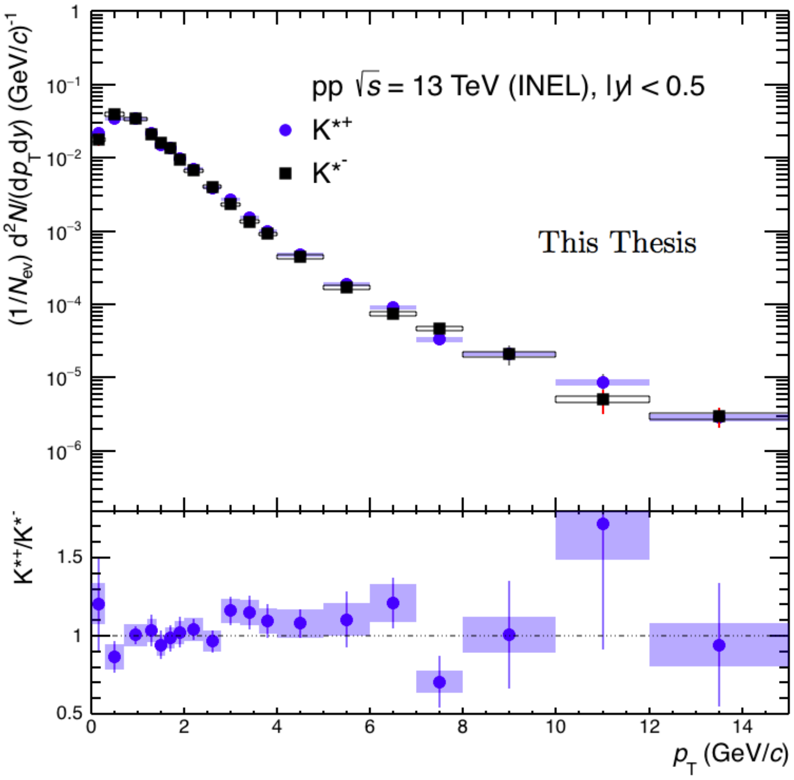

FIGURE 7.10: **Top**: p_T spectrum of K^{*+} (blue circles) and K^{*-} (black squares). Statistical uncertainties are shown as vertical lines and systematic uncertainties as bars. **Bottom**: Ratio of the p_T spectrum K^{*+}/K^{*-}.

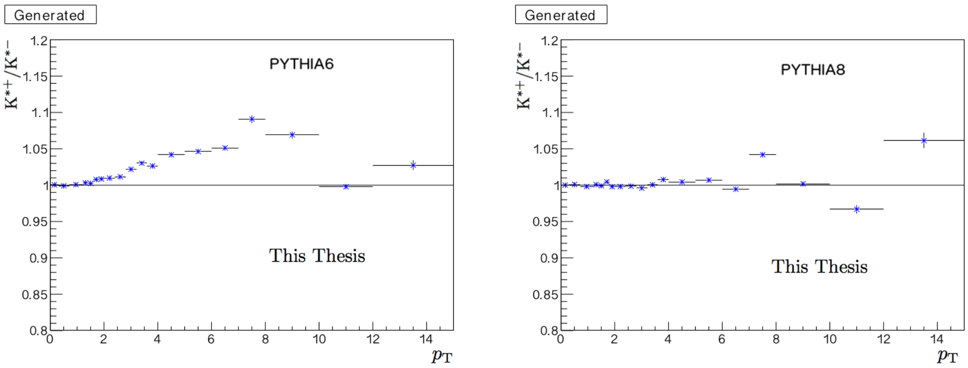

FIGURE 7.11: Ratio of generated K^{*+}/K^{*-} as predicted by PYTHIA6 - Perugia 2011 (left) and PYTHIA8 - Monash 2013 (right) event generator

Chapter 8

Multiplicity dependence of $K^{*\pm}$ production in pp collisions at 13 TeV

As discussed in Section 1.5 and 2.3, recent observations at the LHC have shown striking similarities between Pb-Pb collisions, which are expected to produce a thermally and kinematically equilibrated medium, and high-multiplicity p-Pb and pp collisions. In the elementary collisions a large variation of the characteristics of the event and of the strange particle production rate has been observed as a function of the charged particle multiplicity density. Studies of the resonance yield as a function of the charged particle multiplicity generated in the collision, show that at a given multiplicity, particle production is independent of the system size and collision energy. Moreover a suppression of the $K^{*}(892)^{0}$ production has been shown in high multiplicity pp collisions, which is consistent with the presence of re-scattering effect in an hadronic phase in high multiplicity pp collisions. In the following the measurement of the $K^{*\pm}$ p_{T} spectra as a function of the charged particle multiplicity is discussed.

8.1 K^{*}(892)$^{\pm}$ reconstruction in in different event multiplicity classes

8.1.1 Event, multiplicity, track and V0 selection

The data used in this analysis was collected by ALICE detector during 2016 pp run. About 450 million events were analysed. The used minimum-bias trigger required hits in both V0 arrays, in coincidence with proton bunches arriving from both directions, as for LHC15f period analysed for the measurement of $K^{*}(892)^{\pm}$ and $K^{*}(892)^{0}$ inelastic spectra described in Chapters 5 and 6. Beam-induced background and pile-up events have been removed offline. Moreover primary vertex of the selected events should be located within ±10 cm of the nominal centre of the ALICE detector. The analysed events have been selected by the "INEL > 0" event class, which is defined as the set of inelastic collisions with at least one charged particle in the range $|\eta| < 1$. The INEL > 0 sample is divided into multiplicity classes based on the total charged particle multiplicity measured in both V0 detectors, which is called the "V0M" multiplicity. Thus, the event classes are determined by the multiplicity at forward rapidities, while the K$^{*\pm}$ is measured at mid-rapidity ($|y| < 0.5$). This is to avoid correlations between the resonance yields and the multiplicity estimator. The multiplicity classes 0-1%, 1-5%, 5-10%, 10-20%, 20-30%, 30-40%, 40-50%, 50-70%, and 70-100% have been studied.

The same selection criteria described in Section 5.1.2 have been used for the selection of the primary $\pi^{\pm}$ and K^0_S. Only two cuts are different. The 'ad hoc' p dependent cut used for the identification of the primary particles for LHC15f dataset has been replaced with a standard 3σ cut. For the V0 selection a fixed range of ± 30 MeV/c^2 around the nominal K^0_S mass has been used for the mass tolerance, instead of a p_T dependent value.

8.2 Yield Estimation

Signal extraction and raw estimation procedure are equal to the one used for inelastic p_T spectrum measure which are discussed in Chapter 4. p_T distributions of the raw yield obtained for the different multiplicity classes are shown in Figure 8.1.

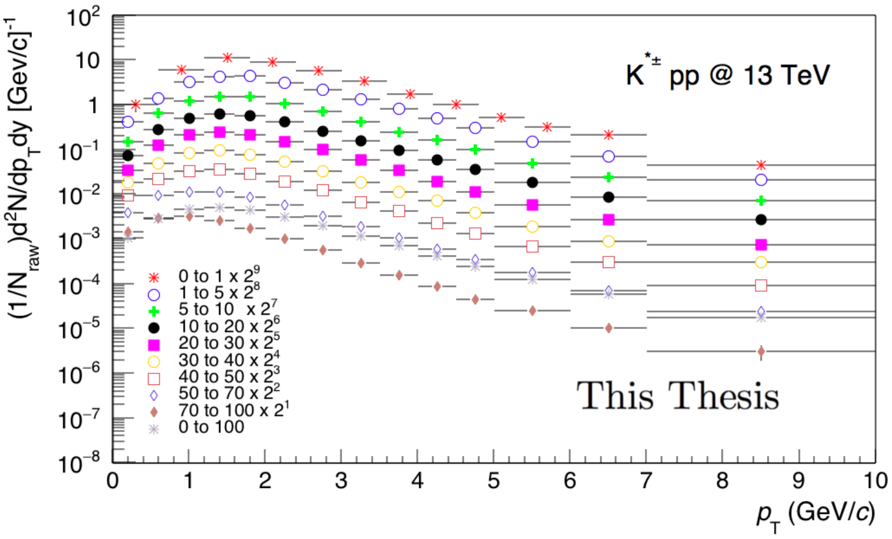

FIGURE 8.1: Raw p_T spectra for K$^{*\pm}$ in different charged multiplicity bins in pp collisions at $\sqrt{s}$ =13 TeV

Detector acceptance × efficiency p_T distribution for various multiplicity has been estimated using PYTHIA8 Monte Carlo generator. Acceptance × efficiency has been estimated for each multiplicity bin individually but no multiplicity dependence has been observed (see Figure 8.2), so the efficiency estimated in the 0-100% multiplicity bin has been used for all multiplicity bins. The efficiency for 0-100% multiplicity bin in pp collisions at 13 TeV is shown in Figure 8.3.

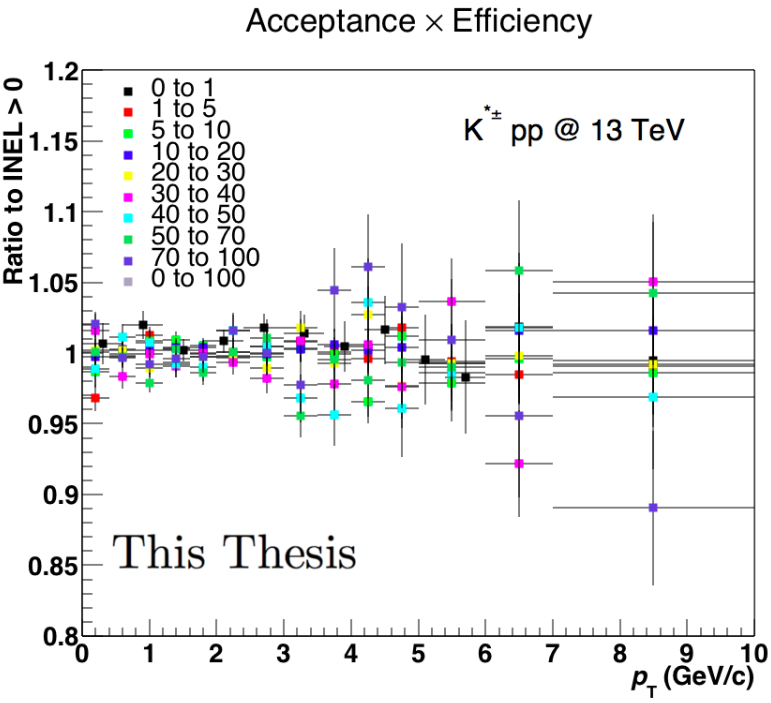

FIGURE 8.2: Ratio of acceptance × efficiency distributions in various multiplicity bins compared to the acceptance × efficiency distribution in INEL > 0 pp collisions at 13 TeV

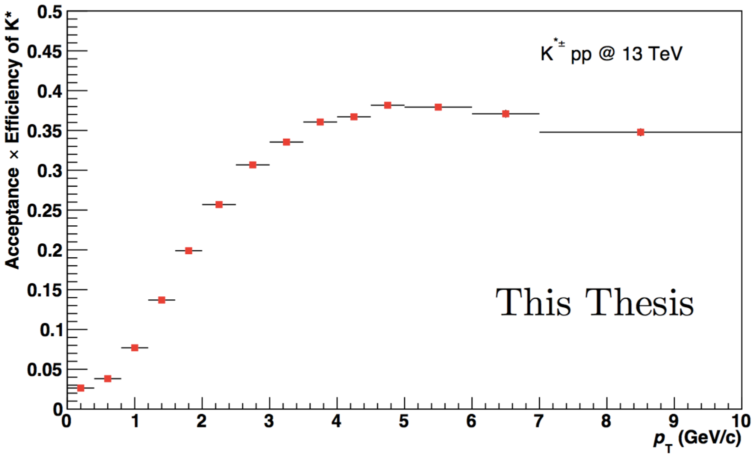

FIGURE 8.3: K$^{*\pm}$ Acceptance × efficiency in INEL > 0 (0-100%) pp collisions at 13 TeV

The yield has been estimated by the following formula:

$$\frac{d^2N}{dp_T dy} = \frac{\text{RawCounts}}{N_{evt} \times BR \times \Delta p_T \times \Delta y} \frac{1}{\epsilon_{rec}} \times f_{norm} \times f_{SL} \tag{8.1}$$

where ϵ_{rec} is the acceptance × efficiency of the detector, f_{norm} (see Table 8.1) is applied in order to normalise to the true number of INEL > 0 pp collisions in

TABLE 8.1: Correction factor (f_{Norm}) for event normalisation in each charged particle multiplicity class

centrality (%)	f_{Norm}
0-1	0.9825
1-5	0.999
5-10	0.9982
10-20	0.9978
20-30	0.9937
30-40	0.9870
40-50	0.9761
50-70	0.9491
70-100	0.8729
0-100	0.9468

the given multiplicity class, and f_{SL} is applied to account the signal loss due to trigger and event selection cuts.

Signal loss corrections (f_{SL}) are calculated as discussed in Chapter 5.2.2 and are shown for various multiplicity classes in the Figure 8.4. As a raw estimation of the expected total systematic uncertainties the ones estimated for the inelastic K$^{*\pm}$ spectrum have been used.

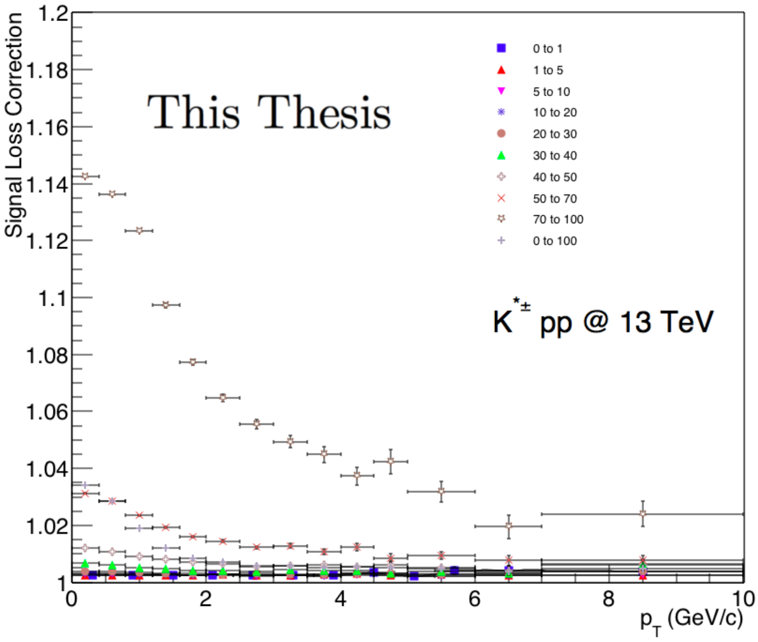

FIGURE 8.4: Signal Loss correction for K$^{*\pm}$ for different multiplicity bins in pp collisions at 13 TeV

8.3 Results for K$^{*\pm}$ production in different charged particle multiplicity classes

In Figure 8.5, the K$^{*\pm}$ p_T spectra estimated for the different charged particle multiplicity classes are shown. The ratios of the K$^{*\pm}$ spectrum with the K^{*0} ones obtained in the same collision and multiplicity bins are shown in Figures 8.6. The shape of the p_T distributions of the two mesons are equal. Also the obtained yields, are rather equal inside the estimated uncertainty.

The modifications of the p_T spectra with the event multiplicity are checked from the ratios of each individual p_T spectrum to the inclusive INEL > 0 spectrum (Figure 8.7). For $p_T < 4$ GeV/c the hardening of the p_T spectra from low to high multiplicity is clearly visible. For higher p_T, the spectra in different multiplicity classes all have the same shape, indicating the processes that change the shape of the p_T spectra in different multiplicity classes are dominant at low p_T. Similar results were reported for K^{*0} (see Figure 8.8), ϕ, K^0_S, Λ, Ξ, and Ω in the same collision system at $\sqrt{s}$ = 7 and 13 TeV (54; 91).

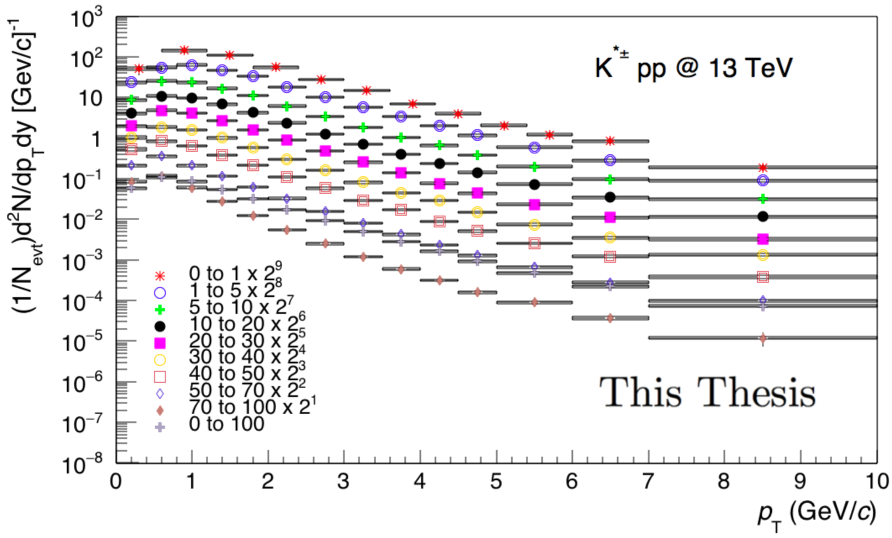

FIGURE 8.5: p_T spectrum for K$^{*\pm}$ in different charged particle mulplicity classes in pp collisions at $\sqrt{s}$ =13 TeV

As described in Chapter5, the p_T spectra have been integrated and fitted with Levy-Tsallis function to obtain the dN/dy and the mean p_T at the different charged particle multiplicity classes. In Figure 8.9, they are reported as a function of charged particle multiplicity density estimated by the average $dN_{ch}/d\eta$ in $|\eta| < 0.5$. Yield and mean p_T increase with the increase of the event multiplicity, confirming that the production of the particles depend mainly from the multiplicity of the collision that from the collision system or energy.

The ratios of p_T-integrated particle yields K$^{*\pm}$/K and K^{*0}/K are shown in Figure 8.10 as function of the charged particle multiplicity density. Within their uncertainties the ratios of charged and neutral K* are equal. It is interesting to

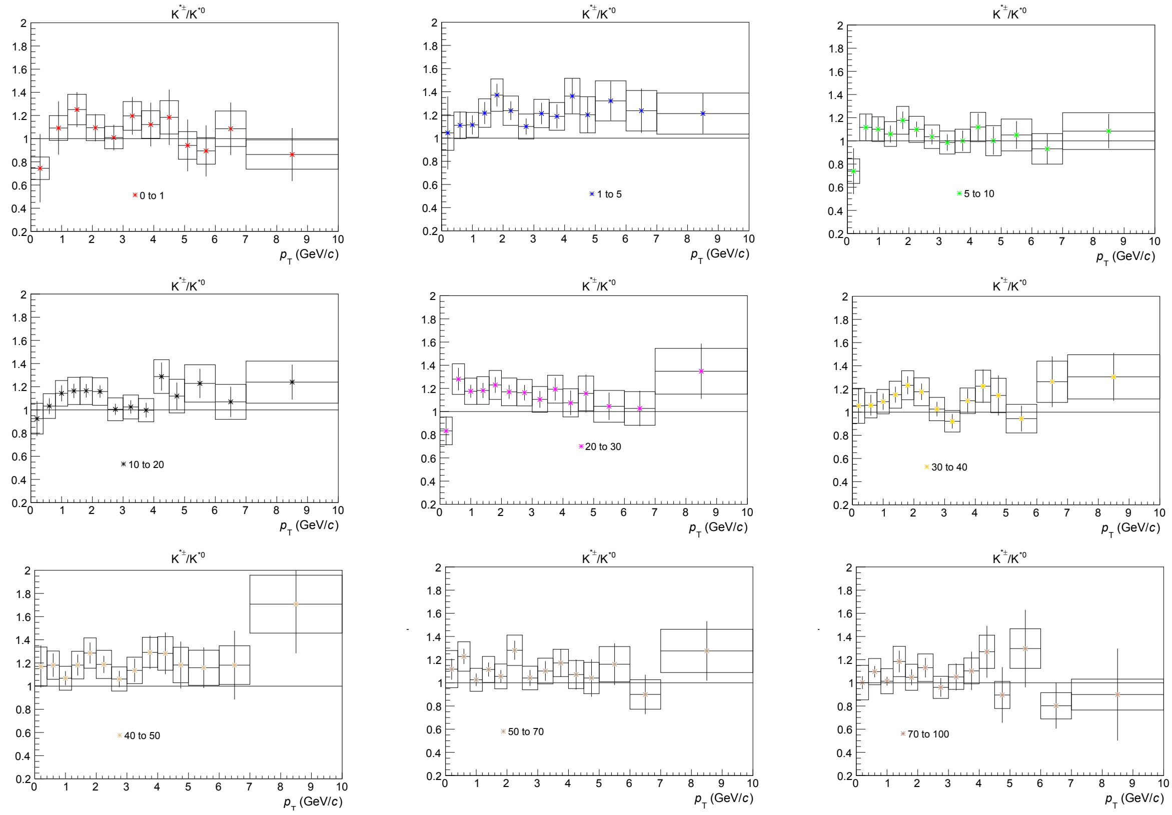

FIGURE 8.6: Ratio of $K^{*\pm}$ to K^{*0} p_T spectra in the same charged particle multiplicity classes

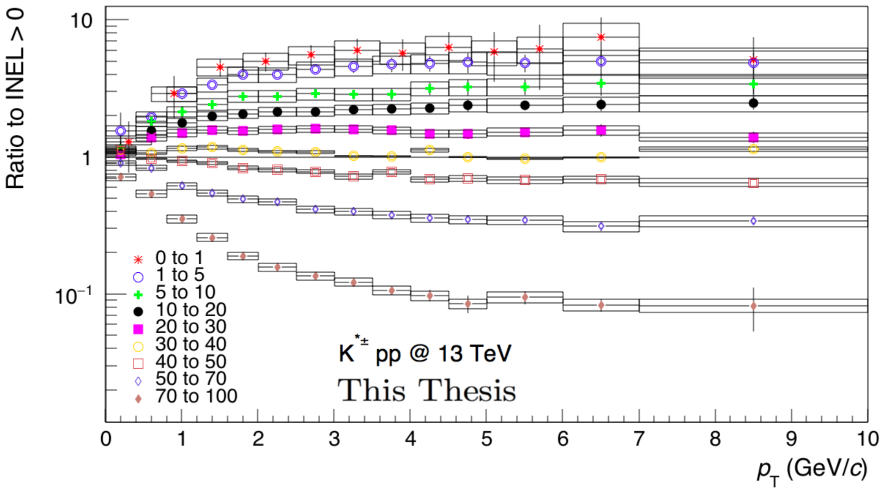

FIGURE 8.7: Ratios of the $K^{*\pm}$ p_T spectra in different charged particle multiplicity classes to the full INEL > 0 spectrum in pp collisions at $\sqrt{s}$ = 13 TeV

see that $K^{*\pm}/K$ decrease with increasing event multiplicity. As discussed in Section 2.2, a decrease in K^{*0}/K in central Pb-Pb collisions is due to the presence of a large rescattering in the hadronic phase of the resonance decay products.

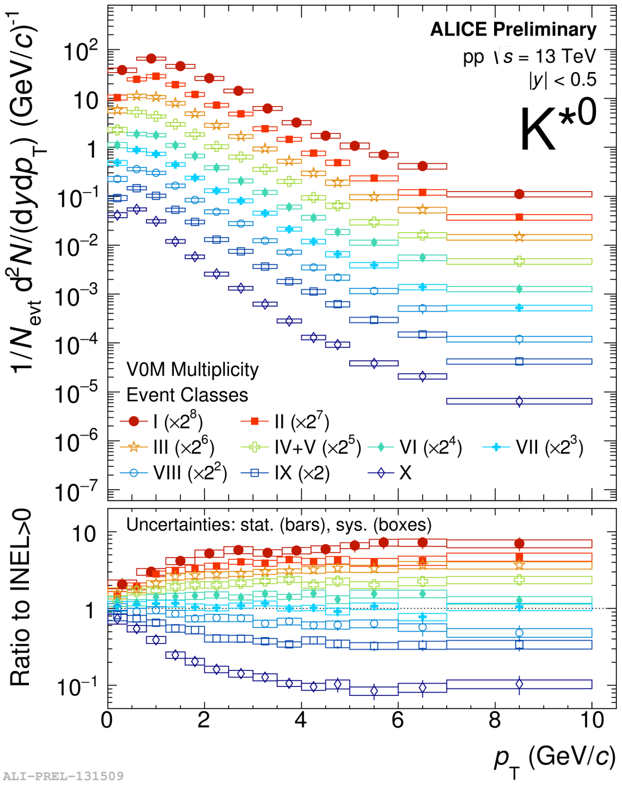

FIGURE 8.8: (Top) p_T spectra of K^{*0} mesons in pp collisions at 13 TeV in V0M multiplicity event classes. (Bottom) Also shown are the ratios of these p_T spectra to the full 0-100% (INEL $>$ 0) p_T spectrum.

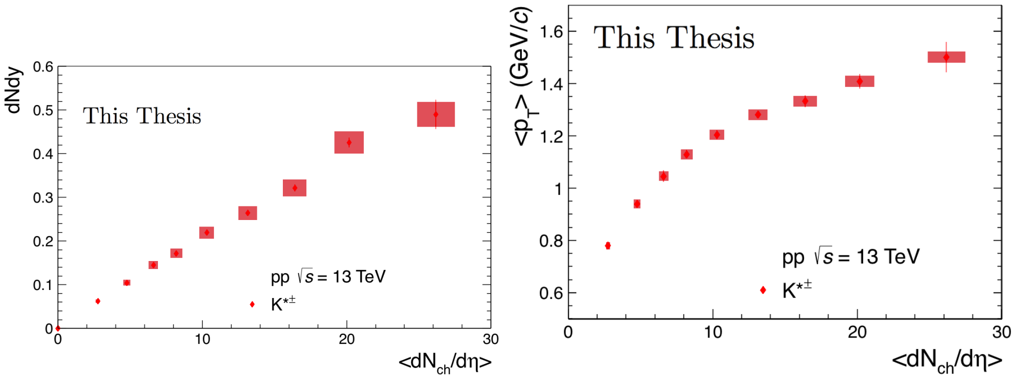

FIGURE 8.9: (Left) dN/dy and (Right) $\langle p_T \rangle$ as a function of charged particle multiplicity density for K$^{*\pm}$ in pp collisions at 13 TeV

Then this apparent multiplicity dependent suppression of the K$^{*\pm}$/K ratio confirms the trends shown in Figure 2.15 for K^{*0}/K ratio in pp and p-Pb collisions, and could indicate the presence of a hadron-gas phase with non-zero lifetime in high-multiplicity pp collisions at $\sqrt{s} = 13$ TeV.

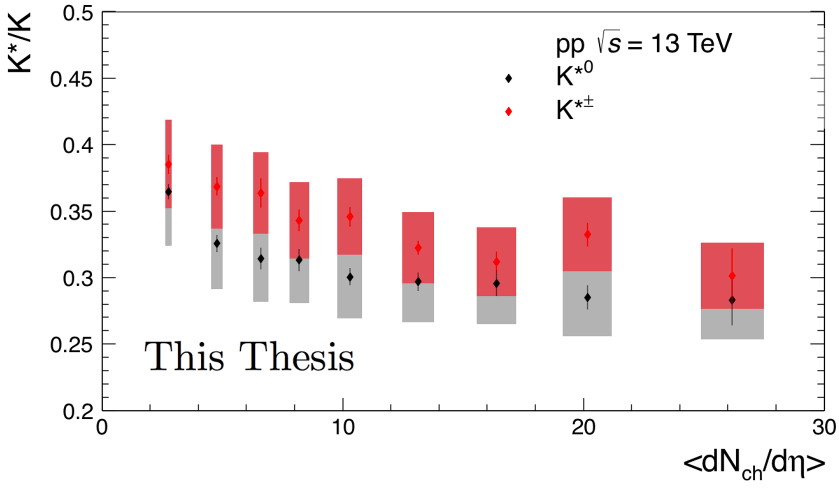

FIGURE 8.10: K$^{*\pm}$/K and K^{*0}/K ratio as a function of charged particle multiplicity density in pp collisions at $\sqrt{s}$ =13 TeV

Conclusions

In this thesis, the production of $K^*(892)^\pm$ resonance has been studied in mid-rapidity ($|y| \leq 0.5$) pp collisions at 13 TeV centre-of-mass energy. This is the first measurement of $K^*(892)^\pm$ resonance at the LHC. $K^{*\pm}$ yield has been measured by the ALICE detector both in inelastic collisions and as a function of the event charged multiplicity and then new codes and analysis procedures have been developed for this analysis and implemented in the AliROOT package. $K^*(892)^0$ has also been studied at 13 TeV pp collisions, to test the analysis procedure as well as compare $K^{*\pm}$ since both resonances have similar mass and quark content. This analysis exploits the extensive particle identification (PID) capabilities of the ALICE detectors, in particular it uses the Time Projection Chamber (TPC) and Time of Flight (TOF). This measurement of a strange resonance production in pp collisions helps in understanding the hadronic production processes, and constraining the theoretical models, and the QCD inspired event generators. Short-lived resonances are good probes to characterise the fireball formed in heavy-ion collisions. This measurement in pp collision is an important reference for the future studies of $K^{*\pm}$ production in Pb-Pb collisions. The reported measurement of the yields as a function of the multiplicity of the pp collisions confirms the peculiarity of the high multiplicity pp collisions, already observed in these last years.
A brief introduction has been given on the ALICE experiment with a special focus on PID through TPC and ALICE tracking capability. A careful description of the charged multiplicity determination in pp collisions with the ALICE detector has been also done. Analysis strategy for K^{*0} and $K^{*\pm}$ has been discussed in detail through its various stages. The signal is extracted via a $\pi^\pm K^\mp$ or $\pi^\pm K^0_S$ invariant mass analysis. The resonance signal appears as a peak sitting on a residual background. After subtraction of the combinatorial background the signal and the residual background are appropriately fitted to extract the raw yields. For $K^{*\pm}$, the correction terms that contribute to the yield estimate have been discussed in detail, as well as the main sources of systematic uncertainty. The sophisticated procedure used to obtain an accurate estimate of the systematic uncertainty due to the selection cuts used for the identification of the particle daughters of the resonance has been clearly described. The transverse momentum spectra of the $K^{*\pm}$ have been reported for minimum bias events in the range $0 < p_T < 15$ GeV/c and as a function of charged particle multiplicity in the range $0 < p_T < 10$ GeV/c. Total yield and the mean p_T have been estimated from these p_T spectra. An extensive study on the properties of $K^{*\pm}$ such as its

mass and width has been performed and reported. The minimum bias results have been approved by the collaboration and presented at various conferences, and these results compared with the ones obtained in pp collisions at 5.02 and 8 TeV should soon be published from the ALICE collaboration.
Thanks to the results of this thesis has been observed as the K$^{*\pm}$ p_T spectrum is equal (within the estimated uncertainties) to the K^{*0}. No difference has been observed between the K^{*+} and K^{*-} p_T spectrum. Ratio of K$^{*\pm}$/K has been found to be equal to the K^{*0}/K ratio and is rather independent from the pp collision energy. The measured K$^{*\pm}$/pion ratio confirms its independence from the collision energy, which suggests no strangeness enhancement in minimum bias pp collision. From the comparison with K$^{*\pm}$ p_T spectrum at lower pp collision energies, it has been observed that for $p_T > 1$ GeV/c the spectra are harder with increasing collision energy, while a constant value is observed for the particles generated in soft interactions. The measured p_T spectrum has been compared with predictions of some events generators, as PYTHIA8 - Monash 2013, PYTHIA6 - Perugia 2011 and EPOS-LHC. None of the three are able to well describe the measured p_T spectrum.
Additionally, production of K$^{*\pm}$ as a function of charged particle multiplicity density in pp collisions at $\sqrt{s}$ = 13 TeV was studied. Yield and mean p_T for K$^{*\pm}$ are found to increase with the increase of the event multiplicity, confirming that the production of the particles depend mainly from the multiplicity of the collision that from the collision system or energy. Ratios of charged and neutral K* to kaons are found to be equal as function of $\langle dN_{ch}/d\eta \rangle$ within uncertainties. It is interesting to see that K$^{*\pm}$/K decrease with increasing multiplicity. As discussed in Chapter 2, a decrease in K^{*0}/K in central Pb-Pb collisions has been attributed to re-scattering of the decay products in the hadronic phase. Then this hint of decrease in high-multiplicity pp collisions could indicate the presence of a hadron-gas phase with non-zero lifetime.

Bibliography

[1] S. Erikson, *Forge of Darkness: Book One of the Kharkanas Trilogy (A Novel of the Malazan Empire)*. The Kharkanas Trilogy. Tom Doherty Associates, 2018. `https://books.google.it/books?id=uySxtAEACAAJ`.

[2] E. Schrödinger, "An undulatory theory of the mechanics of atoms and molecules," *Phys. Rev.* **28** (Dec, 1926) 1049–1070. `https://link.aps.org/doi/10.1103/PhysRev.28.1049`.

[3] **UA1** Collaboration, G. Arnison *et al.*, "Experimental Observation of Isolated Large Transverse Energy Electrons with Associated Missing Energy at $\sqrt{S} = 540$-GeV," *Phys. Lett.* **B122** (1983) 103–116.

[4] **D0** Collaboration, S. Abachi *et al.*, "Search for the top quark in $p\bar{p}$ collisions at $\sqrt{s} = 1.8$ TeV," *Phys. Rev. Lett.* **72** (1994) 2138–2142.

[5] M. L. Perl and A. et. al., "Evidence for anomalous lepton production in $e^{+} - e^{-}$ annihilation," *Phys. Rev. Lett.* **35** (Dec, 1975) 1489–1492. `https://link.aps.org/doi/10.1103/PhysRevLett.35.1489`.

[6] **CMS** Collaboration, S. Chatrchyan *et al.*, "Observation of a new boson at a mass of 125 GeV with the CMS experiment at the LHC," 2012.

[7] "The existence of a neutron," *Proceedings of the Royal Society of London A: Mathematical, Physical and Engineering Sciences* **136** no. 830, (1932) 692–708, `http://rspa.royalsocietypublishing.org/content/136/830/692.full.pdf`. `http://rspa.royalsocietypublishing.org/content/136/830/692`.

[8] D. H. PERKINS, "Nuclear disintegration by meson capture," *Nature* **159** (01, 1947) 126 EP –. `https://doi.org/10.1038/159126a0`.

[9] P. Braun-Munzinger, "Chemical equilibration and the hadron QGP phase transition," *Nucl. Phys.* **A681** (2001) 119–123, `arXiv:nucl-ex/0007021 [nucl-ex]`.

[10] F. Karsch and E. Laermann, "Thermodynamics and in medium hadron properties from lattice QCD," `arXiv:hep-lat/0305025 [hep-lat]`.

[11] K. Johnson, "The M.I.T. Bag Model," *Acta Phys. Polon.* **B6** (1975) 865.

[12] U. W. Heinz, "Concepts of heavy ion physics," in *2002 European School of high-energy physics, Pylos, Greece, 25 Aug-7 Sep 2002: Proceedings*, pp. 165–238. 2004. `arXiv:hep-ph/0407360 [hep-ph]`. `http://doc.cern.ch/yellowrep/CERN-2004-001`.

[13] K. Urmossy and T. S. Biro, "Cooper-Frye Formula and Non-extensive Coalescence at RHIC Energy," *Phys. Lett.* **B689** (2010) 14–17, `arXiv:0911.1411 [hep-ph]`.

[14] D. Molnar and M. Gyulassy, "Saturation of elliptic flow and the transport opacity of the gluon plasma at RHIC," *Nucl. Phys.* **A697** (2002) 495–520, `arXiv:nucl-th/0104073 [nucl-th]`. [Erratum: Nucl. Phys.A703,893(2002)].

[15] B. Betz, "Jet Quenching in Heavy-Ion Collisions - The Transition Era from RHIC to LHC," *Eur. Phys. J.* **A48** (2012) 164, `arXiv:1211.5897 [nucl-th]`.

[16] M. L. Miller, K. Reygers, S. J. Sanders, and P. Steinberg, "Glauber modeling in high energy nuclear collisions," *Ann. Rev. Nucl. Part. Sci.* **57** (2007) 205–243, `arXiv:nucl-ex/0701025 [nucl-ex]`.

[17] **ALICE Collaboration** Collaboration, B. A. et al., "Pion, kaon, and proton production in central pb-pb collisions at $\sqrt{s_{\rm NN}}$=2.76 TeV," *Phys. Rev. Lett.* **109** (Dec, 2012) 252301. `https://link.aps.org/doi/10.1103/PhysRevLett.109.252301`.

[18] B. Muller, J. Schukraft, and B. Wyslouch, "First Results from Pb+Pb collisions at the LHC," *Ann. Rev. Nucl. Part. Sci.* **62** (2012) 361–386, `arXiv:1202.3233 [hep-ex]`.

[19] A. Andronic, P. Braun-Munzinger, K. Redlich, and J. Stachel, "The statistical model in Pb-Pb collisions at the LHC," *Nucl. Phys.* **A904-905** (2013) 535c–538c, `arXiv:1210.7724 [nucl-th]`.

[20] P. Huovinen and P. V. Ruuskanen, "Hydrodynamic Models for Heavy Ion Collisions," *Ann. Rev. Nucl. Part. Sci.* **56** (2006) 163–206, `arXiv:nucl-th/0605008 [nucl-th]`.

[21] E. Schnedermann, J. Sollfrank, and U. Heinz, "Thermal phenomenology of hadrons from 200A GeV S+S collisions," Nov, 1993. `https://link.aps.org/doi/10.1103/PhysRevC.48.2462`.

[22] **STAR** Collaboration, B. I. Abelev *et al.*, "Systematic Measurements of Identified Particle Spectra in pp, d^+ Au and Au+Au Collisions from STAR," *Phys. Rev.* **C79** (2009) 034909, `arXiv:0808.2041 [nucl-ex]`.

[23] **ALICE** Collaboration, N. Jacazio, "Measuring hydrodynamical expansion via the production of identified hadrons in Pb−Pb collisions with ALICE," in *53rd Rencontres de Moriond on QCD and High Energy Interactions (Moriond QCD 2018) La Thuile, Italy, March 17-24, 2018*. 2018. `arXiv:1806.07617 [nucl-ex]`.

[24] "On the theory of quantum mechanics," *Proceedings of the Royal Society of London A: Mathematical, Physical and Engineering Sciences* **112** no. 762, (1926) 661–677, `http://rspa.royalsocietypublishing.org/content/112/762/661.full.pdf`. `http://rspa.royalsocietypublishing.org/content/112/762/661`.

[25] R. Hagedorn, "Statistical thermodynamics of strong interactions at high energies," *Nuovo Cimento, Suppl.* **3** no. CERN-TH-520, (1965) 147–186. `http://cds.cern.ch/record/346206`.

[26] P. Braun-Munzinger, K. Redlich, and J. Stachel, "Particle production in heavy ion collisions," `arXiv:nucl-th/0304013 [nucl-th]`.

[27] F. Becattini, "An Introduction to the Statistical Hadronization Model," in *International School on Quark-Gluon Plasma and Heavy Ion Collisions: past, present, future Villa Gualino, Torino, Italy, December 8-14, 2008*. 2009. `arXiv:0901.3643 [hep-ph]`.

[28] A. Andronic, P. Braun-Munzinger, and J. Stachel, "Hadron production in central nucleus-nucleus collisions at chemical freeze-out," *Nucl. Phys.* **A772** (2006) 167–199, `arXiv:nucl-th/0511071 [nucl-th]`.

[29] D. D. Chinellato and the Alice Collaboration, "Strangeness production at lhc energies as measured with alice," *Journal of Physics: Conference Series* **556** no. 1, (2014) 012010. `http://stacks.iop.org/1742-6596/556/i=1/a=012010`.

[30] A. K. (on behalf of ALICE collaboration), "Highlights from ALICE." Quark Matter, Venice, 2018.

[31] S. Hamieh, K. Redlich, and A. Tounsi, "Canonical description of strangeness enhancement from p-A to Pb Pb collisions," *Phys. Lett.* **B486** (2000) 61–66, `arXiv:hep-ph/0006024 [hep-ph]`.

[32] J. Rafelski and B. Müller, "Strangeness production in the quark-gluon plasma," *Phys. Rev. Lett.* **48** (Apr, 1982) 1066–1069. `https://link.aps.org/doi/10.1103/PhysRevLett.48.1066`.

[33] J. Rafelski, "Strangeness production in the quark gluon plasma,". `http://cds.cern.ch/record/147788`.

[34] P. Koch, B. Muller, and J. Rafelski, "Strangeness in Relativistic Heavy Ion Collisions," *Phys. Rept.* **142** (1986) 167–262.

[35] **NA57** Collaboration, F. Antinori *et al.*, "Enhancement of hyperon production at central rapidity in 158-A-GeV/c Pb-Pb collisions," *J. Phys.* **G32** (2006) 427–442, `arXiv:nucl-ex/0601021 [nucl-ex]`.

[36] **NA57** Collaboration, F. Antinori *et al.*, "Strangeness enhancements at central rapidity in 40 A GeV/c Pb-Pb collisions," *J. Phys.* **G37** (2010) 045105, `arXiv:1001.1884 [nucl-ex]`.

[37] **STAR** Collaboration, B. I. Abelev *et al.*, "Enhanced strange baryon production in Au + Au collisions compared to p + p at $\sqrt{s_{\mathrm{NN}}} = 200$-GeV," *Phys. Rev.* **C77** (2008) 044908, `arXiv:0705.2511 [nucl-ex]`.

[38] **ALICE** Collaboration, B. B. Abelev *et al.*, “Multi-strange baryon production at mid-rapidity in Pb-Pb collisions at $\sqrt{s_{NN}}$ = 2.76 TeV,” *Phys. Lett.* **B728** (2014) 216–227, `arXiv:1307.5543 [nucl-ex]`. [Erratum: Phys. Lett.B734,409(2014)].

[39] A. Tounsi and K. Redlich, “Strangeness enhancement and canonical suppression,” `arXiv:hep-ph/0111159 [hep-ph]`.

[40] A. Andronic, P. Braun-Munzinger, and J. Stachel, “Thermal hadron production in relativistic nuclear collisions: The Hadron mass spectrum, the horn, and the QCD phase transition,” *Phys. Lett.* **B673** (2009) 142–145, `arXiv:0812.1186 [nucl-th]`. [Erratum: Phys. Lett.B678,516(2009)].

[41] J. Cleymans, I. Kraus, H. Oeschler, K. Redlich, and S. Wheaton, “Statistical model predictions for particle ratios at $\sqrt{s_{NN}} = 5.5$ tev,” *Phys. Rev. C* **74** (Sep, 2006) 034903. `https://link.aps.org/doi/10.1103/PhysRevC.74.034903`.

[42] **STAR Collaboration and STAR-RICH Collaboration** Collaboration, J. e. a. Adams, “Azimuthal anisotropy in au+au collisions at $\sqrt{s_{NN}} = 200$ GeV,” *Phys. Rev. C* **72** (Jul, 2005) 014904. `https://link.aps.org/doi/10.1103/PhysRevC.72.014904`.

[43] **ALICE Collaboration** Collaboration, K. e. a. Aamodt, “Elliptic flow of charged particles in pb-pb collisions at $\sqrt{s_{NN}} = 2.76\ \ \text{TeV}$,” *Phys. Rev. Lett.* **105** (Dec, 2010) 252302. `https://link.aps.org/doi/10.1103/PhysRevLett.105.252302`.

[44] **STAR Collaboration** Collaboration, A. et. al., “Elliptic flow in $au + au$ collisions at $\sqrt{s_{\mathrm{nn}}} = 130$GeV,” *Phys. Rev. Lett.* **86** (Jan, 2001) 402–407. `https://link.aps.org/doi/10.1103/PhysRevLett.86.402`.

[45] **PHENIX Collaboration** Collaboration, S. S. e. a. Adler, “Elliptic flow of identified hadrons in Au + Au collisions at $\sqrt{s_{NN}} = 200\ \ \text{GeV}$,” *Phys. Rev. Lett.* **91** (Oct, 2003) 182301. `https://link.aps.org/doi/10.1103/PhysRevLett.91.182301`.

[46] **CMS** Collaboration, V. Khachatryan *et al.*, “Observation of Long-Range Near-Side Angular Correlations in Proton-Proton Collisions at the LHC,” 2010.

[47] W. Li, “Observation of a ’Ridge’ correlation structure in high multiplicity proton-proton collisions: A brief review,” *Mod. Phys. Lett.* **A27** (2012) 1230018, `arXiv:1206.0148 [nucl-ex]`.

[48] **PHOBOS** Collaboration, B. Alver *et al.*, “System size dependence of cluster properties from two-particle angular correlations in Cu+Cu and Au+Au collisions at s(NN)**(1/2) = 200-GeV,” *Phys. Rev.* **C81** (2010) 024904, `arXiv:0812.1172 [nucl-ex]`.

[49] J.-Y. Ollitrault, "Anisotropy as a signature of transverse collective flow," *Phys. Rev. D* **46** (Jul, 1992) 229–245. `https://link.aps.org/doi/10.1103/PhysRevD.46.229`.

[50] **CMS** Collaboration, S. Chatrchyan *et al.*, "Observation of long-range near-side angular correlations in proton-lead collisions at the LHC," *Phys. Lett.* **B718** (2013) 795–814, `arXiv:1210.5482 [nucl-ex]`.

[51] **ALICE** Collaboration, B. Abelev *et al.*, "Long-range angular correlations on the near and away side in p-Pb collisions at $\sqrt{s_{NN}} = 5.02$ TeV," *Phys. Lett.* **B719** (2013) 29–41, `arXiv:1212.2001 [nucl-ex]`.

[52] **ATLAS** Collaboration, G. Aad *et al.*, "Observation of Associated Near-Side and Away-Side Long-Range Correlations in $\sqrt{s_{NN}}$=5.02??TeV Proton-Lead Collisions with the ATLAS Detector," *Phys. Rev. Lett.* **110** no. 18, (2013) 182302, `arXiv:1212.5198 [hep-ex]`.

[53] **ALICE** Collaboration, B. B. Abelev *et al.*, "Multiplicity Dependence of Pion, Kaon, Proton and Lambda Production in p-Pb Collisions at $\sqrt{s_{NN}} =$ 5.02 TeV," *Phys. Lett.* **B728** (2014) 25–38, `arXiv:1307.6796 [nucl-ex]`.

[54] **ALICE** Collaboration, S. Acharya *et al.*, "Multiplicity dependence of light-flavor hadron production in pp collisions at $\sqrt{s}$ = 7 TeV," *Submitted to: Phys. Rev.* (2018) , `arXiv:1807.11321 [nucl-ex]`.

[55] E. Shuryak and I. Zahed, "High-multiplicity pp and pA collisions: Hydrodynamics at its edge," *Phys. Rev.* **C88** no. 4, (2013) 044915, `arXiv:1301.4470 [hep-ph]`.

[56] S. T. Sjostrand, T. Mrenna and P. Skands, "A brief introduction to PYTHIA 8.1," *Comput. Phys. Commun.* **178** (2008) 852, `arXiv:0710.3820`.

[57] C. Bierlich, G. Gustafson, L. Lönnblad, and A. Tarasov, "Effects of Overlapping Strings in pp Collisions," *JHEP* **03** (2015) 148, `arXiv:1412.6259 [hep-ph]`.

[58] T. Pierog *et al.*, "EPOS LHC: test of collective hadronization with LHC data," `arXiv:1306.0121`.

[59] A. Ortiz Velasquez, P. Christiansen, E. Cuautle Flores, I. Maldonado Cervantes, and G. Pai?, "Color Reconnection and Flowlike Patterns in pp Collisions," *Phys. Rev. Lett.* **111** no. 4, (2013) 042001, `arXiv:1303.6326 [hep-ph]`.

[60] **ALICE** Collaboration, J. Adam *et al.*, "Enhanced production of multi-strange hadrons in high-multiplicity proton-proton collisions," *Nature Phys.* **13** (2017) 535–539, `arXiv:1606.07424 [nucl-ex]`.

[61] K. Redlich and A. Tounsi, "Strangeness enhancement and energy dependence in heavy ion collisions," *Eur. Phys. J. C* **24** no. 4, (2002) 589–594. `https://doi.org/10.1007/s10052-002-0983-1`.

[62] F. Becattini and J. Manninen, "Strangeness production from sps to lhc," *Journal of Physics G: Nuclear and Particle Physics* **35** no. 10, (2008) 104013. `http://stacks.iop.org/0954-3899/35/i=10/a=104013`.

[63] S. T. Sjostrand, T. Mrenna and P. Skands, "PYTHIA 6.4 physics and manual," *J. High Energy Phys.* **05** (2006) 026, `arXiv:0603175`.

[64] S. Höche, "Introduction to parton-shower event generators," in *Proceedings, Theoretical Advanced Study Institute in Elementary Particle Physics: Journeys Through the Precision Frontier: Amplitudes for Colliders (TASI 2014): Boulder, Colorado, June 2-27, 2014*, pp. 235–295. 2015. `arXiv:1411.4085 [hep-ph]`.

[65] B. Andersson, G. Gustafson, G. Ingelman, and T. Sjostrand, "Parton Fragmentation and String Dynamics," *Phys. Rept.* **97** (1983) 31–145.

[66] P. Skands, "Tuning Monte Carlo generators: the Perugia tunes," *Phys. Rev.* **D 82** (2010) 074018, `arXiv:1005.3457`.

[67] S. Skands, P.Z. Carrazza and J. Rojo, "Tuning PYTHIA 8.1: the Monash 2013 tune," *Eur. Phys. J.* **C 74 (8)** (2014) 3024, `arXiv:1404.5630`.

[68] C. A. et al., "A study of the general characteristics of proton-antiproton collisions at âĹŽs=0.2 to 0.9 tev," *Nuclear Physics B* **335** no. 2, (1990) 261 – 287. `http://www.sciencedirect.com/science/article/pii/055032139090493W`.

[69] R. P. Feynman, *The Behavior of Hadron Collisions at Extreme Energies*, pp. 289–304. Springer Netherlands, Dordrecht, 1988. `https://doi.org/10.1007/978-94-009-3051-3_25`.

[70] J. D. Bjorken and E. A. Paschos, "Inelastic electron-proton and γ-proton scattering and the structure of the nucleon," *Phys. Rev.* **185** (Sep, 1969) 1975–1982. `https://link.aps.org/doi/10.1103/PhysRev.185.1975`.

[71] H. J. Drescher, M. Hladik, S. Ostapchenko, T. Pierog, and K. Werner, "Parton based Gribov-Regge theory," *Phys. Rept.* **350** (2001) 93–289, `arXiv:hep-ph/0007198 [hep-ph]`.

[72] K. Werner, B. Guiot, I. Karpenko, and T. Pierog, "A unified description of the reaction dynamics from pp to pA to AA collisions," *Nucl. Phys.* **A931** (2014) 83–91, `arXiv:1411.1048 [nucl-th]`.

[73] A. G. Knospe, C. Markert, K. Werner, J. Steinheimer, and M. Bleicher, "Hadronic resonance production and interaction in partonic and hadronic matter in the EPOS3 model with and without the hadronic afterburner UrQMD," *Phys. Rev.* **C93** no. 1, (2016) 014911, `arXiv:1509.07895 [nucl-th]`.

[74] K. Werner, B. Guiot, I. Karpenko, T. Pierog, G. Sophys, and M. Stefaniak, "System size dependence of particle production in epos," *Journal of*

Physics: Conference Series **1070** no. 1, (2018) 012007. http://stacks.iop.org/1742-6596/1070/i=1/a=012007.

[75] E. L. Bratkovskaya, W. Cassing, V. P. Konchakovski, and O. Linnyk, "Parton-Hadron-String Dynamics at Relativistic Collider Energies," *Nucl. Phys.* **A856** (2011) 162–182, arXiv:1101.5793 [nucl-th].

[76] S. Juchem, W. Cassing, and C. Greiner, "Quantum dynamics and thermalization for out-of-equilibrium phi**4 theory," *Phys. Rev.* **D69** (2004) 025006, arXiv:hep-ph/0307353 [hep-ph].

[77] Bratkovskaya, E.L., Moreau, P., Palmese, A., Cassing, W., Seifert, E., and Steinert, T., "Signatures of chiral symmetry restoration and its survival throughout the hadronic phase interactions," *EPJ Web Conf.* **171** (2018) 02004. https://doi.org/10.1051/epjconf/201817102004.

[78] A. Ilner, D. Cabrera, C. Markert, and E. Bratkovskaya, "K^* vector meson resonances dynamics in heavy-ion collisions," *Phys. Rev.* **C95** no. 1, (2017) 014903, arXiv:1609.02778 [hep-ph].

[79] A. Ilner, J. Blair, D. Cabrera, C. Markert, and E. Bratkovskaya, "Probing the hot and dense nuclear matter with $K^*, \bar{K}^*$ vector mesons," arXiv:1707.00060 [hep-ph].

[80] **ALICE** Collaboration, K. Aamodt *et al.*, "Two-pion Bose-Einstein correlations in central Pb-Pb collisions at $\sqrt{s_{NN}} = 2.76$ TeV," *Phys. Lett.* **B696** (2011) 328–337, arXiv:1012.4035 [nucl-ex].

[81] **Particle Data Group** Collaboration, K. Olive *et al.*, "Review of Particle Physics," *Chin. Phys.* **C38** (2014) 090001.

[82] S. Borsányi, Z. Fodor, C. Hoelbling, S. D. Katz, S. Krieg, C. Ratti, and K. K. Szabó, "Is there still any tcmystery in lattice qcd? results with physical masses in the continuum limit iii," *Journal of High Energy Physics* **2010** no. 9, (Sep, 2010) 73. https://doi.org/10.1007/JHEP09(2010)073.

[83] S. A. Bass *et al.*, "Microscopic models for ultrarelativistic heavy ion collisions," *Prog. Part. Nucl. Phys.* **41** (1998) 255–369, arXiv:nucl-th/9803035 [nucl-th]. [Prog. Part. Nucl. Phys.41,225(1998)].

[84] S. A. Bass, A. Dumitru, M. Bleicher, L. Bravina, E. Zabrodin, H. Stöcker, and W. Greiner, "Hadronic freeze-out following a first order hadronization phase transition in ultrarelativistic heavy-ion collisions," *Phys. Rev. C* **60** (Jul, 1999) 021902. https://link.aps.org/doi/10.1103/PhysRevC.60.021902.

[85] C. Markert, R. Bellwied, and I. Vitev, "Formation and decay of hadronic resonances in the QGP," *Phys. Lett.* **B669** (2008) 92–97, arXiv:0807.1509 [nucl-th].

[86] **ALICE** Collaboration, S. Acharya *et al.*, "Production of the $\rho(770)^0$ meson in pp and Pb-Pb collisions at $\sqrt{s_{\mathrm{NN}}}$ = 2.76 TeV," `arXiv:1805.04365 [nucl-ex]`.

[87] **ALICE Collaboration** Collaboration, J. e. a. Adam, "$K^*(892)^0$ and $\phi(1020)$ meson production at high transverse momentum in pp and pb-pb collisions at $\sqrt{s_{NN}} = 2.76$ tev," *Phys. Rev. C* **95** (Jun, 2017) 064606. `https://link.aps.org/doi/10.1103/PhysRevC.95.064606`.

[88] A. K. (on behalf of ALICE collaboration), "Energy and centrality dependence of resonance production in heavy-ion collisions at the LHC." Quark Matter, Venice, 2018.

[89] **STAR** Collaboration, B. I. Abelev *et al.*, "Hadronic resonance production in d+Au collisions at $\sqrt{s_{\mathrm{NN}}}$ = 200-GeV at RHIC," *Phys. Rev.* **C78** (2008) 044906, `arXiv:0801.0450 [nucl-ex]`.

[90] A. Collaboration, "Production of $\sigma(1385)^{\pm}$ and $\xi(1530)^0$ in p-pb collisions at $\sqrt{s_{\mathrm{nn}}}$ = 5.02 tev," *The European Physical Journal C* **77** no. 6, (Jun, 2017) 389. `https://doi.org/10.1140/epjc/s10052-017-4943-1`.

[91] **ALICE** Collaboration, A. K. Dash, "Multiplicity dependence of strangeness and hadronic resonance production in pp and p-Pb collisions with ALICE at the LHC," in *27th International Conference on Ultrarelativistic Nucleus-Nucleus Collisions (Quark Matter 2018) Venice, Italy, May 14-19, 2018*. 2018. `arXiv:1807.07469 [hep-ex]`.

[92] **ALICE** Collaboration, B. Abelev *et al.*, "Production of $K^*(892)^0$ and $\phi(1020)$ in pp collisions at $\sqrt{s} = 7$ TeV," *Eur. Phys. J.* **C72** (2012) 2183, `arXiv:1208.5717 [hep-ex]`.

[93] **ALICE** Collaboration, B. B. Abelev *et al.*, "Production of $\Sigma(1385)^{\pm}$ and $\Xi(1530)^0$ in proton-proton collisions at $\sqrt{s} = 7$ TeV," *Eur. Phys. J.* **C75** no. 1, (2015) 1, `arXiv:1406.3206 [nucl-ex]`.

[94] F. W. Bopp, R. Engel, and J. Ranft, "Rapidity gaps and the PHOJET Monte Carlo," in *High energy physics. Proceedings, LAFEX International School, Session C, Workshop on Diffractive Physics, LISHEP'98, Rio de Janeiro, Brazil, February 16-20, 1998*, pp. 729–741. 1998. `arXiv:hep-ph/9803437 [hep-ph]`.

[95] Celeste Fionda, Fiorella Maria, "Energy and multiplicity dependence of strange and non-strange particle production in proton-proton collisions at the lhc with alice," *EPJ Web Conf.* **171** (2018) 19004. `https://doi.org/10.1051/epjconf/201817119004`.

[96] **ALICE** Collaboration, J. Adam *et al.*, "Production of K* $(892)^0$ and ϕ (1020) in p-Pb collisions at $\sqrt{s_{\mathrm{NN}}}$ = 5.02 TeV," *Eur. Phys. J.* **C76** no. 5, (2016) 245, `arXiv:1601.07868 [nucl-ex]`.

[97] C. Shen, U. Heinz, P. Huovinen, and H. Song, "Radial and elliptic flow in Pb+Pb collisions at the Large Hadron Collider from viscous hydrodynamic," *Phys. Rev.* **C84** (2011) 044903, `arXiv:1105.3226 [nucl-th]`.

[98] V. Minissale, F. Scardina, and V. Greco, "Hadrons from coalescence plus fragmentation in *aa* collisions at energies available at the bnl relativistic heavy ion collider to the cern large hadron collider," *Phys. Rev. C* **92** (Nov, 2015) 054904. `https://link.aps.org/doi/10.1103/PhysRevC.92.054904`.

[99] L. Evans and P. Bryant, "LHC Machine," *JINST* **3** (2008) S08001.

[100] **ALICE** Collaboration, K. Aamodt *et al.*, "The ALICE experiment at the CERN LHC," *JINST* **3** (2008) S08002.

[101] **ATLAS Collaboration** Collaboration, *ATLAS: technical proposal for a general-purpose pp experiment at the Large Hadron Collider at CERN*. LHC Tech. Proposal. CERN, Geneva, 1994. `https://cds.cern.ch/record/290968`.

[102] **CMS Collaboration** Collaboration, *Technical proposal*. LHC Tech. Proposal. CERN, Geneva, 1994. `https://cds.cern.ch/record/290969`. Cover title : CMS, the Compact Muon Solenoid : technical proposal.

[103] *LHCb : Technical Proposal*. Tech. Proposal. CERN, Geneva, 1998. `https://cds.cern.ch/record/622031`.

[104] **LHCf Collaboration** Collaboration, O. Adriani, L. Bonechi, M. Bongi, R. D'Alessandro, D. A. Faus, M. Haguenauer, Y. Itow, K. Kasahara, K. Masuda, Y. Matsubara, H. Menjo, Y. Muraki, P. Papini, T. Sako, T. Tamura, S. Torii, A. Tricomi, W. C. Turner, J. Velasco, and K. Yoshida, "Technnical Proposal for the CERN LHCf Experiment: Measurement of Photons and Neutral Pions in the Very Forward Region of LHC," Tech. Rep. CERN-LHCC-2005-032. LHCC-P-007, CERN, Geneva, Sep, 2005. `https://cds.cern.ch/record/887108`. revised version submitted on 2005-10-04 11:34:56.

[105] **TOTEM Collaboration** Collaboration, W. e. a. Kienzle, "TOTEM, Total Cross Section, Elastic Scattering and Diffraction Dissociation at the LHC: Technical Proposal," Tech. Rep. CERN-LHCC-99-007. LHCC-P-5, CERN, Geneva, Mar, 1999. `https://cds.cern.ch/record/385483`.

[106] J. Alme *et al.*, "The ALICE TPC, a large 3-dimensional tracking device with fast readout for ultra-high multiplicity events," *Nucl. Instrum. Meth.* **A622** (2010) 316–367, `arXiv:1001.1950 [physics.ins-det]`.

[107] T. A. collaboration, "Performance of the alice vzero system," *Journal of Instrumentation* **8** no. 10, (2013) P10016. `http://stacks.iop.org/1748-0221/8/i=10/a=P10016`.

[108] **ALICE Collaboration** Collaboration, C. e. a. Fabjan, *ALICE trigger data-acquisition high-level trigger and control system: Technical Design Report*. Technical Design Report ALICE. CERN, Geneva, 2004. `https://cds.cern.ch/record/684651`.

[109] J. Durand *et al.*, "CASTOR: Operational issues and new Developments,". `https://cds.cern.ch/record/865802`.

[110] **ALICE** Collaboration, P. Saiz, L. Aphecetche, P. Buncic, R. Piskac, J. E. Revsbech, and V. Sego, "AliEn - ALICE environment on the GRID," *Nucl. Instrum. Meth.* **A502** (2003) 437–440.

[111] R. Brun and F. Rademakers, "ROOT: An object oriented data analysis framework," *Nucl. Instrum. Meth.* **A389** (1997) 81–86.

[112] R. Brun, F. Carminati, and S. Giani, "GEANT detector description and simulation tool," *CERN-W5013* (1994) .

[113] A. Fasso, A. Ferrari, S. Roesler, P. Sala, F. Ballarini, A. Ottolenghi, G. Battistoni, F. Cerutti, E. Gadioli, M. Garzelli, A. Empl, and J. Ranft, "The physics models of FLUKA: status and recent development," *eConf* **C0303241** no. hep-ph/0306267, (Jun, 2003) MOMT005. 10 p. `https://cds.cern.ch/record/625976`.

[114] **ALICE** Collaboration, B. Abelev *et al.*, "Performance of the ALICE Experiment at the CERN LHC," *Int. J. Mod. Phys.* **A29** (2014) 1430044, `arXiv:1402.4476 [nucl-ex]`.

[115] **ALICE** Collaboration, K. Aamodt *et al.*, "Charged-particle multiplicity measurement in proton-proton collisions at $\sqrt{s} = 0.9$ and 2.36 TeV with ALICE at LHC," *Eur. Phys. J.* **C68** (2010) 89–108, `arXiv:1004.3034 [hep-ex]`.

[116] **ALICE Collaboration** Collaboration, B. e. a. Abelev, "Centrality determination of pb-pb collisions at $\sqrt{s_{NN}} = 2.76$ tev with alice," *Phys. Rev. C* **88** (Oct, 2013) 044909. `https://link.aps.org/doi/10.1103/PhysRevC.88.044909`.

[117] A. Ilner, D. Cabrera, P. Srisawad, and E. Bratkovskaya, "Properties of strange vector mesons in dense and hot matter," *Nucl. Phys.* **A927** (2014) 249–265, `arXiv:1312.5215 [hep-ph]`.

[118] S. I. Bityukov, "Signal Significance in the Presence of Systematic and Statistical Uncertainties," *JHEP* **09** no. hep-ph/0207130, (Jul, 2002) 060. 9 p. `http://cds.cern.ch/record/569413`.

[119] P. Crochet and P. Braun-Munzinger, "Investigation of background subtraction techniques for high mass dilepton physics," *Nucl. Instrum. Meth.* **A484** (2002) 564–572, `arXiv:nucl-ex/0106008 [nucl-ex]`.

[120] R. Brun, P. Buncic, F. Carminati, A. Morsch, F. Rademakers, and K. Safarík, "Computing in ALICE," *Nucl. Instrum. Methods Phys. Res., A* **502** (2003) 339–346. `http://cds.cern.ch/record/624987`.

[121] **STAR** Collaboration, J. Adams *et al.*, "K(892)* resonance production in Au+Au and p+p collisions at $\sqrt{s_{\mathrm{NN}}}$ = 200 GeV at STAR," *Phys. Rev.* **C71** (2005) 064902, `arXiv:nucl-ex/0412019 [nucl-ex]`.

[122] **DELPHI** Collaboration, P. Abreu *et al.*, "Production characteristics of K^0 and light meson resonances in hadronic decays of the Z^0," *Z. Phys.* **C65** (1995) 587–602.

[123] **ALICE** Collaboration, B. B. Abelev *et al.*, "$K^*(892)^0$ and $\phi(1020)$ production in Pb-Pb collisions at $\sqrt{sNN}$ = 2.76 TeV," *Phys. Rev.* **C91** (2015) 024609, `arXiv:1404.0495 [nucl-ex]`.

[124] M. Floris, "Hadron yields and the phase diagram of strongly interacting matter," *Nucl. Phys.* **A931** (2014) 103–112, `arXiv:1408.6403 [nucl-ex]`.

[125] T. Ullrich and Z. Xu, "Treatment of Errors in Efficiency Calculations," Tech. Rep. physics/0701199, Jan, 2007. `http://cds.cern.ch/record/1010669`.

[126] C. Tsallis, "Possible Generalization of Boltzmann-Gibbs Statistics," *J. Statist. Phys.* **52** (1988) 479–487.

[127] R. Barlow, "Systematic errors: Facts and fictions," in *Advanced Statistical Techniques in Particle Physics. Proceedings, Conference, Durham, UK, March 18-22, 2002*, pp. 134–144. 2002. `arXiv:hep-ex/0207026 [hep-ex]`. `http://www.ippp.dur.ac.uk/Workshops/02/statistics/proceedings/ /barlow.pdf`.

[128] **ALICE Collaboration** Collaboration, "ALICE luminosity determination for pp collisions at $\sqrt{s} = 13$ TeV,". `https://cds.cern.ch/record/2160174`.

[129] C. Loizides, J. Kamin, and D. d'Enterria, "Improved monte carlo glauber predictions at present and future nuclear colliders," *Phys. Rev. C* **97** (May, 2018) 054910. `https://link.aps.org/doi/10.1103/PhysRevC.97.054910`.

[130] K. Garg, "First results on $\mathrm{K}^*(892)^\pm$ resonance production in pp collisions with ALICE at the LHC," 2018. `arXiv:1811.10916 [hep-ex]`.

[131] B. Andersson, S. Mohanty, and F. Soderberg, "The Lund fragmentation process for a multigluon string according to the area law," *Eur. Phys. J.* **C21** (2001) 631–647, `arXiv:hep-ph/0106185 [hep-ph]`.

[132] **ALICE** Collaboration, K. Aamodt *et al.*, "Production of pions, kaons and protons in pp collisions at $\sqrt{s} = 900$ GeV with ALICE at the LHC," *Eur. Phys. J.* **C71** (2011) 1655, `arXiv:1101.4110 [hep-ex]`.